The Influence of Unsteady Wind on the Performance and Aerodynamics of Vertical Axis Wind Turbines

A Dissertation Submitted for the Degree of Doctor of Philosophy

by

Louis Angelo M. Danao

The University of Sheffield
Department of Mechanical Engineering
September 2012

Abstract

Interest in small–scale wind turbines as energy sources in the built environment has increased due to the desire of consumers in urban areas to reduce their carbon footprint. Vertical axis wind turbines (VAWTs) have shown to be potentially well suited within the urban landscape. However, there is a large gap in the fundamental understanding of VAWT operation in turbulent, unsteady wind that is typical of the built environment.

This dissertation investigates the aerodynamics and performance of VAWTs in fluctuating wind through experiments and numerical simulations. All experimental investigations utilise a low–speed open section wind tunnel. The use of a shutter mechanism that generates unsteady wind in the wind tunnel is detailed. Performance measurements for turbine power use a validated method previously developed in the same laboratory with slight modification for unsteady wind performance. Both steady and unsteady power performance tests results are presented. Near–blade flow physics during steady wind operation is scrutinised using Particle Image Velocimetry (PIV).

Complementing the findings in experiments, numerical simulations using Unsteady Reynolds Averaged Navier–Stokes Computational Fluid Dynamics (URANS CFD) are employed. The numerical model is validated using experimental data. Blade force measurements that are not available from experiments are extracted from the numerical models to provide additional insight for performance analysis. A survey of varying unsteady wind parameters is conducted to examine the effects of various unsteady wind conditions on the performance of the VAWT. The aerodynamics is inspected through vorticity visualisations alongside blade force metrics to link performance to blade stall. Results show marginal improvement on VAWT performance (CP) with small wind speed fluctuations versus steady wind CP. Operating the VAWT at tip speed ratios (λ) higher than steady wind peak CP λ also improve performance. Conditions other than the stated above reduce VAWT CP.

Declaration

Described in this dissertation is work performed in the Department of Mechanical Engineering, the University of Sheffield between December 2009 and August 2012. I hereby declare that no part of this work has been submitted as an exercise for a degree at this or any other university. This dissertation is entirely the result of my own work and includes nothing which is the outcome of collaboration, except when stated otherwise. This dissertation contains 122 figures and approximately 45,000 words.

Signed:

Louis Angelo M. Danao

Dated: ____/____/_____

Dedicated to my wife Nina, for believing in me.

Acknowledgements

First and foremost, I would like to thank my supervisor, Dr Robert Howell, for his advice and encouragement all throughout the last three years. His invaluable insight and consistent mentoring have made my work more enjoyable and interesting. Furthermore, I would like to thank Professor Ning Qin for his very useful comments in my early days of CFD modelling.

I would also like to thank several persons in my research group. Jonny's well explained demonstrations regarding the ins and outs of wind tunnel work and VAWT performance testing using his spin down technique have brought my experience in experimental aerodynamics work from virtually nothing to acceptable levels. His assistance in the PIV measurements was extremely helpful. Furthermore, I would like to thank Jon, Oke, Joe and Dorit for extra hands and constructive comments in my experiments and CFD work. Additional thanks are extended to the technicians in the workshop for all fabrication work they have done for my experiment setup.

On a personal note, I am particularly grateful to my family especially my wife Nina and daughter Toni for keeping me grounded and sane as I ventured into this journey. Their love and support have kept me positive and helped me stay in the right path.

Finally, I would like to thank the Almighty God for the strength and patience He has given me, without which I would have certainly failed.

The Engineering Research and Development for Technology program of the Department of Science and Technology through the University of the Philippines – College of Engineering is gratefully acknowledged for the financial assistance that allowed me to pursue this endeavour.

Nomenclature

Symbols

A	rotor frontal swept area, $2RL$, (in hotwire anemometry, constant 1)
AR	blade aspect ratio, L/c
B	in hotwire anemometry, constant 2
c	blade chord
C_d	drag coefficient
C_l	lift coefficient
C_m	moment coefficient
CP	power coefficient
d_c	characteristic dimension of obstacle
d_d	diameter of tracer particle
D_g	gust length
d_o	pressure outlet boundary distance from VAWT axis
d_s	side wall boundary distance from VAWT axis
f_c	characteristic frequency of unsteady wind
F_d	drag force
F_l	lift force
gr	inflation growth rate of mesh
I_{rig}	rotor rotational mass moment of inertia
k_g	reduced gust frequency
k–ε	turbulence model based on turbulent kinetic energy and turbulent dissipation
k–ε RNG	variant of k–ε using Re-Normalisation Group methods
k–ω	turbulence model based on turbulent kinetic energy and specific dissipation
k–ω SST	variant of k–ω by Menter (1993)
L	blade length
N	number of blades, (in statistics, number of sample points)
n	in hotwire anemometry, constant 3
p	ambient pressure (Pascals)
P	ambient pressure (mmHg)
P_B	blade power (three blades)
P_w	wind power
q	dynamic pressure
R	rotor radius, (in ideal gas law, specific gas constant)
Re	blade Reynolds number
R_g	number of revolutions per wind cycle

Symbols continued . . .

S–A	Spalart–Allmaras turbulence model
S_k	Stoke's number
s_y	standard error
t	time
T	temperature
T_{app}	applied brake torque
T_b	blade torque (single blade)
T_B	blade torque (three blades)
T_{res}	resistive torque
Tu	turbulence intensity
U	instantaneous wind speed, (invorticity, velocity along x–axis)
U_∞	free stream wind speed
U_{amp}	amplitude of fluctuation of unsteady wind
U_{mean}	mean speed of unsteady wind
V	hotwire voltage, (invorticity, velocity along y–axis)
V_b	blade velocity, $R\omega$
W	relative velocity of wind with respect to blade, (invorticity, velocity along z–axis)
y^+	dimensionless wall distance
y_i	sample value
$\hat{y}$	fit value

Greek symbols

α	angle of attack
α_A	amplitude of angle of attack
α_o	mean angle of attack
ΔCP	change in CP
Δt	in CFD, time step size
θ	azimuth position
κ	pitching aerofoil reduced frequency
λ	tip speed ratio, $R\omega/U_\infty$
λ^*	tip speed ratio at peak CP
λ_{mean}	tip speed ratio corresponding to ω_{mean}
μ	laminar viscosity
μ_f	dynamic viscosity of fluid
μ_t	turbulent viscosity
ξ	rotor angular acceleration
ρ	air density
ρ_d	density of tracer particle
σ	rotor solidity, Nc/R
$\overline{\Phi}$	3D vorticity
Φ_z	vorticity along z–axis
τ	tracer particle response time
ω	rotor angular speed
ω_{mean}	in unsteady wind, mean of ω

Abbreviations

CFD	Computational Fluid Dynamics
DES	detached eddy simulation
FOV	field of view
HAWT	horizontal axis wind turbine
LES	large eddy simulation
LEV	leading edge vortex
NACA	National Advisory Committee for Aeronautics
OES	organised eddy simulation
PIV	Particle Image Velocimetry
RANS	Reynolds Averaged Navier–Stokes
TEV	trailing edge vortex
URANS	Unsteady RANS
VAWT	vertical axis wind turbine
VTM	vorticity transport model

Contents

List of Figures

List of Tables

Chapter 1
Introduction

A general consensus has been made in the recent years that the effects of climate change are becoming more severe and prevalent [1]. The main cause of the increasing rate of undesirable climatic conditions has been identified as greenhouse gas emissions from the burning of fossil fuels used primarily for energy generation and transportation purposes. For this reason, there has been a pressing need to reduce emissions through the use of technologies that are capable of extracting energy from the environment whilst being non–polluting and sustainable. Several alternative sources to fossil fuels have been identified: tidal, solar, biomass, and wind. These are branded as 'renewables' and have attracted significant research attention in the past decades. Of these renewable sources, the contribution of wind to the total energy generation of the U.K. has been steadily rising over the last few years and has seen the greatest increase in 2011 of 68% for offshore installations and 45% for onshore [2]. Wind has also been the leading renewable technology for electricity generation with 45% of the total 2011 renewable production. Despite these numbers, the total consumption of electricity from renewable sources only account for 9.4%. And the proportion of

wind in the overall consumption is very low at 0.7% [3]. As a result, further research is needed to increase the understanding of this renewable power source to promote its wider adoption.

Wind turbines can be classified into two general types: drag machines (Figure 1.1a) and lift machines (Figure 1.1b & c). Drag machines generate forces through the creation of large separated flows and move slower than the wind. The most common application of these devices is in water pumping. In lift machines, the wind is made to follow a curved path as it passes about a rounded object. The turning of the fluid generates forces on the object, typically of an aerofoil profile, thus producing the required thrust. Blade speeds are most often greater than the wind speed and far exceeds what is possible in drag machines. Lift machines are thus more favourable from an energy production view point due to a greater potential for energy extraction.

a. b. c.

Figure 1.1. Examples of wind turbines: a) drag VAWT[1], b) lift HAWT[2], c) lift VAWT[3].

There are two main methods of extracting energy utilising the lift concept: horizontal axis wind turbines or HAWT (Figure 1.1b) and vertical axis wind turbines or VAWT (Figure 1.1c). HAWTs have received significant research and development work over the decades giving them a well–established and mature technology base that makes them the preferred configuration in all large scale wind farm installations. VAWTs on the other hand have not been given the same attention. The complex aerodynamic and structural aspects of VAWT operation

[1] Oy Windside Production Ltd., http://www.windside.com.
[2] Wikimedia Commons, Creative Commons Attribution 2.0 Generic license.
[3] Quiet Revolution Ltd., http://www.quietrevolution.com.

make their understanding and optimisation difficult which is one of the reasons why they are less favoured than their horizontal counterparts.

There are several points of contention on the use of VAWTs over HAWTs. The key point that prevails is the generally perceived superior performance of HAWTs over VAWTs. Nevertheless, VAWTs present a number of potential advantages over HAWTs when it comes to applications in the built environment:

- easier maintenance because of the rotor's proximity to the ground. VAWTs are typically smaller in scale and mounted on masts that are many times shorter than conventional HAWT installations. Additionally, the rotor sits on a bearing and drives the generator below it.
- no need to yaw to the wind thus reducing the efficiency loss when tracking changes in wind direction.
- sound emissions are usually lower as they operate at lower tip speed ratios [4]. This can also reduce structural issues such as vibration that result from high centrifugal forces.
- potentially lower manufacturing costs due to the simplicity of the straight blade shape.
- better performance in skewed flow [5].

VAWTs are not without their disadvantages when compared to HAWTs. The most common are:

- lower efficiency due to the additional drag of blades moving against the wind. Moreover, HAWTs are presumably more optimised in their design as a consequence of greater efforts made in research and development.
- less access to stronger winds in higher elevations.
- complex aerodynamics resulting in continuously fluctuating blade loading during operation and therefore a lower fatigue life cycle.
- difficult to implement variable pitch without complicated mechanisms. HAWT blades can be pitched easily to the optimum angle of attack to maximise energy extraction.

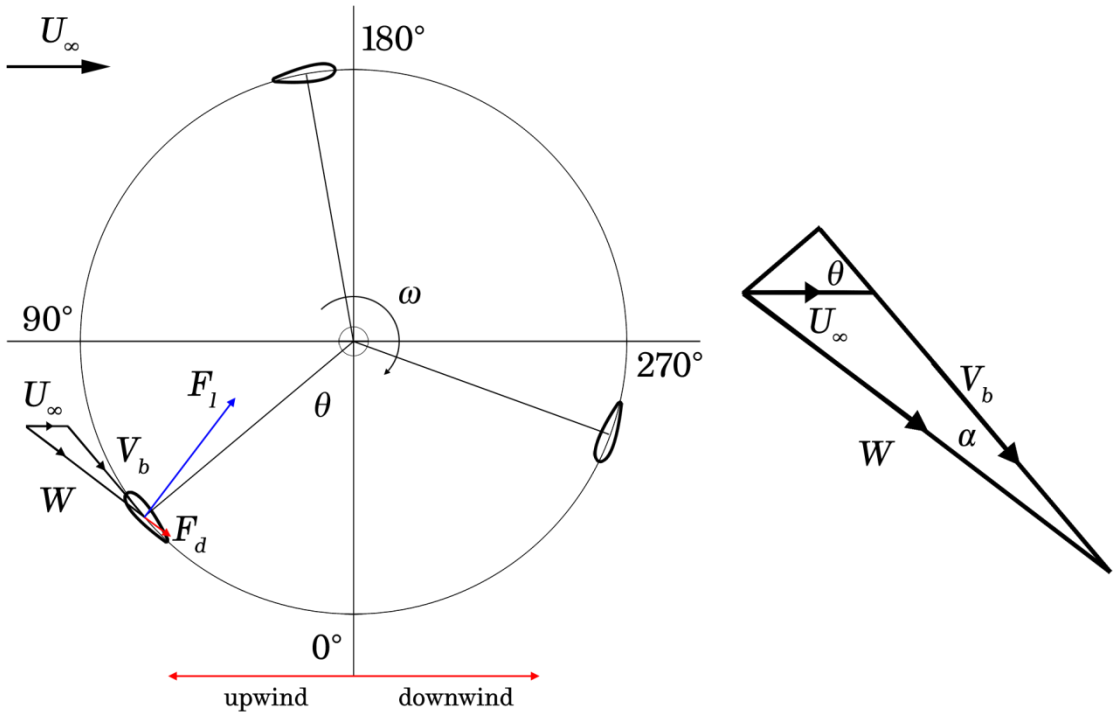

Figure 1.2. An illustration of the vectors on a VAWT blade.

During operation, a VAWT blade experiences cyclic variations in angle of attack α. As such, the blade may undergo stalled and unstalled conditions as well as interact with its own wake and that of other blades within one rotation. Figure 1.2 illustrates the kinematic and kinetic vectors on a VAWT blade. As the VAWT rotates with angular velocity ω in a flow of wind speed U_∞, the velocity of the wind relative to the blade, W, changes and is given by

$$W = U_\infty + V_b \tag{1.1}$$

where $V_b = -\omega R$ and R is the radius of the VAWT. This velocity fluctuates from a maximum of $(\lambda + 1)U_\infty$ to a minimum of $(\lambda - 1)U_\infty$, where λ is the tip speed ratio. At the same time, the angle of attack α also varies periodically between positive and negative values. The magnitudes of the relative velocity and the angle of attack are given by

$$W = U_\infty \sqrt{1 + 2\lambda \cos\theta + \lambda^2} \tag{1.2}$$

$$\alpha = \tan^{-1}\left(\frac{\sin\theta}{\lambda + \cos\theta}\right) \tag{1.3}$$

where θ is the azimuth angle and is measured from the vertical Y–axis in the clockwise direction.

A major assumption used in this analysis is the constant direction of the free stream velocity vector U_∞, herein termed as geometric assumption. In as much as the traditional definition of aerodynamic coefficients are based on the free stream, effects of the rotor impedance on the flow streamlines that the blades encounter are neglected and conventional ways of defining the coefficients are followed. A localised effective wind speed has been presented by Edwards et al [6] and Raciti Castelli et al [7] to 'correct' this assumption leading to more accurate estimates of α. However, the method will not be useful in this thesis because it involves averaging velocity flow fields over a complete VAWT rotation in steady wind and will not work when unsteady wind cycles comprising of multiple VAWT cycles are considered. Therefore, only the geometric assumption will be used all throughout.

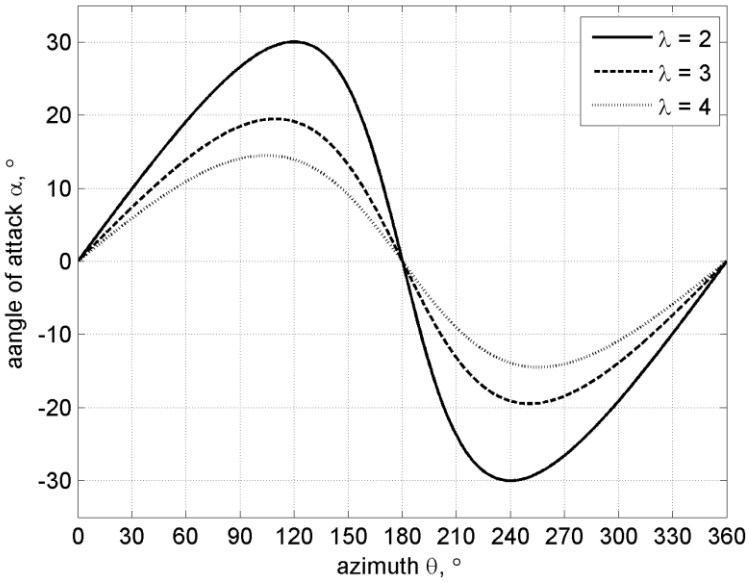

Figure 1.3. Computed angle of attack based on geometric assumption.

The variation of α closely resembles a sine wave as shown in Figure 1.3. This perceived variation is relative to a reference frame attached to the rotating VAWT with its origin at the VAWT axis. As the tip speed ratio λ increases, the skewness of the α variation reduces and the profile comes closer to a sine wave (zero skew).

As a blade rotates, the flow will have a certain incidence on it thereby generating the aerodynamic lift F_l and drag F_d (Figure 1.2). Both of these forces will have components along the tangential and normal directions. The normal components do not influence the energy generation of the rotor. However, they are a key factor when it comes to structural considerations. The tangential components are the primary driving forces that dictate the performance of the VAWT and give rise to the instantaneous blade torque T_b :

$$T_b = \left(F_l \sin\alpha + F_d \cos\alpha\right) R \tag{1.4}$$

There is also the aerodynamic moment about the blade, whose contribution to the overall torque is dependent on where the blade is mounted chord–wise. This is usually small and may be neglected when the mounting point is within the general area of the aerodynamic centre of the profile. Given that a VAWT will likely have more than one blade, the instantaneous rotor power P_B is computed as

$$P_B = N\omega T_b \tag{1.5}$$

$$P_w = \tfrac{1}{2}\rho A U_\infty^3 \tag{1.6}$$

$$\mathrm{CP} = \frac{P_B}{P_w} \tag{1.7}$$

where N is the number of blades. The instantaneous wind power P_w is a function of the VAWT swept area $A = 2RL$ where L is the blade length, the air density ρ, and the free stream wind speed U_∞ (Eq. 1.6). Finally, the instantaneous power coefficient CP is the ratio of P_B and P_w (Eq. 1.7).

In steady wind conditions, the VAWT CP is normally computed by averaging the instantaneous blade torque over one rotor cycle thus making the CP independent of azimuth position and giving a single–valued metric of the VAWT performance. In unsteady wind conditions, performance is computed by averaging P_B and P_w over one wind cycle before taking their ratio.

1.1 Research Objectives

So much of the work on VAWT research is focused on steady wind conditions. If their use in the built environment is to be successful, current efforts related to small scale VAWT should concentrate more on unsteady wind performance since the wind in the urban terrain is never steady, which makes all of the steady wind analyses of less use.

The accurate assessment of the effects of unsteady wind on the performance of the VAWT poses a significant challenge. Experimentally the concept of generating periodic fluctuations of wind speed in the wind tunnel is not well established and difficult to implement. Measurement of the performance entails the use of high resolution data logging instrumentation so that the unsteady nature of VAWT operation is captured. The present literature on numerical simulations of VAWTs subjected to unsteady wind is very limited and majority use mathematical models that derive blade forces from table lookups of static aerofoil data. High resolution Navier–Stokes based Computational Fluid Dynamics (CFD) models that are independent of such tables barely exist.

It is the aim of the present work to fill in the gaps in the literature and provide a substantial knowledgebase on both experimental and numerical methods, data and analyses that will increase the current understanding of VAWT performance to include not just steady wind conditions but also fluctuating winds that are characteristic of the built environment. The research described in this dissertation includes the development of a mechanism to generate sinusoidal

wind fluctuations in a wind tunnel facility and the use of previously developed measurement tools within the laboratory to measure VAWT aerodynamics and performance. Additionally, the development of a CFD–based numerical model is presented and validated against experiments to aid in the analysis of how and why a VAWT performs as it does in unsteady wind. The crucial linking of aerodynamics and performance is a key point in this body of work which will provide a more complete picture of VAWT operation in unsteady wind.

It is not the aim of this research to provide absolute values of VAWT performance that may be used for comparison to commercially available machines. The present work is limited to a VAWT that operates in much lower Reynolds numbers and has a scale that does not exist in the current market. The data presented in this dissertation is exclusively for a wind tunnel VAWT and as such the conclusions are only applicable to rotors of similar scale. Nevertheless, most of the flow physics will be similar such that the methods developed and analyses presented may be transferable to larger scales.

1.2 Synopsis

The structure of the dissertation is arranged as follows:

Chapter 2 presents a review of the present body of literature related to VAWTs from the early work on momentum modelling to modern numerical methods including CFD and turbulence modelling. Studies on VAWT performance influenced by geometric characteristics are also reviewed.

Chapter 3 outlines and describes the newly developed experimental methods used in the determination of VAWT CP as well as the campaign of particle image velocimetry (PIV) measurements. Experimental error analysis is presented to provide a feel of the accuracy and consistency of the measured data.

Chapter 4 details the development of the numerical model starting with the verification of the wind tunnel model in terms of its spatial and temporal characteristics, moving on to the selection of suitable turbulence models for the CFD solver, and finally to the validation of the CFD model using experimental performance and visualisation data.

In Chapter 5, the results of the performance measurements using a spin–down technique is presented. PIV visualisations of the near–blade flow field are used to link the aerodynamics of steady wind VAWT operation to its performance at two different tip speed ratios. Unsteady wind performance data is presented and analysis provided for a reference case after which effects of variations of operating conditions are compared.

In Chapter 6, numerical results for both steady and unsteady wind conditions are presented in a similar style to the experimental results chapter. Steady wind performance and aerodynamics are linked using plots of aerodynamic force coefficients and vorticity flow field images. Unsteady wind performance is broken down into sections to give a step–by–step analysis of parameter fluctuations that lead to the final unsteady CP. Visualisations of vorticity are also made available to complement the performance data provided. A reference case is described and subsequently compared to cases of different operating conditions. The important relationship of VAWT CP and blade aerodynamics is presented to connect flow physics to the VAWT performance in unsteady wind.

Chapter 7 brings all findings from the experimental and numerical work into a summary of gained knowledge and contributions to the state of the art in VAWT research. Suggestions to future work follow the summary.

1.3 Publications

During the course of research, several components of the work have been presented and published in a conference and published in relevant journals. The following is a list of the papers co–written by the Author in chronological order:

Danao, L.A., and Howell, R., 2012, "*Effects on the Performance of Vertical Axis Wind Turbines with Unsteady Wind Inflow: A Numerical Study*," 50th AIAA Aerospace Sciences Meeting including the New Horizons Forum and Aerospace Exposition, Nashville, Tennessee.

Edwards, J.M., Danao, L.A., and Howell, R., 2012, "*Novel Experimental Power Curve Determination and Computational Methods for the Performance Analysis of Vertical Axis Wind Turbines*," Journal of Solar Energy Engineering, 134(3), pp. 11.

Danao, L.A., Qin, N., and Howell, R., 2012, "*A Numerical Study of Blade Thickness and Camber Effects on Vertical Axis Wind Turbines*," Proceedings of the Institution of Mechanical Engineers, Part A: Journal of Power and Energy, 31 July 2012, doi: 10.1177/0957650912454403, pp. 15.

There are also a number of papers co–written by the Author that were submitted for publication in various journals. These are the following:

Danao, L.A., Eboibi, O., Howell, R., "*An Experimental Investigation into the Influence of Unsteady Wind in the Performance of a Vertical Axis Wind Turbine*". Submitted to Applied Energy.

Eboibi, O., Danao, L.A., Howell, R., "*A Numerical Study of the Influence of Reynolds Number and Solidity on the Performance of Vertical Axis Wind Turbines*". Submitted to Proceedings of the Institution of Mechanical Engineers, Part A: Journal of Power and Energy.

Edwards, J., Danao, L.A., Howell, R., "*The Flow Physics and Performance of a Small-Scale Vertical Axis Wind Turbine, Including Flowfield Visualisations by PIV*". Submitted to Wind Energy.

Edwards, J., Danao, L.A., Howell, R., "*CFD Simulation of the Flow Physics and Performance of a Small-Scale Vertical Axis Wind Turbine, Including a Validation Study Using PIV and Performance Measurements*". Submitted to Wind Energy.

Wang, S., Hughes, K.J., Ingham, D.B., Ma, L., Pourkashanian, M., Tao, Z., Edwards, J., Howell, R., Danao, L.A., Sobotta, D., Qin N., "*An experimental investigation into the aerodynamics of a vertical axis wind turbine using PIV*". Submitted to Wind Engineering and Industrial Aerodynamics.

Chapter 2
Literature Review

2.1 Introduction

The objective of this chapter is to put into perspective the motivation for the work conducted in this thesis by presenting a chronological and systematic review of the relevant literature. The contributions and limitations of the published material is assessed and discussed to establish the gaps in the field of VAWT research, some of which this project aims to fill. Further to the discussion of literature presented herein, relevant sections in the results chapters will contain topic–specific reviews of related literature.

This chapter is divided into three main sections: numerical modelling, computational fluid dynamics, and basics of VAWT performance. The contributions of each are discussed to show the current understanding of the different factors that affect the performance of the VAWT.

2.2 Numerical Modelling of the VAWT

Research into the VAWT design was carried out as long ago as the 1970's notably at the USA Department of Energy Sandia National Laboratory. Both numerical and experimental studies were performed that set the baseline for subsequent research in the field, from the development of mathematical models to experimental work and more recently to high fidelity computational models.

The main objective of numerical modelling of the VAWT is to create a mathematical representation of the problem such that extensive studies can be performed at relatively low cost. Parametric design studies that involve multiple candidate aerofoils with several geometric configurations subjected to various operating conditions can be carried out in a virtual environment without the need for fabrication work and setup that laboratory experiments entail.

There are generally two well accepted types of numerical modelling used in current research work. The first is usually termed mathematical modelling where the VAWT problem is described in mathematical expressions in which the flow field and blade loading are solved using simplistic generalisations derived from fundamental aerodynamic theories. As in the case of blade element momentum models, the flow properties around the VAWT blade are assumed and blade loading is determined by referring to static aerofoil data from published experimental data. More accurate models employ the use of dynamic stall models (another set of mathematical models) that emulate the loading that is expected in a pitching and/or plunging aerofoil and use these effects to complement the static aerofoil data set. The main advantage of mathematical models is the speed at which solutions are arrived at. Typically the computing costs are very low and results are available in minutes to hours. The downside is the lack of fidelity when it comes to near wall modelling. As such, the boundary layers on blade surfaces cannot be studied in detail. They cannot necessarily be trusted beyond conservative limits.

The second class of numerical modelling is computational fluid dynamics (CFD). In this approach, the entire flow field including the near wall can be computed using several forms of the Navier–Stokes equations. Reynolds Averaged Navier Stokes (RANS) is one such form and uses turbulence closure equations, known as turbulence models, to make the problem solvable. The fluid domain is discretised into cells or elements and all flow variables calculated for each. There is an intrinsic advantage to this method because there is no assumption made as to the forces acting on the blades and no lookup to data tables. All pressure and viscous loads are computed for each and every fluid cell or element. This in turn avoids the use of inappropriate data sets that could give misleading results. Due to the high fidelity of the solution, the major disadvantage to using CFD is the enormous computing costs that it demands. Solutions can be obtained from as low as tens of hours to a few weeks depending on how fine the domain is meshed. Fortunately with the advances in computing hardware including multi–core chips that offer parallel computing on a desktop machine and increasing storage sizes that can accommodate gigabytes of data, CFD has become a more widely used tool in VAWT research.

In the following sections, a review of the current body of literature involving mathematical modelling of the VAWT is presented. The advantages and disadvantages of each are laid out and an attempt to present a chronological development of the state of the art in VAWT research is made.

2.2.1 Momentum Theory

As early as the 1970s, work has been carried out to adapt the concept of blade element momentum theory into VAWT aerodynamics. Templin [8] proposed in 1974 the single stream tube model as a prediction tool for the calculation of VAWT performance. The model incorporates the actuator disc theory derived from Glauert's [9] analysis of a propeller. When applied to the VAWT, the rectangular frontal swept area is analogous to the circular swept area of the

propeller. This theory assumes a constant velocity induction all throughout (Figure 2.1) the swept area and is derived from the notion that the streamwise drag is equal to the change in momentum.

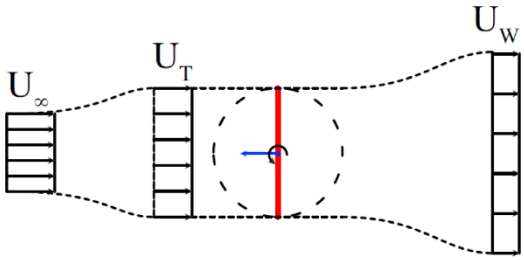

Figure 2.1. Templin's single stream tube model, adapted from [10].

A major drawback of Templin's model is the simplification of the interference that causes velocity induction. Although this is an acceptable approximation for lightly loaded blades, the assumption breaks down at highly loaded or high solidity conditions. As the blades rotate, the force that they exert on the fluid stream greatly varies due to a constantly changing apparent angle of attack. Reducing this variation into a single value causes the predictions to deviate significantly from experimental data.

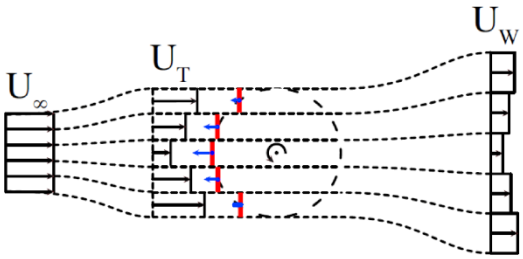

Figure 2.2. Strickland's multiple stream tube model, adapted from [10].

To account for variation in blade loading at different azimuth positions, Strickland [11] proposed an improvement to Templin's model by splitting the stream tube into multiple strips or filaments, each with its own actuator disc. As such, variation in the induced velocity across the swept area (Figure 2.2) can be taken into account for more accurate prediction of blade loading. This model included lift forces as well as drag effects from the derived local angle of attack and experimental data tables. Strickland's model shows improved performance

predictions versus the single stream tube model with less overestimation especially for highly loaded and high solidity VAWTs.

Prior to Strickland's model, Wilson and Lissaman [12] proposed a form of the multiple stream tube model that only accounts for lift forces in blade loading effectively assuming inviscid flow and uses the theoretical lift force instead of actual experimental data. Their model is still an improvement over the single stream tube and requires less computational cost as compared to Strickland's model.

Although the multiple stream tube concept greatly improves the prediction of VAWT performance, there is still an inherent flaw in the theory. The blade loading in the downwind pass is not considered. The overall performance of a VAWT is highly dependent on the upwind as well as the downwind blade loading. It is a major consideration in VAWT aerodynamics. Paraschivoiu [13] in 1981 proposed the double multiple stream tube model where each strip in the stream tube has two actuator discs, one each for both upwind and downwind pass. With this additional actuator disc, the forces on the blades as they pass the downwind are more accurately assessed due to a secondary velocity induction.

2.2.2 Vortex models

Vortex models are potential flow models that aim to calculate the velocity field within and around the VAWT by considering the influence of vorticity in the wake of the blades. The turbine blade is represented by bound vortex filaments and the strength of these vortices is determined using aerofoil coefficient data sets and applying locally calculated relative velocity and angle of attack. The strength of the bound vortex changes over time with a spanwise vortex regularly shed from the trailing edge. The strength of the shed vortex is equal to the change in the bound vortex strength. The velocity induced by a shed vortex is determined using the Biot–Savart law, which associates the induced velocity to the filament

strength. The local flow velocity is calculated using the unperturbed free stream value and the induction of all shed vortex filaments in the flow field.

Larsen [14] is credited with one of the earliest vortex models developed. Later on, further models were introduced by Fanucci and Walters [15], Holme [16], and Wilson [17] with common underlying assumptions: a) all models were two dimensional but were used to represent full three dimensional problems, b) angle of attack considered were small effectively removing blade stall from the analysis, c) blade loading analysis only valid for lightly loaded rotors.

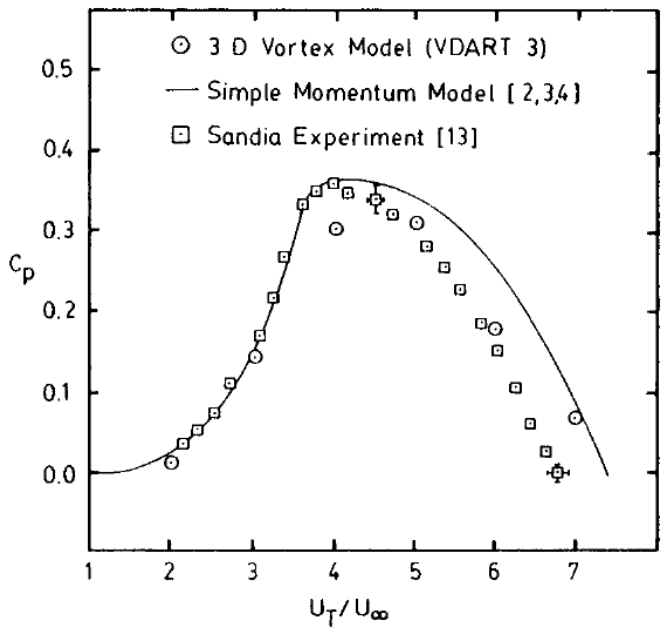

Figure 2.3. Strickland's vortex model vs. experiments and momentum model [18].

Strickland [18] presented in 1979 an improvement of the vortex model by incorporating 3D effects, dynamic stall, and free wake. Reasonably good agreement in results was seen versus momentum models (Figure 2.3). However, it was observed that the model results deviated from experiments with high solidity rotors and that there was difficulty in getting consistent experimental data for some cases which may have contributed to the mismatching of model and experiment.

Cardona [19], in 1984, introduced an improved version of Strickland's model by incorporating curvature effects suggested by Migliore [20] in 1980. He observed better agreement of his model to experiments both in instantaneous blade loading as well as overall power coefficients.

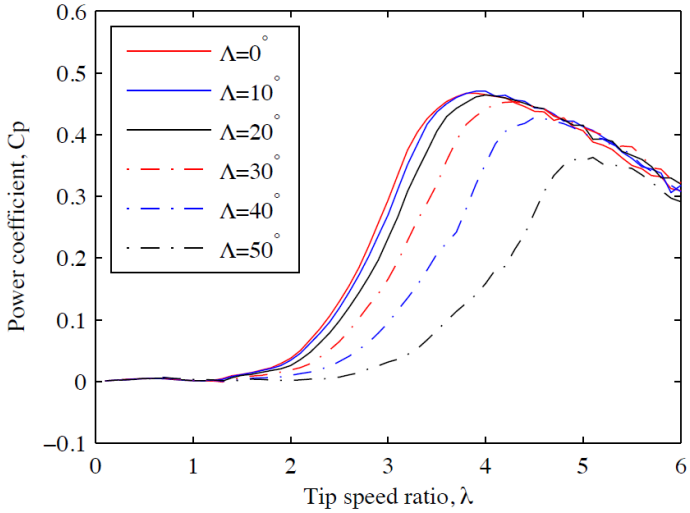

Figure 2.4. Effect of blade sweep on power coefficient [21].

With the resurgence of interest in recent years over VAWT modelling, a new set of vortex models have been developed in the past few years that build up on previous work. In 2009, McIntosh and Babinsky [21] presented a two dimensional swept vortex model that incorporates blade sweep and unsteady wind considerations in the analysis. The model was validated using force data from steady wind experiments conducted in a full scale rotor and very good agreements were seen in both swept and unswept configurations. It was seen that blade sweep reduces the cyclic loading that blades see but at the same time reduces the overall power coefficient because the operating tip speed ratio is pushed to higher values where more power conversion losses are observed (Figure 2.4).

2.2.3 Other models

A 3D free–wake panel method was presented by Dixon et al [22] in 2008 to model a vertical axis wind turbine of arbitrary configuration. The model was validated by comparison with 2D–stereo Particle Image Velocimetry (PIV) and smoke trail studies for a straight-bladed VAWT. It was shown that the wake deformation has an obvious effect on the angles of attack seen by the blade and is confirmation of the inaccuracy of using the geometric angle of attack in VAWT aerodynamic analysis. Initial results show that tip vortices from a straight bladed VAWT move inwards due to wake roll-up behaviour in addition to self–induction. Wake expansion is shown to be asymmetric in the XY and YZ planes (Figure 2.5) owing wake self-influence and as a consequence of the cycloidal motion of the VAWT blades.

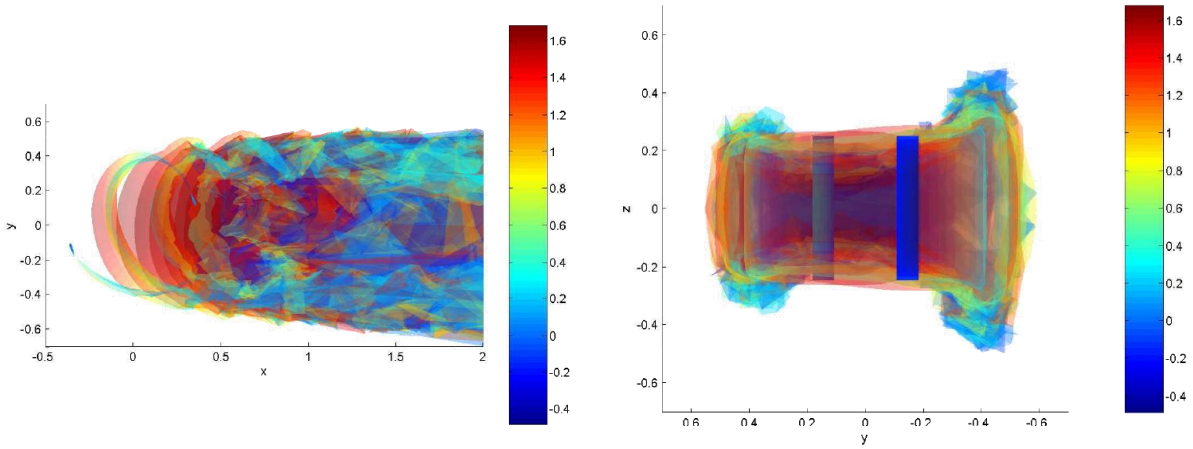

a. b.

Figure 2.5. Asymmetry in the wake from Dixon's free–wake panel code: a) XY plane, b) YZ plane [22].

In 2010, Scheurich et al [23] used the vorticity transport model (VTM) developed by Brown [24] for VAWT analysis and showed good agreement to experimental performance data. The VTM uses the vorticity transport formulation of the Navier–Stokes equations initially applied to helicopter blades. The model is capable of calculating local angle of attack and relative velocity but still relies on static aerofoil data coupled with the Leishman–Beddoes dynamic

stall model to predict blade loading. Both swept and unswept blade configurations were studied and results were consistent to the work done by McIntosh in as far as blade loading is concerned. They argued that much of the disagreement in previous modelling was the lack of fidelity in the blade–wake interaction that has significant effects on the aerodynamic blade loading. This was particularly significant for blade–tip vortical structures released in the upwind pass that are entrained within the VAWT domain causing blade-wake interaction in the downwind pass. The unsteady power coefficients of swept and unswept blades were presented and it was shown that there is not much change in the average CP between the two cases. The difference only lies on the amplitudes of the CP fluctuation over a full rotation of the rotor.

2.2.4 Summary

Numerical modelling has been instrumental in spurring the interest in VAWT research. Through early attempts of quantifying the performance of the VAWT, significant insight has been provided into the understanding of the fundamental aerodynamics that prevails. Despite the advances in numerical models that provide more complex and more accurate representations of the flow physics that exists within the VAWT domain, they still are not sufficient in giving near–blade visualisations of the flow that predominantly dictate blade and overall rotor performance. A table of selected mathematical models most influential to VAWT studies is presented in Table 2.1.

Mathematical Model	Main Features	Limitations	Computing Cost	Computing Speed	Agreement with Experimental Data
Single Stream Tube Model (SSTM) by R.J. Templin (1974)	– analytical model based on Glauert's Actuator Disc Theory – uniform induced velocity across the entire VAWT – $Re = 3\times10^5$ to 3×10^6	– lightly loaded blades – no blade stall – geometric angle of attack – look up to static aerofoil data for blade force – no near blade flow physics – no blade–wake interaction	low	fast	over prediction of maximum CP from 7% to 16%
Multiple Stream Tube Model (MSTM) by J.H. Strickland (1975)	– extension of Templin's SSTM using multiple stream tubes – each stream tube has its own actuator disc – $Re = 3\times10^5$ to 3×10^6 , heavily loaded blades and high solidity	– no blade stall – geometric angle of attack – look up to static aerofoil data for blade force – no near blade flow physics – no blade–wake interaction	low	fast	over prediction of maximum CP from 6% to 8%
Double Multiple Stream Tube Model (DMSTM) by I. Paraschivoiu (1981)	– extension of Strickland's MSTM by splitting each stream tube into upwind and downwind sections, each with its own actuator disc – dynamic stall corrections for static aerofoil data – $Re = 3\times10^5$ to 3×10^6, corrected angle of attack	– look up to static aerofoil data for blade force – no near blade flow physics – no blade–wake interaction	low	fast	over prediction of maximum CP by 3%
3D Vortex Model by J.H. Strickland (1979)	– potential flow solver using bound vortex filaments around a blade – velocity induction computed using Biot–Savart law – 3D effects, dynamic stall, free wake, blade–wake interaction, heavily loaded blades, $Re = 3\times10^5$ to 3×10^6	– works only for low solidity – look up to static aerofoil data for blade force – no near blade flow physics	low	fast	under prediction of maximum CP by 17%
Free Vortex Model by S. McIntosh (2007)	– 2D vortex model with blockage effects – capable of unsteady wind analysis – free wake development and vortex merger – $Re = 2\times10^5$ to 4×10^5, corrected angle of attack – dynamic stall corrections for static aerofoil data	– look up to static aerofoil data for blade force – correction factors for finite blade span and spoke drag – no near blade flow physics	low to moderate	moderate to fast	under prediction of maximum CP by 5%
Vorticity Transport Model by F. Scheurich (2010)	– 3D vorticity–velocity form of Navier–Stokes equations – capable of unsteady wind analysis – free wake and blade–wake interactions, dynamic stall – $Re = 2\times10^5$ to 4×10^5, corrected angle of attack – dynamic stall corrections for static aerofoil data	– look up to static aerofoil data for blade force – no near blade flow physics	low to moderate	moderate to fast	under prediction of maximum CP by 3%

Table 2.1. Summary of VAWT mathematical models.

2.3 Computational Fluid Dynamics

Significant advances in computational hardware resources have driven research into high fidelity numerical simulations using Reynolds Averaged Navier–Stokes based Computational Fluid Dynamics. The fine detail of CFD brings significant insight into the understanding of the performance of VAWTs and as such is an attractive method of choice. The ability of CFD to compute for aerodynamic forces on blades takes away the need for static and dynamic aerofoil data lookup which is an inherent prerequisite of the mathematical models presented above. The unsteady nature of the VAWT problem necessitates a highly flexible and adaptable code that RANS based CFD is able to provide.

2.3.1 URANS and LES

Simao Ferreira et al [25] presented a systematic analysis of a two-bladed 2D VAWT configuration. A series of tests were conducted in an attempt to come up with a model that was independent of grid spacing and time step size. Validation was made by way of comparing vortical structures generated by CFD to stereo particle image velocimetry (PIV) data. Different commonly used turbulence models were tested at relatively low average Reynolds numbers of 52,000 and 70,000. Results show the suitability of PIV data for validation purposes but also the unsuitability of one turbulence model for the highly unsteady problem. Although good agreement was observed between CFD and PIV flow structures, no attempt was made to compare force data from CFD to that of experiments. As such, a definitive conclusion to the suitability of the CFD model could not be made.

In 2008, Hamada et al [26] presented 2D and 3D CFD simulation results of a roof–top H–VAWT using the commercial package Fluent. Different variations of the k–ε turbulence model were used on a mesh that has undergone sensitivity studies in grid spacing and time step size, both of which are necessary owing to

the unavailability of validation data. They have shown that power extraction in the upwind greatly influences performance in the downwind. Also, lift coefficients are inherently large in the upwind due to dynamic stall effects. In their 3D model, blade tip vortices, centre shaft wake and support arm wake caused significant reduction in the performance when compared to their 2D model. A major drawback of this study was the lack of benchmarking of the presented numerical results to actual measurements. The conclusions made were only good for comparative purposes and not an authoritative statement of overall VAWT performance.

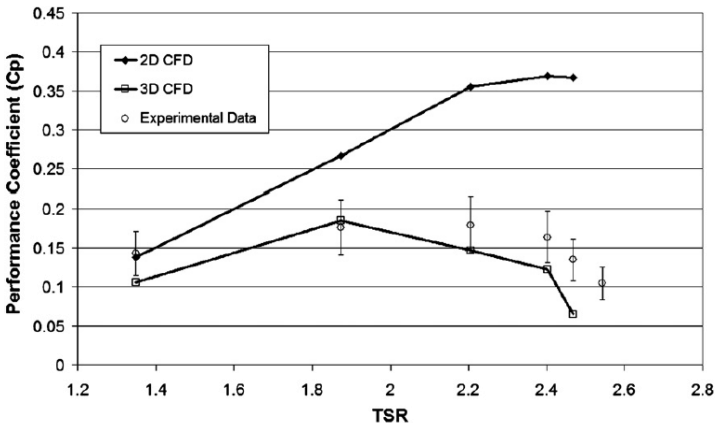

Figure 2.6. CP curves of wind tunnel model [27].

Similar studies were conducted by Howell et al [27], Edwards et al [28] and Raciti Castelli et al [7] that have shown consistent results in the observed gap between 2D and 3D performance curves. Howell et al [27] based their model on a wind tunnel scale VAWT of 0.043m diameter and 0.020m height running at average Reynolds numbers of about 30,000. Only half of the VAWT was modelled as it was symmetric with respect to the horizontal plane. Turbulence model selection was based solely on information provided by the CFD software documentation and educated assumptions of the expected flow features. As such, the k–ε RNG was chosen with wall functions enabled. Over prediction of power coefficient (CP) was observed for the 2D cases while good agreement was seen with the 3D cases versus experiment results (Figure 2.6). Similar to earlier work conducted, a full validation of the numerical model was not performed. This time,

the lack of flow visualisation hampered the success of developing a reliable CFD model that would give the needed confidence to the numerical results.

More recently, McLaren et al [29] performed 2D CFD simulations for a high solidity, small scale H–type VAWT. The three-bladed rotor was operating at an average Reynolds number of 360,000 over a wide range of blade speed ratios. Commercial code Ansys CFX was used for the simulations and model validation was made by comparing lift coefficients of static NACA0012 aerofoil runs to experimental data by Sheldahl and Klimas [30]. The hybrid k–ω shear stress transport (SST) was considered the turbulence model most appropriate to carry out the dynamic modelling that the problem requires. 2D VAWT simulations were conducted over blade speed ratios covering the full operating conditions of a typical VAWT from the dynamic stall region, to the power producing region, up to the viscous effects region. Results are consistent to previous studies wherein actual 3D experimental data are significantly lower than 2D CFD predicted performance (Figure 2.7). A correction factor was applied to the 2D CFD results to account for the major 3D components of the problem that are not modelled in the 2D simulations. The effect of lower actual incident wind velocity due to stream tube expansion to the two orthogonal directions relative to the flow was considered to be a significant factor to the perceived flow velocity by the blades.

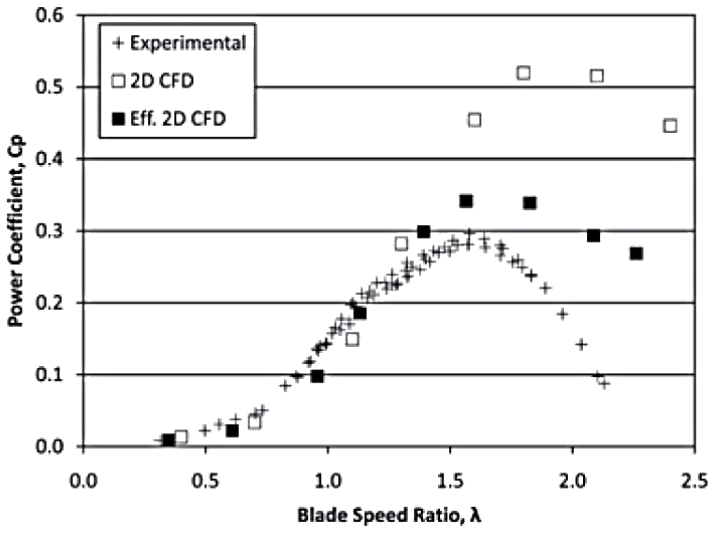

Figure 2.7. VAWT CP for 2D, effective 2D, and experiments [29].

Although the numerical work presented was compared to experimental data as part of the validation of the models, there has never been a validation study that both addresses the force aspect as well as the flow aspect of validation across a wide range of operating conditions. Edwards et al [6] provided the necessary resolution to this dilemma by performing a validation of the CFD model using both performance data from a novel experimental method and from PIV visualisations. The validation study was twofold in a sense that firstly, the selection of appropriate turbulence model was narrowed down by means of a pitching aerofoil study using experimental data from Lee and Gerontakos [31] and secondly, the CFD model of the VAWT was tested using experimentally generated data. For the turbulence model study, it was determined that the k–ω SST turbulence model was the best candidate for the highly dynamic and unsteady problem of a pitching aerofoil characteristics of whom are not too different from a VAWT blade. To address the force component of the VAWT validation, a set of spin-down tests were conducted to measure the blade performance by deriving instantaneous torque from the decelerating rotor dynamics. Flow validation used PIV visualisations at three different blade speed ratios. Corresponding operating conditions of the VAWT were simulated in CFD.

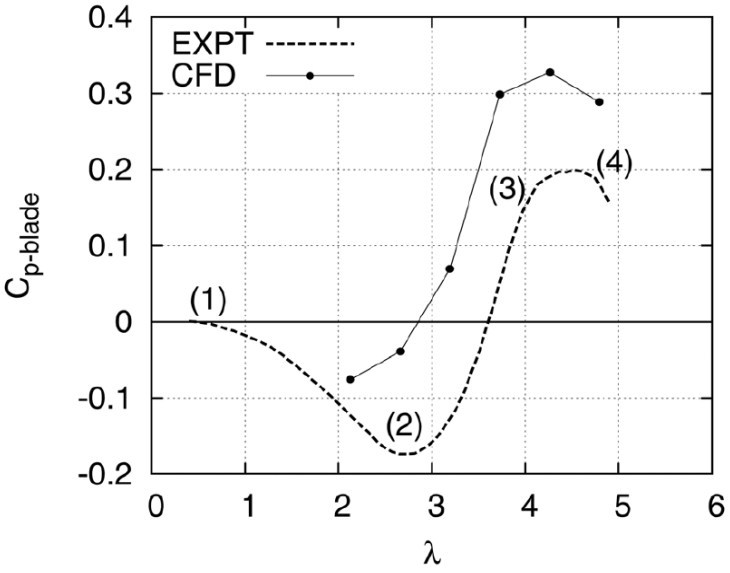

Figure 2.8. Spin down and CFD CP results [6].

Similar to observations by previous researchers, Edwards et al have seen that 2D CFD simulations show an over prediction in blade performance when compared to actual 3D experiment measurements (Figure 2.8). As such, similar reasons to explain this difference were argued to support the difference seen. In terms of the flow predictions, it was shown that the initial stalling of the VAWT blade in the upwind pass was delayed in the CFD by as much as 10° (Figure 2.9). This is an additional reason for the over prediction of the CP since prolonged attached flow meant prolonged positive torque generation by the blades. The downwind pass shows the blade stalling to be in sync between CFD and PIV (Figure 2.10). However, there is delayed reattachment that is seen at about 300° azimuth in the CFD that could account for decreased torque generation.

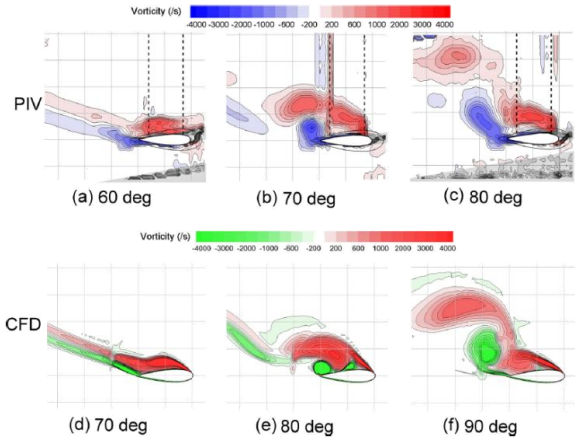

Figure 2.9. Upwind blade stalling [6].

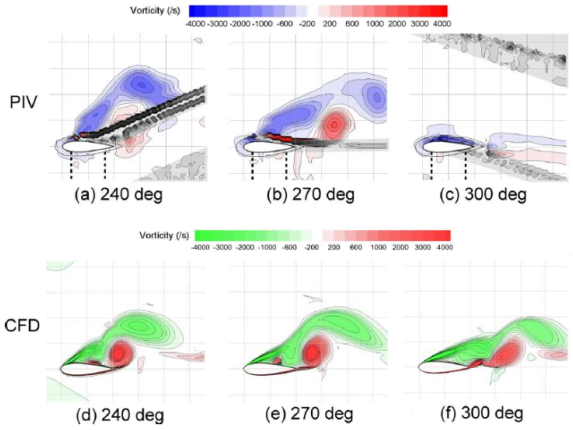

Figure 2.10. Downwind blade stalling [6].

While the high fidelity in RANS CFD models already offers significant insight into the aerodynamics that affect VAWT performance, the simplification in RANS of the normally random behaviour of turbulence has led some work to go further by employing large eddy methods that do not filter out this random feature. Strictly speaking, large eddy simulations (LES) are only applicable to 3D models as turbulence is 3D in nature. But it is possible to implement this method to 2D problems by assuming quasi-2D flows. LES is more computationally expensive than RANS because almost all scales of the turbulent flow are resolved except the near wall region where near wall modelling is used. Iida et al [32] were one of the

early investigators of VAWT aerodynamics using LES. They have shown that LES is able to predict VAWT performance better than momentum theory especially at low blade speed ratios where dynamic stall is present. The mesh used in the simulations contained approximately 800,000 elements which is a rather small number for an LES model.

Simao Ferreira et al [33] published in 2007 their study on VAWT modelling using different turbulence models that include, among others, LES and detached eddy simulations (DES). Compared to the Iida model, their mesh contained almost double the number of cells at 1.6×10^6. Even then, they commented that it is not fine enough for the requirements of large eddy methods. However, the results for the DES simulations show that it is more suitable than LES probably due to better near wall modelling. When compared to their RANS models, both DES and LES are better able to predict large eddies generated and shed by the blades at critical azimuth positions. DES is also superior when it comes to sensitivity to space and grid refinement making it suitable for simulations where validation data is unavailable or non–existent.

2.3.2 Turbulence Modelling and Dynamic Stall

In 1937, Taylor and von Karman [34] proposed the following definition of turbulence: “Turbulence is an irregular motion which, in general, makes its appearance in fluids, gaseous or liquid, when they flow past solid surfaces or even when neighbouring streams of the same fluid flow past or over one another.” Turbulence is an inherently three dimensional and time dependent problem. Therefore, an enormous amount of information is necessary to completely describe a turbulent flow. In most cases, what the engineer requires is the prediction of the physically meaningful properties of the flow, not the complete time history of every flow property over all spatial coordinates.

Turbulence consists of random fluctuations of the various flow properties and a statistical approach to solving it is deemed appropriate. A procedure introduced by Reynolds in 1895 best serves this purpose, where all quantities are expressed as the sum of the mean and fluctuating parts. Then the time average of the continuity and the Navier–Stokes equations are formed. The nonlinearity of the Navier–Stokes equations introduces unknown stresses throughout the flow. Derived equations for the stresses result in additional unknown quantities, which require closure equations, herein termed as turbulence models.

In this thesis, the problem is well within the incompressible region. The equations for conservation of mass and momentum for incompressible flow are

$$\frac{\partial u_i}{\partial x_i} = 0 \tag{2.1}$$

$$\rho \frac{\partial u_i}{\partial t} + \rho u_j \frac{\partial u_i}{\partial x_j} = -\frac{\partial p}{\partial x_i} + \frac{\partial t_{ji}}{\partial x_j} \tag{2.2}$$

where u_i is velocity, x_i is position, t is time, p is pressure, ρ is density and t_{ij} is the viscous stress tensor defined by

$$t_{ij} = 2\mu s_{ij} \tag{2.3}$$

where μ is molecular viscosity and s_{ij} is the strain–rate tensor,

$$s_{ij} = \frac{1}{2}\left(\frac{\partial u_i}{\partial x_j} + \frac{\partial u_j}{\partial x_i} \right) \tag{2.4}$$

Rewriting and simplifying the previous equations yield the Navier–Stokes equation in conservation form.

$$\rho\frac{\partial u_i}{\partial t}+\rho\frac{\partial}{\partial x_j}\left(u_i u_j\right)=-\frac{\partial p}{\partial x_i}+\frac{\partial}{\partial x_j}\left(2\mu s_{ij}\right) \tag{2.5}$$

Time averaging Eqs. 2.1 and 2.5 yields the Reynolds Averaged equations of motion in conservation form,

$$\frac{\partial U_i}{\partial x_i}=0 \tag{2.6}$$

$$\rho\frac{\partial U_i}{\partial t}+\rho\frac{\partial}{\partial x_j}\left(U_j U_i+\overline{u_j' u_i'}\right)=-\frac{\partial P}{\partial x_i}+\frac{\partial}{\partial x_j}\left(2\mu S_{ji}\right) \tag{2.7}$$

Rewriting Eq. 2.7 in its reverse yields its most recognizable form.

$$\rho\frac{\partial U_i}{\partial t}+\rho U_j\frac{\partial U_i}{\partial x_j}=-\frac{\partial P}{\partial x_i}+\frac{\partial}{\partial x_j}\left(2\mu S_{ji}-\overline{\rho u_j' u_i'}\right) \tag{2.8}$$

Equation 2.8 is usually referred to as the Reynolds–averaged Navier–Stokes equation, where the quantity $-\overline{\rho u_j' u_i'}$ is known as the Reynolds–stress tensor. The averaging process effectively introduces unknowns, through the Reynolds–stress components, without any additional equations. The closure problem of turbulence is essentially devising approximations for the unknown correlations in terms of flow properties that are known so that a sufficient number of equations exist.

In CFD simulations of VAWTs, the selection of an appropriate turbulence model is not a simple process. A turbulence model is deemed appropriate if it is validated against experimental data in both force and flow predictions. The accuracy of blade force predictions is a very important component of validation because it directly influences the prediction of the power coefficient of the modelled rotor. Additionally flow predictions are equally important because they dictate the near–wall phenomenon that affects both blade force and shed wake. The possibility of the presence of dynamic stall increases the requisite for correct

force and flow predictions. Unfortunately for a lot of VAWT research work, there is very little or no available experimental data to which the models can be compared to. This has serious implications because researchers resort to extensive checks following recommended numerical guidelines but are never able to validate the model as physically correct. The problem is exacerbated by the simplification of the VAWT into a two–dimensional CFD model without adequate explanation of the limitations of the model and acceptable rationalisation of the differences between CFD results and experiments.

One of the major stumbling blocks of mathematical modelling of the VAWT is the dynamic stall phenomenon usually expected in many operating conditions. When an aerofoil is under oscillating motion in a moving fluid, stalling can be considerably delayed beyond the static stall angle. A consequence of this is that static aerofoil data is no longer suitable because the forces on the blade exceed static stall values and large hysteresis are exhibited with respect to the instantaneous angle of attack (Figure 2.11). This is more prominent in oscillations with amplitudes in the order of the static stall angle [35]. Without any doubt, this poses similar or even greater challenge to CFD modelling because the absence of a reference case that is the static aerofoil to which CFD can benchmark from adds to the uncertainty of the solution.

Dynamic stall is characterised by the shedding of a vortex over the suction surface of an aerofoil under pitching motion in a stream of fluid. If the frequency, amplitude and maximum incidence are sufficiently high, an organised and clearly defined shedding of vortices is observed. Dynamic stall is broadly characterised by the following sequence of events:

STAGE 1: at incidence past the static stall angle, flow reversal develops near the trailing edge of the aerofoil and moves forward to the leading edge.

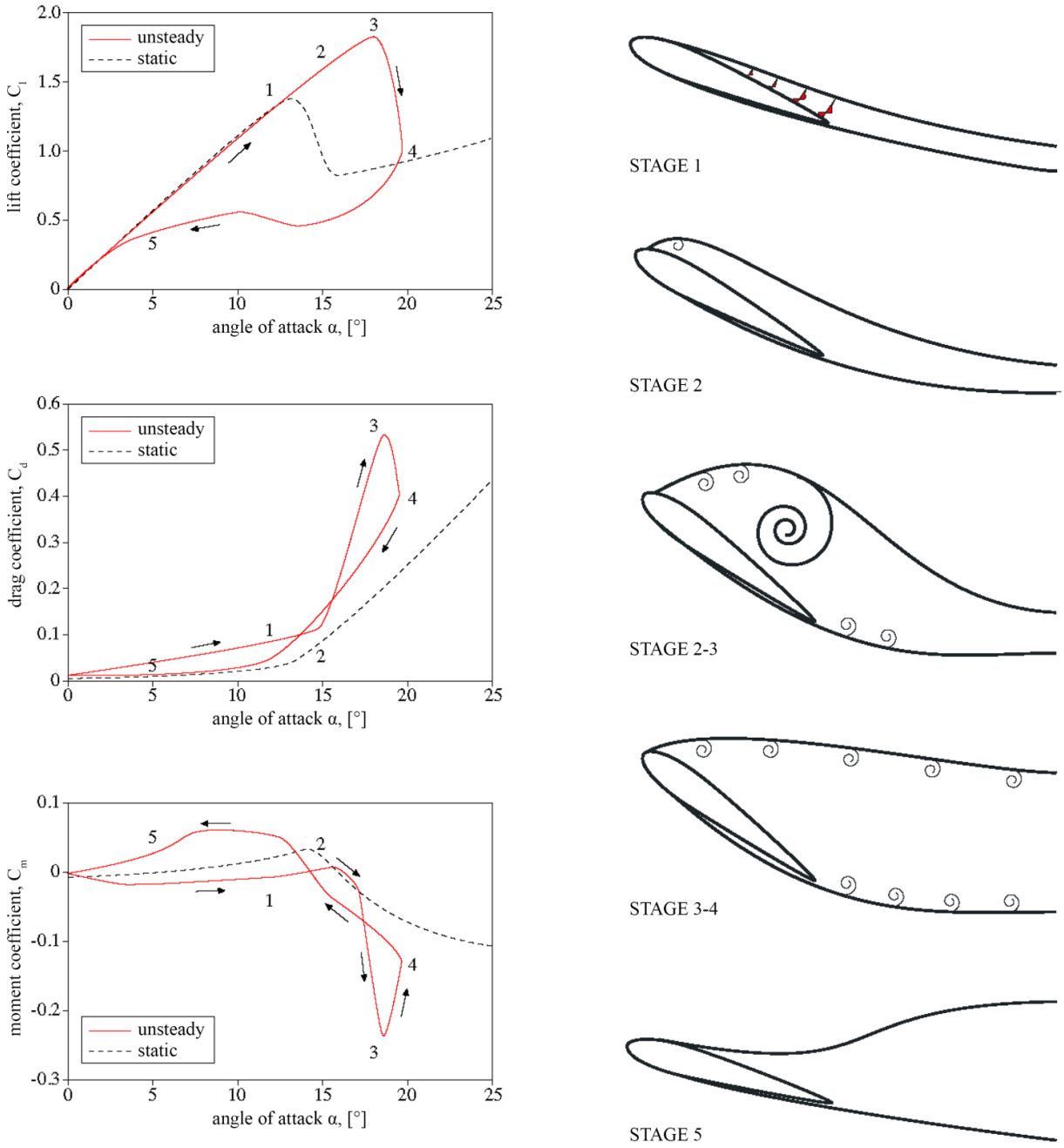

Figure 2.11. An illustration of the dynamic stall process (adapted from [10]).

STAGE 2: further increase in incidence causes the separation point to move towards the leading edge. The boundary layer starts to separate and the centre of pressure moves downstream causing the nose of the blade to pitch down. The boundary layer separation also induces an increase in drag. Lift continues to increase way beyond maximum static values. The free–shear layer that is formed in the leading edge starts to roll up forming the dynamic stall vortex.

STAGE 3: the dynamic stall vortex continues to grow due to further input of vorticity from the leading edge separation causing the lift to continue to rise and reach maximum values.

STAGE 4: as the dynamic stall vortex leaves the blade surface, there is a sharp drop in the lift and full separation takes place. Depending on the rate of pitching, subsequent growth of leading edge vortices may occur alongside the roll up of trailing edge vortex structures forming a band of alternately shed vortex blobs behind the blade.

STAGE 5: decreasing incidence eventually causes the flow to reattach to the blade starting from the leading edge and moving downstream towards the trailing edge. Similar delays are observed in the reattachment process causing the lift to undershoot static values before full recovery of the flow closing the hysteresis loops of the force and moment coefficients.

Correct modelling of dynamic stall is essential in a VAWT because of its direct effects on the torque generated by the blades. Also, shed vortical structures in the upwind affect the downwind performance of the blades. Simao Ferreira et al [25, 33] investigated dynamic stall modelling in VAWTs using various turbulence models and observed that fully turbulent schemes suppress the development of the leading edge separation bubble and reduce the maximum normal force on the blade. Resorting to a purely laminar model may partially correct the problem but additional refinement in the time grid size is necessary and leads to over–prediction of the generation and evolution of shed vorticity. It was also seen that there is an inability of the turbulence models to correctly model large eddies. Despite detailed comparisons of CFD models to PIV data, they have not presented anything with respect to force predictions that ultimately dictate power production. They argue that the lack of validation data makes it difficult to properly select the best turbulence model for the VAWT problem.

Hamada et al [26] discussed the effects of dynamic stall with respect to force coefficient variation against azimuthal position and noted that the lift generated

by the VAWT blade exceeds static stall values in the upwind pass. There is also a significant difference seen in the predicted lift between the upwind and downwind pass which proves that the VAWT blade cannot be directly compared to a pitching aerofoil. However, they have not shown a systematic method of selecting the appropriate turbulence model but instead relied on available literature to assess the suitability of a turbulence model for problems involving large flow separations that is present in the VAWT problem. There was also the lack of validation data to which the CFD model can be compared to.

To address the issue of non–availability of VAWT validation data, some work has been conducted with pitching aerofoils that exhibit very similar dynamic stall events with VAWTs. The close likeness of VAWT blades and pitching aerofoils in as far as dynamic stall is concerned make pitching aerofoils a viable validation candidate. In 2008, Martinat et al [36] studied a pitching NACA0012 aerofoil at 10^5 and 10^6 Reynolds numbers and have shown that standard turbulence models have a significant dissipative character that attenuates the instabilities and vortex structures related to dynamic stall. On the other hand, organised eddy simulation (OES) and the SST model have shown better prediction of dynamic stall especially at high Reynolds numbers but show to have a need of transition modelling at low Reynolds numbers.

Wang et al [37, 38] presented in 2010 a numerical investigation of turbulence modelling of dynamic stall of low Reynolds number oscillating aerofoils. They observed that k–ω SST based DES is more superior in predicting the dynamic stall process over RANS models k–ε RNG, k–ω standard, k–ω SST, and transition SST. Good agreement was seen with the transition SST model in the pitching up stroke where the predicted maximum lift coefficient is very close to experiments. Where the transition SST fails, the DES is seen to prevail. Better prediction in lift coefficient was seen in the DES model with less undershoot in the pitching down stroke. Although detailed comparison with force predictions was performed, the lack of flow validation through comparison of vorticity fields is seen as the

downfall of their study. Their extensive presentation of CFD visualisations is not complemented by comparison to actual experimental visualisation such as smoke streaks and PIV that were available in the case studies [31, 39] that they have analysed.

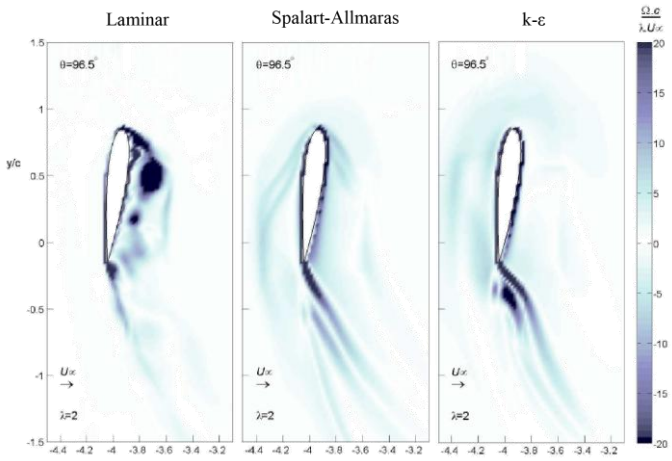

Figure 2.12. Vorticity plots of turbulence model study [25].

The popularity of some turbulence models has influenced the direction of numerous research works on VAWT modelling. For its robust qualities and proven record of excellent predictions in a variety of engineering problems, the standard k–ε model and its variants have become a popular choice of researchers. Simao Ferreira et al [25] investigated the use of the standard k–ε model on a VAWT running at λ = 2 observed that the fully turbulent model suppressed the development of the leading edge separation bubble seen in their PIV tests and predicted by a fully laminar model (Figure 2.12). The predicted normal and tangential forces on the blade were also seen to be opposite in trend versus the laminar model.

Hamada et al [26] and Howell et al [27] used the three available variants of the k–ε model in commercial CFD package Fluent in their simulations and have shown that the k–ε standard model deviates from k–ε RNG and k–ε Realizable in the torque predictions. They argue that for problems involving strong streamline curvatures, vortices and rotation, the standard variant is less superior to the RNG

and Realizable models. Moreover, the Realizable variant is prone to produce non–physical turbulent viscosities when the domains include stationary and rotating fluid zones. Two dimensional and three dimensional CFD models were studied and it was seen that the RNG variant consistently over–predicted the CP for the 2D model while under–predicting CP in the 3D case. Although reasonable agreement was seen between the 3D model and experiments, the CFD predictions tended to diverge from measurements as λ increased. The only non–conforming result was at the highest test wind speed and highest λ where the predicted CP was above the measure CP and within the assumed experimental error.

Recently, Beri et al [40] and Untaroiu et al [41] used the k–ε model to examine self–starting capabilities of VAWTs. Beri et al [40] concluded that cambered aerofoils have the potential for self start but unfortunately reduce the peak efficiency. A static aerofoil study was presented as validation of their CFD model and it was observed that the RNG model properly predicted the lift forces on the aerofoil at low incidence but show delayed stalling when compared to experimental data. They contended that the model was suitable for VAWT simulations because the incidence angle of the flow relative to the VAWT blades is said to be within the low range. This is only true if the operating conditions were such that no observed stalling of the blades is expected i.e. high λ beyond the peak performance point. Low λ usually push the performance of the VAWT within the dynamic stall region where incidence angles exceed static stall values of up to 1.5 times. Delayed stalling causes inaccuracies in performance prediction because it induces longer positive torque production of the blades resulting to higher power production.

Untaroiu et al [41] carried out 2D and 3D simulations of a wind tunnel scale VAWT using the standard k–ε model to study self–starting potential of a high solidity rotor and found consistent results to what has been reported by Howell et al [27] regarding over–prediction of 2D models and under–prediction of 3D models. During the rotor start–up, simulations show a very steep ramp up of the

rotor's angular speed versus experiments. There is also the absence of the intermediate velocity plateau seen in experiments before full operating speed is attained. This was claimed to be an effect of poor near–wall modelling of the k–ε resulting to lower viscous drag induced and may be avoided by using more superior turbulence models for wall bounded flow problems such as k–ω and its variants.

Raciti Castelli et al [7, 42] conducted 2D and 3D, single and three bladed VAWT simulations in an attempt to develop a performance prediction methodology based on CFD. A modelling strategy was presented and validated using wind tunnel measured performance of a full scale low solidity VAWT. To assess the suitability of a turbulence model, the wall y^+ parameter was inspected. Wall y^+ is a dimensionless wall distance that gives an indication of the position of a point within the boundary layer. In most cases, this point is selected to be the centre of the cell that is adjacent to the wall. It has been observed that for models with wall functions enabled ($y^+ > 30$), the k–ω model was appropriate whereas models with enhanced wall treatment ($y^+ \approx 1$) necessitated the use of the k–ε Realizable model. Their basis for this conclusion was a statistical study of the y^+ parameter and the suitability of the turbulence model was dependent on the distance of the mean y^+ from recommended values and degree of the spread of the wall y^+ about the mean. A comparison between 2D CFD predicted CP and experimental data has shown that 2D results over–predict CP but replicate the general curve. There was no inspection and assessment of the flow field as to the model's accuracy in predicting stall and reattachment which is critical in explaining performance trends.

The inability of the k–ε turbulence model to properly compute the flows of many engineering problems with strong adverse pressure gradients and separation led to the development of alternative turbulence models that can address the issue. The behaviour of turbulent boundary layers up to separation was a challenge to the family of k–ε models that researchers turned to another

well–established turbulence model known to be more superior in near wall modelling, the k–ω model. This does not come without its own drawbacks. The k–ω model, shown to be successful for flows with moderate adverse pressure gradients, fails to predict flows with pressure induced separation and shows a strong sensitivity to the values of ω in the free stream [43].

Despite this limitation, researchers were still motivated to use this alternative turbulence model in VAWT simulations. Amet et al [44] conducted 2D simulations at two extreme tip speed ratios, λ = 2 and λ = 7. Lift (Figure 2.13) and drag coefficients around a full rotation were compared to experiments performed by Laneville and Vittecoq [45]. Although the general shape and trend of the curves were similar, significant differences were observed between simulations and experiments. There is a clear upward shift of the CFD–computed lift coefficients but maximum values are very close to experimental values. A non–zero lift is seen in the simulation at zero incidence whereas experiments show negligible lift. However, they question the validity and accuracy of the experimental data instead of discussing the possible reasons for the differences. Though they mention the main weakness of the k–ω turbulence model in terms of convecting large eddies that are detached from the blade that may explain the major differences in the force coefficients, the experimental data is downplayed by justifying the correctness of the CFD results using data from an inviscid mathematical model coupled with geometric angle of attack assumption, both of which are significant deviations from the realistic VAWT aerodynamics. In 2011, Nobile et al [46] compared the k–ω model against the k–ε model and a new variant of the k–ω model, the k–ω SST. The vorticity field predictions of the k–ω model were put side by side with the PIV data of Simao Ferreira [33, 47] and a key difference was observed. While the separation point and depth of stall prediction was better than the k–ε model, the evolution of the dynamic stall vortex was still suppressed and significant dissipation of the eddies was seen. The absence of the trailing edge vortex expected from the dynamic stall process is also noted.

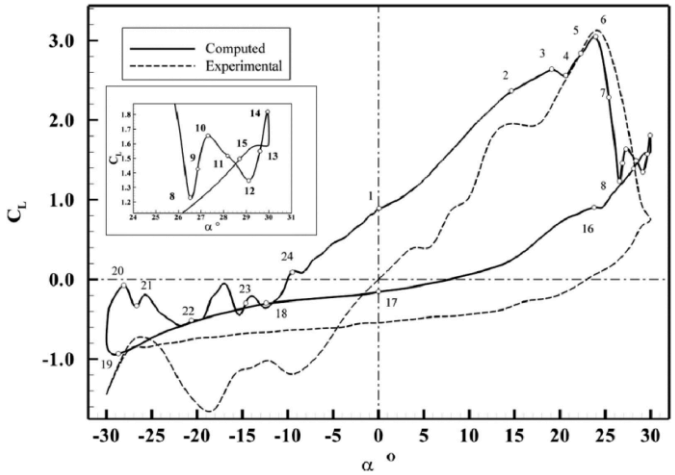

Figure 2.13. Lift hysteresis loops for a VAWT blade [44].

The hybrid turbulence model k–ω SST has seen popular use as a step forward in VAWT modelling because it combines the near wall capabilities of the k–ω model and the free stream stability of the k–ε model. Some research works have been carried out on VAWT simulations that also include applications in water turbines. Dai et al [48] and Consul et al [49] conducted numerical studies on tidal turbines of the Darrieus type. Dai et al performed a study on the effects of scale on a straight–bladed turbine in an effort to predict the performance of large scale tidal turbines. The obtained results are in good agreement with expected values and trends. Hydrodynamic performance and structural load predictions were considered acceptable despite the lack of proper validation of the CFD model. Instead of a thorough validation, a sensitivity analysis was carried out on the time step size. A comparison of turbine performance is presented for one operating condition and shown that the k–ω SST only slightly over predicts CP in spite of the fact that the simulation is 2D. They continue to conclude that the model is sufficiently validated and is further used on a 1MW scale model.

Consul et al [49] in 2009 performed numerical investigations on the effects of solidity on a tidal turbine. Validation of the 2D model by way of static aerofoil study on lift and drag predictions was done on published experimental data by Sheldahl and Klimas [30] of a NACA0015 profile. The one–equation Spalart–Allmaras (SA) turbulence model was compared to the two–equation k–ω SST

model and minor differences in lift and drag were seen between the two. Both deviate from experimental results in terms of the predicted stalling angle and maximum lift before stall. The average error of the numerically computed drag of the SA model is seen to be greater than the k–ω SST model while the errors of computed lift are very similar. This difference was observed to be more prominent at higher angles of incidence. Also, at higher angles of incidence a periodic vortex wake was generated by the k–ω SST model while an unrealistic erratic result was seen in the SA model, an expected behaviour since the k–ω SST model is adept at simulating grossly separated flows.

In 2011, McLaren et al [29] tested the predictive capabilities of the k–ω SST model by conducting static aerofoil tests on a NACA0015 blade at Reynolds number of 360,000. Similar to the reference case used by Consul et al earlier, lift and drag predictions of three turbulence models were compared against experimental data. A better trend was seen with the k–ω SST model results versus the k–ω standard model and the k–ε standard model. The latter two models over predict maximum lift and stalling angle while very close outcomes are seen with the k–ω SST model.

A point of contention can be made with a lot of the work presented above when it comes to the efforts in the validation of the CFD models. The reference point to which the models are compared to do not represent the unsteady flow behaviour that is seen in VAWT dynamics. The rigorous prerequisites of modelling a pitching and plunging aerofoil in constantly changing relative velocities and incidences are satisfied neither by a static aerofoil study nor by simple numerical sensitivity analyses. The wide range of possible flow conditions that a VAWT blade encounters within one operating condition warrants a validation method that can live up to the demands of a highly transient problem. Modelling the stalling and reattachment of flow on a VAWT blade directly affects the predicted performance of the wind machine and as such is critical to the validity of the

numerical model being used. A more thorough validation that covers both force prediction as well as flow prediction is necessary to address this need.

Edwards et al [6] and Danao et al [50] addressed the challenge of proper validation of the CFD model by conducting a systematic one–to–one evaluation of force and flow predictions to both published pitching aerofoil data as well as their own generated VAWT experimental data. The process of narrowing down the list of turbulence model candidates involved the investigation of a pitching aerofoil study conducted by Lee and Gerontakos [31]. What Edwards et al found out is that the most appropriate turbulence model that correctly predicts both the forces (Figure 2.14) and the flows (Figure 2.15) past an oscillating aerofoil is the k–ω SST. They have shown that the k–ω SST is the closest when it comes to pitching aerofoil simulations but for VAWT simulations, at there is a slight delay in the predicted stalling (Figure 2.9) in the upwind pass and reattachment of flow (Figure 2.10) in the downwind pass of the blades when compared to their PIV data. Also, full stall is not seen in the simulations at λ = 4 while such is observed in experiments. Regardless of this discrepancy, this is the first time that a complete validation is performed for a VAWT CFD model.

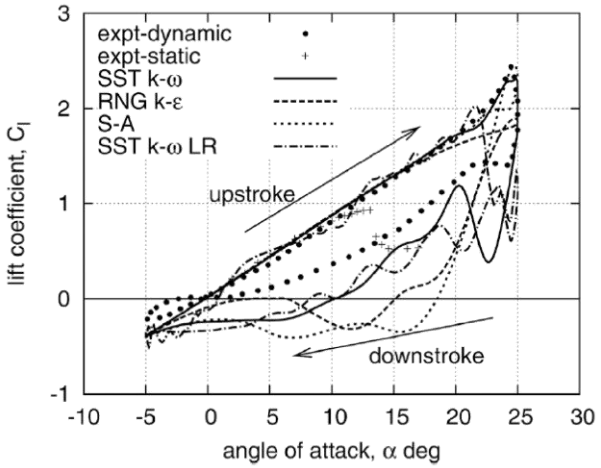

Figure 2.14. Lift coefficient predictions of different turbulence models [6].

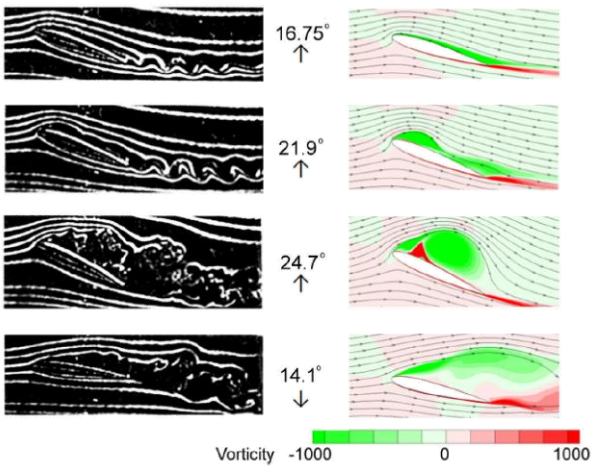

Figure 2.15. Flow predictions of k–ω SST model versus experiments [6].

Further investigations by Danao and Howell [51] improve on this by considering Transition SST turbulence model previously examined by Wang et al [38]. It was observed that the Transition SST resolves the delayed stalling at $\lambda = 2$ that is seen in the fully turbulent k–ω SST and better prediction in the blade force is also achieved resulting to closer prediction of CP to experiments (Figure 2.16). The use of the Transition SST model also predicts the stalling of the blades at $\lambda = 4$, a factor in the significant reduction of CP at high λ. There is a perceived convergence of performance predictions between the transitional model and the fully turbulent model at $\lambda > 5$. It seems that the Transition SST is behaving more like its fully turbulent cousin causing similar values in rotor efficiency.

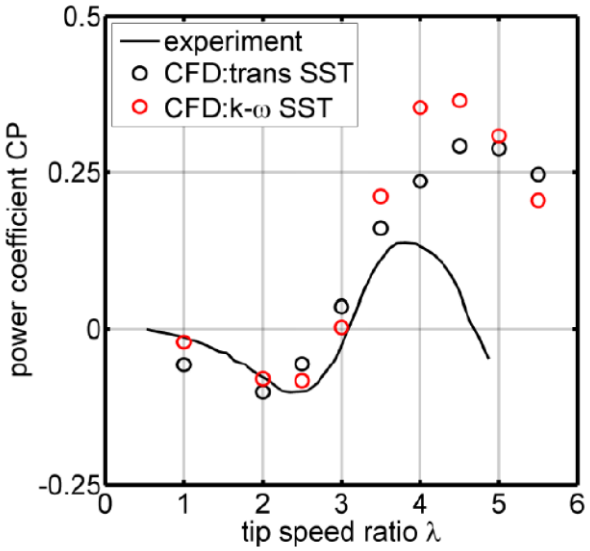

Figure 2.16. Power coefficient plot of wind tunnel scale VAWT [51].

2.3.3 Summary

Significant advances in the study of VAWTs using CFD have been made, all pointing to the ability of the k–ω SST turbulence model in properly modelling the unsteady aerodynamics that accompanies the operation of VAWTs. Investigations using the Transition SST turbulence model are in its infancy but have shown promising results that improve on the excellent agreement of its fully turbulent cousin when it comes to force and flow predictions of dynamic stall and its effects that is ever present in the VAWT problem. A table of selected CFD models most influential to VAWT studies is presented in Table 2.2.

CFD Model	Main Features	Limitations	Computing Cost	Computing Speed	Agreement with Experimental Data
R.J. Howell (2010)	– 3D wind tunnel model with wall functions – 1.3×10^6 cells, $Re = 3\times10^4$ to 4×10^4, k–ε *RNG*, high solidity – commercial software Fluent – surface roughness study	– fully turbulent model – no experimental visualisations for flow validation – no blade stall analysis – no central shaft and spokes	high	slow	deviation of predicted maximum CP from –20% to +6%
M. Raciti Castelli (2011)	– 2D wind tunnel model with near wall modelling – 1×10^6 cells, $Re = 8\times10^4$ to 1.6×10^5, k–ε *Realizable*, full numerical verification – commercial software Fluent – high solidity, corrected angle of attack estimation, blade force and stall analysis	– fully turbulent model – no experimental visualisations for flow validation – no central shaft and spokes	moderate to high	slow to moderate	over prediction of maximum CP by 80%
C.J. Simao Ferreira (2007)	– 2D wind tunnel model – 1.6×10^6 cells, $Re = 5\times10^4$, laminar, URANS, LES, DES – commercial software Fluent – full numerical verification, flow validation using PIV – blade force and stall analysis	– single blade VAWT – no experimental performance data for force validation – single operating λ	high	slow	good agreement of stall and vortex shedding with PIV
K. McLaren (2011)	– 2D open field model with near wall modelling – 4.85×10^5 nodes, $Re = 3.6\times10^5$, k–ε, $k-\omega$ SST, high solidity – correction factors for 3D stream tube expansion – commercial software CFX – blade force and stall analysis	– static aerofoil force validation – no flow validation	moderate	moderate	over prediction of maximum CP by 13%
J.M. Edwards (2012)	– 2D wind tunnel model with near wall modelling – 1.5×10^5 cells, $Re = 2\times10^4$ to 1×10^5, $k-\omega$ SST – commercial software Fluent – full numerical verification, full force and flow validation – blade force and stall analysis – corrected angle of attack estimation	– fully turbulent model – delay in blade upwind stall prediction – no correction for 3D analysis	moderate	moderate	over prediction of maximum CP by 65%
L.A.M. Danao (2012)	– 2D wind tunnel model with near wall modelling – 1.5×10^5 cells, $Re = 2\times10^4$ to 1×10^5, $k-\omega$ SST, transition SST – commercial software Fluent – full numerical verification, full force and flow validation – blade force and stall analysis – unsteady wind analysis	– no correction for 3D analysis	moderate	moderate	over prediction of maximum CP by 66%

Table 2.2. Summary of VAWT CFD models.

2.4 Performance Basics

The performance of the VAWT is highly influenced by its geometric properties and a better understanding of the effects of different parameters is essential in the design process. The individual parameters and their effects are not completely independent of each other but rather interlinked and complicated. A straightforward single parameter analysis is therefore not able to conclusively assess the optimal performance point but can only suggest trends in the variation of performance versus the geometric properties under study. Nevertheless efforts in understanding the individual effects have been numerous and a summary of the critical parameters are presented.

2.4.1 Aerofoil Profile

Symmetric aerofoils have been a popular choice for VAWT applications due to the availability of aerodynamic performance data. As early as 1937, performance of NACA aerofoils have been investigated by Jacobs and Sherman [52] to make available their section characteristics at any free–air value of Reynolds number. Their study involved a systematic investigation of representative groups of NACA aerofoil profiles in a wide range of Reynolds numbers using static aerofoil tests of lift and drag. From this dataset, Healy [53, 54] developed a multiple stream tube model for the VAWT and conducted an analysis of the effects of thickness and camber on VAWT performance. It was concluded that thicker aerofoils perform better especially at lower Reynolds number due to their resistance to stall. However, this was disputed by Danao et al [55] in their CFD study of thickness and camber. It was shown that thinner aerofoils, through stronger pressure gradients, produce higher values of lift. In Healy's study, camber was seen to have negative effects and sections closer to symmetric profiles were desired.

Sheldahl and Klimas [30] published a comprehensive experimental dataset of symmetric NACA aerofoils with VAWT applications in mind. The section data

requirements for VAWT applications are broader in scope than those encountered by the aircraft industry. The maximum value of angle of attack that a VAWT blade section is exposed to normally exceeds 25° especially near the ends of the curved blades of the traditional troposkein design of the Darrieus concept. Static aerofoil tests were conducted and an extrapolation code was developed to generate performance data at Reynolds numbers outside the experimental range most especially at the low end where much of the operating conditions exist. Primarily the effect of blade thickness on symmetric NACA profiles was studied from 0° to 180° angle of attack and data for both increasing and decreasing incidence was taken to show hysteresis of aerofoil performance.

Baker [56] and Kirke [57] analysed the performance of cambered aerofoils and concluded that to maximise power extraction, the use of cambered or angled blades is beneficial because such profiles will significantly increase the performance in the upwind where most of the power is produced. This can also benefit from self–starting capabilities because cambering pushes the performance curve to lower λ. At low Reynolds number conditions, a separation bubble evolving at the leading edge is inevitable. Reattachment on the trailing edge needs to be encouraged to negotiate the pressure rise and sustain the lift prior to full stall. A section with a more rounded nose and cambered leading edge is argued to accomplish the job.

Parametric studies by McIntosh [10] using a free vortex model code have shown that thinner aerofoils produce higher maximum CP versus thicker sections. The NACA0012 CP curve is seen to have a sharp drop from the maximum on both sides while thicker profiles display flatter top and gentler rounded drop in CP (Figure 2.17). Maximum CP is also observed to shift to lower λ. Thicker aerofoils are desirable in gusty conditions because turbines operating at lower tip speed ratios will experience smaller fluctuations in λ during the gusts and the drop in CP is also reduced. Danao et al [55] studied the effects of thickness and camber on VAWT performance by testing several candidate profiles in 2D CFD simulations.

Results show that thinner symmetric sections produce higher maximum CP while cambered sections improve the overall performance of thick aerofoils (Figure 2.18). Slight camber along the blade path is seen to be desirable while inverted configurations are detrimental to power extraction especially in the downwind.

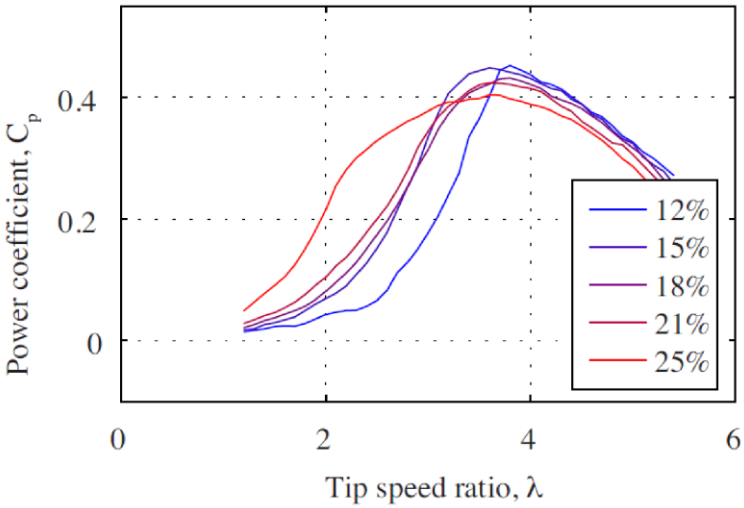

Figure 2.17. Free vortex results on the effect of blade thickness on VAWT CP [10].

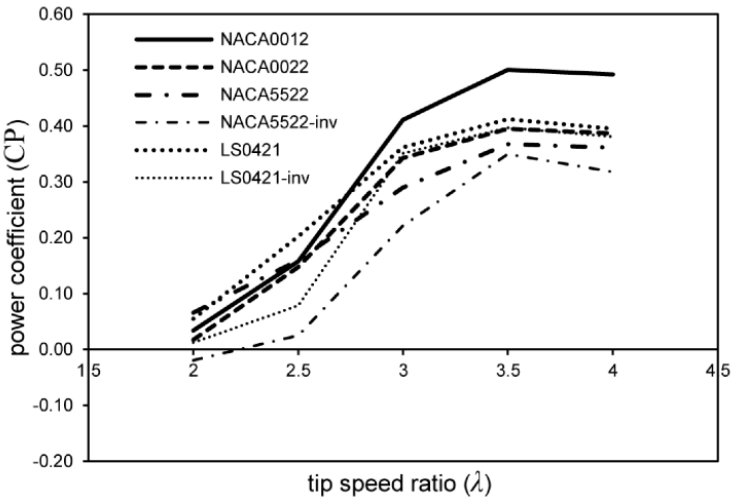

Figure 2.18. CFD results on the effect of thickness and camber on VAWT CP [55].

2.4.2 Solidity

The effect of solidity on the output of VAWTs is strong influencing both the maximum CP as well as the tip speed ratio at which maximum CP is attained. As a general rule, low solidity machines operate efficiently at high λ producing flatter performance curves and gentler slopes. High solidity rotors tend to operate at low λ with sharp peaks and narrower operating bands. The usual definition of solidity for VAWTs is:

$$\sigma = \frac{Nc}{R} \tag{2.9}$$

where N is the number of blades, c is the blade chord, and R is the rotor radius. As can be seen in the equation, variation of solidity can be effected by changing either the number of blades or the size of the blade chord assuming the rotor radius is kept constant. Increasing the number of blades causes more wake to be convected downstream leading to a more complicated blade–wake interactions downwind. On the other hand, increasing the blade chord size increases the blade Reynolds number which reduces the low Reynolds number effects such as dynamic stall and laminar–turbulent transition. In both cases, as solidity increases solid blockage increases inducing a bigger expansion of the stream tube. This causes greater deviation of perceived local flow incidence from geometric angle of attack assumptions. In addition, the variation in solidity affects turbine loading and therefore the strength of the wake, finite length effects through changes in blade aspect ratio and spoke drag effects (larger blades require larger support arms).

In 1998, Kirke [57] compiled several work by different authors involving different solidities (Figure 2.19). It is clear that very high solidities are not preferred because of lower peak CP and very narrow and steep performance curve. Very low solidities are equally undesirable because of very high operating speeds and also low peak CP. Consul et al [49] presented in 2009 a study on

solidity by varying blade number on a tidal turbine. Two and four bladed configurations were tested in 2D CFD simulations and results show an increase in maximum CP from 0.43 for σ = 0.019 to 0.53 for σ = 0.038. Also peak CP shifts from λ = 6 to λ = 4 as solidity increases. They argue that the four–bladed turbine presents larger impedance, which results in a reduction in streamwise flow velocity between the lower and higher solidity configurations. Lower flow velocity consequently reduces maximum angle of incidence perceived by the blades. This has significant effects on blades stalling. At high λ, low incidence limits the power take off resulting to lower CP. At low λ, stalling is minimised and power take off is increased thereby increasing the CP. At λ = 4, not only is the CP higher for the higher solidity but a flatter torque ripple is observed inducing more even loading experienced by the four bladed turbine. This is particularly favourable with regard to generator loading and fatigue issues.

A solidity study by McIntosh [10] reveals that maximum CP is achieved between σ = 0.2 to σ = 0.25 and a steep drop in maximum CP for σ < 0.2 while a more gentle decrease for σ > 0.25 (Figure 2.20). Again, low solidities produce 'soft' power curves with flat tops, low gradients and higher optimum λ. On the other hand, high solidities generate narrower power curves with lower optimum λ. It is therefore solidity that dictates the trade between high performance machines and configurations more tolerant to unsteady wind.

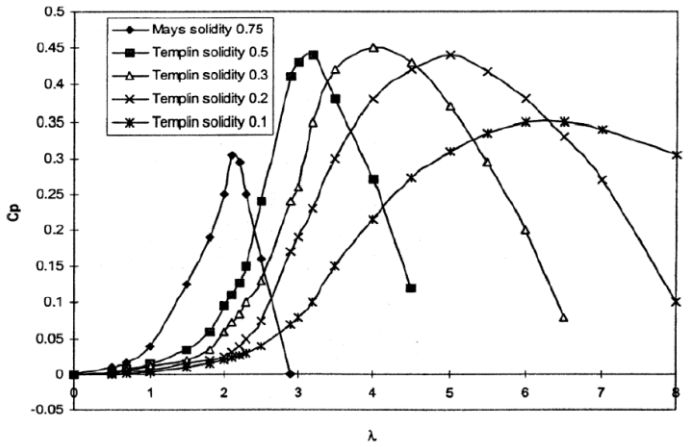

Figure 2.19. Effects of solidity on VAWT CP [57].

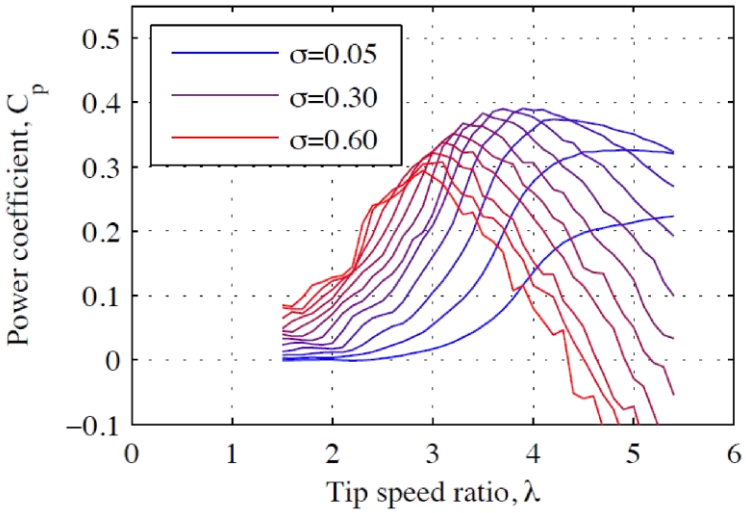

Figure 2.20. Free vortex results on the influence of solidity on CP [10].

2.4.2 Blade Sweep

Blade sweep is a geometric alteration of the conventional H configuration of the VAWT. Instead of using straight blades, twisted or canted blades are employed. Helically twisting the blades, as in the Quiet Revolution machines [58], have been shown to produce smoother torque output that can increase the life of the mechanical components of the VAWT. McIntosh and Babinsky [21] investigated the effects of different blade sweep angles using a free vortex model and observed that there is large reduction in the in–plane cyclic loads with the application of sweep. Unfortunately, a reduction in maximum CP is also seen due to higher changes in angle of attack that causes earlier stalling of the blades. This earlier stalling moves the maximum CP point to higher λ. Scheurich et al [59] and Scheurich and Brown [60] examined the aerodynamic performance of three blade configurations, straight blades, curved blades, and helically twisted blades using a vorticity transport model. VAWTs with straight or curved blades are known to suffer from substantial oscillatory loads in the frequency of the blade passage that can fatigue the rotor the rotor structure and reduce the design life. In contrast, the helically twisted turbine yields a steady power output and a higher mean CP.

The advantages of helically twisted blades are offset by the difficulties in manufacturing and increased cost. Recently, Armstrong et al [61] and Armstrong and Tullis [62] proposed a solution to this problem by 'canting' the blades. A canted blade is essentially a straight blade rotated about the mid span then twisted on its longitudinal axis to maintain constant local pitch of the chord relative to the shaft. To maintain the same turbine height, the blade length is increased by about 40%. Wind tunnel tests of a turbine with height of 2.93m and swept area equal to 8.16m^2 were conducted at a wide range of wind speeds. Results indicate that canting does not have a significant effect on the CP but moves the peak operating point to higher λ. Flow visualisations using arrays of bi–colour Mylar tufts show less flow separation on canted blades both on canted blade peak power λ and on straight blade peak power λ. There is an observed recovery of reversed flow at earlier azimuths which is thought to have suppressed the initiation of dynamic stall and is a favourable change of behaviour as compared to straight blades. However, it is not fully explained why the peak CP is only slightly increased. Separation was not seen to extend beyond 180° azimuth and little flow reversal was observed on the downwind pass.

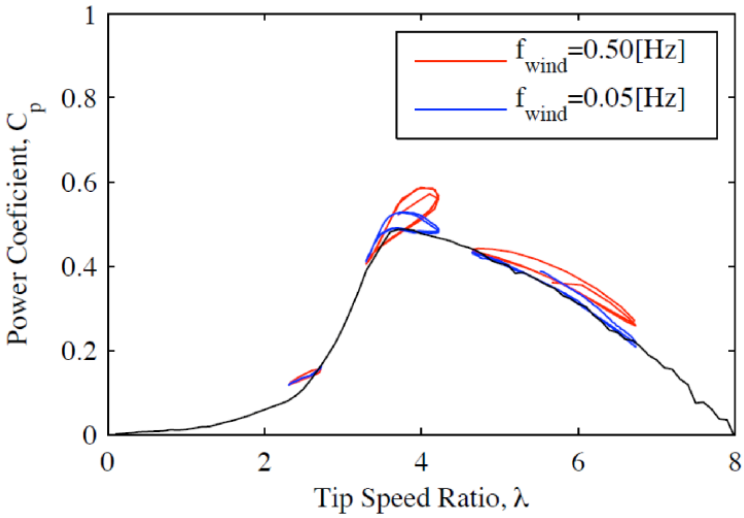

Figure 2.21. Unsteady CP results of sinusoidal wind fluctuations [63].

2.4.3 Unsteady Incoming Wind

Research in unsteady wind effects has only been given attention in the recent years. Very little literature is available since VAWT research is still not fully mature in steady wind flows. Earlier attempts to understand the performance of VAWTs in unsteady wind were carried out by McIntosh et al [63, 64] through numerical modelling. The VAWT was subjected to fluctuating free stream of sinusoidal nature while running at a constant rotational speed. An increase in energy extraction was attained using a rotational speed greater than the calculated steady state maximum. The over–speed control technique resulted to a 245% increase in energy extracted. Further improvements in the performance can be attained by using a tip speed ratio feedback controller incorporating time dependent effects of gust frequency and turbine inertia giving a further 42% increase in energy extraction. At low frequencies of fluctuation (0.05Hz) away from stall, the unsteady CP closely tracks the steady CP curve (Figure 2.21). However at higher frequencies (0.5Hz), the unsteady CP is seen to form hysteresis loops with averages greater than steady predictions.

Hayashi et al [65] examined the effects of gusts on a VAWT by subjecting a wind tunnel scale rotor to a step change in wind velocity. Two types of control were implemented: constant rpm and constant load torque. When subjected to a step change in wind speed from 10m/s to 11m/s under constant rpm control, the VAWT torque was observed to respond almost instantaneously and attained a steady state in less than 3s (Figure 2.22a). However when constant load torque control was employed, the initial response is similar to the constant rpm control where the torque instantly jumps to a higher level. The subsequent behaviour is a combination of a gradual increase in rpm (Figure 2.22b) with a slow decrease in torque (Figure 2.22c) until steady state is attained. Despite an observed transient VAWT response that does not follow steady state power curves, they contend that the adopted step change in wind speed is not normally observed in the real world

and most likely a more gradual increase is expected. The VAWT behaviour will thus follow a quasi–static condition during the gust.

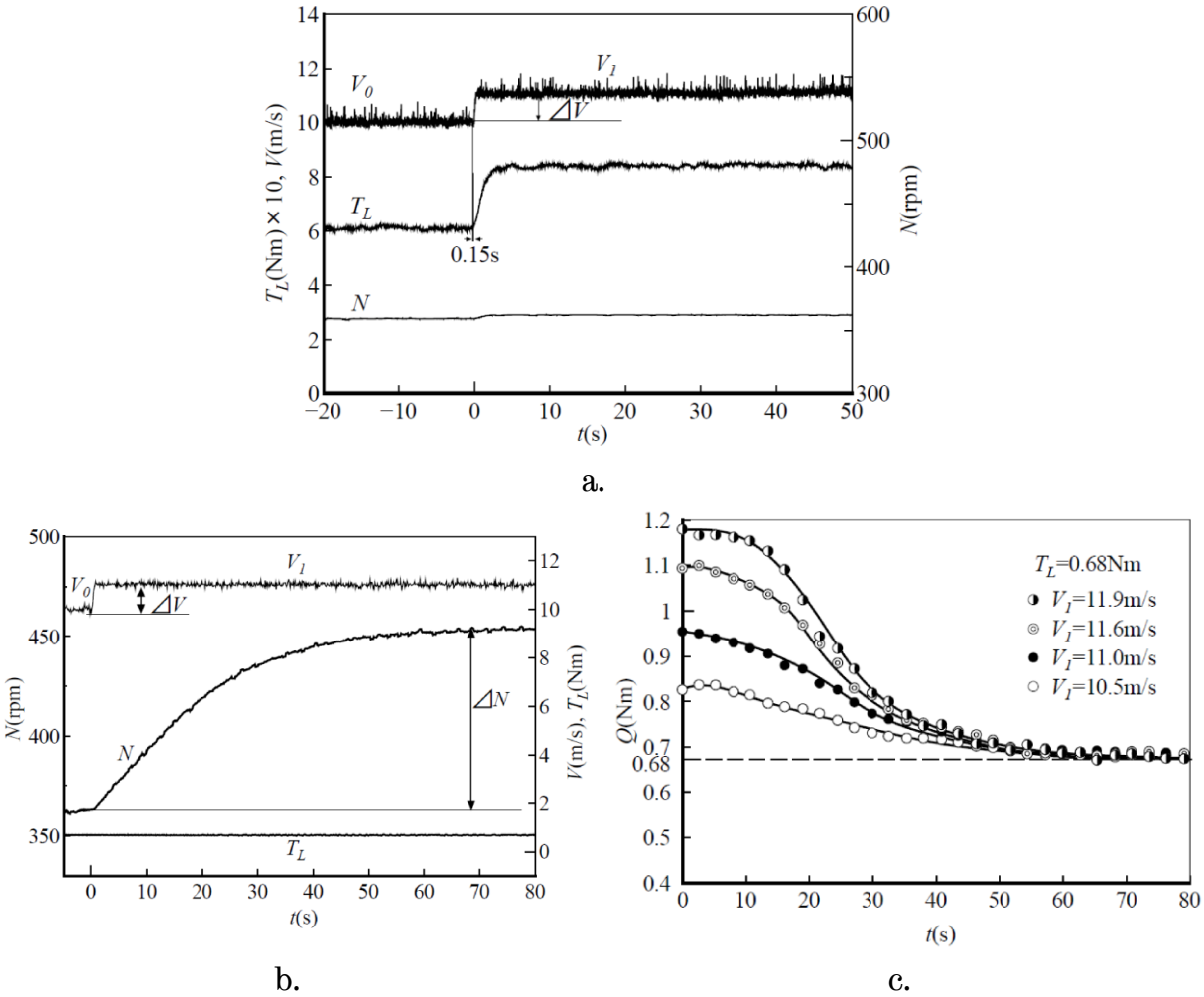

Figure 2.22. Response of VAWT to step change in wind [65]: a) constant rpm control, b) rpm response to constant load torque control, c) VAWT torque response in constant load torque control.

In 2010, Kooiman and Tullis [66] experimentally tested a VAWT within the urban environment to assess the effects of unsteady wind on aerodynamic performance. Temporal variation in speed and direction was quantified and compared to a base case wind tunnel performance. Independence of the performance in directional fluctuations was seen while amplitude–based wind speed fluctuation decreased the performance linearly. For their particular urban site, the degradation in performance was deemed minimal. Danao and Howell [51] conducted CFD simulations on a wind tunnel scale VAWT in unsteady wind

inflow and have shown that the VAWT performance generally decreased in any of the tested wind fluctuations. The amplitude of fluctuation studied was 50% of the mean wind speed and three sinusoidal frequencies were tested: 1.16Hz, 2.91Hz, and 11.6Hz where the fastest rate is equal to the VAWT rotational frequency. The two slower frequencies of fluctuation showed a 75% decrease in the wind cycle mean performance while the fastest rate caused a 50% reduction. Closer investigation revealed that for a 2.91Hz fluctuation rate a large hysteresis is seen in the unsteady CP of the VAWT within one wind cycle (Figure 2.23). This hysteresis occurs in the positive amplitude portion of the wind fluctuation where the blades passing the upwind progressively stall at earlier azimuths and experience very deep stall due to significant reduction in the effective λ (Figure 2.24). Negative amplitude in wind fluctuation does not produce significant hysteresis. However, the unsteady CP traces a curve that does not follow the steady CP curve but somehow crosses it down to a lower level performance curve.

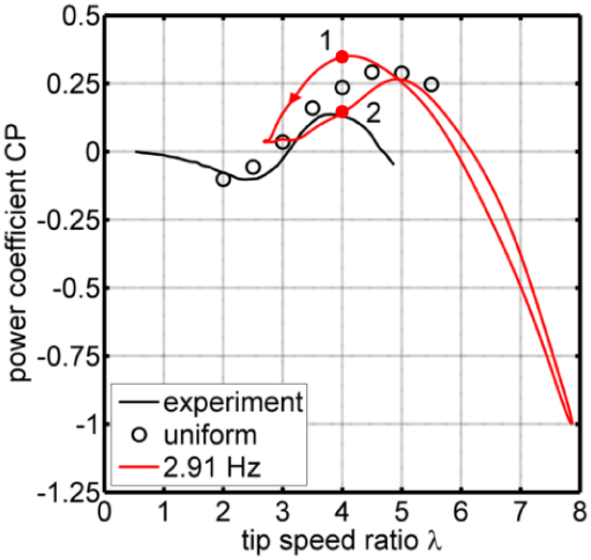

Figure 2.23. Unsteady CP of VAWT in 2.91Hz fluctuating wind [51].

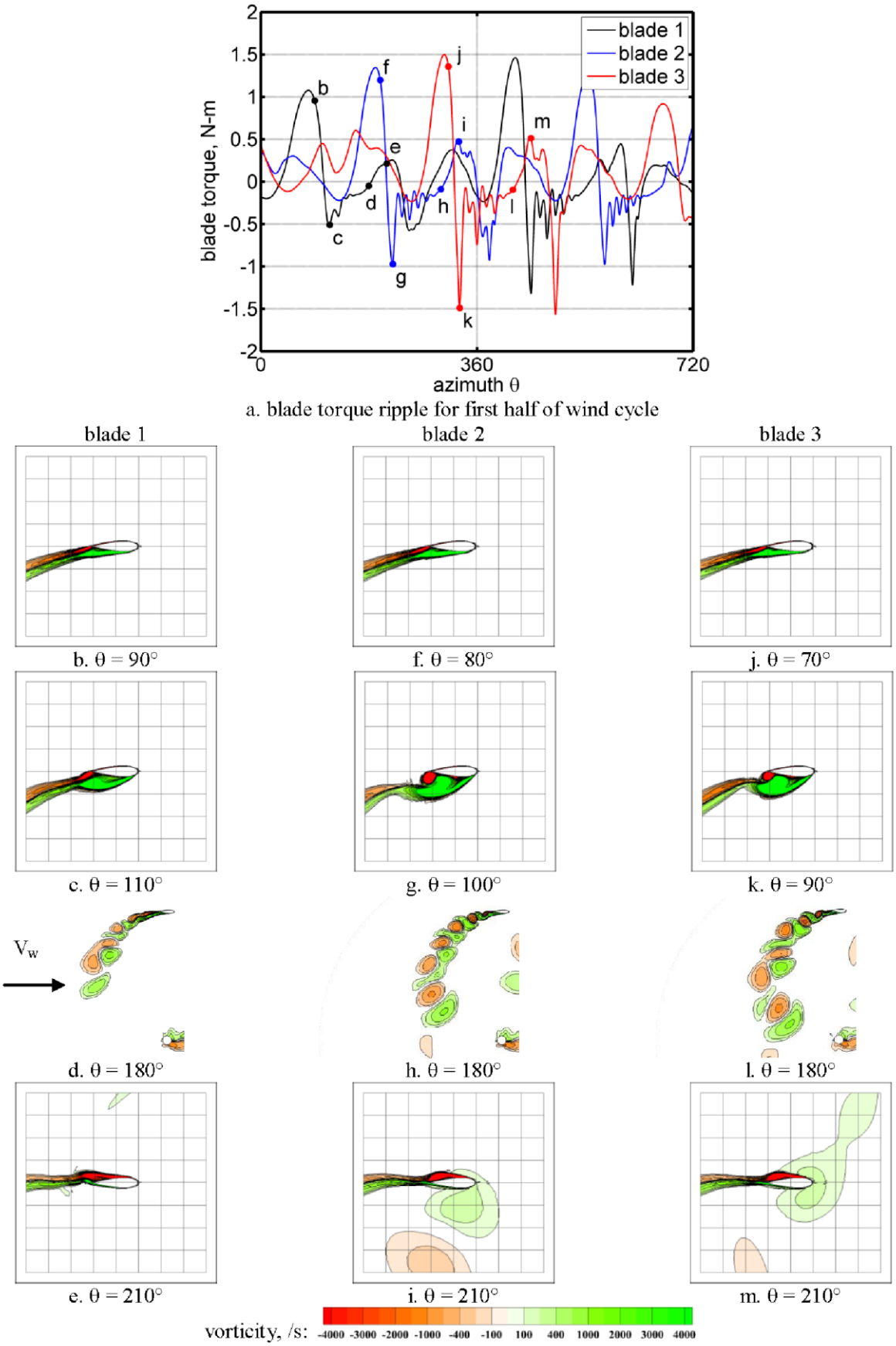

Figure 2.24. Stalling mechanisms of blades in unsteady wind [51].

Following the work of Hayashi in 2009, Hara et al [67] studied the effects of pulsating winds on a VAWT and the dependence of the performance to changes in the rotor's moment of inertia. The fluctuating wind was not sinusoidal but alternating gusts and lulls that were equally distant from a mean wind speed (Figure 2.25a). This was implemented by a blade pitch–controlled fan blowing to an Eiffel–type wind tunnel with the rotor 1.5m from the tunnel outlet (Figure 2.25b). Results show a phase delay in the response of the rotational speed from the wind variation but held a constant value of about $\pi/2$ regardless of amplitude. This was explained as an effect of the distance of the VAWT from the tunnel outlet where the hotwire was installed. The energy efficiency of the VAWT was observed to be constant in changing rotor moment of inertia and fluctuation frequency but a decrease is seen when fluctuations have large amplitudes. Further work for a larger scale VAWT using numerical techniques confirm their experimental observations and a locus of torque is produced as the VAWT response to the cyclic changes in wind speed (Figure 2.26).

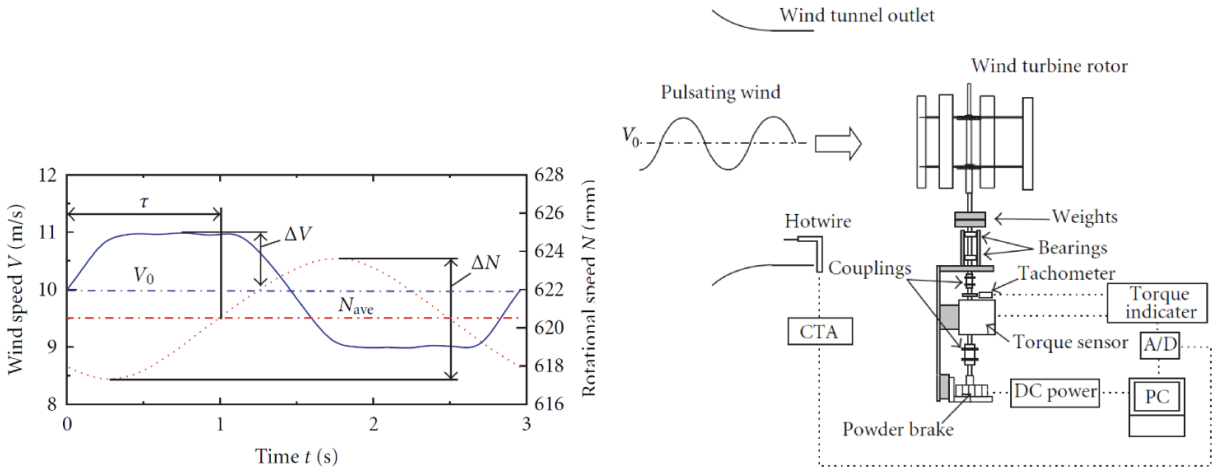

a. b.

Figure 2.25. Experimental setup of Hara et al [67] for pulsating winds: a) sample of phase–averaged pulsating wind data with rotor rpm response, b) VAWT and accessories relative to the wind tunnel outlet.

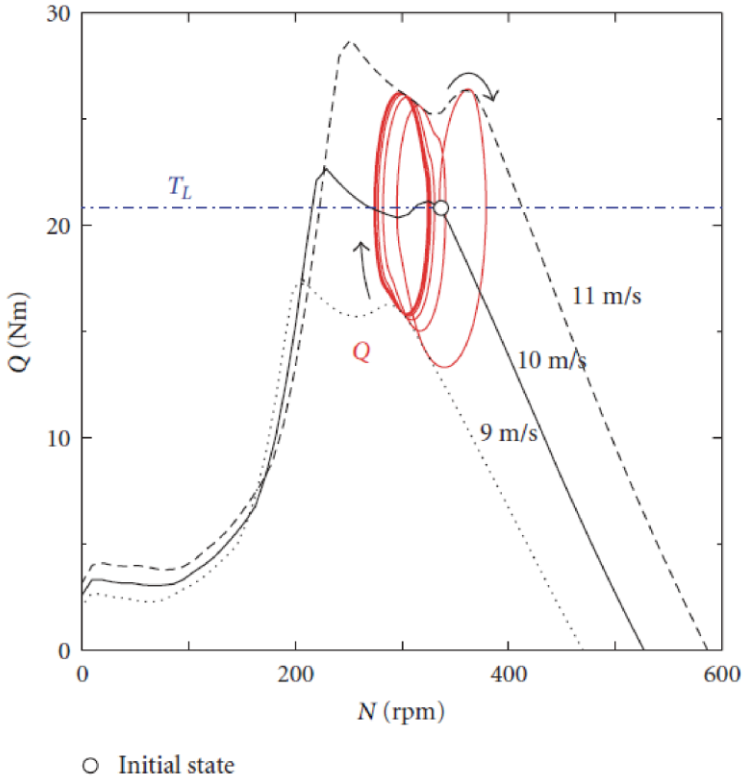

Figure 2.26. Numerical results for locus of torque, Q, of pulsating wind where mean wind velocity U = 10m/s, wind cycle period T = 16s [67].

In 2012, Scheurich and Brown [60] published their findings on a numerical model of VAWT aerodynamics in unsteady wind conditions. The fluctuating wind had a mean speed of 5.4m/s with a fluctuating frequency of 1Hz. Different fluctuation amplitudes were investigated for three blade configurations: straight, curved, and helical. Constant rotational speed was used in the numerical simulations and the boundary extents were far enough for the model to be considered as open field. Both straight (Figure 2.27a) and curved blades exhibited considerable variation in blade loading which is also observed in steady wind results. These variations in CP over one revolution are more significant than those induced by the unsteadiness of the wind. Helical blades perform much better with the unsteady CP tracing the steady performance curve quite well (Figure 2.27b). Overall performance degradation is observed when fluctuation amplitudes are high while the effect of frequency is minor for practical urban wind conditions. Hysteresis loops of the CP are seen on the helical configuration

that extend beyond the steady CP variation especially for the high frequency of wind fluctuation.

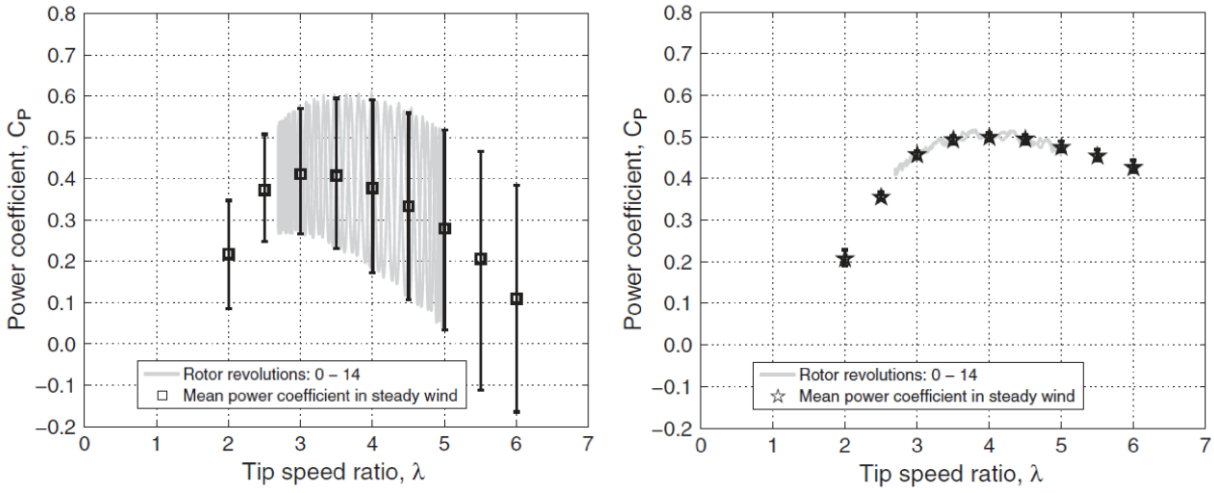

a. b.

Figure 2.27. Unsteady CP in unsteady wind [60] at ±30% fluctuation amplitude: a) straight blade, b) helical blades.

2.5 Summary

The existing literature related to the state of the art in VAWT research has been presented. Early efforts to understand VAWT performance was done through numerical work based on theories adapted from the aircraft industry. Mathematical models represented the VAWT initially in very simplistic terms as in the single stream tube model describing the loading on blades with reference to static aerofoil data and gradually developed into more complex yet more realistic modelling of the aerodynamics surrounding the VAWT including the double multiple stream tube model, vortex models, and vorticity transport model where the complexity of the aerodynamics is represented by more intricate modelling of unsteadiness like dynamic stall and blade–wake interactions. Although mathematical models have provided significant insight into the general behaviour of the VAWT within acceptable turnaround times, there has not been enough fidelity in the data that explain the aerodynamics in sufficient detail.

Computational fluid dynamics provided the required fine detail but at a cost. Nevertheless, advances in the understanding of the unsteady aerodynamics have been attained through CFD as exponential improvements in computing resources are achieved. Being an emerging field that is seen to be in need of substantial input given the limited capabilities of mathematical models and the inherent difficulties in experimental testing, major breakthroughs in the modelling of turbulence has led to more accurate prediction of the flow of physics that influence the overall performance of VAWTs. Through CFD validated by experiments, fundamental understanding of VAWT aerodynamics in steady wind conditions have been accomplished that have provided in–depth understanding of the factors that influence steady wind performance mainly linked to the geometric characteristics of the rotor such as blade section profile, solidity, and blade sweep.

Current understanding of VAWT aerodynamics is limited to steady wind performance. Very few attempts have been made to establish how a VAWT operates in unsteady wind conditions and why. A couple of numerical models have conflicting conclusions in the effects of the unsteady inflow to the power coefficient of the VAWT. The validity of these numerical models is questionable since they have been tested and compared to steady wind experimental data and assumed to be capable of predicting unsteady wind performance. The available experimental data fails to successfully identify the main reasons for the observed changes in performance for the VAWT from steady wind cases. The large gap in the fundamental aerodynamics of VAWTs in unsteady wind conditions has been the primary motivation why this body of work was carried out. The development of a reliable experimental testing apparatus that is capable of carrying out VAWT experiments in fluctuating winds is necessary for generating the much needed data that is lacking in literature. Through intensive CFD modelling, the flow physics surrounding VAWT blades in fluctuating winds can be investigated to link the flow predictions to the performance and provide a complete picture of the aerodynamics.

Chapter 3
Experimental Methods

3.1 Introduction

In this chapter, the experiment methods used to acquire performance data and relevant flow visualisation are discussed. Initially the experiment facility is described in sufficient detail and the procedure adapted to obtain and process the data is discussed. Lastly, an analysis of the possible sources of experimental errors is presented.

The experimental facility in the Department of Mechanical Engineering for wind turbine testing was established by Ph.D. student Mr. Jonathan Edwards who was a more senior student to the Author within the research group. Mr. Edwards designed and assembled all the necessary components of the testing rig including the rotor assembly, the start–up mechanism, the measurement assemblies (torque, angular speed, and wind speed), the control assemblies for the motor drive, and the development of the data logging Labview program. The Author's

own contribution to the test facility is mainly for the generation of the unsteady wind flow in the tunnel. As such, the standard procedure for VAWT testing was already in place and was adapted for the current research work undertaken. The steady wind performance of the VAWT was determined using the method developed by Mr. Edwards. The test protocol for visualisation measurements using PIV was also co–developed by Mr. Edwards and the Author during the conduct of all preliminary PIV experiments. Subsequent experiments for the final test conditions were also performed by the Author with Mr. Edwards. The unsteady wind performance of the VAWT was determined by adapting the steady wind data logging code and customising it for unsteady wind testing requirements which was generally conducting higher frequency of data recording.

3.2 Wind Tunnel Facility

The University of Sheffield – Department of Mechanical Engineering's low–speed wind tunnel was used for the experiments. The tunnel is an open-circuit suction device with an axial fan located at the outlet (Figure 3.1). The wind tunnel has a total length of 8.5m, including the 3m long test section. At the tunnel inlet, a honeycomb mesh (with cells 10mm wide and 100mm long) straightens the flow and breaks up any large scale flow structures present in the room. After the honeycomb downstream is a fine mesh screen with 1mm cell size that further breaks up flow structures smaller than the honeycomb cells and generates small scale turbulence that help even out the flow. A short settling section after the fine mesh permits turbulence and non-uniformities to dissipate, after which the flow is accelerated by a two way 6.25:1 contraction cone leading to the 1.2m high × 1.2m wide test section. A turbulence grid is placed at the inlet of the test section to generate turbulence at the VAWT test position of about 1% intensity. Oscillating vertical wooden shutters are placed downwind just before the end of the test section for generating the required back pressure in unsteady wind experiments. These shutters can be held stationary for steady wind experiments. The tunnel fan was controlled via a variable frequency drive that allowed the precise setting

of the fan speed in 1rpm resolution with a maximum speed of just over 900rpm theoretically producing wind speeds close to 25m/s. For the current work, structural safety reasons dictated a maximum of 10m/s to limit the aerodynamic forces generated in the VAWT.

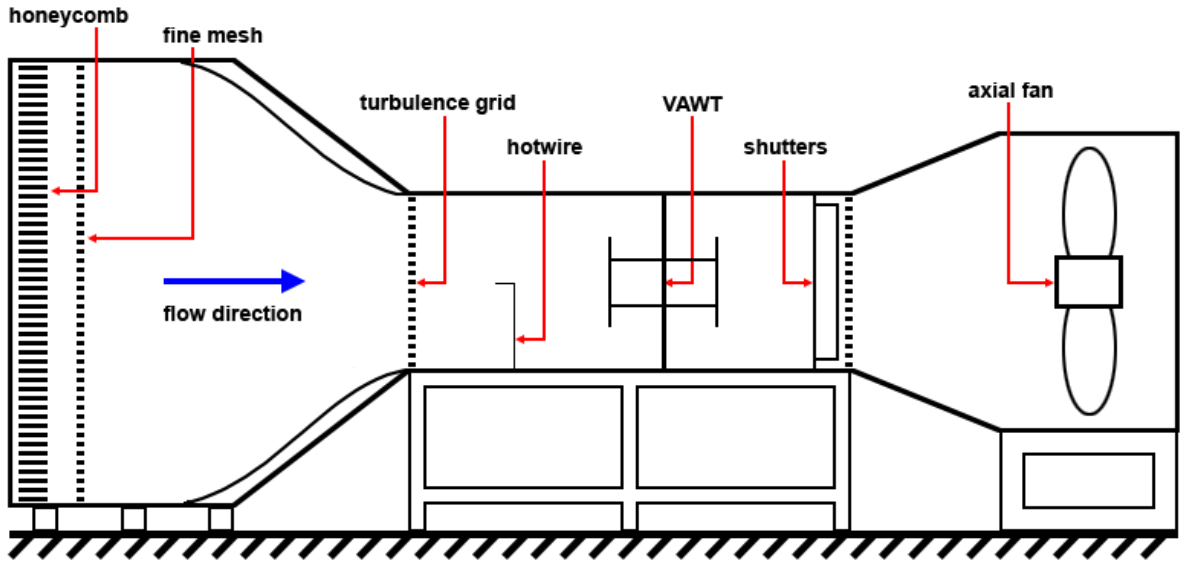

Figure 3.1. University of Sheffield wind tunnel facility.

3.3 Wind Turbine Model

The rotor is a straight–bladed VAWT with a 27mm diameter central shaft running through the top and bottom walls of the test section. The rotor is mounted in the centre of the test section area but is slightly downstream along the test section length. There are three NACA0022 blades with chord c = 0.04m each supported by two NACA0026 spokes of 0.03m chord at 25% and 75% blade length positions. There is an insert at the junction of the blade and the support arm that allows for different fixing angle configurations. For the entirety of this study a 0° fixing angle is used. A radial line from the VAWT centre to the blade perpendicularly intersects the chord at 0.5c. A hub is used to rigidly connect the support arms to the central shaft. The rotor diameter R is 0.35m and the blade span L is 0.6m giving the VAWT a solidity of σ = 0.34 following the conventional

definition ($\sigma = Nc/R$) and a wind tunnel blockage ratio of 0.29 ($2RL/A$, where A: test section area). Figure 3.2 details the final design of the rotor.

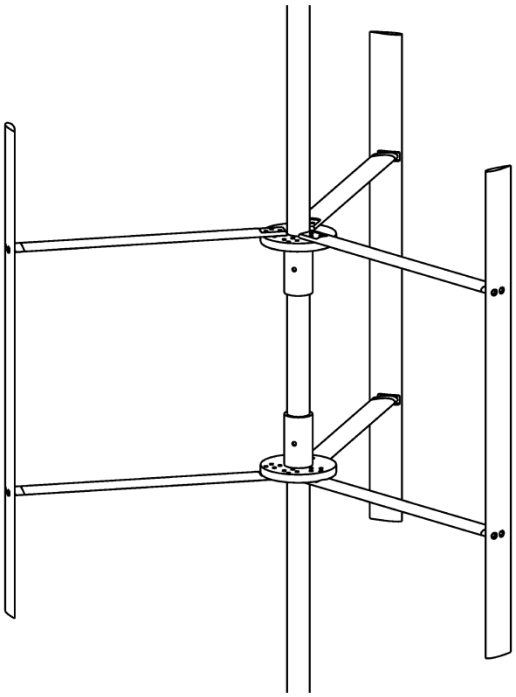

a. 3D view

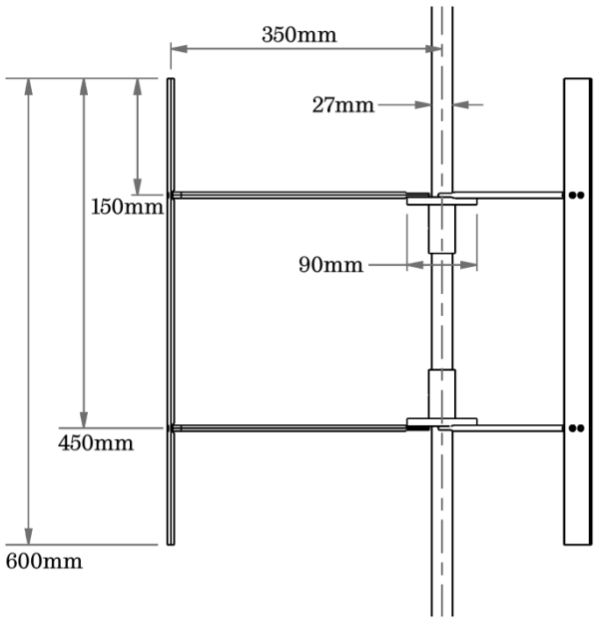

b. side view

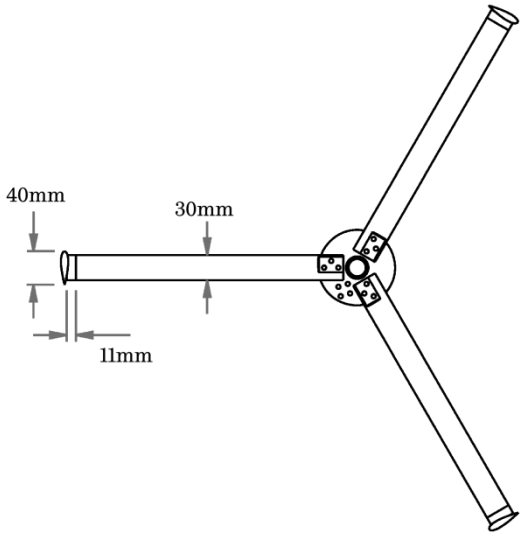

c. top view

Figure 3.2. VAWT rotor design (adapted from [68]).

3.4 Start–up Mechanism

The wind tunnel VAWT is typical of any lift–based VAWT of this scale where the machine is not capable of self–starting even at high wind speeds. A negative performance band at low λ prevents the VAWT from coming up to operating speed by itself. A start up mechanism provides the necessary drive to bring the rotor to the required λ where the rotation can be sustained with the VAWT's positive performance. A 250W DC motor was coupled to an electromagnetic clutch at the top of the rotor rig. The clutch is capable of completely disengaging the motor from the rotor shaft for tests that required the complete isolation of the VAWT from unknown or unquantifiable rotational resistance. This is particularly important for power measurement tests. For tests where control of the VAWT rpm is required, the clutch connects the motor to the rotor shaft so that the rotor rpm can be set and held at a constant value. This is useful when conducting PIV measurements where λ is in the negative performance band.

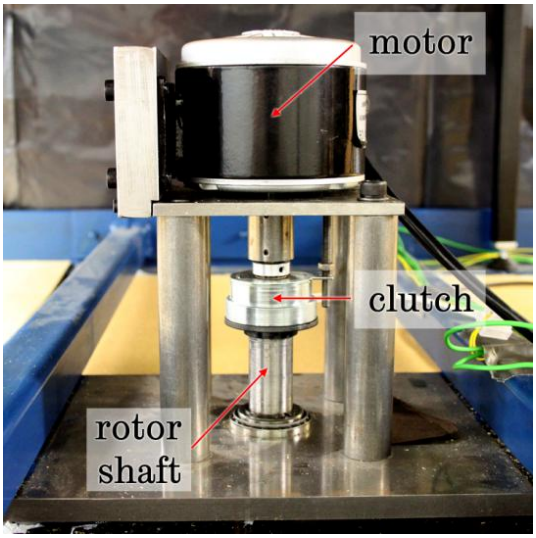

Figure 3.3. Start–up mechanism.

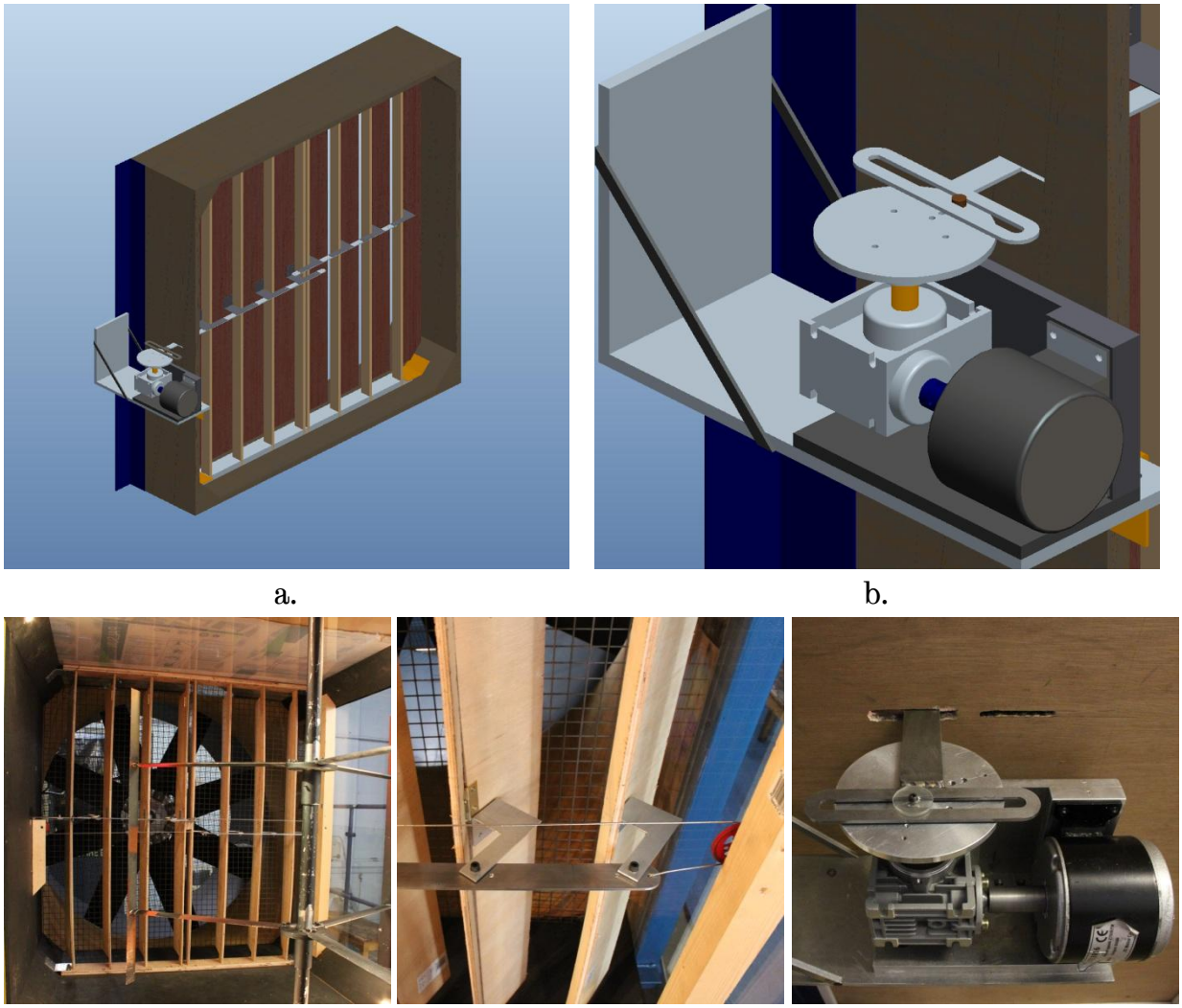

a. b.

c. d. e.

Figure 3.4. Mechanism to generate unsteady wind: a) CAD model of the shutter mechanism, b) CAD detail view of the mechanism drive, c) fully open vertical shutters with the VAWT in the foreground, d) detail view of bar linkage with partially closed shutters, e) motor–gearbox drive with pin–slot linkage.

3.5 Shutter Mechanism

The design of the shutter mechanism was initially carried out in CAD to test the feasibility of the linkage mechanism using the kinematic features of the CAD software (Figure 3.4a & b). When the design was verified to be feasible, drawings were produced from the CAD model for fabrication in the workshop. To generate unsteady flow in the wind tunnel, the shutter mechanism is actuated by energising the DC motor drive. The vertical shutters can oscillate at different closing angles and speeds. Bigger closing angles generate higher amplitudes while

faster oscillation produces higher frequency fluctuations. There are four adjacent wooden slats on the right that close to the right wall and another four on the left that close to the left wall. This arrangement is constructed to avoid a biased lateral movement of the flow due to a non-symmetrical obstruction downwind, thereby minimising any unnecessary direct or indirect effects on the VAWT performance. With respect to the VAWT, the back pressure produced by the shutters is expected to be symmetric. However even without the shutter mechanism, the VAWT wake is not expected to be symmetric. A DC motor coupled to a 75:1 worm gear speed reducer drives a mechanism composed of bar linkages, cables and pulleys, and a pin–slot linkage (Figure 3.4d & e).

3.6 Measurement Instrumentation

3.6.1 Rotational Velocity

To measure the rotor rotational velocity, an Avago optical encoder (model: AEDA-3300-TAM) with 3000 pulses per revolution was used. The encoder output was connected to a National Instruments BNC 2090 connector block. A National Instruments PCI–6220 data acquisitions card interfaced the connector block to a standard personal computer.

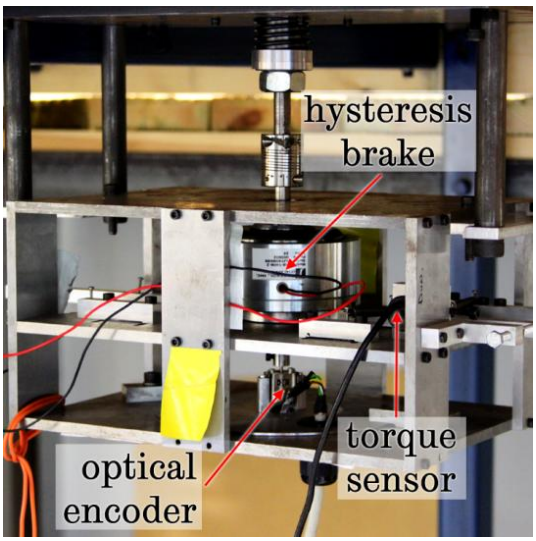

Figure 3.5. Torque and rpm measurement assembly.

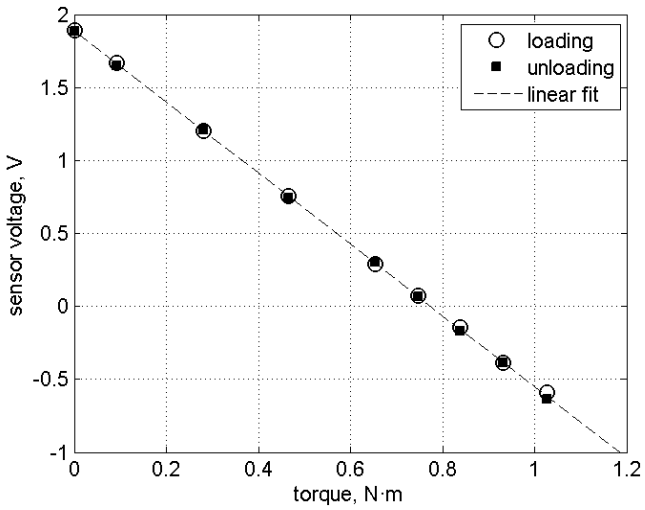

Figure 3.6. Calibration fit for the torque sensor, adapted from [68].

3.6.2 Torque

Blade torque was not directly measured in the experiments but derived from its fundamental relationship to rotational acceleration (see Sec. 3.6). For tests that are within the positive performance region of the VAWT, applying a brake torque was necessary to prevent the rotor from over speeding and causing structural and safety issues. A Magtrol hysteresis brake (model: HB-140-M2) was used for this purpose. As current is applied to the hysteresis brake, a magnetic field proportional to the current is established within the device producing the desired braking effect. The braking torque T_{app} is independent of the rotational speed of the rotor and as such provides a constant brake regardless of the running conditions of the VAWT. To measure the applied torque T_{app}, the brake is mounted on a spring balance and a Sangamo DC miniature displacement transducer (model: DFG/2.5) measures the linear displacement of the transducer core attached to a point on the balance with known lever arm length of 155mm from the brake centre. Although the movement of the balance is rotational, the full stroke of the displacement transducer is only 2.5mm rendering the rotational displacement practically linear. The transducer voltage was linearly proportional to the displacement and a calibration curve fit (Figure 3.6) was obtained by loading the system with static standard weights. Maximum error was observed to be ±0.01Nm.

3.6.3 Wind Velocity

High frequency measurement of wind speed is carried out using a constant temperature hotwire anemometer (probe model: Dantec Type 55 P16). The hotwire was positioned 0.6m from the bottom wall, 0.5m from the right wall, and 0.4m downstream of the test section inlet. It was calibrated using a highly sensitive Furness Controls FCO510 micromanometer with a stated accuracy of 0.25% between 10% (20Pa) and 100% (200Pa) of the reading scale. A Pitot–static tube was connected to micromanometer and mounted 0.1m to the left and 0.1m down of the hotwire position. Hotwire measurements were performed across the entire tunnel cross sectional area up to 0.1m from the tunnel walls and the variations in the readings between different positions were within the measurement variation of one position. As such, flow was considered to be uniform throughout and the selected final position of the hotwire is considered acceptable and representative of the general flow velocity in the tunnel. The reference velocities for hotwire calibration were derived from the differential pressure readings using the ambient temperature from a digital thermometer and ambient pressure from a mercury barometer taken at the start of each series of tests in a day. The entire calibration procedure was conducted within 10 minutes of the ambient temperature and pressure measurements to keep the calibration data within similar conditions.

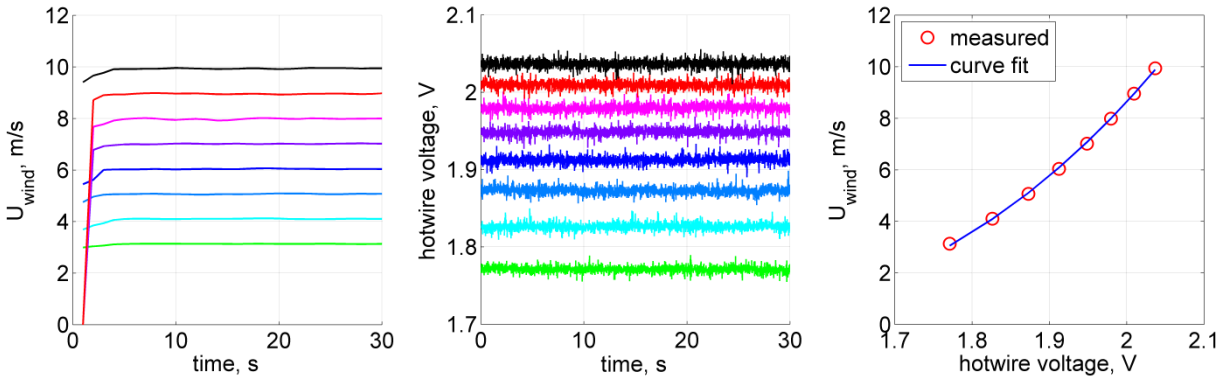

a. b. c.

Figure 3.7. Hotwire calibration plots: a) wind speed calculated from differential pressure readings, b) hotwire voltage readings, c) calibration curve fit.

The tunnel fan was run at various constant speeds and at each fan speed, the flow was allowed to settle before measurements were made. A total of 8 constant wind speeds were tested covering a range of approximately 3m/s up to 10m/s. For each test wind speed, both differential pressure readings from the micromanometer and voltage readings from the hotwire were recorded for 30s. The fastest logging frequency of the micromanometer was 1Hz so this was used for all the tests. The hotwire logging frequency was tested at frequencies of 100Hz, 1000Hz, and 10,000Hz. The final logging frequency was set to 100Hz which was determined to be adequate to capture the unsteadiness in the flow velocity due to turbulence effects. During each test, the first 5 seconds of manometer data was discarded. The average of the last 25s of the manometer data and the 30s of the hotwire data were taken and used in computing for the coefficients of a simplified form of King's Law equation (3.1) for hotwire anemometry using a simple least–squares curve fitting method.

$$V^2 = A + B \cdot U^n \tag{3.1}$$

where V: hotwire voltage
U: wind speed
A, B, n: constant coefficients, $n \sim 0.5$

Determining the flow turbulence was an important part of the experiments as the measured turbulence was eventually used in the boundary conditions of the numerical simulations. With a turbulence grid in place at the start of the test section, it was necessary to find the level of turbulence of the flow at the position of the VAWT since a decay in turbulence intensity Tu is expected between these two points. The hotwire was traversed downstream in increments of 0.2m from its initial position up to near the upstream most position of the VAWT blades at 1.4m from the test section inlet. Figure 3.8 shows a plot of the measured Tu versus measurement position. At the initial measurement point of x = 0.4m from the test section inlet, Tu = 3.43%. It rapidly decays down to 1.80% after only a 0.4m movement downstream at x = 0.8m. By the time the wind has reached x = 1.4m, Tu has dropped to a value of 1.04%.

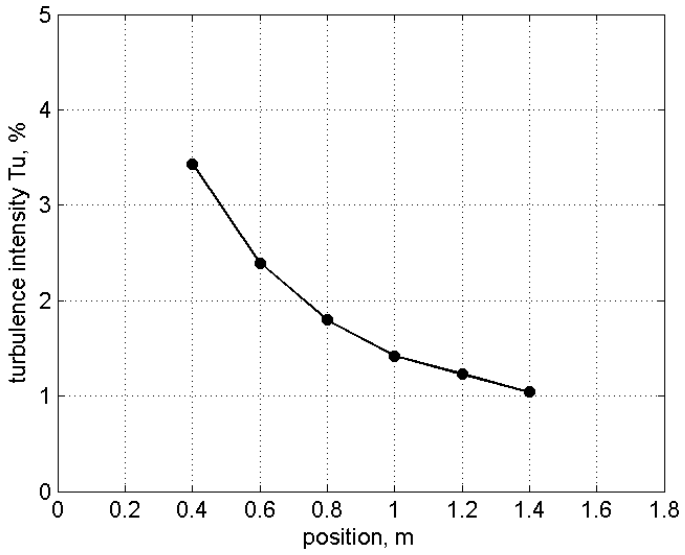

Figure 3.8. Turbulence intensity decay in the wind tunnel
(x = 0: test section inlet).

3.7 Steady Wind Performance

Measurement of the steady blade power used an indirect method following a procedure developed by Edwards [68]. The VAWT blade performance was measured by spinning the rotor down from a high rotational speed and the deceleration monitored using the optical encoder. The instantaneous acceleration is the ratio of the change in angular speed ω over the elapsed time between the two ω readings, given by

$$\xi = \frac{\omega_2 - \omega_1}{t_2 - t_1} \tag{3.2}$$

where ξ: angular acceleration
ω: angular speed
t: time

For each wind speed condition, two spin down tests were needed to determine the blade performance of the VAWT. The first involves the spin down of the rotor without the blades. This is necessary to determine the system resistance which includes the drag induced by the support arms, and bearing and mechanical friction. After this test, T_{res} is established via Eq. 3.3 for the specific wind speed

that the spin down test was performed. In all resistive spin down cases, there was no need to apply a brake to the system because there was no positive performance expected without the blades attached. Also, it was seen that the resistive load of the system was independent of the wind speed, i.e. the T_{res} curves for all resistive spin down tests coincide with each other.

$$T_{res} = I_{rig}\xi \tag{3.3}$$

where I_{rig}: rotational mass moment of inertia.

The second spin down with the blades attached measured the full rotor performance including blade tip effects and blade–support arm junction effects. Blade torque T_B (of three blades, differentiated from the single blade torque T_b of Eq. 1.4) was deduced from the difference between the rotor torque $I_{rig}\xi$ and the system resistance T_{res}. It is necessary to separate the blade performance from the contribution of other design components not only for design considerations but also for direct comparison to 2D CFD models where only blades are analysed. For tests at wind speeds greater than 7m/s, the application of the hysteresis brake was required because of positive rotor performance which caused the VAWT to cut–in and not come to a full stop. Blade power was deduced by subtracting both system resistance and brake torque applied T_{app} from the rotor torque. The equation for this relationship is shown in Eq. 3.4.

$$T_B + T_{res} + T_{app} = I_{rig}\xi \tag{3.4}$$

where T_B: 3–blade torque
T_{res}: resistive torque
T_{app}: applied brake torque
I_{rig}: rotational moment of inertia of the VAWT

Plots of ω versus time are shown in Figure 3.9 for the two spin down tests. In both tests, the rotor is spun to a high rpm corresponding to a maximum λ of almost 5 for each wind speed being tested so that full coverage of the performance curve can be obtained. Figure 3.9b clearly shows the influence of the blades on the

rotation of the rotor. The time to spin the rotor up is much longer with the blades on than without. There is also a distinct plateau in rpm which indicates positive blade performance, counteracting the resistive loads such as mechanical friction, aerodynamic drag, and brake torque (when applicable).

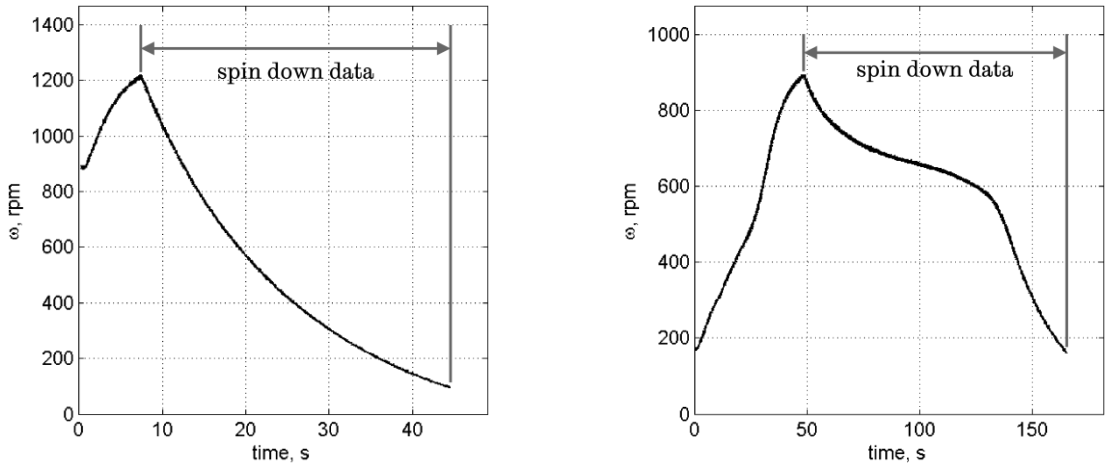

a. b.

Figure 3.9. Sample spin down data plots: a) without blades, b) with blades.

An important consideration in the test assumptions is that the addition of the blades does not have an effect on the resistive loads in the system. There are several likely reasons for which this might not the case. For one, the increased weight of the rig may alter the bearing friction. To verify this, the pre–tension spring that holds the rig firmly in place was further compressed to simulate an added weight into system. Spin down tests with the additional load were conducted and the resulting T_{res} compared to the baseline case. There was no significant difference observed in the overall system resistance with the added load. Another consideration that may affect the resistive loads in the system was the blade–support arm junction which may increase or decrease the system drag. Additionally, with the support arm ends not exposed to tip effects, a reduction in drag may be probable. Assessing the individual effects is difficult and the degree of their influence on the overall value of T_{res} is likely very small. It is assumed that the tests are satisfactory in establishing the overall resistive loads in the system.

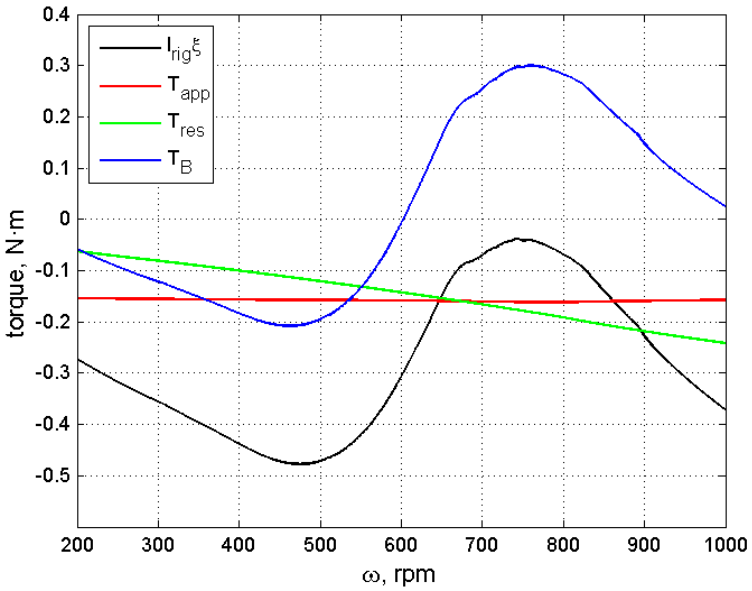

Figure 3.10. An illustration showing the results for the torque terms vs. ω as determined from two spin down tests at 8m/s.

Figure 3.10 shows a sample result for a set of spin down tests at 8m/s. The variations of the torque terms in Eq. 3.4 are presented versus ω covering an equivalent λ range of about 1 – 5. The total rotor torque $I_{rig}\xi$ is seen to be completely in the negative region. This is expected and necessary for the spin down to be carried out. The $T_{app} \approx -0.16$N·m is the constant braking torque applied during the complete rotor spin down test. The T_{res} is seen to increase in magnitude as ω increases. Blade torque T_B varies from the negative region at low λ to positive values above ω = 602rpm corresponding to a λ = 2.9. Maximum T_B is 0.30N·m at ω = 759rpm (λ = 3.9) while minimum T_B is –0.21N·m at ω = 462rpm (λ = 2.2).

3.8 Unsteady Wind Performance

Determining the unsteady blade CP of the VAWT running in unsteady wind is very similar to the steady wind case. The fundamental relationship of the torque terms involved is identical. The only difference would be in the manner by which data is collected. For the unsteady wind experiments, a quasi–steady condition was sought first before any data logging was performed. The wind must have been

fluctuating at a constant amplitude and frequency. This was controlled by setting a constant power input into the shutter mechanism drive to effect the desired fluctuation. The VAWT rpm was also required to fluctuate in a periodic manner. This was more difficult to attain since there is no active control system and the rotor was left by itself to adjust to the unsteady flow. Nevertheless, a periodic state was usually attained within 10 minutes. Only after attaining periodicity can data collection commence.

Two minutes worth of data was logged for each test condition. This roughly gives about 30 cycles of fluctuation at the slowest rate. The cycle average was computed and formed the basis for the unsteady performance analysis. As mentioned in the introduction of this chapter, the only modification to the test procedure developed by Mr. Edwards was to increase the data logging frequency of the Labview script to properly track the unsteady nature of the logged variables. From an initial 10Hz logging frequency, the rate was subsequently doubled 3 times over until the program was recording data at 80Hz. It was determined that 40Hz logging rate is sufficient in capturing the unsteadiness of the U and ξ. The highest frequency of 80Hz already showed the effects of noise on the signal, cancelling the averaging step in the Labview code intended to filter out the noise.

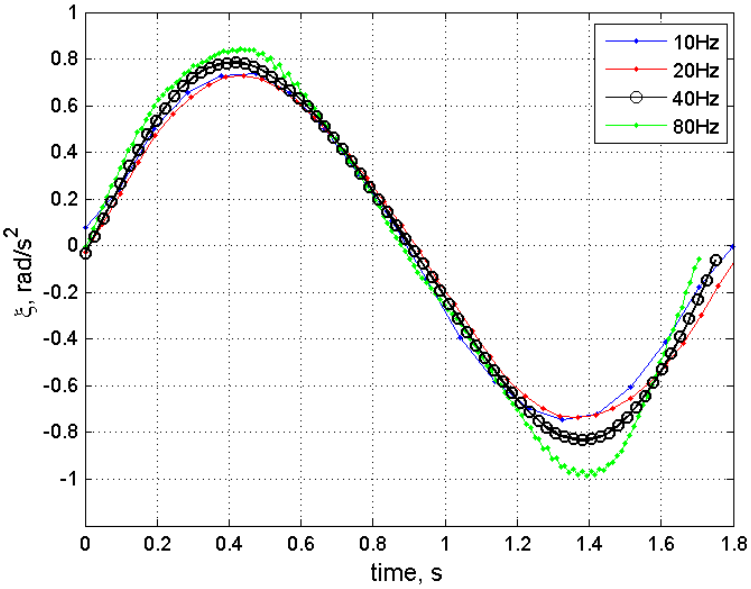

Figure 3.11. Study on data logging frequency and its effects on computed ξ.

3.9 Particle Image Velocimetry

In order to examine the flow physics surrounding the VAWT blades, Particle Image Velocimetry (PIV) was utilised. The basic principle of PIV is to capture a pair of images of the flow under study with a specific time interval between them. Each image is generated by seeding the fluid domain with particles that are assumed to follow the flow dynamics and illuminating a plane of particles using some sort of light source such as a laser sheet. The slight difference in particle positions between images is used to compute for the velocity flow field.

First attempts to study the flow physics around VAWT blades were performed by Fujisawa and Takeuchi [69] followed by Fujisawa and Shibuya [70]. In both studies, the flow field was visualised by a tracer method with plastic microspheres of 30–50μm diameter. Images were captured using a monochrome CCD camera which was fixed in a rotating table that moved in sync with the rotating blade. The VAWT had a single straight blade of a NACA0018 section with chord c = 0.01m, span L = 0.135m, and rotor radius R = 0.03m and made of acrylic resin. The blade was fixed on an end plate with no central shaft to facilitate visualisation all around the rotation. The experiment was carried out in water tunnels with maximum flow velocity U = 0.05m/s giving a Re = 2,000. The light source was a set of stroboscopes triggered by a photosensor connected to the rotating end plate. The time interval between the two flashes was set to 2 or 3ms depending on the λ being tested.

Simao Ferreira et al [47, 71-73] conducted PIV experiments on a larger VAWT in a wind tunnel. The work was performed at $Re = 5 \times 10^5$ and 7×10^5 and λ = 2, 3, and 4. The flow was seeded using a fog machine with approximately 1μm droplets. The particles were illuminated using a light sheet generated by a Nd:YAG laser (200mJ/pulse) that was approximately 2mm thick at the field of view (FOV). A narrowband green filter was used for daylight interference on a CCD camera with 1,374 × 1,040 pixels. The time interval between pulses was set to roughly 8–pixel

displacement assuming local velocities are 4 times the free stream values. At each azimuth position, 30 to 100 images were taken analysed with an iterative multi–grid window deformation technique.

3.9.1 PIV Equipment

A Dantec Dynamics 2D PIV system was used for all visualisation tests. The system has a Litron Nano–S–65 Nd:YAG laser which emitted light with a maximum energy of 65mJ per pulse at a wavelength of 520nm. A 4 megapixel CCD camera was used to capture the images. A TSI 9306A Six Jet Atomiser generated tracer particles of olive oil that had an approximate size of 2μm in diameter.

In PIV, particle motion is the measured quantity and is used to represent the fluid velocity field. Therefore, it is extremely important that the particles' tendency to attain velocity equilibrium with the fluid is achieved and can be properly quantified. The ability of tracer particles to follow the flow is measured using Stokes number S_k such that a value $\ll 0.1$ gives a tracing error of less than 1% [74]. S_k is defined via Eq. 3.5.

$$S_k = \frac{\tau U}{d_c} \tag{3.5}$$

$$\tau = \frac{\rho_d d_d^2}{18\mu_f} \tag{3.6}$$

where
- τ: response time of the particle
- U: velocity of the fluid under study
- d_c: characteristic dimension of the obstacle
- ρ_d: density of the tracer particle
- d_d: diameter of the tracer particle
- μ_f: dynamic viscosity of the fluid

The response time τ of the tracer particle should be faster than the smallest time scale of the flow and can be deduced using Eq. 3.6. Assuming a density of

920kg/m^3 for olive oil, τ was computed to be about 1.1×10^{-5}. The characteristic dimension used was the chord length of the blade while the velocity of the fluid was set to U = 40m/s derived from the maximum computed local velocity of a comparable CFD simulation at λ = 4. These values led to a $St \approx 0.01$ which meant that the particles should follow fluid streamlines closely and avoid deviating from the flow during rapid changes in flow speed and direction.

Seeding was carried out by running the wind tunnel fan for 8 minutes while introducing the particles upstream essentially seeding the entire laboratory room. This was found to be the most effective way to achieve adequate and uniform seeding distribution and density. After every 30 minutes of testing, the seeding was topped–up for 1 minute. The laser was mounted on an elevated platform outside the wind tunnel. The position of the laser sheet plane was approximately midway between the support arm and the blade end (Figure 3.12). This was selected to be within the region that best represented a quasi–2D flow that can be compared to CFD results. Anywhere near the blade ends or the support arms (green regions) experienced flow that were influenced by these geometric features causing significant deviation from the quasi–2D flow sought after.

The number of samples taken per azimuth position was carefully chosen after a systematic study of the effects of sample number on the calculated vorticity. The smallest sample size tested was 5 while the maximum was 200. Beyond 45 samples, there was little change observed in vorticity plots. Since the time to acquire images was not an issue, 100 images were taken per azimuth position to give statistical confidence in the averaged results. The time interval between pulses was also investigated and 15μs was seen as a suitable time gap that allowed enough time for slow moving particles to move within the interrogation window in sufficient distance whilst preventing fast moving particles from exiting the window and being completely lost.

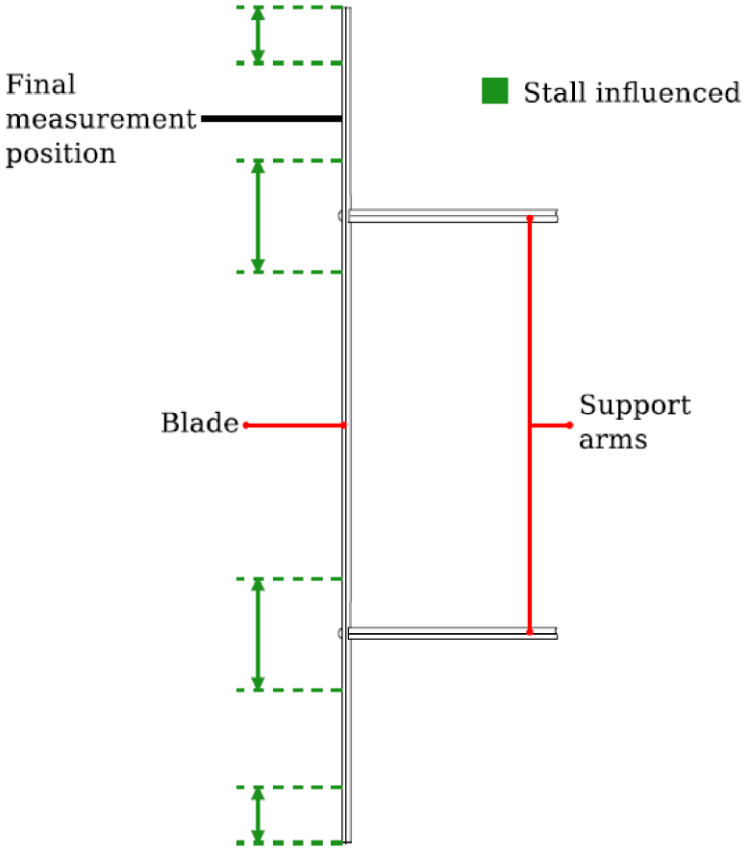

Figure 3.12. Diagram showing the final position of the laser sheet plane (adapted from [68]).

An almost complete map of the whole rotation was generated by taking 28 azimuth positions around at 10° intervals starting at θ = 0°. The presence of support frames blocked the camera view at θ = 20°, 30°, 150°, 160°, 200°, 210°, 330°, and 340°. A camera rig was installed on top of the wind tunnel to capture the end view of the blade perpendicular to the laser sheet plane. The camera was mounted on a rotating arm with the axis in line to the VAWT axis thereby permitting the positioning of the FOV to the desired azimuth. Triggering the laser to fire and the camera to capture exactly on the desired azimuth was achieved using the additional channel in the encoder that gave a once–per–rev pulse and syncing the trigger to the passing of a specific blade in the FOV. The radial position of the camera was set such that the blade was in the centre and the chord line parallel to one edge of the FOV (Figure 3.13).

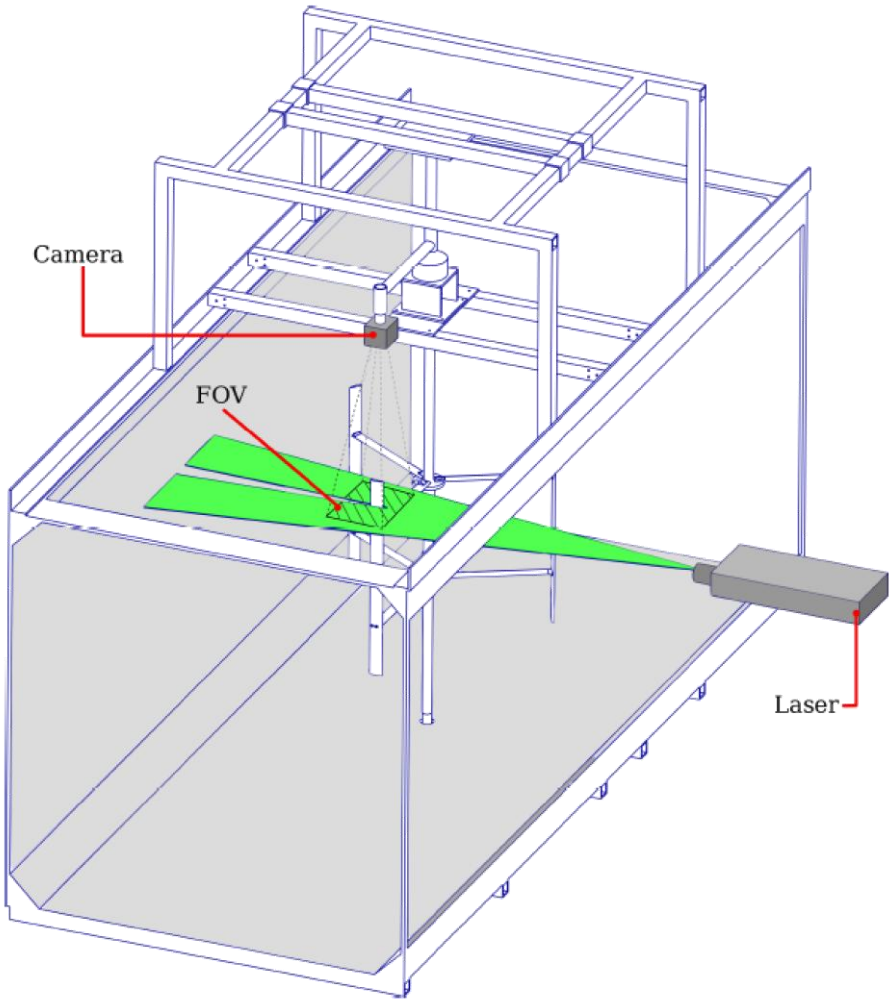

Figure 3.13. An illustration of the position of the laser sheet relative to the camera and the blade, showing the location of the FOV (adapted from [68]).

The interrogation window size was set to 32 × 32 pixels with 25% overlap, resulting in an 85 × 85 matrix of the 2,048 × 2,048 pixel FOV. The approximate size of the FOV was 140mm × 140mm. An adaptive correlation was used to process the images and a subsequent a 3 × 3 window moving average filter was applied to remove spurious vectors with magnitudes exceeding 20% of the neighbouring vectors. Invalid regions such as the blade shadow and the flow next to the blade wall were masked out and excluded in the data. A sample processed image is shown in Figure 3.14. The scale of the vorticity presented is the scale used all throughout the study and ranges from –5000 to 5000 /s.

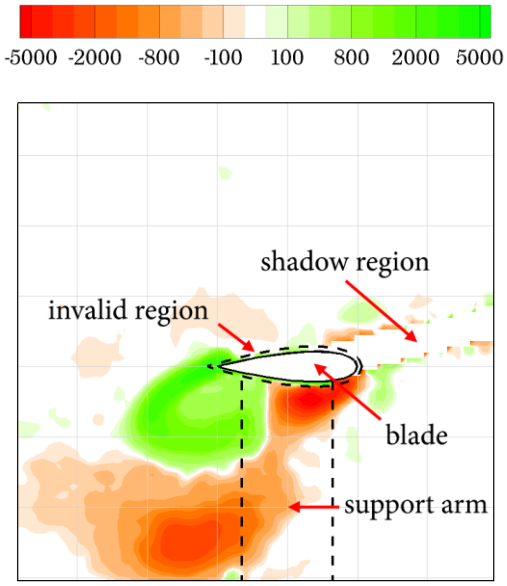

Figure 3.14. Sample plot of vorticity showing important regions in the PIV image.

The vorticity plot in Figure 3.14 is a vector map derived from the velocity flow field. The general form of vorticity in 3D is the curl of the velocity field,

$$\overline{\Phi} = \nabla \times \overline{U} = \left(\frac{\partial W}{\partial y} - \frac{\partial V}{\partial z} \right) \hat{i} + \left(\frac{\partial U}{\partial z} - \frac{\partial W}{\partial w} \right) \hat{j} + \left(\frac{\partial V}{\partial x} - \frac{\partial U}{\partial y} \right) \hat{k} \tag{3.7}$$

For data involving only 2 dimensions, such as in the case of 2D PIV and 2D CFD, the vorticity reduces to a single vector along the z–axis and is given by

$$\Phi_z = \frac{\partial V}{\partial x} - \frac{\partial U}{\partial y}. \tag{3.8}$$

Vorticity has been chosen as the parameter of all flow physics plots as it shows a good indication of separation and reattachment, wake convection and interaction, and presence of shed vortices, all of which are critical to the analysis linking aerodynamics to performance.

3.10 Experimental Error Analysis

3.10.1 Air Temperature and Pressure

The air temperature in the wind tunnel was measured using a digital thermometer. The precision of the thermometer was 0.1°C. The ambient air pressure was also measured using a mercury barometer with a precision of 0.05mmHg. It is necessary to measure both the air temperature and pressure to be able to derive the ambient air density using the ideal gas law. The relationship used to calculate the air density ρ is given as

$$\rho = \frac{p}{RT} \tag{3.9}$$

$$\%\text{error} = \frac{\left(\rho_{new} - \rho_{ref}\right)}{\rho_{ref}} \times 100 \tag{3.10}$$

where p is the ambient pressure in Pascals, R is the specific gas constant of dry air (287.058 J/kg·K), and T is the ambient temperature in Kelvin. At standard conditions of 15°C and 101,325Pa, an error in temperature of ±0.1°C and in pressure of ±0.05mmHg results in a maximum error in air density of about ±0.04% as shown in Table 3.1 where the first entry is the reference case. This maximum error is considered to be negligible. Percent error is defined in Eq. 3.8 and is adapted to any error computation throughout the remainder of the section.

T (°C)	P (mmHg)	ρ (kg/m^3)	%error
15	760	1.2250	
15.1 (+0.1°C)	760.05 (+0.05mmHg)	1.2246	–0.028
14.9 (–0.1°C)	759.95 (–0.05mmHg)	1.2253	0.028
14.9 (–0.1°C)	760.05 (+0.05mmHg)	1.2255	0.041
15.1 (+0.1°C)	759.95 (–0.05mmHg)	1.2245	–0.041

Table 3.1. Error in air density relative to errors in temperature and pressure readings.

3.10.2 Flow Velocity

Flow velocity is not measured directly but derived from multiple measurements of the dynamic pressure of the flow in the tunnel and the calibration of a hotwire anemometer which was performed at the start of every test day. A set of steady wind speed measurements was taken by increasing the wind tunnel fan speed from 135rpm to 415rpm in 40rpm increments. For each fan setting, the dynamic pressure was read using the micromanometer which had a precision of 0.01Pa. The flow velocity is derived from the air density and dynamic pressure measurements using the following relationship

$$q = \frac{1}{2}\rho U^2 \tag{3.11}$$

where q is the dynamic pressure in Pascals, and U is the flow velocity in m/s. The greatest errors in the computation are expected in the lowest velocity region where the accuracy of the pressure readings is just an order of magnitude smaller than the measured values. A sample computation is presented in Table 3.2 for velocities close to 3m/s and the maximum error observed is ±0.085%. When velocities close to the VAWT operating condition of 7m/s are considered, the maximum error is ±0.017% as shown in Table 3.3. Similarly, these errors are taken to be negligible.

q (Pa)	U (m/s)	%error
5.9	3.104	
5.91 (+0.01Pa)	3.106	0.085
5.89 (–0.01Pa)	3.101	–0.085

Table 3.2. Error in flow velocity at 3m/s relative to errors in air density and dynamic pressure readings.

q (Pa)	U (m/s)	%error
29.6	6.952	
29.61 (+0.01Pa)	6.953	0.017
29.59 (–0.01Pa)	6.951	–0.017

Table 3.3. Error in flow velocity at 7m/s relative to errors in air density and dynamic pressure readings.

U (m/s)	P_w (W)	%error
7.000	88.24	
7.001 (+0.02%)	88.29	0.06
6.965 (–0.02%)	86.18	–0.06

Table 3.4. Error in wind power at 7m/s relative to errors in flow velocity and air density computations.

Errors in flow velocity estimation usually have significant effects on the computed wind power going through the VAWT because the relationship is cubic as presented in Eq. 1.6. Despite the cubic relationship, the maximum computed error in wind power is only ±0.06% (Table 3.4) assuming a rounded–up *U*–error of ±0.02% at 7m/s.

When considering flow velocity measurements using the hotwire, a Least Squares fit was utilized to determine the constant coefficients of the King's Power Law (Eq. 3.1) relating the hotwire voltage readings to the velocity values derived from the differential pressure readings. The standard error which describes the variance of the error of the fit from the actual values is given by

$$s_y = \sqrt{\frac{1}{N-2}\sum_{i=1}^{N}\left(y_i - \hat{y}\right)^2} \tag{3.12}$$

where N is the number of sample points, y_i is the actual value of the variable, and $\hat{y}$ is the best fit estimate of the variable in question. Ideally the standard error of both voltage and wind speed should be taken into account. However, the NI PCI–6220 is a 16–bit DAQ with a measurement range of ±10V resulting to a precision error in the voltage readings of 3e–4 and was considered negligible. This simplifies the error analysis to inaccuracies in wind speed estimates. With a computed error of less than ±0.5% for wind speed estimates from differential pressure readings, the standard error for the flow velocity estimates using the hotwire is calculated to be ±0.05m/s. This leads to a maximum error in the wind power computations of about ±2.15% (Table 3.5). Since all measurements required high frequencies of data logging that the micromanometer is incapable of doing,

the hotwire data is taken as the velocity data for all measurements. As such, the errors taken are the hotwire measurement errors.

U (m/s)	P_w (W)	%error
7.0	88.24	
7.05 (+0.05m/s)	90.14	2.158
6.95 (–0.05m/s)	86.36	–2.128

Table 3.5. Error in wind power at 7m/s relative to errors in flow velocity from hotwire readings.

3.10.3 RPM Measurements

Accurately measuring the rotational speed of the VAWT plays a significant role in the estimation of the rotor power. The blade torque T_B is derived using the rotational velocity recorded in rpm, the applied torque T_{app}, and the resistive torque T_{res} corresponding to the rpm as defined in Eq. 3.4. The optical encoder used to monitor the instantaneous rpm has 3000 slots resulting in a precision of 0.8rpm, assuming measurement errors of ±1 pulse per rev. To quantify the effects of inaccuracies in rpm measurements, two λ conditions were selected in the spin down test taken close to 7m/s. These represent the conditions near minimum and maximum CP for the spin down test being considered. As seen in Table 3.6, the maximum error in blade power P_B is very small at ±0.24%. The error is practically negligible compared to the error in wind power estimates.

rpm	T_{res} (N·m)	T_B (N·m)	P_B (W)	%error
high λ				
668.0	–0.14979	0.15087	10.554	
668.8 (+0.8rpm)	–0.14997	0.15105	10.579	0.2430
667.2 (–0.8rpm)	–0.14960	0.15068	10.528	–0.2426
low λ				
454.0	–0.10305	–0.19412	–9.229	
454.6 (+0.8rpm)	–0.10320	–0.19397	–9.238	0.0977
453.2 (–0.8rpm)	–0.10290	–0.19427	–9.220	–0.0980

Table 3.6. Error in blade power relative to the errors in rpm readings.

3.10.4 Torque Measurements

Accurate measurement of the torque is important when the hysteresis brake is used. From the calibration of the torque sensor, the observed maximum error is ±0.01N·m. Similar to the selected conditions in Sec. 3.10.3, two λ cases near minimum and maximum CP for the spin down test close to 8m/s were investigated. As shown in Table 3.7, the maximum in blade power error due to errors in applied brake readings is ±4.8%.

T_{app} (N·m)	T_B (N·m)	P_B (W)	%error
high λ			
–0.16108	0.28953	23.437	
–0.15108 (+0.01N·m)	0.27953	22.627	–3.454
–0.17108 (–0.01N·m)	0.29953	24.246	3.454
low λ			
–0.15638	–0.20661	–10.515	
–0.14638 (+0.01N·m)	–0.21661	–11.024	–4.840
–0.16638 (–0.01N·m)	–0.19661	–10.006	4.840

Table 3.7. Error in blade power relative to errors in applied torque readings.

3.10.5 Cumulative Error in CP

The propagation of all errors in measured and derived variables have a significant effect on the overall estimation of the power coefficient CP. The major factors that influence the outcome of CP calculations appear to be the measurements in applied brake influencing T_B and the derived flow velocities U from hotwire voltage readings (Eq. 1.7). To test the cumulative effect on CP, the spin down test close to 8m/s is inspected. At maximum CP, the actual wind speed is 7.5m/s. Introducing ±2.15% error in P_w and ±4.8% error in P_B result in a maximum error in CP of roughly ±7% (Table 3.8).

P_w (W)	P_B (W)	CP	%error
108.527	23.437	0.216	
110.861 (+2.15%)	24.562 (+4.8%)	0.222	2.594
106.194 (–2.15%)	24.562 (+4.8%)	0.231	7.103
110.861 (+2.15%)	22.312 (–4.8%)	0.201	–6.804
106.194 (–2.15%)	22.312 (–4.8%)	0.210	–2.708

Table 3.8. Error in CP relative to errors in P_w and P_B values.

Chapter 4
Numerical Methods

4.1 Introduction

The development of the numerical model used in all CFD simulations in this thesis is presented in this chapter. A detailed description of the numerical domain is initially presented which outlines the general features of the model such as multiple meshes, boundary extents and conditions, and inlet and outlet conditions. Next, the different parametric studies are presented to provide in–depth understanding as to why specific features in the model are used such as blade node density, domain size, time step size, and turbulence model. Finally, the numerical model is compared to experimental data to assess its capability in predicting performance data such as aerodynamic forces and resulting flow field.

4.2 CFD Solver

The CFD package, Ansys Fluent 13.0, was used for all the simulations performed in this study. The code uses the finite volume method to solve the governing equations for fluids. More specifically in this project the incompressible, unsteady Reynolds Averaged Navier–Stokes (URANS) equations are solved for the entire flow domain. The coupled pressure–based solver was selected with a second order implicit transient formulation for improved accuracy. All solution variables were solved via second order upwind discretisation scheme since most of the flow can be assumed to be not in line with the mesh [75].

The entire domain was initialised using the inlet conditions that were pre–determined to provide a matching turbulence intensity decay that was observed in the experiments. The inlet turbulence intensity was set to Tu = 8% with a turbulence viscosity ratio of μ_t/μ = 14. The Tu decay in the numerical model is very close to the observed decay in the experiment as shown in Figure 4.1.

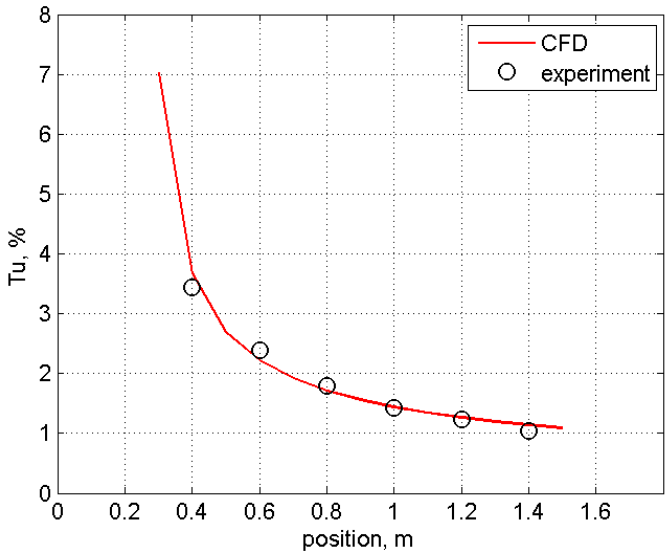

Figure 4.1. Comparison of turbulent intensity decay between CFD and experiments (x = 0: test section inlet).

4.3 Numerical Model of the Wind Tunnel VAWT

A two–dimensional CFD model was used to represent the VAWT and the wind tunnel domain. This was based on the review of relevant literature [6, 7, 25-29, 33, 42, 44, 49, 51, 76] that has shown that a 2D model is sufficient in revealing the factors that influence the performance and majority of flow physics that surround the VAWT. The contributions of blade end effects and blade–support arm junction effects are neglected but deemed acceptable since these can be considered as secondary. Two dimensional VAWT models are essentially VAWTs with infinite aspect ratio blades. The effect of blade aspect ratio (AR) comes in the form of shifting the CP curve upwards and to the right as AR increases [10], but the general shape is maintained. Full 3D models were tested using coarse meshes but due to their immense computational time requirements, were eventually shelved. The complexity, as well as the computational expense for a full three dimensional model cannot be justified by the additional insight that such a model can offer and is left for future work.

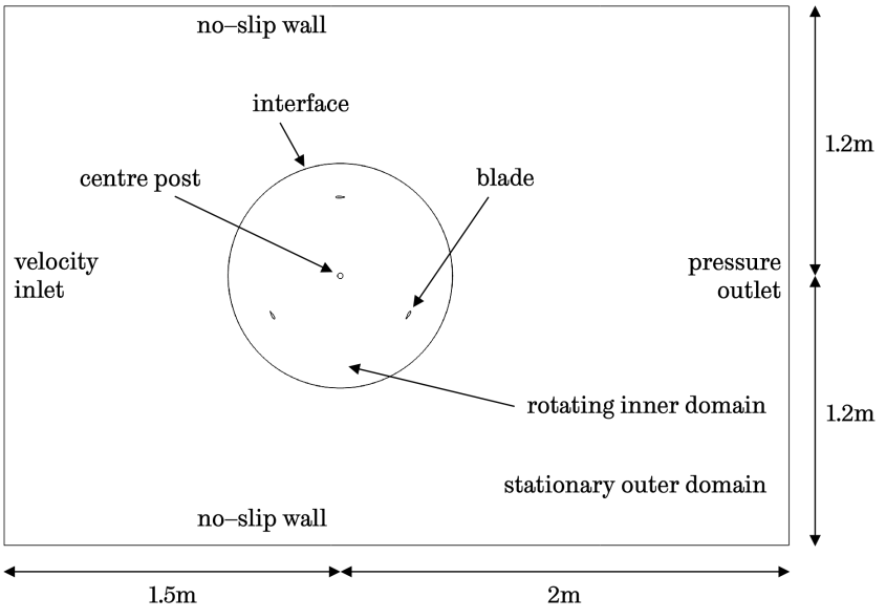

Figure 4.2. An illustration of the 2D numerical domain.

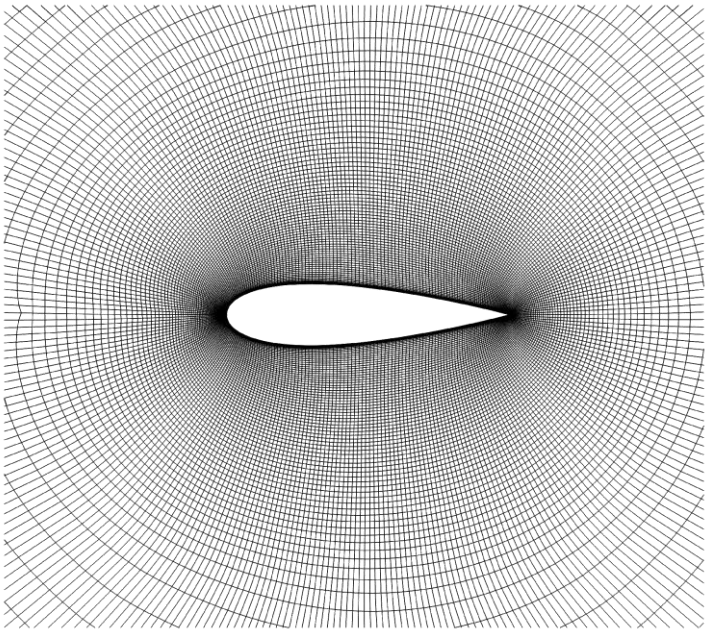

Figure 4.3. The near–blade mesh of the numerical model.

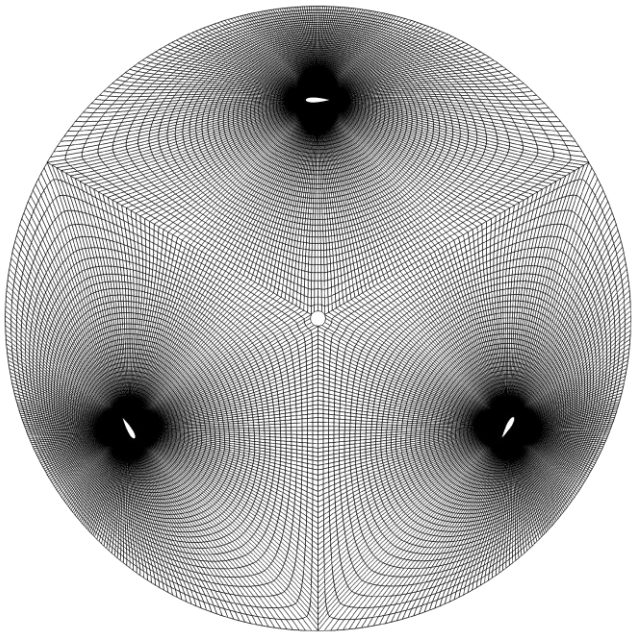

Figure 4.4. The rotating inner domain mesh of the numerical model.

The domain mesh was created directly in the grid generation software Gridgen where the aerofoil coordinates of a NACA022 profile were imported to define the blade shape. The surrounding geometry was defined based on studies of the extents of the boundaries that are detailed in later sections. There is an inner circular rotating domain connected to a stationary rectangular domain via a sliding interface boundary condition that conserves both mass and momentum.

No–slip boundaries are set to represent the wind tunnel walls while a velocity inlet and a pressure outlet are used for the test section inlet and outlet, respectively. The rotation of the inner domain relative to the outer domain is prescribed within the software that implements the algorithm for the sliding mesh technique. Care is taken such that tolerance between meshes in the interface region is kept low to avoid excessive numerical diffusion.

Each blade surface was meshed with 300 nodes and clustering in the leading and trailing edges was implemented to provide the required refinement in regions where high gradients in pressure and flow were expected. A node density study was performed to determine the appropriate number of surface nodes and is presented in Sec. 4.3.3. The O–type mesh was adapted for the model, where a boundary layer was inflated from the blade surface (Figure 4.3). The motivation behind using the O–type mesh instead of the conventional C–type used in aerofoil studies was primarily because the expected wake is not fixed on a specific path relative to the blade but rather varying greatly in direction swaying from one side to another side. The use of a C–type mesh would not be beneficial as the tail of the wake from the blade will not always fall within the refined tail mesh. The first cell height used was such that the y^+ values from the flow solutions did not exceed 1, the limit of the turbulence model that was chosen for the simulations (Sec 4.3.4). To ensure proper boundary layer modelling, the growth rate of the inflation was set to 1.1 to give a minimum of 30 layers within the boundary layer, after which a larger growth rate of 1.15 was implemented. Beyond the blade surface of about a chord width, the rotating inner domain mesh was generated such that the maximum edge length of the cells did not exceed $0.5c$ within the VAWT domain (Figure 4.4). This was adapted to minimise the dissipation of the turbulent structures generated by the blades in the upwind region that may interact with the other blades in downwind region. A smoothing algorithm in the meshing software was used to reduce the angle skewness of the cells such that the maximum was observed to be less than 0.6.

To reduce computation time, the outer domain was coarsely meshed with a rough maximum edge length of the cells set to c (Figure 4.5). This dissipated the high gradients in the wake, such as shed vortices, but the general velocity deficit was still captured. The distance of the velocity inlet boundary from the VAWT axis was set to 1.5m, 0.3m short of the actual 1.8m in the experiment setup. This was not considered an issue since the modelled turbulence intensity decay in the simulations matched that of the experiments and is thought to be much more important.

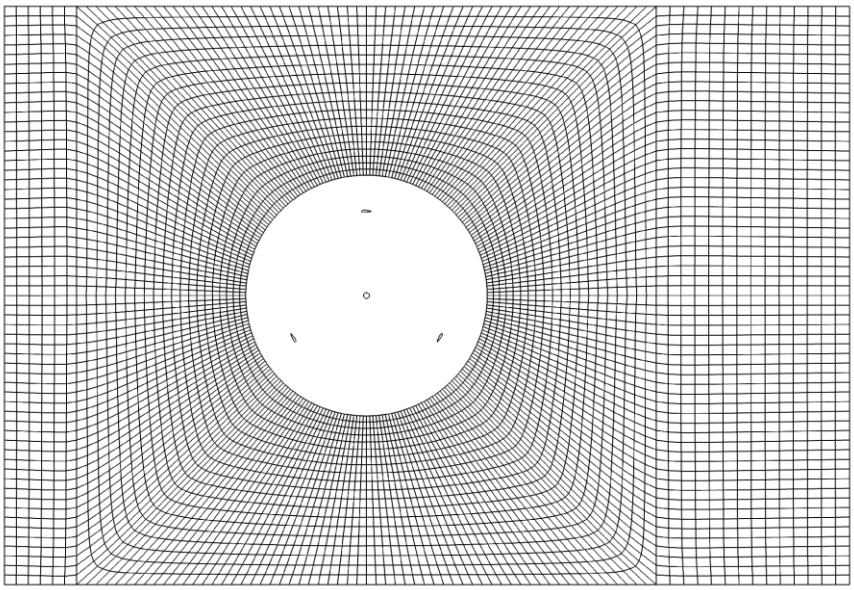

Figure 4.5. The stationary outer domain mesh of the numerical model.

The pressure outlet boundary was set to d_o = 2m from the VAWT axis. This has been selected as a distance between the actual test section outlet of 1.2m and the position of the wind tunnel fan of about 3m. In the actual wind tunnel setup, the test section outlet was fitted with a steel matting grid of the same wire thickness and mesh size as the turbulence grid in the inlet. This will have had a definite effect on the developed wake of the VAWT, breaking up the large vortex structures generated from the blades. There is also the presence of the shutter flaps, that is considered to influence the destruction of the shed vortices. As such, a long fluid domain behind the VAWT was deemed unnecessary from a numerical standpoint since full wake development was not one of the objectives of the

study. An outlet distance study was conducted to investigate the effects of wake development on the performance of the VAWT and is presented in Sec. 4.3.2.

The side wall distance was set to d_s = 1.2m from the VAWT axis. This is double the actual wind tunnel wall distance of 0.6m. The blockage of the 2D numerical model matches that of the 3D wind tunnel model and is equal to 0.29. Since the study is mainly focused on the aerodynamics of the VAWT in unsteady wind conditions within a wind tunnel domain, blockage was not a primary consideration in the simulations since no reference to actual field test data is made. Nevertheless, a wall distance study was carried out to examine the effects of blockage in the 2D simulations. This is presented in Sec. 4.3.2.

Time step convergence was monitored for all conserved variables and it was observed that acceptable levels of residuals (less than 1×10^{-6}) were attained after 6 rotations of the VAWT. This meant that periodic convergence was also achieved. The T_b for one blade monitored all though 10 rotations is shown in Figure 4.6. After the sixth rotation, the peaks of the upwind torque for cycles 7 through 10 are level and the downwind ripple match closely. The difference in average torque between cycle 7 and cycle 10 is around 0.5%

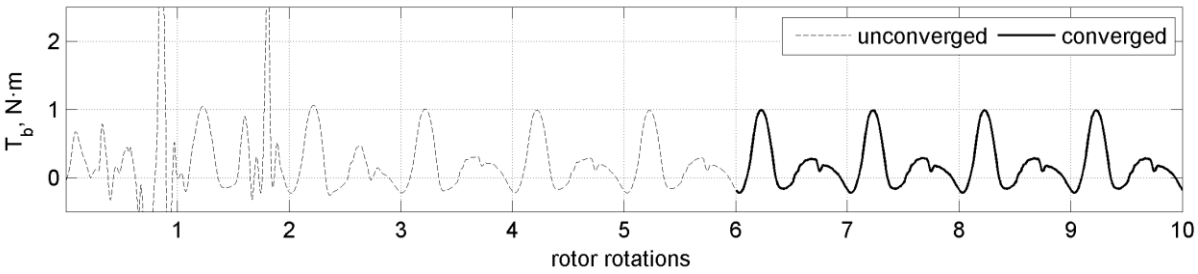

Figure 4.6. Blade torque ripple of one blade for 10 full rotations.

4.3.1 Blade and Near–blade Mesh

The spatial resolution of the near–blade mesh was a critical consideration of the overall quality of the numerical domain. The appropriate number of nodes on the aerofoil surface and the rate of the boundary inflation were the main factors

that influence the accuracy of the forces generated on the blade surface. A comprehensive study was conducted to determine the suitable surface node density that will give accurate results in the most reasonable amount of computation time. To accomplish the task, five surface node densities were tested at two λ and the blade torque for one blade in one full rotation were compared.

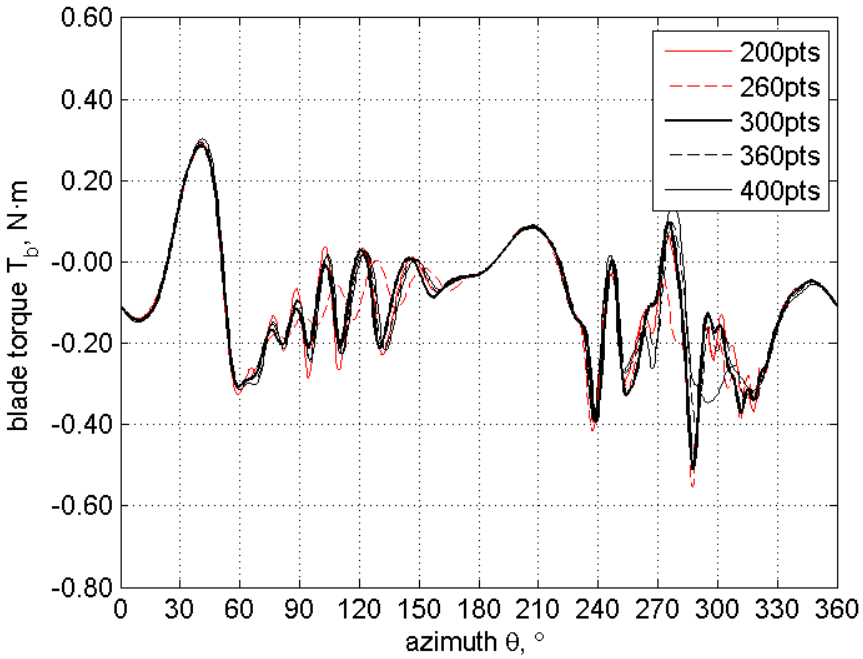

Figure 4.7. Blade torque for node density study at $\lambda = 2$.

The first test was carried out at $\lambda = 2$. A plot showing the results is presented in Figure 4.7. There is significant difference in the torque ripple between the different node densities for this λ, notably in the regions where there is increased generation of shed vortices ($60° < \theta < 180°$ and $240° < \theta < 330°$). Outside these azimuth positions, the torque curves are very close to each other such that they are already overlapping in most areas. A node density of 300 points is considered to be a reasonable number in so far as accuracy of the predicted torque is concerned. For this λ, the greatest difference in CP between the cases is $\Delta CP = 0.0054$ between node densities 200 and 260 (6.8% difference in magnitude) while a $\Delta CP =$ of 0.0019 is observed between node densities 300 and 360 (2.4% difference in magnitude). The actual values of the CP for this test all fall within the negative performance region.

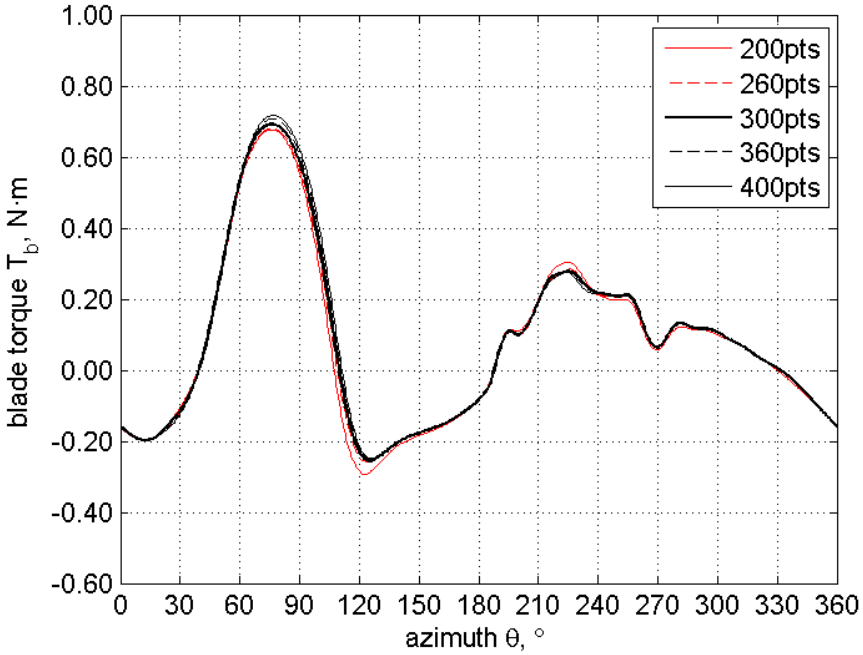

Figure 4.8. Blade torque for node density study at $\lambda = 4$.

The second test was conducted at $\lambda = 4$. Figure 4.8 shows the results of the blade torque for one complete rotation. There is more agreement in the torque prediction between the node densities with a major deviation observed at $\theta = 120°$ and $\theta = 225°$ where torque for the mesh with 200 points is clearly different from the results of the other node densities. The greatest difference in CP is between 200 and 260 points at $\Delta CP = 0.0088$ (5.8% difference in magnitude) while a $\Delta CP = 0.0075$ is seen between 300 and 360 points (4.5% difference in magnitude). The final node density was set to 300 points as this was seen to the most appropriate density to be used for both low λ and high λ.

The inflation of the boundary layer mesh was controlled by the growth rate of the first layer. A study on the influence of growth rate on predicted torque was carried out to find the most suitable value across a wide range of λ. In a similar manner to the node density study, the growth rate was tested at two different λ. The first test was conducted at $\lambda = 2$. Figure 4.9 shows the results of the predicted blade torque for one full rotation. One cannot see a convergence of results towards an appropriate growth rate at this λ with significant difference across the entire rotation from the prediction of the initial blade stall near $\theta = 40°$ to the

subsequent shedding of vortices from θ = 60° to θ = 180° all the way to the downwind pass from θ = 230° to θ = 330°.

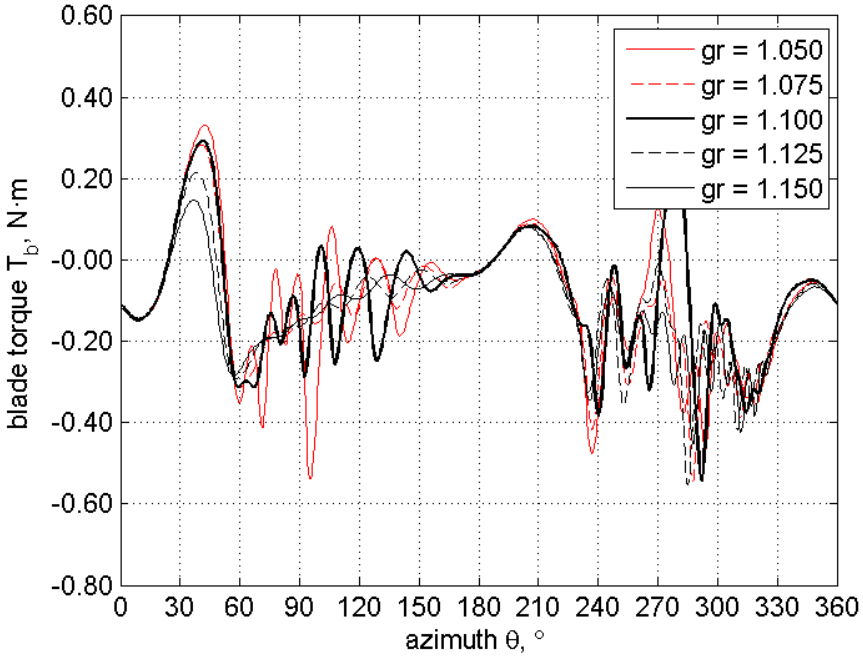

Figure 4.9. Blade torque for growth rate study at λ = 2.

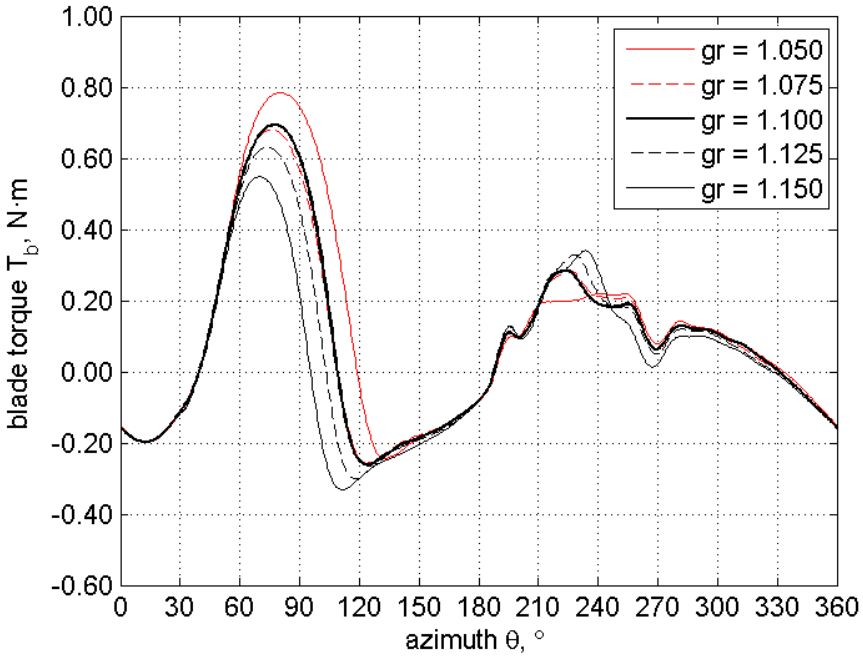

Figure 4.10. Blade torque for growth rate study at λ = 4.

A second test was carried out at λ = 4 where the VAWT is in the positive performance region. A more conclusive data set is seen with an observed

convergence in predicted torque between gr = 1.075 and gr = 1.1 (Figure 4.10). Between these two growth rates, the ΔCP is 2.5×10^{-4} (0.2% difference in magnitude). A gr = 1.05 does not produce the same torque prediction despite being a finer mesh. As seen in Figure 4.10, the predicted torque is much higher than the other growth rates with a maximum value of T_b = 0.78N·m compared to the results for gr = 1.1 where maximum T_b is 0.69N·m. There is also delayed stalling for gr = 1.05 in the upwind of about 10° that does not match the observed PIV measurements at θ = 120°. For this reason, the growth rate was set to gr = 1.1 for the rest of the numerical simulations.

4.3.2 Domain Size

The extents of the stationary domain were dictated by the necessity to properly simulate the wind tunnel configuration within two dimensions. As previously mentioned, the distance of the inlet boundary of the numerical domain from the VAWT was set such that the turbulence intensity decay matched that of the wind tunnel measurements. For both the side walls and the outlet boundaries, independent studies were carried out to determine the effects of the distance of said boundaries to the predicted CP in a wide range of λ.

Side Wall Distance d_s

The position of the wind tunnel walls in the 2D domain is the main parameter that influences blockage. Since it is difficult to validate the blockage effects of the 2D model versus the actual experiments, it was deemed sensible to match only the blockage ratio of the two. However, a one–to–one comparison between 2D models can be performed to assess the effects of blockage in the predicted performance to give insight on the trend of CP as a function of blockage.

The distance of the side wall from the VAWT axis was first set to d_s = 0.6m. This is the side wall distance of the actual wind tunnel. For the 2D numerical model,

the computed blockage ratio is 0.58. This is double the actual blockage ratio of the wind tunnel at 0.29. The effects are seen to be the significant over prediction of CP at λ = 4.5 and λ = 5 (Figure 4.11). From Sec. 3.10.5 the maximum experimental CP at 7.5m/s is 0.216 while the predicted CP at λ = 4.5 and λ = 5 are both greater than 0.4. With the tunnel walls much closer to the VAWT, the flow velocities seen by the blades are greatly increased thereby increasing the generated lift by the blades and suppressing of blade stall due to lower perceived α. As d_s is increased to 1.2m, the predicted maximum CP drops from 0.51 at λ = 5 to CP = 0.27 at λ = 4.5. A d_s of 1.2m gives a blockage ratio equivalent to the actual wind tunnel blockage ratio. Further increasing d_s only slightly reduces the CP between λ = 4 to λ = 5 by as much as ΔCP = 0.03. As such, the d_s selected for the rest of the numerical work was 1.2m.

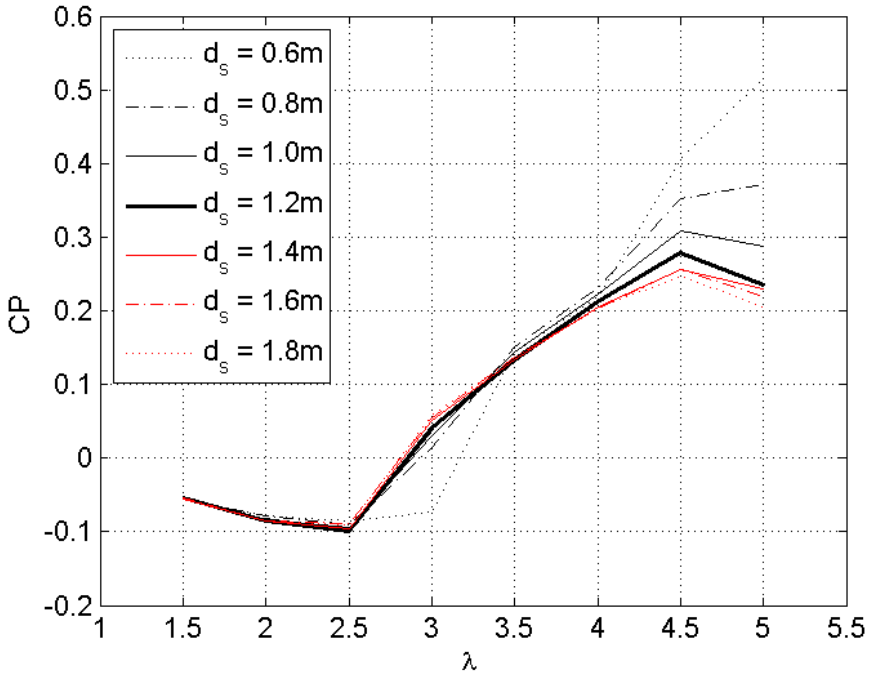

Figure 4.11. Blockage study results for the 2D numerical model.

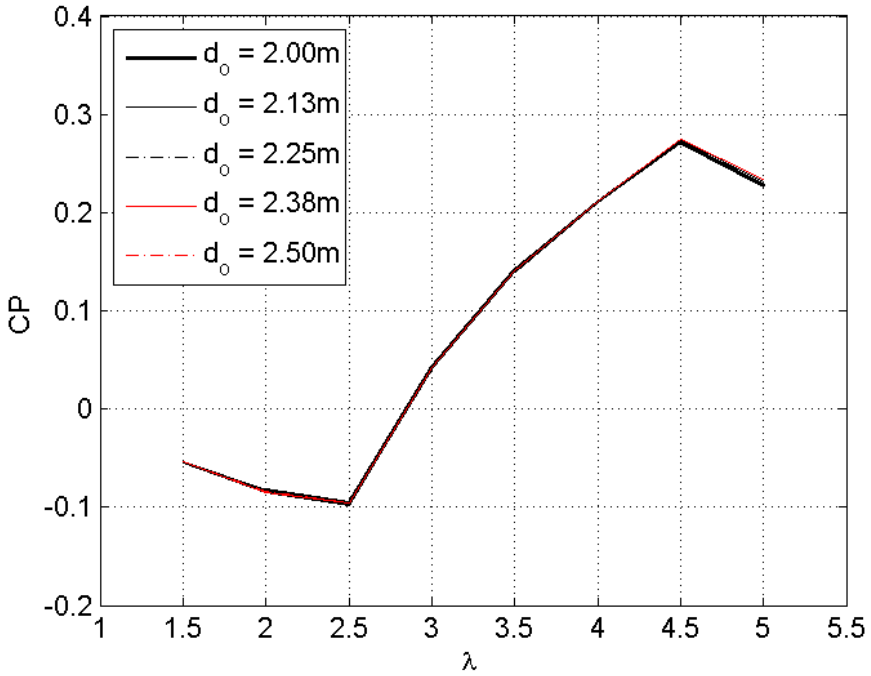

Figure 4.12. Domain length study results for the 2D numerical model.

Outlet Distance d_o

The outlet distance d_o was investigated to assess the influence of wake development on the predicted CP. The shortest d_o was set to 2.0m which is between the wind tunnel test section outlet and the axial fan position. As d_o is increased, very little change in CP is observed with a maximum ΔCP = 0.004 at λ = 5 (Figure 4.12). This is deemed to be very small and therefore negligible. As such, the initial d_o of 2.0m is chosen for all the remaining numerical runs.

4.3.3 Time Step Size

Sufficient temporal resolution is necessary to ensure proper unsteady simulation of the VAWT. Different time step sizes Δt that are equivalent to specific rotational displacements along the azimuth were tested. The largest Δt used was equal to a $\Delta t = 1^\circ\omega^{-1}$ (time for one degree equivalent rotation) and was subsequently halved twice over to get $\Delta t = 0.5^\circ\omega^{-1}$ and $\Delta t = 0.25^\circ\omega^{-1}$. All three Δt's were tested at λ = 2 and λ = 4. Results for both λ are presented in Figure 4.13 and Figure 4.14. It is clear that there is a delay in the torque ripple for the coarsest Δt =

$1°\omega^{-1}$ for λ = 2 while the two finer Δt's are in good agreement especially in the upwind (Figure 4.13). A small difference in predicted magnitude of T_b between Δt = $0.5°\omega^{-1}$ and $0.25°\omega^{-1}$ is seen from θ = 280° to θ = 330° but the peaks and troughs are still in sync. In terms of CP, there is negligible difference between the three Δt's with a maximum ΔCP of only 0.003. A similar agreement between the three Δt's is observed at λ = 4 with the maximum ΔCP of 0.003 as well. From Figure 4.14, there is very little variation between the three cases with the only noticeable difference in the torque ripple from θ = 260° to θ = 290°. The upwind is accurately predicted by the three Δt's with all capturing the maximum T_b around θ = 80°. The maximum T_b in the downwind is also properly predicted by all Δt's at θ = 240°. Since time accurate simulations is required for this study, the chosen time step size was $\Delta t = 0.5°\omega^{-1}$ so that the vortex shedding at λ = 2 is correctly modelled and was adapted for the remaining runs.

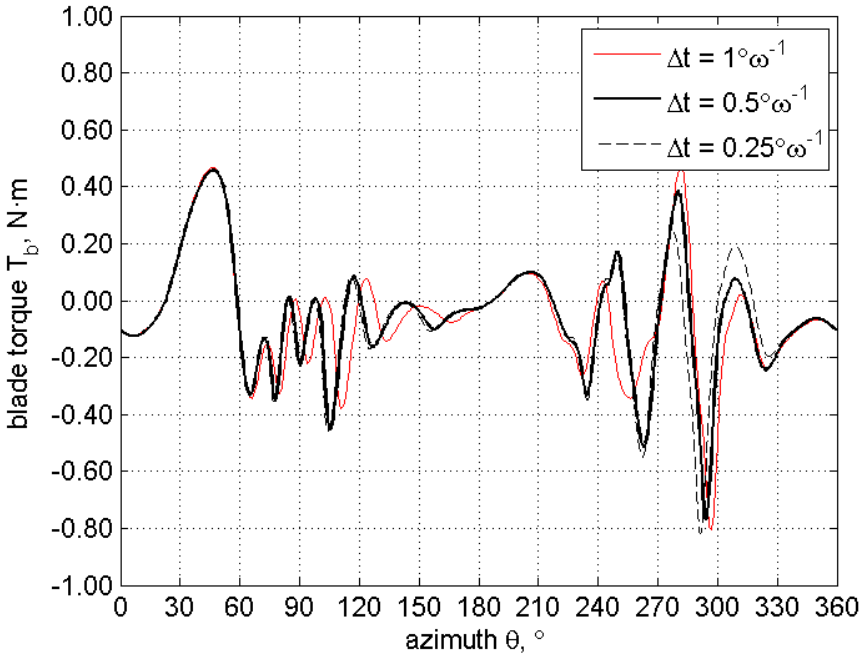

Figure 4.13. Time step size study results at λ = 2.

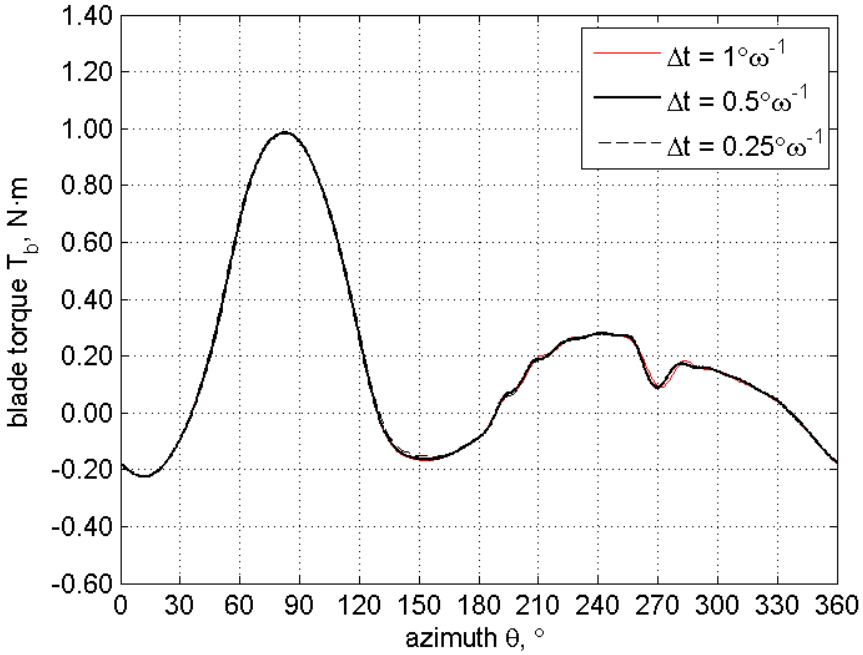

Figure 4.14. Time step size study results at λ = 4.

4.3.4 Turbulence Model Selection

To aid in the proper selection of the appropriate turbulence model for the problem, a pitching aerofoil study was conducted for initial validation. This was carried out to reduce the list of turbulence models available for use. Final validation of the turbulence models was performed ultimately by comparison of VAWT CFD visualisations to VAWT PIV data. It should be noted that the pitching motion does not fully capture the actual flow around a VAWT blade since there is also a varying incoming flow velocity aspect around a VAWT blade that is not present in an aerofoil pitching about a fixed point. The rates of change in the angle of attack are also different which may lead to different flow behaviour between the two. However, it is believed that the dynamic interactions of a pitching aerofoil with a moving fluid are very close to that of a moving VAWT blade in as far as lift and stall are concerned. This is a better method compared to static aerofoil validation because of the dynamic stall being similar. Another point that supports the use of this method is the variation of the angle of attack as seen by a VAWT blade without velocity induction closely resembles a sine wave albeit skewed. The Author believes that this similarity would result in similar

flow behaviour and dynamic stall characteristics in the sense of testing turbulence modelling. Further validation was conducted by running VAWT simulations on the best candidates of turbulence models to determine the most suitable model for VAWT simulations and is presented in Sec. 4.4.

Experiments carried out by Lee and Gerontakos [31] on a pitching NACA0012 provided the dynamic data of the lift, drag and moment coefficients required for force validation. The blade has a chord length of c = 0.15m and executes a sinusoidal pitching motion about 0.25c with a mean angle of attack of 10°, a pitching magnitude of 15°, and a reduced frequency of κ = 0.1. The free stream wind velocity is 13m/s with turbulence intensity of 0.08% corresponding to a Reynolds number based on chord of Re = 1.35 × 10^5. A fully structured O–grid was used for the simulations. The aerofoil grid comprises 1500 nodes over the surface with first cell height ensuring a $y^+ \approx 1$. The cells expand from the wall at a growth rate of 1.1. The boundary of the domain was set to 20c from the aerofoil. The total model size is approximately 275,000 cells. The pitching motion was controlled by means of a user–defined function that prescribed the angular velocity of the entire domain to match the angular position dictated by the sine wave function $\alpha = \alpha_o + \alpha_A \sin(\omega t)$ where α_o = 10°, α_A = 15°, and ω = 17.33rad/s. A time step size equivalent to $0.1c/U_\infty$ was used.

Different models were tested to reduce the list of turbulence models for this study. The one equation Spalart–Allmaras (S–A) model, and the two equation k–ε RNG and k–ω SST models were selected for the study. The turbulence model Transition SST with free transition prediction was also used to test the current state of the art in transition modelling for suitability in low Reynolds dynamic stall simulations. The S–A model automatically detects low–Reynolds number flows on the wall if the mesh is resolved finely enough adjacent to the wall [75] while the k–ε RNG and k–ω SST are fully turbulent models. The Transition SST model couples the k–ω SST with two other transport equations, one for the

intermittency and one for the transition onset criteria, in terms of momentum–thickness Reynolds number [75].

For this validation study, the initial mesh was constructed following the description mentioned earlier. In order to confirm grid independence, a second and third mesh were constructed with twice and half the resolution in the wall and wall-normal directions. It was determined that the initial mesh was independent as when compared to the finer mesh, results showed negligible difference in lift coefficient predictions. However, when compared to the coarser mesh significant differences in the results were observed. All cases were run until full periodic convergence and it was observed that this happened after just 2 oscillation cycles. Time step convergence was based on a residual drop to 1×10^{-6} and a drop of at least 3 orders of magnitude in each time step.

Figure 4.15 shows the lift coefficient loops versus the angle of attack for the different turbulence models. The static and dynamic experimental results are plotted for comparison. It can be observed that in the upstroke, all of the turbulence models accurately predict lift. Maximum lift is not captured by the k–ε RNG as it prematurely loses lift and proceeds to drop even before reaching the maximum angle of attack. It is necessary to capture the maximum lift because this has a significant effect on the overall performance of the VAWT. In the downstroke, all models under predict the lift with the k–ω SST and Transition SST models being the closest to the experimental results and the S–A being the farthest away. Overall, the most accurate model is the k–ω SST model as far as lift is concerned.

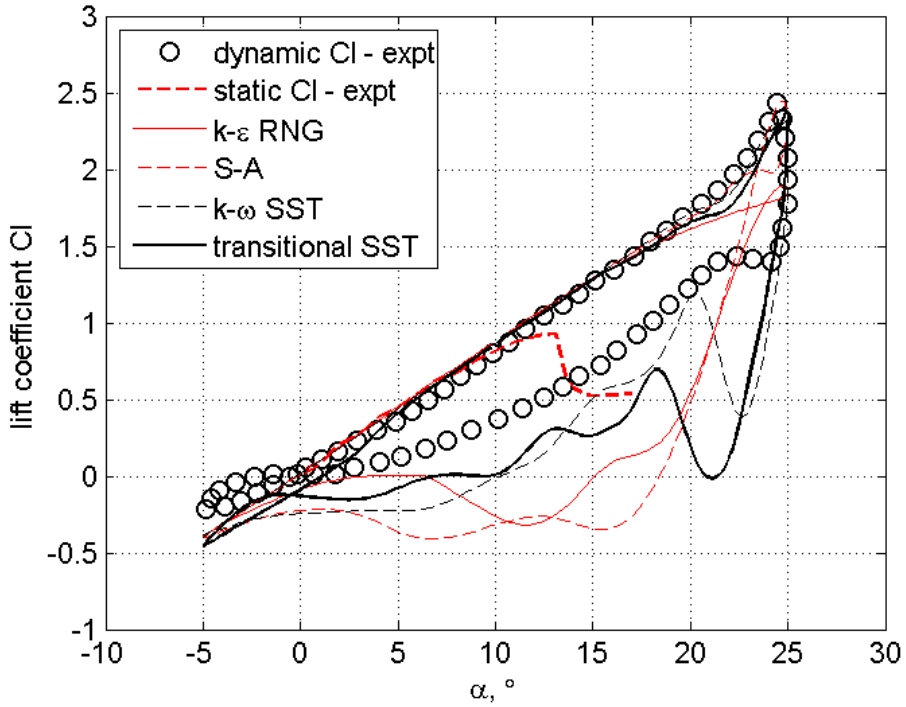

Figure 4.15. Lift coefficient predictions of the different turbulence models tested in the pitching aerofoil study plotted against experiments by [31].

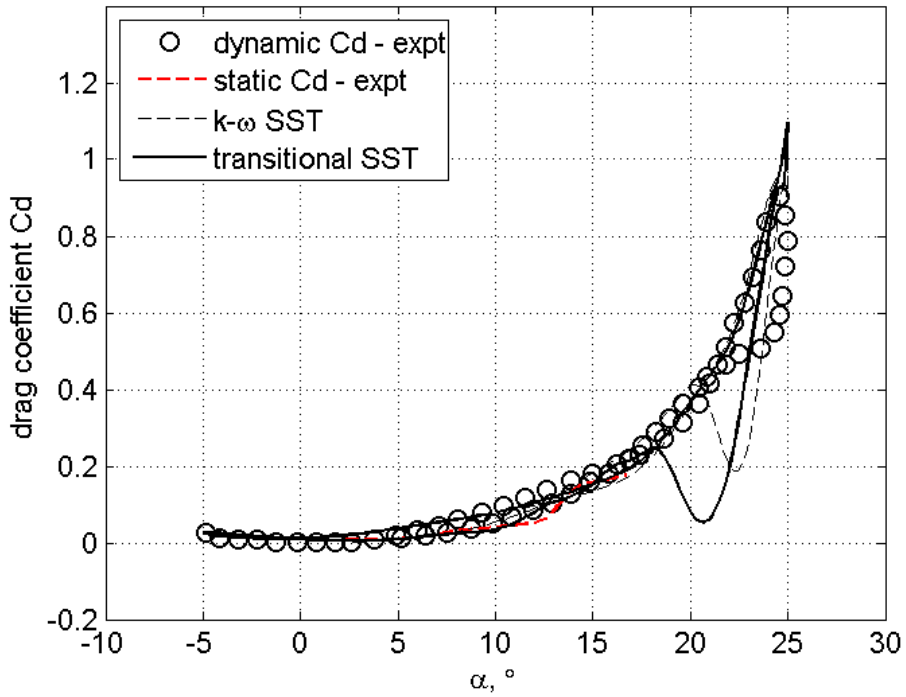

Figure 4.16. Drag coefficient predictions of the two best turbulence models.

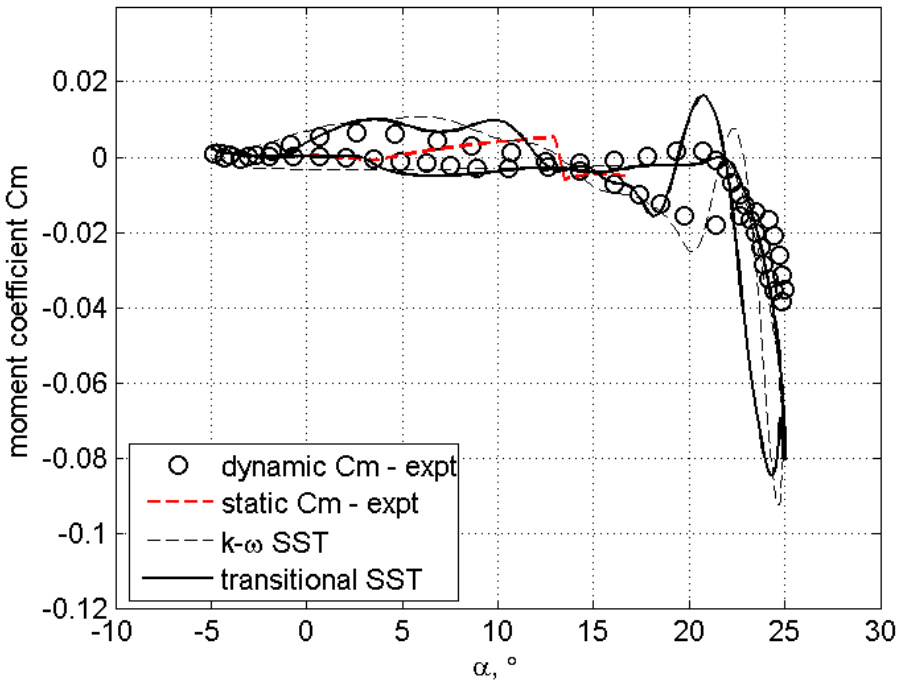

Figure 4.17. Moment coefficient predictions of the two best turbulence models.

Figure 4.16 and Figure 4.17 show the drag and moment coefficient loops for the k–ω SST and Transition SST. The drag is slightly over predicted by both models at α = 25° versus experiment results. The pitching moment is also closely predicted by both models with an exception in the region close to the maximum angle of attack as the computed maximum moment coefficients are more than double that of the experiment results. Again, the k–ω SST model is the best candidate for the turbulence model with the best agreement to experiment results for this pitching aerofoil case. This effect is observed at a *Re* greater than 1×10^5, as seen by the pitching blade. For the VAWT model under study, the range of *Re* is below 1×10^5 and well within the transition region for aerofoil flows. As such, the chosen turbulence model to be used for all runs was the Transition SST.

4.4 Validation of CFD Model

The numerical model developed was checked against experimental data to assess its capability of correctly simulating VAWT flow physics. The validation is not considered exact, since the CFD model is 2D, while the actual problem is 3D.

Nevertheless, a good 2D CFD model will provide substantial insight into the factors driving the performance of the VAWT and a means of checking the model's accuracy in capturing the details of the problem is presented below.

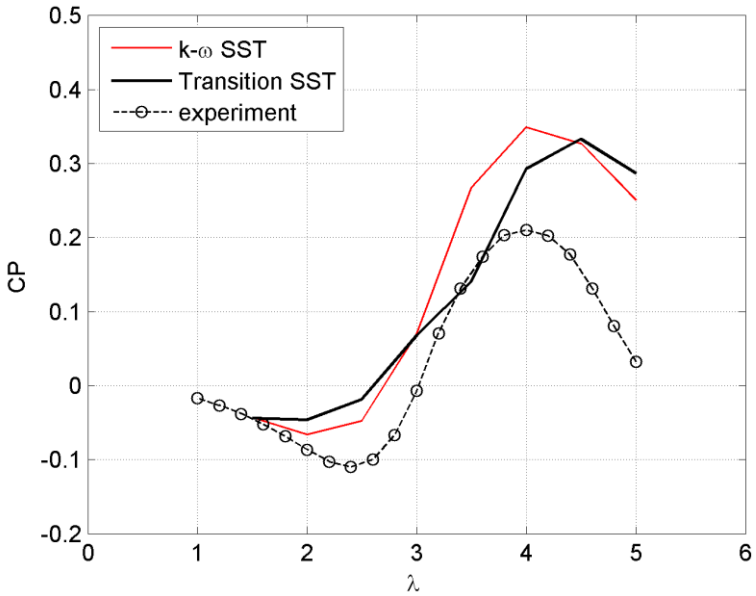

Figure 4.18. Steady CP curves at 7m/s.

4.4.1 Power Coefficient

The first aspect of the model validation is the comparison of the predicted VAWT performance over a wide range of operating speeds. Both the fully turbulent k–ω SST and the Transition SST models were tested against the experimentally derived CP. The steady wind speed chosen was 7m/s and the simulations were run at different tip speed ratios from λ = 1.5 up to λ = 5 in increments of 0.5. It can be seen from Figure 4.18 that both 2D models over–predict CP starting from λ = 2 all the way up to λ = 5. Maximum CP for the fully turbulent model is 0.35 at λ = 4 while the Transition SST model predicts maximum CP = 0.33 at λ = 4.5. The maximum CP for the fully turbulent model occurs at the same λ as that of the experiments. There is a gap in the predicted CP's between the two CFD models from λ = 3 to λ = 4.5 where the fully turbulent model over–predicts the CP much more than the Transition SST model. A convergence of the curves is seen from λ = 1.5 to λ = 3 and also from λ = 4.5 to λ = 5. Higher λ's show the

greatest over–prediction of the CFD models from experiments. This may be due to the effects of finite blade span where the reduction in aspect ratio as seen by McIntosh [10] cause a substantial drop in CP at high λ versus the small drop in CP at low λ.

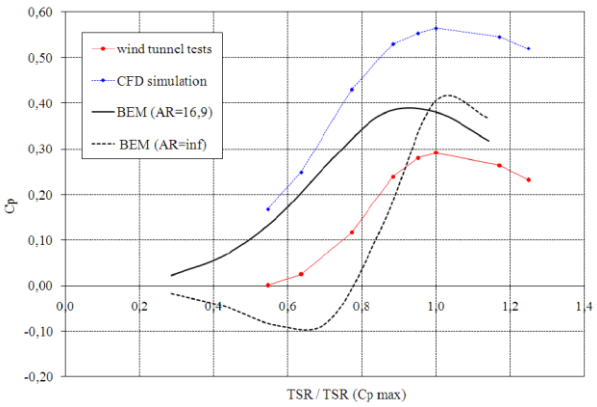

a. Raciti Castelli et al study [42].

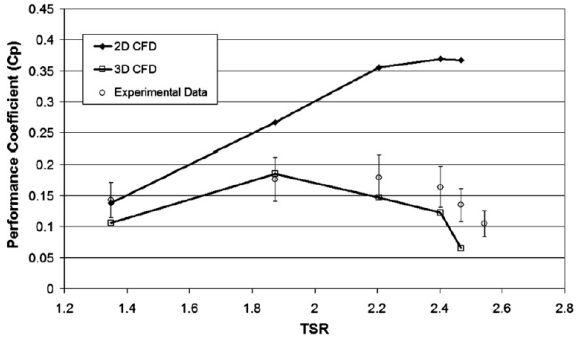

b. Howell et al study [27].

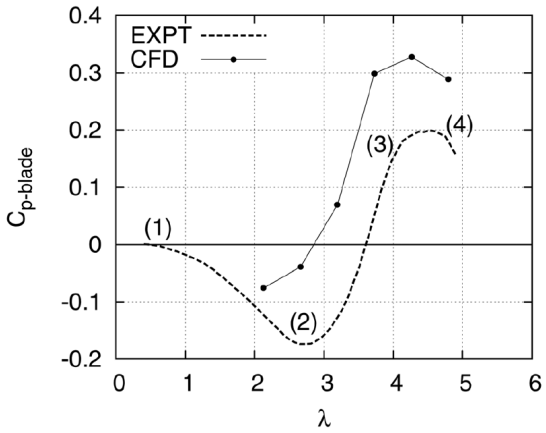

c. Edwards et al study [6].

Figure 4.19. Published results from other studies showing the difference between 2D and 3D data.

The gap in predicted CP was expected since the 2D model does not account for finite blade span as well as for blade–support arm junction effects and support arm drag that are present in the actual setup. The results are consistent to published data by Raciti Castelli et al [42], Howell et al [27] and Edwards et al [6] where 2D CP is over–predicted over the entire range of λ. Raciti Castelli et al compared their 2D simulations to wind tunnel experiments (Figure 4.19a) and argued that the difference is due to blockage effects that increase the flow velocities near the blades to much higher values than the unperturbed flow at the

inlet. Howell et al show an improved match between 3D CFD and experiments (Figure 4.19b). Edwards et al attribute the difference (Figure 4.19c) in predicted CP to finite blade span and blade–support arm junction effects.

Overall, the general trend of the predicted CP matches well with the experimental data. There is an observed negative trough at the low λ which rapidly rises and reaches maximum values near the experiment maximum at $\lambda = 4$ after which a rapid drop in CP is seen. In terms of shape, the fully turbulent model results show a smoother curve and better agreement to experiments while the Transition SST model results do not form a smooth curve and predict maximum CP at a higher λ.

4.4.2 Visualisations

The second aspect of validation is the comparison of flow visualisations between CFD and PIV. This part is an important step since the behaviour of the flow around the VAWT blades add significant insight as to why the CP varies as it does at different operating conditions. The flow physics at two λ are inspected and an assessment of the most appropriate turbulence model is performed based on the accuracy of the predicted stalling and reattachment of the flow on the blades as they go around the VAWT.

Flowfield at $\lambda = 2$

Figure 4.20 shows the vorticity plots for the upwind at $\lambda = 2$. At the start of the rotation, both turbulence models clearly predict fully attached flow. There is an observed wake (green contour) seen on the lower left portion of each CFD image at $\theta = 10°$ that is also visible in the PIV image. This is the wake of the preceding blade already at $\theta = 130°$. Flow continues to be attached until $\theta = 60°$ where both the Transition SST model and PIV reveal a bubble that is forming on the suction surface of the blade. The fully turbulent k–ω SST predicts the same formation of a

separation bubble 10° later at θ = 70°. This delay has a significant effect on the blade torque since this can mean extended generation of lift that may positively affect the predicted performance of the VAWT.

As seen in the PIV at θ = 70° the separation bubble has formed into a dynamic stall vortex and has already been detached from the blade surface. This is properly captured by the Transition SST model. However, the fully turbulent model still predicts the vortex to be on the blade surface. This delay in the formation and detachment of the dynamic stall vortex affects the shedding of the subsequent pairs of leading edge and trailing edge vortices and is evident in the presence of a trailing edge vortex in the FOV of the fully turbulent model at θ = 140° but is not seen on both the Transition SST model and PIV.

The downwind shows better agreement between the two CFD models when it comes to the scale and timing of the shed vortices although slightly smaller when compared to the PIV (Figure 4.21). The flow reattachment is seen to have started earlier in the Transition SST model as the stall is significantly shallower at θ = 280° as compared to the fully turbulent model and PIV. This may, in part, explain the higher predicted CP at this λ. Overall, the timing and depth of stall in the upwind for the Transition SST model matches the PIV quite well while the reattachment of the flow in the downwind is better captured by the fully turbulent model.

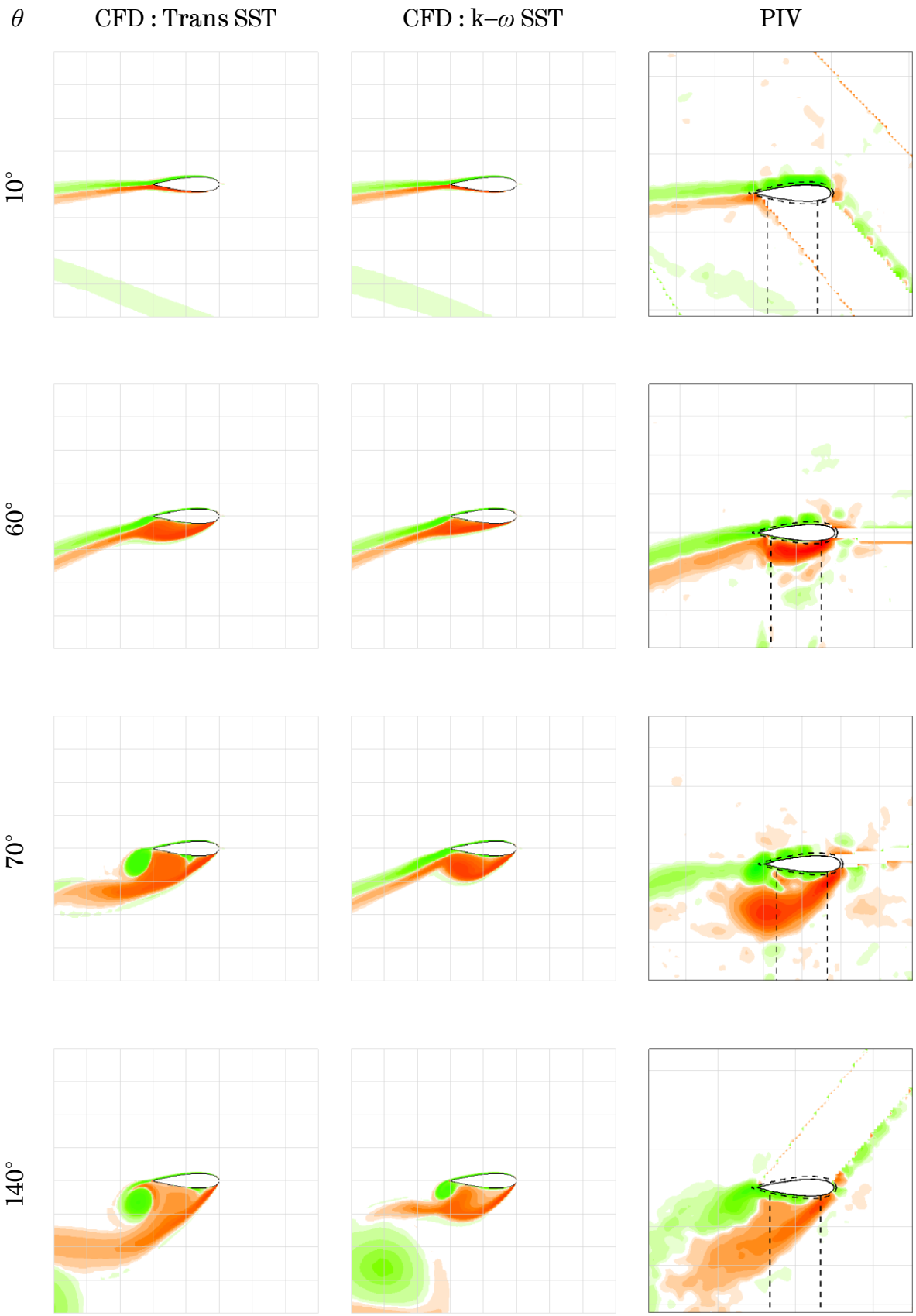

Figure 4.20. Vorticity flow field in the upwind for $\lambda = 2$.

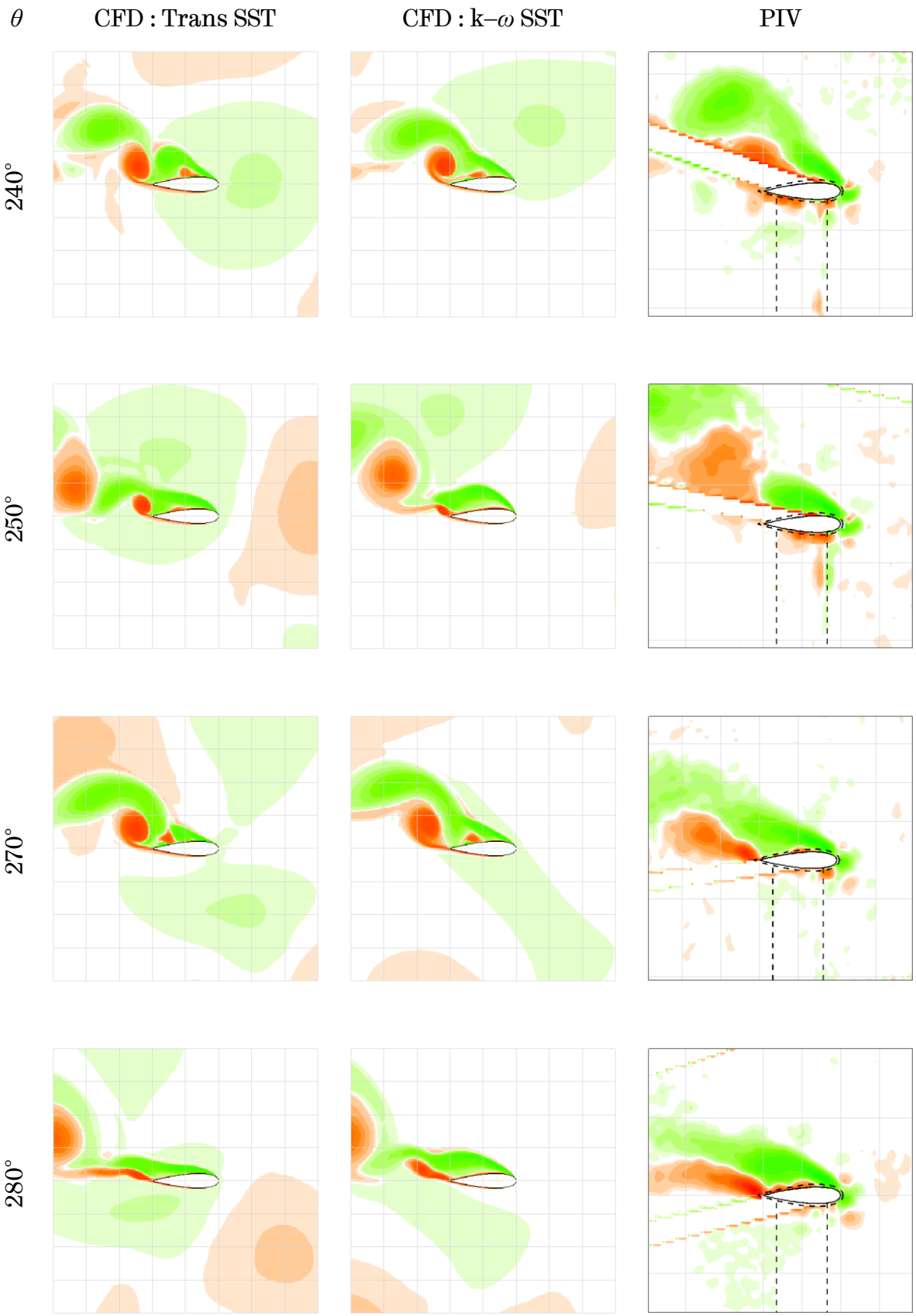

Figure 4.21. Vorticity flow field in the downwind for $\lambda = 2$.

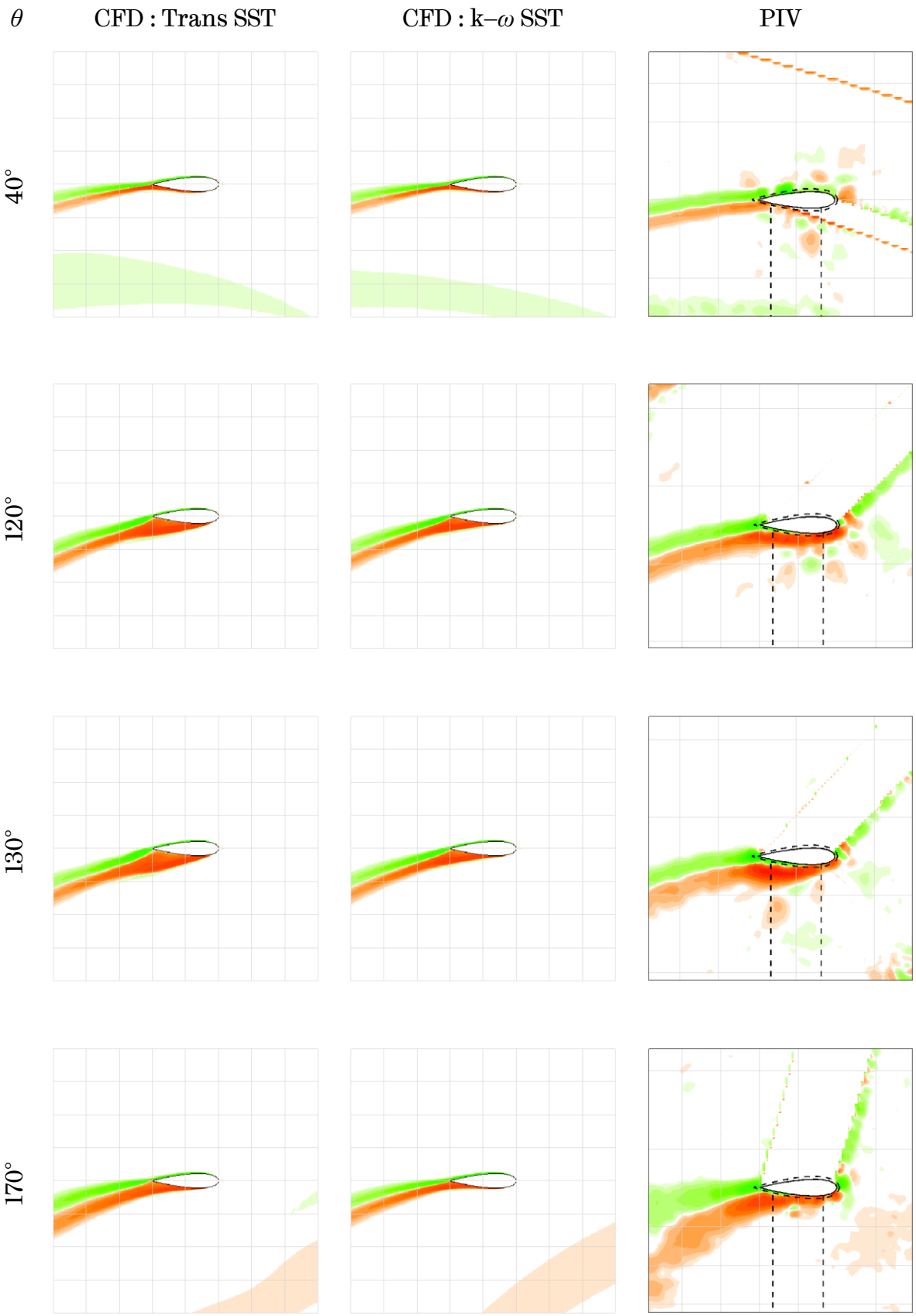

Figure 4.22. Vorticity flow field in the downwind for $\lambda = 4$.

Flowfield at $\lambda = 4$

Vorticity flow field for $\lambda = 4$ are presented in Figure 4.22. For the most part, the flow is attached to the blade. The wake of a previous blade (green contour) is visible in the lower portion of the images at $\theta = 40°$. At $\theta = 120°$, the Transition SST model shows an almost full stall on the suction surface while very light stall is seen in the fully turbulent model and PIV. Ten degrees later at $\theta = 130°$, the Transition SST model shows a deep full stall that is consistent to the PIV while partial stall is still observed in the fully turbulent model. The delay in stalling will have increased the positive performance of the fully turbulent model and pushed the CP to higher values as seen in Figure 4.18. At $\theta = 170°$, the fully turbulent model shows full reattachment of the flow while the PIV still shows partial separation from mid–chord to trailing edge. The Transition SST model is still stalled but to a lesser degree and produces a narrower wake when compared to PIV.

4.5 Summary

Based on the results obtained from both force and flow validation across a wide range of λ, the Transition SST model was selected as the best model that most accurately captures the flow physics of the VAWT. From the correct prediction of start of stall and the rate and scale of shed vortices at $\lambda = 2$ to the stalling and reattachment of flow at $\lambda = 4$, the Transition SST model better calculates the flow physics versus the k–ω SST model. The prediction of stall point and reattachment was the basis for validation and the Transition SST model was considered the better turbulence model. The predicted positive performance of the Transition SST model is closer to experiments with lower values of CP versus the k–ω SST model. All simulations conducted for the unsteady wind study will use the Transition SST model.

Chapter 5
Experimental Results

5.1 Introduction

This chapter details the investigation on the performance of the VAWT in steady and unsteady wind conditions. Baseline performance is set by analysing the steady wind case using power measurements (spin down) and vorticity flow field (PIV). Following the steady wind analysis is the study on the effects of unsteady wind on VAWT performance (CP) through detailed scrutiny of the time–varying kinematics and kinetics that is associated with the fluctuating wind speed.

5.2 Steady Wind Performance

The analysis of the VAWT performance in steady wind conditions is conducted using a two–fold approach. First, the power performance is presented and discussed to give an insight on the behaviour of the performance parameter CP

across a wide range of λ and wind speeds. Secondly, the flow physics is investigated to provide the necessary visualisation of the stall behaviour of the blades at two distinct points in the CP curve.

5.2.1 Determination of the Power Coefficient

Spin down tests were performed at different wind speeds to map the performance of the VAWT. At the start of each test, the wind speed is set whilst the rotor is stationary. During the start of the spin down test, the wind speed is observed to fall from the set speed due to blockage effects before eventually rising as the test ends (Figure 5.1). For the spin down test at the highest wind speed, U = 8.1m/s at the start of the spin down and rose to U = 8.75m/s at the end of the spin down. This results in a data set that does not represent a steady wind case. To correct for this deviation, multiple spin down tests were conducted from a minimum of 5m/s to a maximum of almost 9m/s (Figure 5.2a) and performance of steady wind speeds were interpolated (Figure 5.2b). The interval of wind speeds between tests was not constant but not seen as an issue. Regularity in the spacing was more desired and that the target steady wind speeds fall within the range of the measured wind speeds. For the current work, the minimum target steady wind speed was set to 5m/s, while the maximum was 8m/s. This range clearly falls within the range of all spin down tests conducted.

Performance curves for the different spin down tests are presented in Figure 5.2a. It is seen that the VAWT performance varies considerably with wind speed. At the lowest test wind speed, the entire CP curve is in the negative region. As the test wind speed is increased, the peak CP slowly rises above zero and continues to rise within the same λ region until it reaches a maximum of CP = 0.31 at the optimum tip speed ratio λ^* = 3.9 for the highest test wind speed. To a very small degree, there is an observed convergence of CP curves towards higher test wind speeds especially within the low λ range. Although not comprehensively investigated by the Author, results are consistent to Edwards [68] who has also

shown (Figure 5.3) a convergence in steady CP curves as Reynolds number increases suggesting an approach to independence from Reynolds number effects at higher wind speeds.

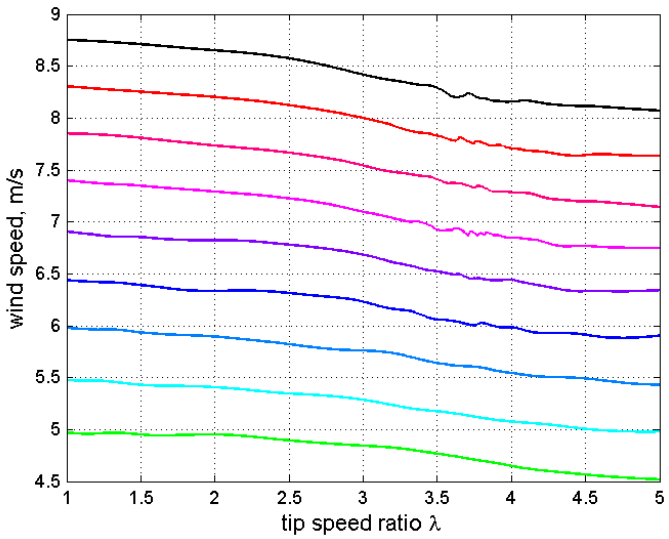

Figure 5.1. Drop in wind speed for each of the spin down tests.

There is a well–defined negative band appearing in the low λ range which is also seen by Edwards [68], Baker [56], Kirke [57] and McIntosh [10]. According to Baker, this negative band, which he termed as the dead band, negatively affects the self–starting capabilities of the VAWT and can be minimised by tilting the blade forward relative to the VAWT axis (re: canting without the twist, see Sec 2.4.2) as well as mounting the blade at a positive yaw (re: fixing) angle. Tilting the blade effectively reduces the effective angle of attack seen by the blades which minimises the occurrence of deep stall at low λ. Edwards has shown that the yawing of the blade such that the leading edge is closer to the VAWT rotation axis causes earlier stall at low λ but the depth of stall is reduced. The effect on the overall performance is a slight increase in CP in the dead band but a significant decrease in CP within the positive performance band. Kirke showed (Figure 5.4) that as the Reynolds number is reduced, there is a deepening of the dead band and the lowering of the overall performance of the VAWT. In his parametric studies, McIntosh demonstrated that a dead band will appear when the stall angle of the aerofoil is reduced. This concurs with Baker's conclusion that lower stall

angles induce deeper dead bands typically seen in thinner aerofoil sections or at low Reynolds number conditions.

Figure 5.2b shows the interpolated curves for constant wind speeds. A convergence is also seen in the curves as wind speed increases. When compared to the data presented by Edwards [68], the maximum value of the interpolated CP for the 7m/s case is higher at 0.21 than the non–interpolated case at 0.14. This is so because at the λ^*, the actual wind speed in the spin down test has dropped to just above 6.5m/s. So the CP value of 0.14 corresponds to this reduced wind speed and not the performance at 7m/s. Despite this difference, the general trends in the CP curve are still similar between the two studies. At low λ, the performance is driven by the drag on the blades producing a deep dead band with the lowest CP of –0.11 at λ = 2.4 (Figure 5.5). Subsequently, a rapid increase in CP is observed until the CP crosses the zero line at λ = 3 and continues to rise until it reaches the maximum value of 0.21 at λ^* = 4.0. Beyond λ^*, the CP rapidly drops to 0.03 at λ = 5.

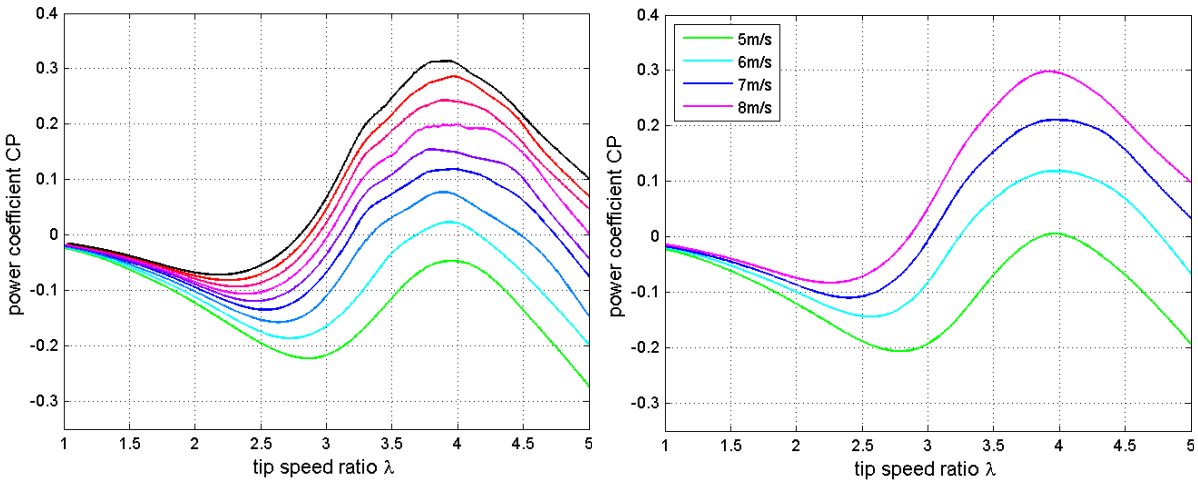

Figure 5.2. CP curves for the spin down tests: a) actual CP curves for all tests, b) interpolated CP curves for steady wind speeds.

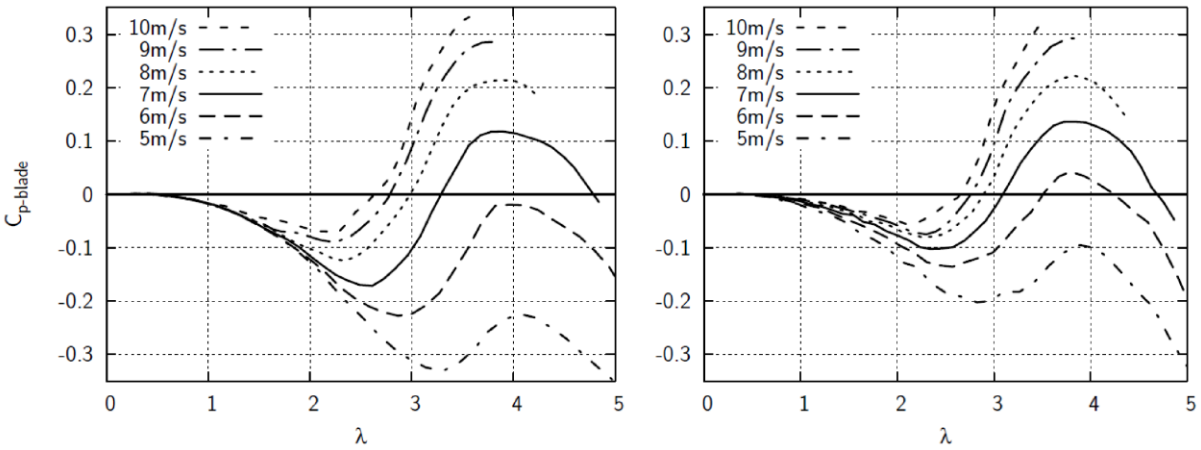

Figure 5.3. Spin down tests at different turbulence intensity levels showing effects of Reynolds number [68]: a) *Tu* = 0.4%, b) *Tu* = 1%.

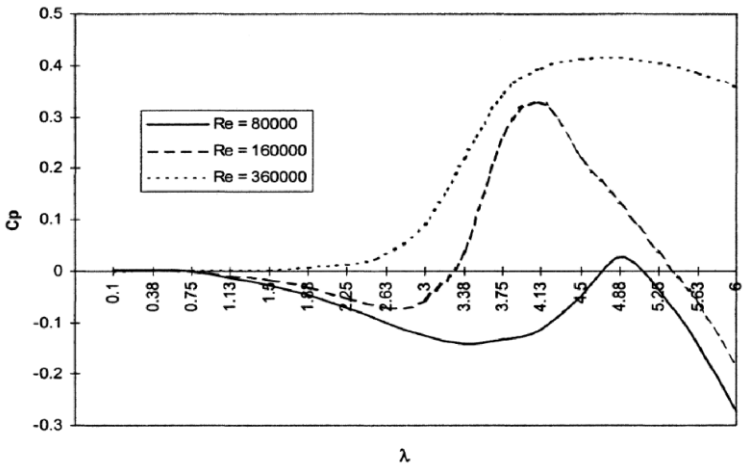

Figure 5.4. Study of Reynolds number effects on VAWT performance [57].

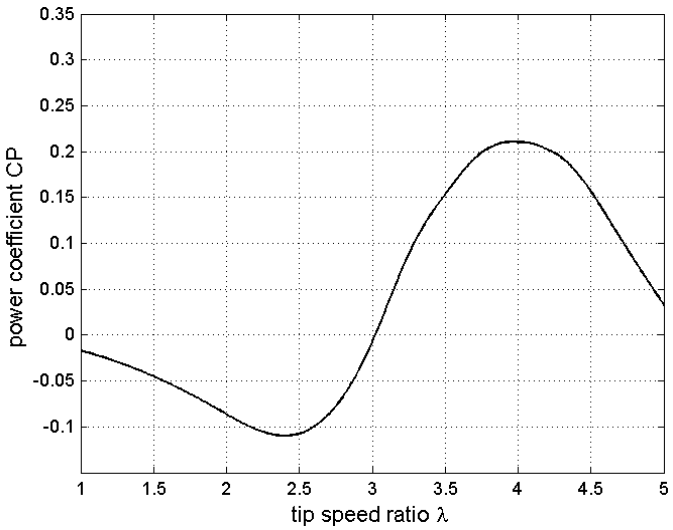

Figure 5.5. Steady wind performance curve of 7m/s.

5.2.2 PIV Visualisations

Visualisations of the flow physics driving the performance of the VAWT were obtained using PIV. The steady wind performance curve chosen is the 7m/s case, as this was the maximum attainable mean wind speed U_{mean} for the unsteady wind tests. As wind speed increases beyond 7m/s, the lowest attainable frequencies of the fluctuating wind speed do not go below 1Hz. Attempts to generate low frequencies of fluctuating wind at mean speeds higher than 7m/s induced high flow resistance to the closing stroke of the shutters such that the latter would not continue to close and eventually stop moving. Increasing the power input in the DC motor drive overcame this resistance but caused the fluctuation frequency to go above the 1Hz limit. The motivation for the 1Hz limit is discussed in a later section detailing the experimental results of the unsteady wind tests.

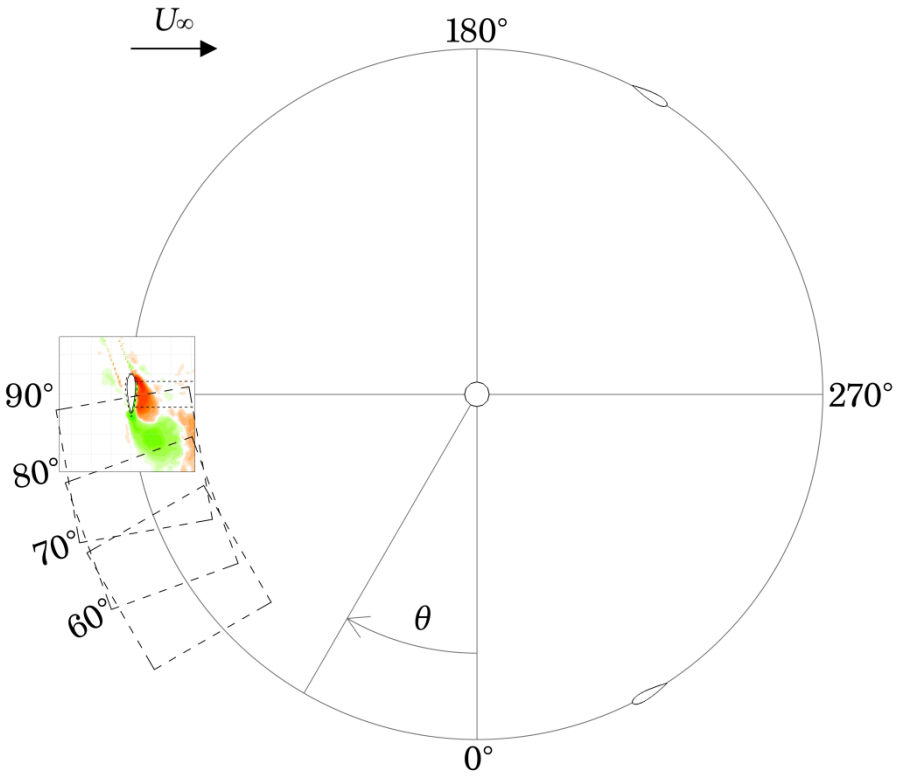

Figure 5.6. Illustration showing a sample PIV image and FOV at different azimuth positions.

The choice of the operating λ where the PIV measurements were taken focused on the extreme points on the CP curve: at λ = 2 where the CP is near the minimum, and at λ = 4 where the CP close to the maximum. Measurements were taken at 10° intervals covering the entire rotation of the blade. Figure 5.6 shows the positions of PIV measurements relative to the VAWT geometry. Care was taken to ensure that the blade was in the centre of the FOV to allow for maximum coverage of the flow features that develop on both sides of the aerofoil and the wake that trails behind it.

Flowfield at λ = 2

The flow is seen to be fully attached to the blade surface from the start of rotation at θ = 0° up to about θ = 50° (Figure 5.7a). A separation bubble starts to develop on the blade at θ = 60° (Figure 5.7b) until it forms into a leading edge vortex (LEV), also called the dynamic stall vortex, that subsequently detaches from the surface completely at θ = 80° (Figure 5.7c). As the LEV develops, a trailing edge vortex (TEV) starts to roll up and increase in size. This first TEV facilitates the completion of the detachment of the LEV by pushing it away from the surface of the blade. At θ = 90° the first TEV leaves the aerofoil surface (Figure 5.7d) just as another LEV develops. The size of the LEV and TEV are roughly the chord length of the blade and shedding of regular and well–defined vortex pairs of comparable size is observed until θ = 120° (Figure 5.7e) after which the shedding becomes more random. This randomness result in the z–vorticity plot as in θ = 170° (Figure 5.7f) where the wake starts to show a band of positive and negative vorticity instead of well–defined vortices. The bands of vorticity are an effect of ensemble averaging 100 images of random shedding for each of the azimuth positions that follow after θ = 120°. The flow continues to be separated beyond midway of the rotation and reattaches after θ = 190° (Figure 5.7g).

The flow reattachment is significantly delayed and stays in that state for a very brief period. In the downwind past θ = 190° the formation of a LEV on the other

side of the blade is observed. This LEV detaches from the aerofoil surface at θ = 240° (Figure 5.7h) and is followed by the TEV that has rolled up and left the blade at θ = 250° (Figure 5.7i). Beyond this point, bands of vorticity are again observed (Figure 5.7j) as the positions of shed vortices differ significantly from one sample to another. Unlike the upwind pass where the reattachment is delayed beyond midway in the rotation, reattachment in the downwind takes place between θ = 350° and θ = 360° (Figure 5.7k & l).

Flowfield at λ = 4

At the start of rotation, there is an observed wake of a previous blade that interacts with the current blade being studied (Figure 5.8a). The flow is fully attached to the blade and stays attached for most of the upwind. Thin bands of vorticity in the wake start to move from the middle of the FOV to bottom (Figure 5.8b, c & d) as the blade turns against the direction of the flow until it reaches θ = 130° (Figure 5.8e) where a trailing edge separation forms. The separation grows into a bubble that eventually bursts at θ = 140° (Figure 5.8f). There is a small TEV that forms but never develops into a large scale chord–sized vortex as previously seen at λ = 2. By θ = 170°, only partial separation is seen and a wake that spreads out is left by the blade (Figure 5.8g). Reattachment of the flow is observed as the blade passes θ = 180° and the wide wake narrows down (Figure 5.8h) and thins out as the blade enters the downwind (Figure 5.8i). For all the downwind images, the flow is observed to be fully attached. This is because of the higher effective λ due to reduced flow velocity through the rotor. Figure 5.8k & l show the wake of a previous blade that comes into the path of the current blade that eventually interacts with it as it passes θ = 360° (or θ = 0°).

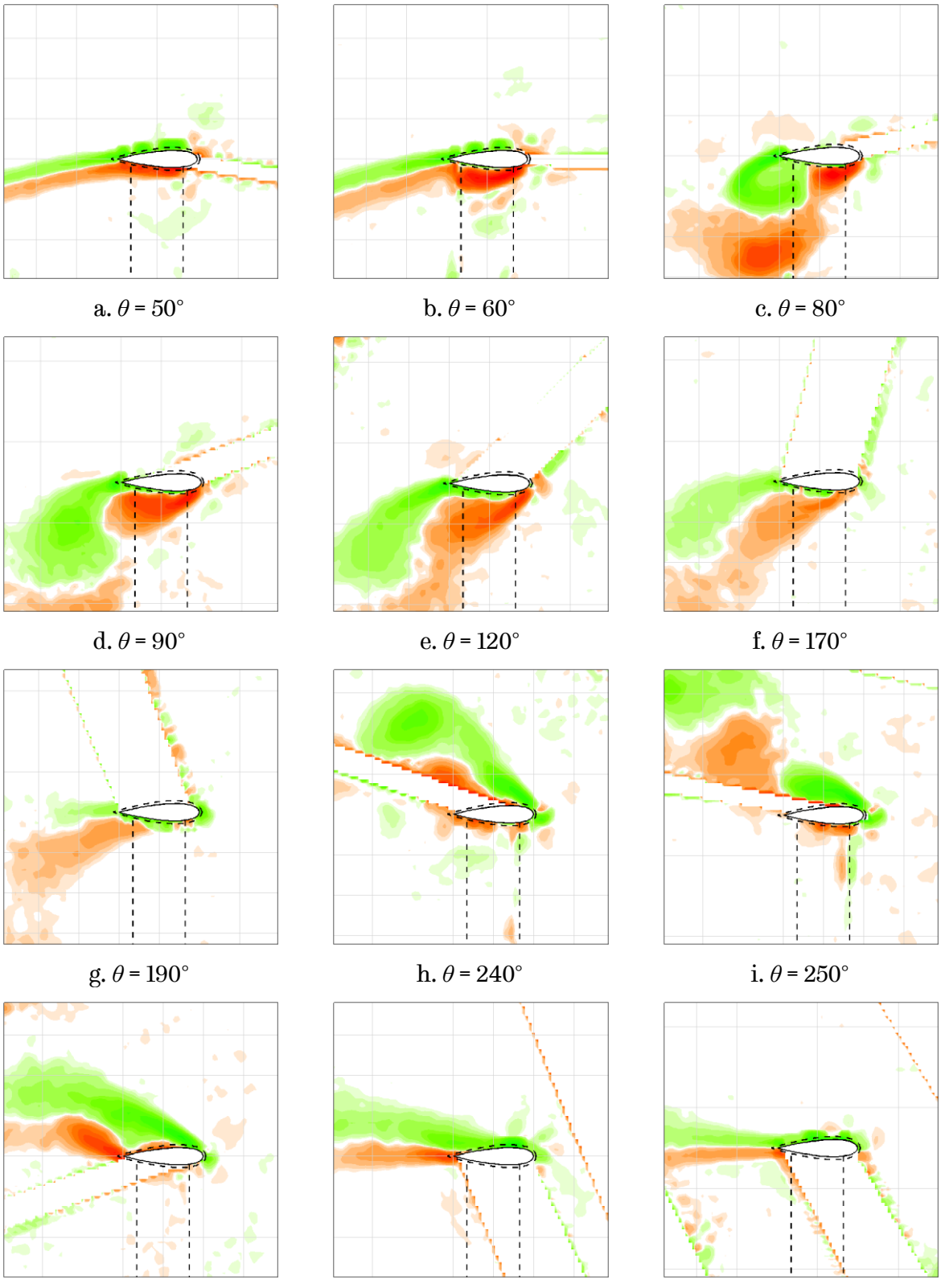

a. $\theta = 50°$ b. $\theta = 60°$ c. $\theta = 80°$

d. $\theta = 90°$ e. $\theta = 120°$ f. $\theta = 170°$

g. $\theta = 190°$ h. $\theta = 240°$ i. $\theta = 250°$

j. $\theta = 290°$ k. $\theta = 350°$ l. $\theta = 360°$

Figure 5.7. PIV images showing z–vorticity at different azimuths for $\lambda = 2$.

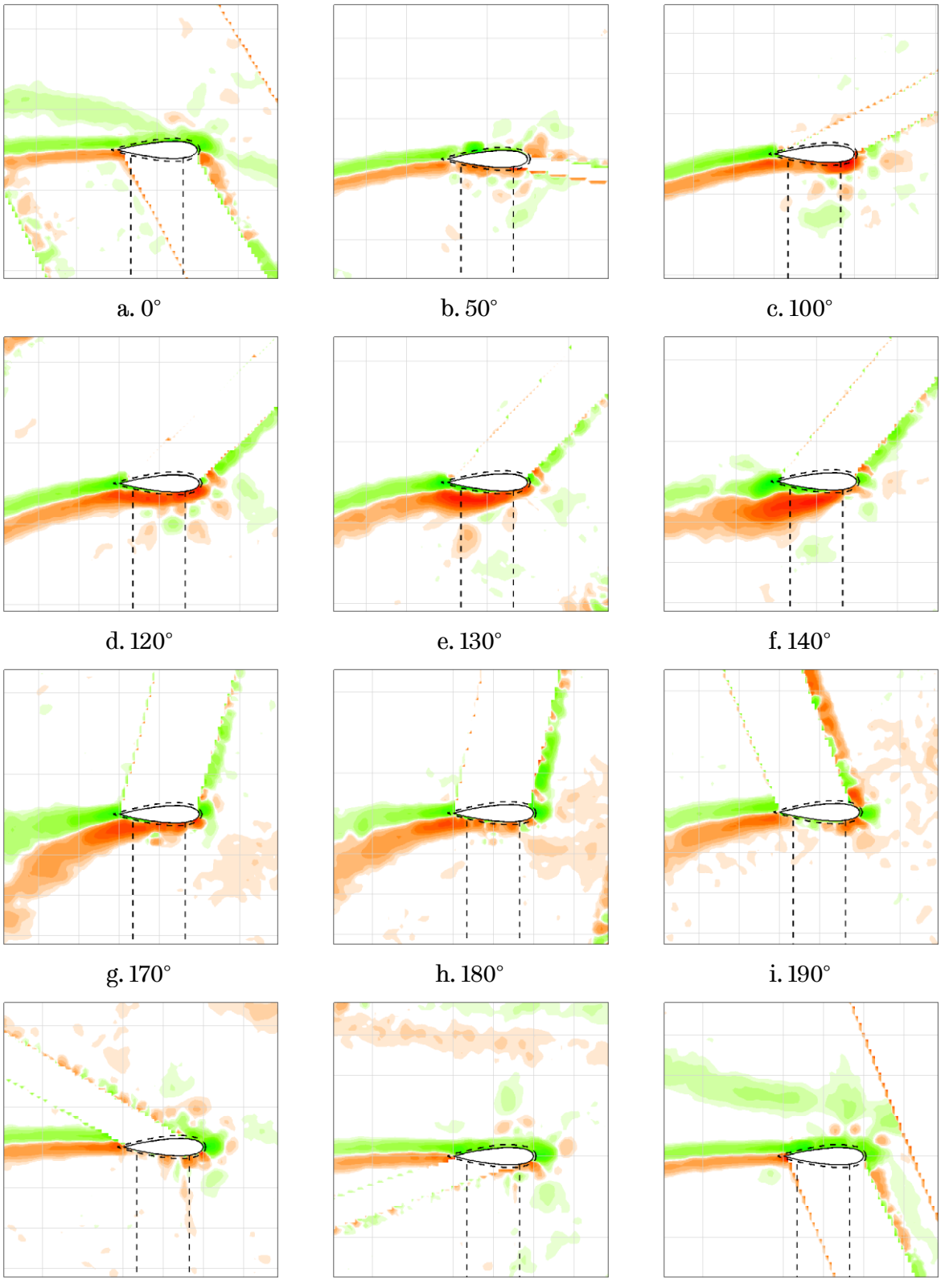

a. 0° b. 50° c. 100°

d. 120° e. 130° f. 140°

g. 170° h. 180° i. 190°

j. 230° k. 290° l. 350°

Figure 5.8. PIV images showing z–vorticity at different azimuths for $\lambda = 4$.

5.3 Unsteady Wind Performance

McIntosh [10] stated that the maximum frequency of wind fluctuations with which VAWTs will have meaningful energy extraction is in the order of 1Hz (i.e. 99% of the power content in the unsteady wind is carried by wind fluctuations at frequencies lower than 1Hz). The present work involves frequencies that are below 1Hz making the unsteadiness well within the range of relevant conditions for investigation. McIntosh proposed a notation to describe the variation in wind speed that a VAWT experiences during a gust. He called this parameter the gust length which is defined as

$$D_g = \frac{U_\infty}{f_c} \tag{5.1}$$

where U_∞ is the mean free stream velocity and f_c is the characteristic fluctuation frequency of the gust. A reduced gust frequency k_{gust} can then be defined relating the rotor's radius R to the characteristic frequency of the fluctuating wind

$$k_{gust} = \frac{2R}{D_g} = \frac{2Rf_c}{U_\infty} \tag{5.2}$$

Consequently the number of rotor revolutions per fluctuation cycle can be computed as a function of the reduced gust frequency and the mean tip speed ratio λ_{mean} where $\lambda_{mean} = \omega_{mean}R/U_{mean}$. It is necessary to use ω_{mean} because in the experiments the rotational speed of the VAWT fluctuates as a response to the unsteady wind. The number of rotor revolutions per wind cycle is defined as

$$R_g = \frac{\lambda_{mean}}{\pi k_{gust}} \tag{5.3}$$

5.3.1 Reference Case

Tests were conducted for a reference case at ω_{mean} = 791 rpm near optimum λ of the steady wind performance curve. The present test parameters (R = 0.35m, f_c = 0.46Hz, U_{mean} = 6.97m/s) result in D_g = 15.15m, k_{gust} = 0.046 and so $R_g \approx 29$ revolutions. The computed gust length is therefore an order of magnitude larger than the rotor diameter implying that the wind turbine should be able to physically resolve the large eddies containing the majority of the unsteady energy within the wind cycle. This does not imply that the turbine will be able to track the optimum λ as the wind fluctuates. It is only argued that the available energy in the unsteadiness is 'visible' to the VAWT and with the appropriate control system the VAWT will be able to extract much of the energy contained within the gust.

It is desired to have a wind turbine with low moment of inertia to reduce the need for highly sensitive measurement sensors and transducers. Doing so allows the VAWT to rapidly respond the changing aerodynamic conditions sufficiently enough to make tangible measurements a possibility. The current VAWT has a rotational mass moment of inertia about the VAWT axis equal to 0.1805kg–m^2. This is high for a VAWT of this scale but is unavoidable because of the use of solid aluminium blades. However, the current set of instrumentation allows for the detection of less than 1rpm change in rotational speed, adequate enough for the entire range of operating conditions.

Figure 5.9a shows the processed data of a sample unsteady wind test with the ensemble average in Figure 5.9b as measured using the hotwire anemometer. The amplitude of fluctuation is about 12% of U_{mean} = 6.97m/s with an f_c = 0.46Hz. The observed periodicity of the fluctuating wind is very good with almost equal magnitudes of peaks and troughs between individual cycles. Maximum positive amplitude is 0.9m/s while maximum negative amplitude is 0.87m/s. The maximum standard deviation of the individual wind cycles from the mean wind

cycle is 0.05m/s, 6% of the amplitude of the fluctuating wind. This shows the effectiveness of the shutter mechanism in generating consistent periodic unsteady wind in the tunnel. Recorded alongside the wind speed are the turbine rpm and applied brake (Figure 5.9c & e). The variation in the turbine's rotational speed is in the same frequency as the wind fluctuations but phase–shifted. It can be seen that this phase difference of the rpm (Figure 5.9d) is 180° relative to the unsteady wind. However, the corresponding fluctuations in the turbine's rotational acceleration (Figure 5.9f) are distinctly in phase with the unsteady wind. In fact, there is a negligible time lag between the fluctuating wind and the fluctuating acceleration indicating a VAWT that is very responsive to the changes in aerodynamic forces at this condition. The mean power of the unsteady wind in one cycle is 85.44W, which is just slightly higher than the power of the mean wind speed at 84.55W. This shows that there is a negligible increase of 1% in available wind energy in the fluctuating free stream when the variation in the wind speed is only 12% of the mean.

There is more variation in the observed rpm and acceleration fluctuations with more uneven peaks and troughs over the entire measured data. The maximum positive amplitude of the fluctuating rpm is 3.15rpm and the maximum negative amplitude is 3.58rpm. The maximum standard deviation of the fluctuating rpm is 0.85rpm, 27% of the amplitude. For the rotational acceleration, the maximum positive amplitude is 1.05rad/s^2 and the maximum negative amplitude is 1.04rad/s^2. The maximum standard deviation of the fluctuating acceleration is 0.17rad/s^2 which correspond to 16% of the amplitude. The unevenness of the rpm and acceleration cycles is most likely the result of the geometrically unbalanced rotor inducing significant differences in the cyclic response of the VAWT to a very regular and periodic unsteady wind.

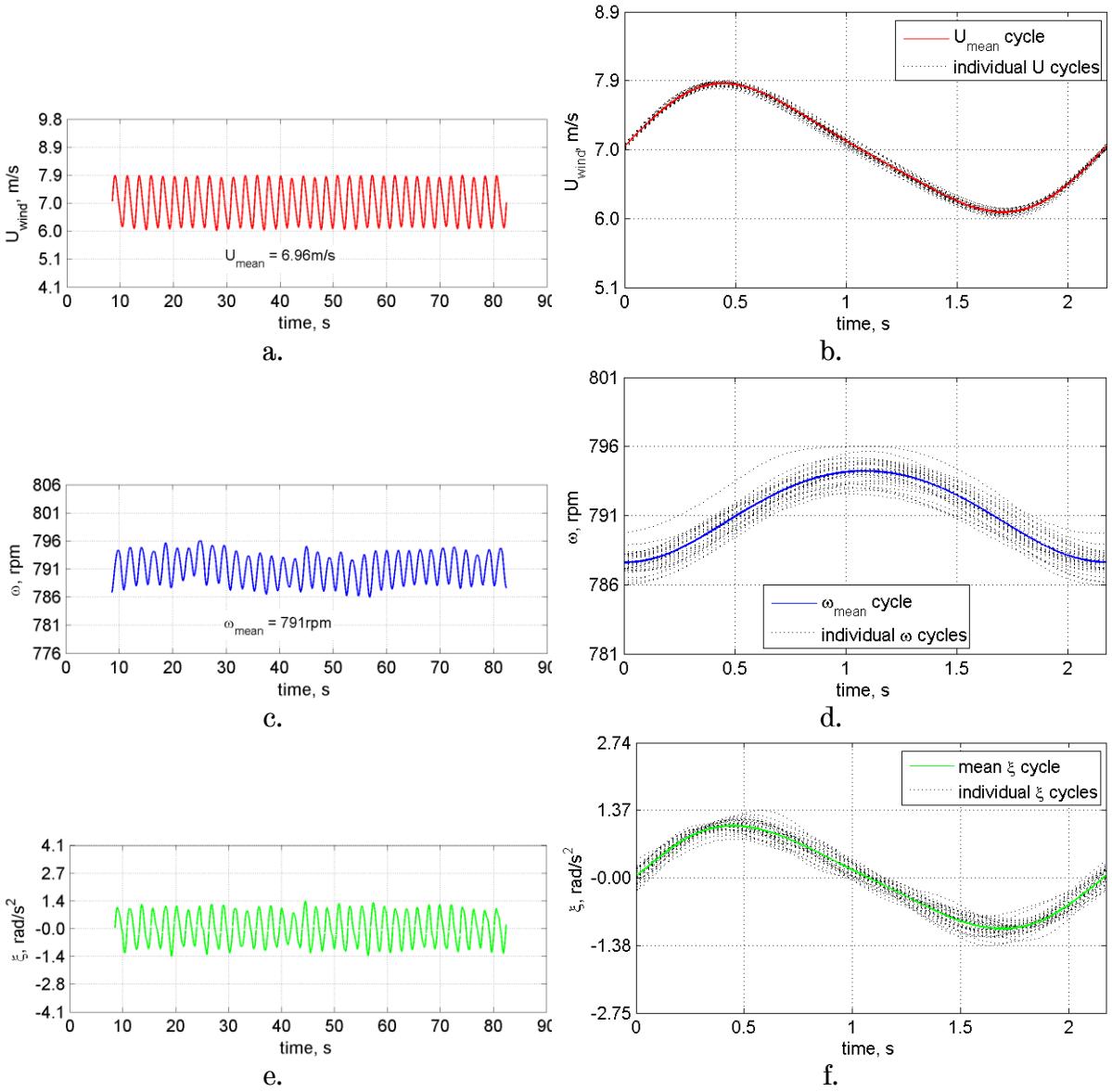

Figure 5.9. Unsteady kinematics for the reference case: a) sample plot of unsteady wind speed data, b) individual wind cycles with the ensemble–averaged wind cycle, c) sample plot of unsteady rpm, d) individual rpm cycles with the ensemble–averaged rpm cycle, e) sample plot of unsteady rotational acceleration, f) individual acceleration cycles with the ensemble–averaged acceleration cycle.

The ensemble average of the kinematic parameters discussed above is shown in Figure 5.10. The profile of the fluctuating wind is very close to a distorted sine wave. The positive fluctuation of the cycle is slightly shorter than the negative section because the latter involves the closing of the shutters, which are against the resisting flow of the wind. The power supply for the shutter drive responds to this resistance by increasing the input current while maintaining a constant

voltage. The absence of a control system on the speed of rotation of the drive causes this skewed unsteady wind profile. Despite the lack of control system for the shutter mechanism, the resulting fluctuating cycle is very close to the desired sinusoidal shape and is considered acceptable.

The fluctuating rpm plot (Figure 5.10b) shows a 180° phase lag from the wind. The peak of the rpm occurs half way in the cycle where the wind speed is close to the mean value. The lowest point in the rpm cycle is at the beginning and end of the cycle where the wind speed is also close to the mean value. This behaviour does not suggest that there is a delay in the response of the VAWT to the fluctuating wind. An inspection of the acceleration shows that the peak and trough of the acceleration coincide with the wind speed extrema well. The distortion in the acceleration curve is also similar to that of the wind profile. When the acceleration of the VAWT is highest, this corresponds to the point of maximum wind speed and the steepest positive slope in the rpm curve. On the other hand, the lowest point in the acceleration curve coincides with the point of lowest wind speed and steepest negative slope in the rpm curve. Therefore the response of the VAWT to the changing wind is considered to be instantaneous. This is expected, since the test conditions are well within the incompressible flow regime and the entire fluid domain in the tunnel test section responds instantaneously to the back pressure induced by the shutters.

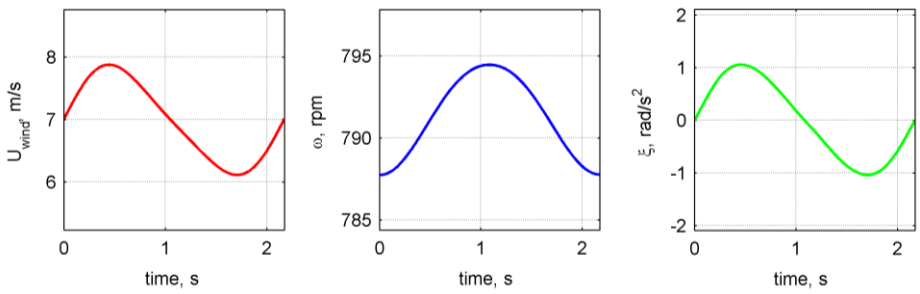

a. b. c.

Figure 5.10. Ensemble average of fluctuating wind, rpm, and acceleration.

With the acceleration known, the instantaneous rotor torque can be derived using the relationship presented in Sec 3.6. The rotor torque $I_{rig}\xi$, which is the net

torque, varies with respect to zero (Figure 5.11a). Positive acceleration produces positive rotor torque and reaches maximum at 0.19N·m. As the wind speed drops to the second half of the cycle, the acceleration plunges to the negative region resulting in negative net torque on the rotor. For the case shown, the applied torque T_{app} is zero while the resistive torque T_{res} is constant at –0.18 N·m. It is important to note that while the resistive torque is the dependent on the rotor rpm and that the rpm is fluctuating with the wind, the amplitude of the rpm fluctuation is very small compared to the magnitude of its mean value. The resistive torque corresponding to the changing rpm has a standard deviation of 7e–04N·m hence a constant resistive torque is observed. Solving for the blade torque T_B from Eq. 3.4 essentially pushes the net torque upward by an amount equal to the resistive torque T_{res}. The unsteady blade power is computed using the known blade torque T_B and rotational speed. Maximum blade power is 31.04W while the minimum is almost zero at –0.27W. The unsteady wind power can easily be derived using Eq. 1.7. Maximum wind power is computed to be 120.11W while the minimum is 56.13W. Figure 5.11b shows the plots for the blade power and the wind power in one fluctuation cycle. The cycle average wind power was mentioned earlier to be 85.44W while the cycle average blade power is 15.35W. The power coefficient of the VAWT over one wind cycle is 0.18.

The unsteady tip speed ratio λ is the instantaneous relationship between the rotational speed and the wind speed. When plotted against time, the unsteady λ curve is a mirror image of the unsteady wind profile (Figure 5.12a). This suggests λ is more sensitive to wind speed changes than to rotational speed variation. As the wind speed fluctuates to the positive peak, the λ drops from 4.11 at the start of the cycle to 3.68 close to the point of maximum wind speed. It does not occur at the point of maximum wind speed because the changing rpm also contributes to the unsteady λ and the relationship is non–linear. After reaching minimum value, λ steadily rises as the wind speed drops to the lowest magnitude. Close to the lowest point of the wind speed cycle, λ attains its maximum value of 4.74.

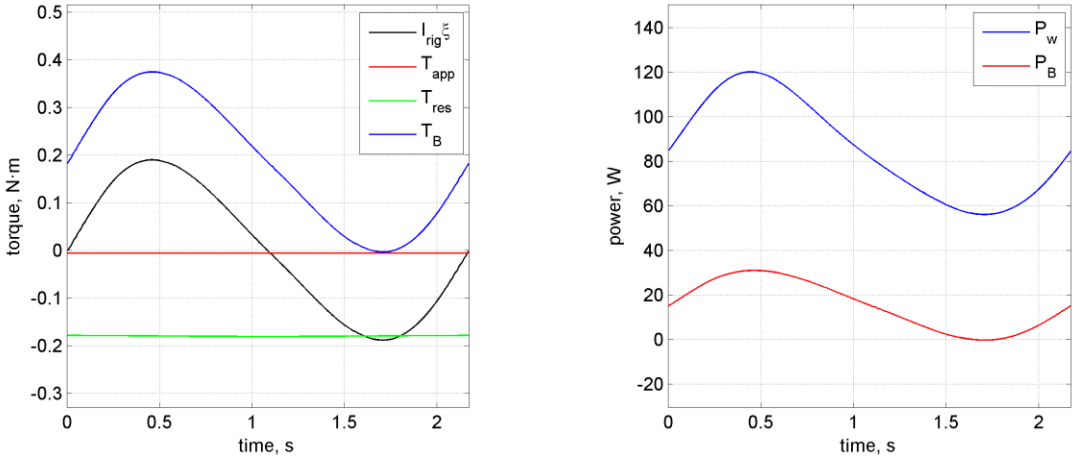

a. b.

Figure 5.11. Unsteady kinetics of the VAWT: a) unsteady torque terms for one cycle, b) unsteady wind power and blade power.

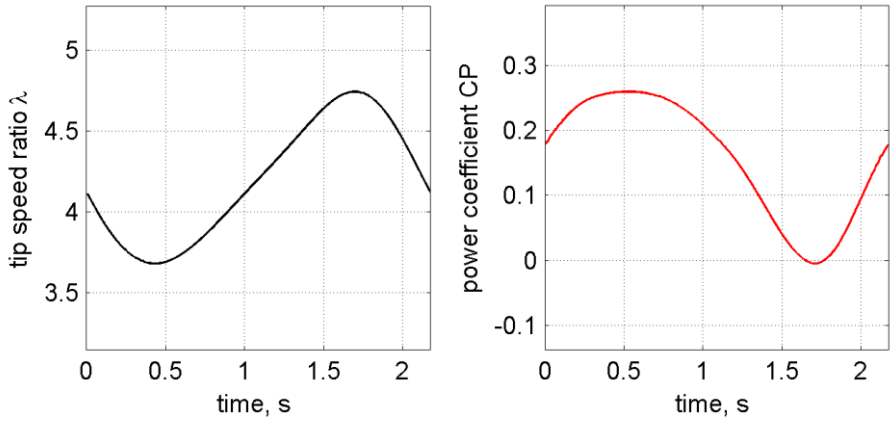

a. b.

Figure 5.12. Unsteady performance of the VAWT vs. time: a) tip speed ratio, b) CP.

From Eqs. 1.5 to 1.7, the CP is dependent on two independent fluctuating parameters: wind speed U and rotational speed ω. The 180° phase difference of ω relative to U does not make the relationship straightforward. The performance of the VAWT is highly dependent on the interaction of the two parameters and this makes the analysis more complicated. Although the profile of the wind speed variation is periodic and close to sinusoidal, the available wind power is a function of the wind speed cubed. However, the blade power is a function of the rotational acceleration derived from the fluctuating rpm. Additionally, wind power varies with larger amplitudes and has a substantially higher mean compared to blade power. This induces a unique variation in the CP as the wind

speed fluctuates. During the first half of the wind cycle where the speed changes from the mean to the maximum value and back, the CP is observed to rise gradually and flattens out early on before coming back to near its original value at the start of the cycle. Conversely the behaviour of the CP in the second half of the cycle is sudden and steep with a deep trough at the point of lowest wind speed. Afterwards, the CP rises rapidly and attains higher values as the wind speed recovers to its mean state. From Figure 5.12b, one can see an increase in CP as the wind speed rises. From the start of the cycle where the CP is 0.18, the performance rises and slowly reaches a maxima of 0.26 after which it drops to 0.19 midway in the cycle. At the start of the second half of the cycle, the drop in the value of the CP is observed to be faster than the section that just preceded it and eventually ends with a value of zero before rising again to 0.18 as the wind cycle is completed. When compared to the increase in CP of 0.08 in the first half of the cycle, the decrease of the CP in the second half is more than double at 0.19. The peak and trough of the unsteady CP curve correspond to the maximum and minimum of the wind speed profile, suggesting a Reynolds number dependence of the CP.

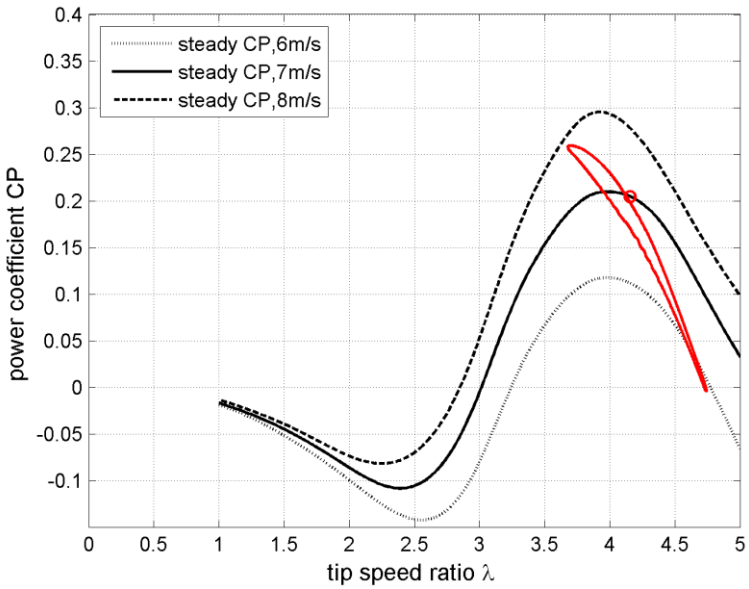

Figure 5.13. Unsteady performance versus steady wind performance.

A further inspection of this behaviour is carried out by overlaying the unsteady CP of the VAWT over CP curves at different steady wind speeds (Figure 5.13). One

can see that the unsteady CP does not follow the steady performance curve of the VAWT at 7m/s. The unsteady curve cuts across the steady CP curves as the performance fluctuates with the changing wind. This is a very different observation compared to similar work by McIntosh et al [63] and Scheurich and Brown [60] on a larger scale VAWT. Both numerical studies show that the performance of a 5kW VAWT in unsteady wind closely follows the steady CP curve when the mean λ is higher than the optimum λ for steady wind. A possible explanation for this is the difference in Reynolds number between the large scale VAWT and the wind tunnel scale VAWT. From a value of 0.18 at the start of the cycle, the unsteady CP increases with the wind speed and approaches the steady CP curve for 8m/s. The subsequent drop in wind speed does not cause the CP to follow the same path in reverse but it traces a new one with slightly higher values. The small hysteresis loop in the unsteady CP implies earlier stall and delayed reattachment as wind speed decreases to and comes from its lowest point in the cycle. As a reference point, the equivalent steady CP of the VAWT at the mean λ is 0.205 while the instantaneous CP at two points in the unsteady curve with the same λ value are both lower and the cycle average CP is also lower. When the wind speed reaches is lowest value in the cycle, the unsteady CP is already lower than the 6m/s steady CP curve even though the actual wind speed is still higher at 6.1m/s.

5.3.2 Effect of Varying the Mean λ

The performance of the VAWT in unsteady wind is further investigated by changing the mean λ while preserving the unsteady profile of the wind. This is accomplished by applying the brake on the VAWT to increase the resistive forces and reduce the mean rpm of the rotor. This has a small effect on the unsteady wind profile but is within reasonable variation so as not to be considered significant. The plots of the fluctuating wind speed for the two different mean λ cases are shown in Figure 5.14a where there is a difference in the observed period of fluctuation between the two. The reference case with the higher mean λ has a

period of t = 2.17s (f_c = 0.46Hz) while the case with the lower mean λ has a period of t = 1.91s (f_c = 0.52Hz). The difficulty in controlling the experimental parameters with their inter–dependent properties implies that the unsteady wind profiles cannot be matched precisely when settings are changed. Nevertheless, the dissimilarity in periods is considered small when compared to the overall effect of the magnitude of the fluctuating wind speed. The mean wind speeds for both cases are very close at 6.97m/s for λ_{mean} = 4.1 and 6.96m/s for λ_{mean} = 3.8. The amplitudes of fluctuation are also very similar at 0.88m/s for λ_{mean} = 4.1 and 0.81m/s for λ_{mean} = 3.8, just more than 12% of the U_{mean}.

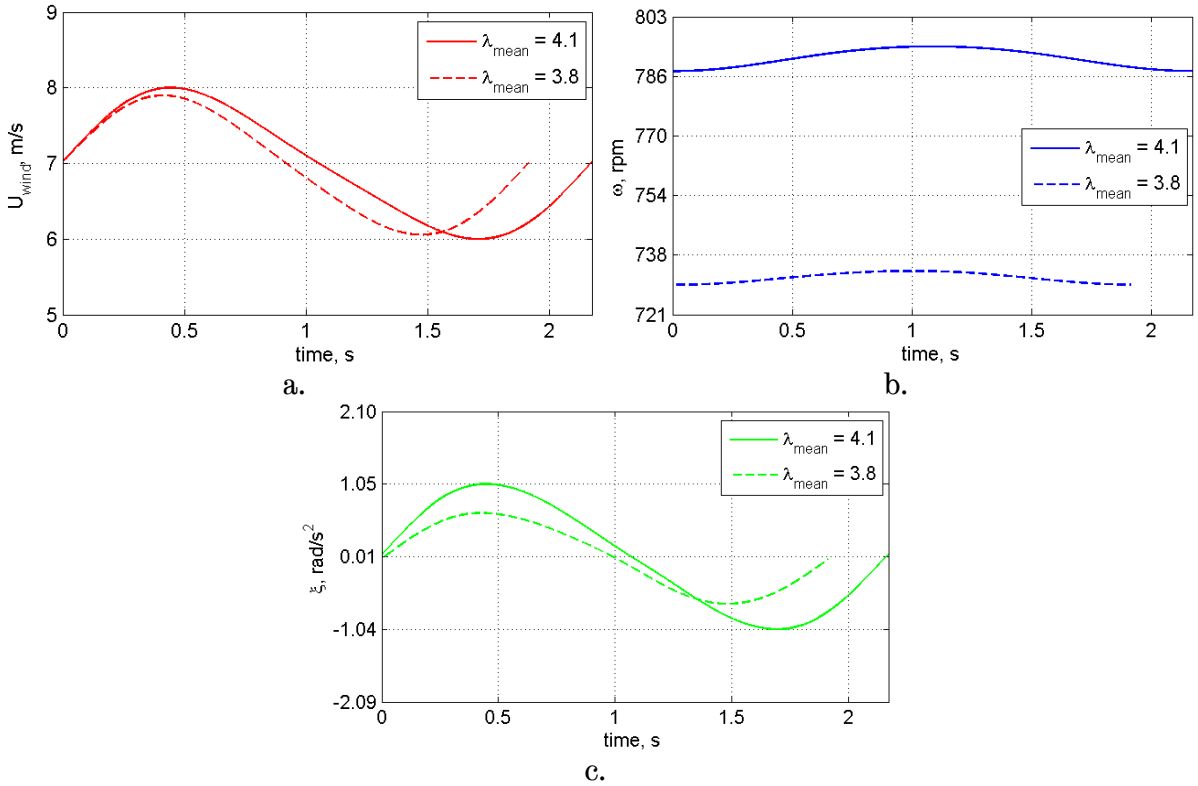

Figure 5.14. Unsteady kinematics for different mean λ: a) wind speed, b) rotational speed, c) rotational acceleration.

Shown in Figure 5.14b is the plot of the unsteady rpm for the two cases. The mean rpm is 791rpm for λ_{mean} = 4.1 while it is 731rpm for λ_{mean} = 3.8 where the resistive torque corresponding to these cases are 0.18N·m and 0.165N·m, respectively. From the torque equation (Eq. 3.4), this suggests a smaller vertical shift of the T_B curve due to the T_{res} term for λ_{mean} = 3.8 from the initial $I_{rig}\xi$ curve

position. However, an additional brake torque T_{app} of 0.03N·m is present for λ_{mean} = 3.8 that pushes the T_B curve further up.

It can be seen that the peak–to–peak value of the rpm fluctuation is 6.73rpm for λ_{mean} = 4.1 and 3.77rpm for λ_{mean} = 3.8. The difference, which is almost double, greatly affects the computed rotational acceleration of the VAWT. More gentle slopes in rpm for λ_{mean} = 3.8 mean lower values of acceleration while larger amplitudes as in the case of λ_{mean} = 4.1 result to higher magnitudes of acceleration (Figure 5.14c). Since blade torque T_B is directly proportional to acceleration, the λ_{mean} = 4.1 case generates greater torque variation than the λ_{mean} = 3.8 case. The amplitudes of fluctuation of λ for the two cases are noticeably different as seen in Figure 5.15a. The amplitude for λ_{mean} = 4.1 is 0.53 while it is 0.46 for λ_{mean} = 3.8. Since the wind speed variation between cases are very similar, λ is now dependent only on the rpm fluctuation. With the observed lower peak–to–peak variation of rpm in λ_{mean} = 3.8, the same can be expected on fluctuating λ with a lower peak–to–peak value.

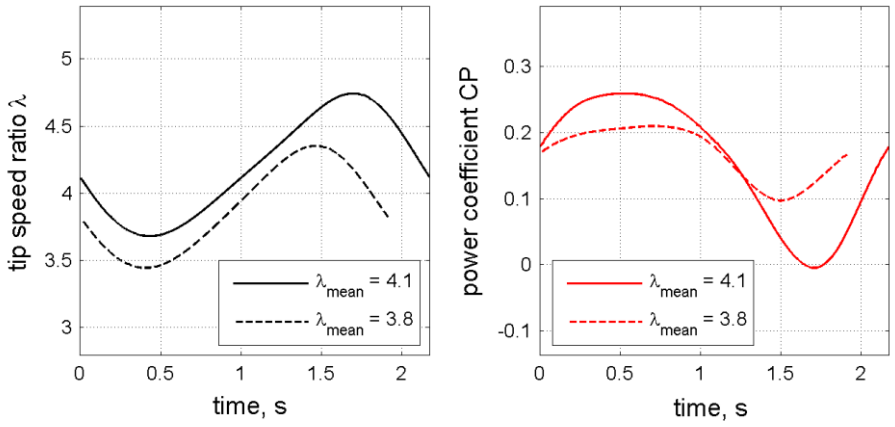

a. b.

Figure 5.15. Unsteady performance of the VAWT for the two λ cases: a) λ vs. time, b) CP vs. time.

The behaviour of the time varying CP cannot be simplified in the same manner. Both cases show a gradual rise and tapering off in CP during the first half of the wind cycle but a steep and sudden drop in the second half (Figure 5.15b). From the

start of its cycle, λ_{mean} = 4.1 gains 0.08 in CP from 0.18 to 0.26 before dropping to 0.19 as the first half of the cycle ends. However, the CP continues to drop and loses more than 0.19 until it reaches less than zero. Similarly, λ_{mean} = 3.8 exhibits an initial slow rise in CP of 0.04 from 0.17 to a peak value of 0.21 and a subsequent deep trough in the second half with a loss of 0.1 as it goes from 0.19 to the lowest value of 0.09. The preceding observations point to a negative bias in CP variation even in a symmetrically fluctuating wind. There is more negative effect in performance despite constant energy content in the wind suggesting that unsteady wind at this condition is detrimental to the overall VAWT performance.

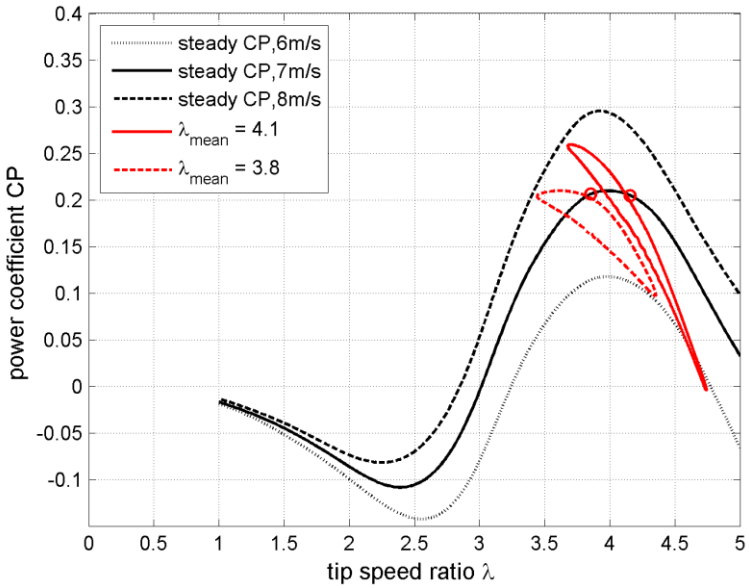

Figure 5.16. Unsteady performance of the VAWT at different mean λ.

The unsteady CP variation of the two λ cases is plotted against λ in Figure 5.16. Compared to λ_{mean} = 4.1, the unsteady CP of λ_{mean} = 3.8 shows a larger hysteresis loop which further supports the argument that it is not possible to trace the unsteady performance of a micro–scale VAWT on steady CP curves. The hysteresis indicates the presence of deeply stalled flow and delayed reattachment, a phenomenon that is likely to occur at λ below the optimum performance point. When the VAWT operates at λ that is below λ^*, the perceived α is much higher than the static stall α and higher than the maximum α seen at λ^*. A likely outcome to this is stalled flow over the suction surface that, in many instances, is deep and

persists for a significant portion of the rotation. McIntosh et al [63] similarly investigated a variety of mean λ and found that hysteresis loops in CP are formed when λ_{mean} is close to the optimum λ. However, the similarity ends there. They have seen a significant increase in the cycle–averaged CP of the VAWT especially at higher f_c whereas this study sees the contrary. The unsteady CP moves between different steady CP curves clearly showing Reynolds number dependency at this scale. Both cases illustrate a trend in the band of unsteady performance. The VAWT CP is expected to fluctuate from one steady CP curve to another depending on the amplitude of the fluctuating wind. For the cases considered, the amplitude is around 0.9m/s hinting that the CP should fluctuate between the 6m/s and 8m/s steady CP curves. The cycle–averaged CP for both cases is 0.18 while the steady wind CP counterparts are just above 0.20.

5.3.3 Effect of Varying the Fluctuation Amplitude

The influence of varying the amplitude of fluctuation was also investigated. Achieving this necessitated the changing of the closing angle of the shutters to change the flow restriction in the test section. As with changing any test parameters from the reference test case, difficulty was encountered in trying to change only one setting without significantly affecting other settings. To achieve the same mean wind speed while having smaller amplitude, getting the same period of fluctuation was inevitably going to be difficult. The new case with the smaller amplitude fluctuation U_{amp} = ±7% has a period of t = 1.87s (f_c = 0.54Hz) (Figure 5.17a). This is close to the λ_{mean} = 3.8 case of the previous section and not too far from the reference case U_{amp} = ±12% of t = 2.17s (f_c = 0.46Hz). The mean wind speed for U_{amp} = ±7% is 6.87m/s, a slight drop from the 6.97m/s wind speed for U_{amp} = ±12%. The 0.1m/s difference between mean values is deemed small since its effect on the wind power is only a 3.5W drop, about 4% power reduction. The amplitude of wind fluctuation for U_{amp} = ±7% is 0.47m/s.

There is a very small difference in the rotational speed profiles between the two cases. As reported in the previous section, the mean rotational speed ω_{mean} for U_{amp} = ±12% is 791rpm. On the other hand ω_{mean} = 795rpm for U_{amp} = ±7%, a mere 0.5% difference. In terms of the resistive torque corresponding to these rpm levels, T_{res} = 0.18N·m for both U_{amp} = ±7% and U_{amp} = ±12%. An expected outcome is the difference in the peak–to–peak value of the rpm fluctuation (Figure 5.17b). For U_{amp} = ±7% this is 3.58rpm, which is about half of the value for U_{amp} = ±12%. The smaller peak–to–peak results in a similar outcome in rotational acceleration as the λ_{mean} = 3.8 case where the gentler slopes in the rpm profile cause smaller magnitudes in rotational acceleration (Figure 5.17c). Consequently, the magnitudes of the unsteady torque are much smaller than the reference case. The mean λ is 4.2 for U_{amp} = ±7%, slightly higher than λ_{mean} = 4.1 for U_{amp} = ±12%. This is to be expected because for the U_{amp} = ±7% case, ω_{mean} is a little higher and U_{mean} is a bit lower. Additionally the amplitude of λ fluctuation is smaller as a direct consequence of the smaller amplitude of the unsteady wind (Figure 5.18a).

The variation of the CP versus time when U_{amp} = ±7% is similar to the previous cases investigated (U_{amp} = ±12% at λ_{mean} = 4.1 and λ_{mean} = 3.8). As already seen in the previous section, where a bias towards the negative performance is observed, such observation is also true with a smaller amplitude of fluctuation (Figure 5.18b). At the start of the cycle, the instantaneous CP is 0.204 and gradually rises to a peak value of 0.257. The subsequent fall of the wind speed causes the CP to follow suit and return to a value close to the initial CP at 0.197. As the wind speed continues to drop to the minimum, the CP also decreases until it reaches its lowest at 0.099. Between the initial CP and the maximum, the increase in CP is 0.053. However, the drop in CP between the initial value and the minimum is almost double at 0.105. The results are consistent to the previous test cases where the overall cycle–averaged CP is reduced when the VAWT is subjected to unsteady wind conditions.

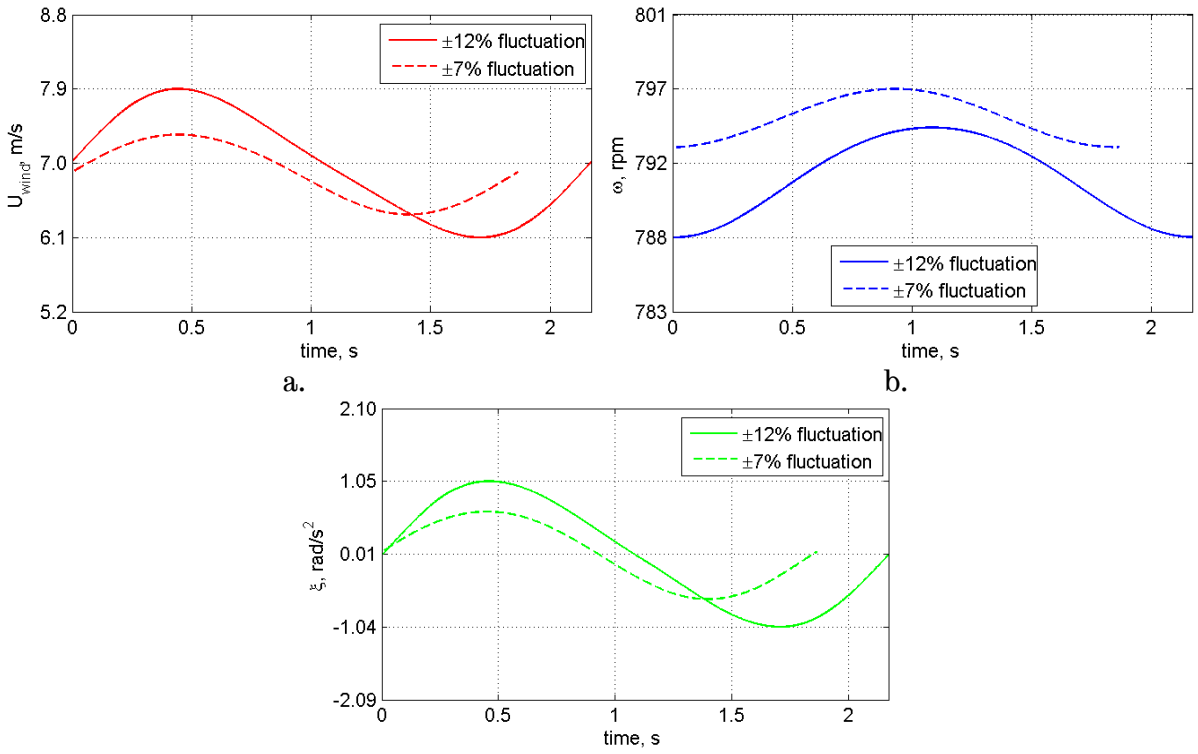

Figure 5.17. Unsteady kinematics for different fluctuation amplitude: a) wind speed, b) rotational speed, c) rotational acceleration.

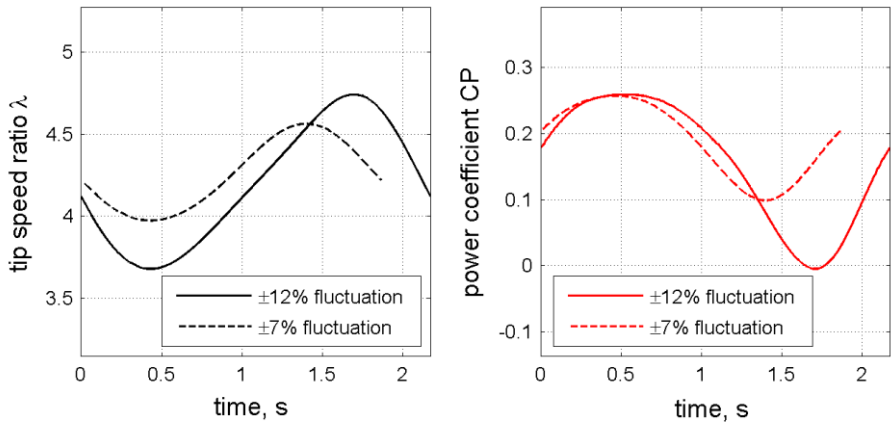

Figure 5.18. Unsteady performance of the VAWT for the two U_{amp} cases: a) λ vs. time, b) CP vs. time.

Figure 5.19 shows the unsteady CP plotted against λ. Noticeably the path that the CP traces does not form a hysteresis loop. This is expected since the wind speed amplitude is small enough that most likely stall is shallow and reattachment is not delayed at these operating λ. Scheurich and Brown [60]

observe a similar trend in the CP curve with varying amplitudes. In their investigation, a fluctuation amplitude of ±30% induces hysteresis in the unsteady CP while a ±10% amplitude does not. The unsteady λ barely drops below the optimum λ value. When the VAWT is operating at these conditions, the blade stall behaviour is similar to a very slowly pitching aerofoil in constant free stream. The separation starts from the trailing edge and moves up towards the leading edge. A leading edge separation bubble never forms and most of the time only partial stall is seen. The path of the unsteady CP is also comparable to the previous results where the curve cuts across the steady CP curves and approaches the adjacent curves as the wind speed fluctuates to its extreme values. The cycle–averaged CP for U_{amp} = ±7% is 0.18, a 0.01 drop from the steady CP value of 0.19.

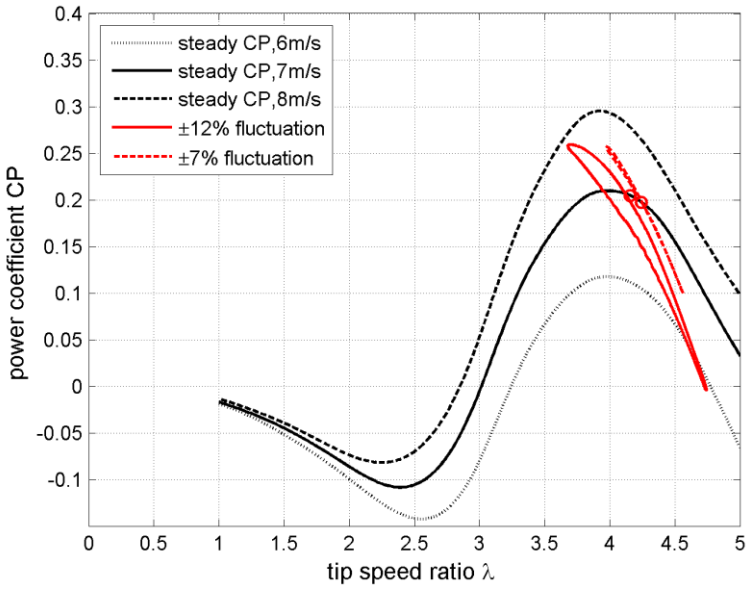

Figure 5.19. Unsteady performance of the VAWT at different U_{amp}.

5.4 Summary

The spin down technique and PIV visualisations have shown to be invaluable tools in the fundamental understanding of VAWT aerodynamics and performance in steady wind conditions. The performance of the VAWT in 7m/s steady wind over a wide range of λ is revealed to have a negative trough from λ = 1 up to λ = 3 with the lowest CP of –0.11 at λ = 2.4. Beyond λ = 3 the CP rises until the maximum value of 0.21 at λ^* = 4.0 after which it falls close to zero at λ = 5. This CP profile is typical of the scale of the VAWT tested where a negative trough is present mostly due to high zero–lift drag that hampers the ability of the rotor to generate positive torque at low λ and self–start. The negative trough is observed to slowly diminish as wind speeds, and consequently, Reynolds number increases. PIV visualisations at low λ reveal the azimuth positions of stalled flow corresponding to poor performance point of the VAWT. At λ = 2, the blade starts to stall around θ = 60° with the development of a leading edge separation bubble that eventually forms into a dynamic stall vortex. This vortex enhances the lift generated on the blade surface before it is eventually shed and a trailing edge vortex rolls up and is cast off from the blade. A series of vortex pairs ensues until the delayed reattachment past θ = 180° where α is computed to be 0°. The higher λ = 4 shows the stalling of the blade in the upwind taking place at a much later azimuth of θ = 130° and reattachment of flow occurring as the blade passes the θ = 180° position.

Unsteady wind experiments have uncovered unsteady VAWT performance that does not follow steady CP curves. For the mean wind speed of U_{mean} = 7m/s, the instantaneous CP rises and approaches the steady CP profile of a higher U_∞ as the wind speed increases. The maximum unsteady CP is 0.26 and is greater than the steady CP maximum. The fall of the U_∞ from the mean to its lowest value causes the CP to fall and move towards the steady CP profile of 6m/s. The cycle–averaged CP of the VAWT is lower at 0.18 compared to the steady CP value of 0.205 at the corresponding λ. Lowering the λ_{mean} from 4.1 to 3.8 still shows the unsteady CP cutting across steady CP curves. However, the unsteady CP profile now shows a

large hysteresis that drastically affects the overall performance of the VAWT despite the minimum CP falling to only 0.09 versus the reference case minimum of just below zero. The cycle–averaged CP of the λ_{mean} = 3.8 case is equal to the reference case at 0.18. When the amplitude of fluctuation U_{amp} is changed instead of the mean tip speed ratio λ_{mean}, a similar deterioration of performance is measured. The extents of the unsteady CP are much shorter than the reference case when the U_{amp} is reduced from ±12% to ±7%. No visible hysteresis in the CP is seen and the reduction in cycle–averaged CP is much less from the steady CP value of 0.19 to the unsteady cycle–averaged CP of 0.18. All in all, unsteady free stream causes a drop in performance of the laboratory scale VAWT tested.

Chapter 6
Numerical Results

6.1 Introduction

This chapter details the numerical investigations on the performance of the VAWT in steady and unsteady wind conditions. Steady wind performance is initially analysed over a tip speed ratio range of $1.5 \leq \lambda \leq 5$ in a constant free stream of U_∞ = 7m/s. Following the steady wind analysis is the investigation of unsteady wind effects on VAWT performance CP through variation of VAWT rotational speed ω and free stream fluctuation amplitude U_{amp}. For each unsteady wind test case, blade force analysis coupled with flow visualisations are presented and discussed in detail to provide an in–depth understanding of the influence of fluctuating free stream to the aerodynamics and performance of a VAWT.

6.2 Steady Wind Performance

The numerical model developed in Chapter 4 was the basis for all numerical studies carried out in this chapter. The performance of the VAWT was investigated under steady wind conditions of U_∞ = 7m/s and was validated against experimental data from Chapter 5. Following the validation is a closer inspection of the numerical data to give a better understanding of the behaviour in VAWT performance across a wide operating range. This is discussed in the following sections.

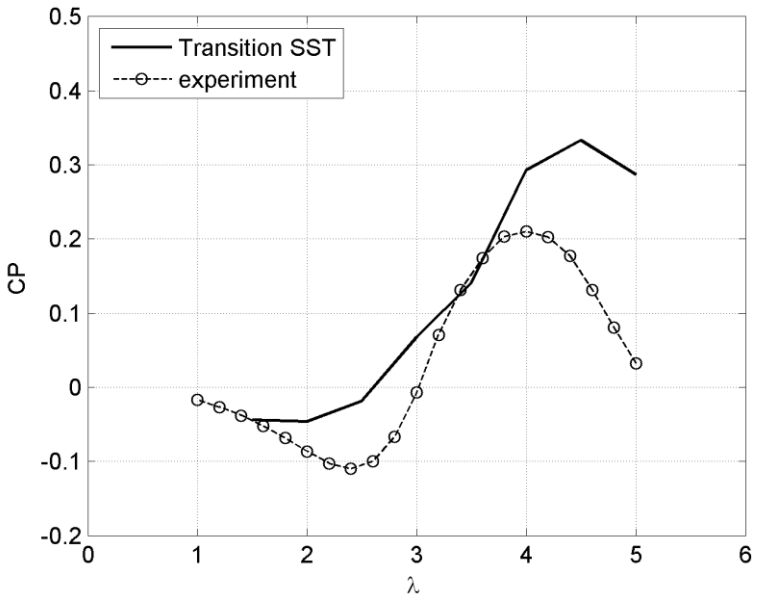

Figure 6.1. Steady wind performance of the VAWT at U_∞ = 7m/s.

6.2.1 Power Coefficient

The variation of CP versus λ was presented in Sec. 4.4.1 and is repeated in Figure 6.1. There is a marked difference between the predicted CP and the actual CP especially in the power producing region ($4 < \lambda < 5$). The maximum measured CP is 0.21 at λ = 4 while the maximum predicted CP is 0.33 at λ = 4.5, a shift of the power curve upwards and to the right is explained by the effects of having infinite AR in the 2D numerical model. Low AR, as is the case of the actual experimental VAWT, increases the induced drag due to tip effects in proportion to the positive

performance of the blades [10]. The negative trough at low λ is still present but is also over predicted by the numerical model from the experiment minimum CP of –0.11 at λ = 2.4 to the predicted –0.04 at λ = 2. The predicted CP does not follow a smooth curve as λ increases from λ = 3 to λ = 4. There is a slight kink in the CP curve at λ = 3.5 towards the right which causes it to touch the experimental CP curve. There is no conclusive explanation to this behaviour despite closer inspection of the blade torque curves and flow visualisations across the entire range of λ.

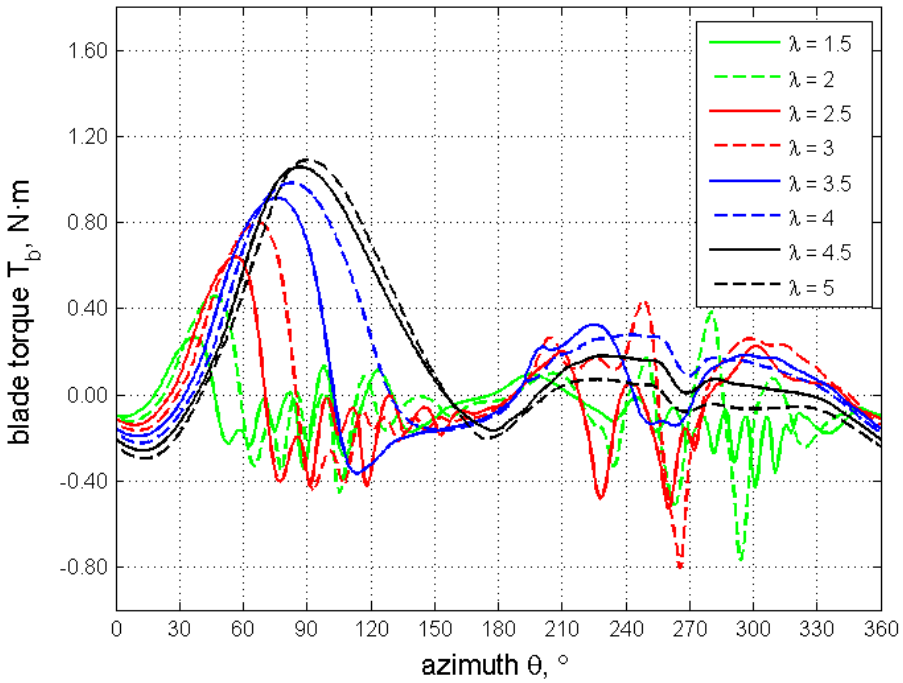

Figure 6.2. Blade torque curves for one blade at U_∞ = 7m/s.

As λ increases from λ = 1.5 to λ = 5, maximum T_b for one full rotation is observed to increase and the stalling in the upwind progressively delayed (Figure 6.2). Downwind performance is also seen to improve as λ increases from λ = 1.5 to λ = 4 resulting in the steady increase in CP. At λ = 4.5, T_b in the downwind is lower than at λ = 4. However, T_b in the upwind is higher and stays positive longer at λ = 4.5 than at λ = 4 which results in a higher CP at λ = 4.5. Upwind performance is very similar for both λ = 4.5 and λ = 5. The main factor for the lower CP at λ = 5 is the poorer performance in the downwind with negative T_b observed to commence at θ

= 258° versus the λ = 4.5 case where T_b dips into the negative region at a much later azimuth of θ = 325°.

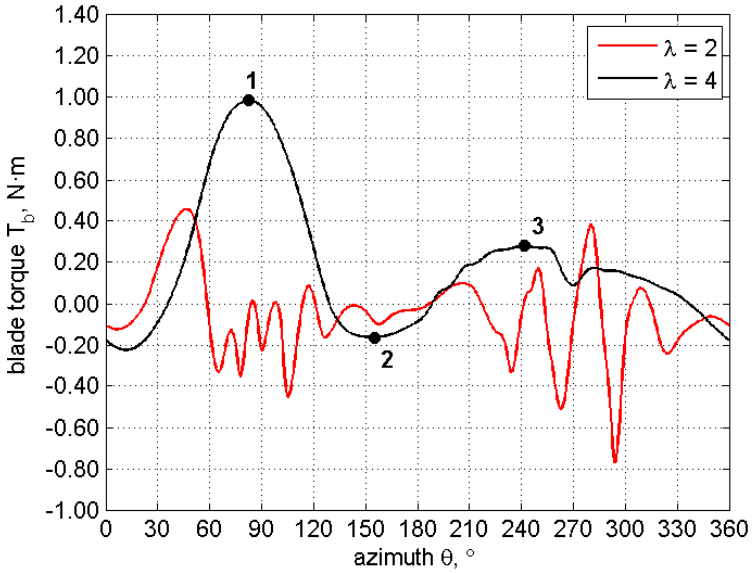

Figure 6.3. Blade torque curves of two λ cases at U_∞ = 7m/s.

The observed differences in the performance of the VAWT at different λ can be explained by analysing the aerodynamic forces on the blade. Traditionally lift and drag coefficients are used as the bases for the assessment of aerofoil performance and this is attempted in the following analysis to further the understanding of VAWT performance using familiar means. Alongside flow visualisations and the CP–λ curve, a complete picture of the VAWT performance can be constructed using detailed comparisons of lift and drag variation as blades go around one full rotation.

Following on from the experimental validation section where two λ are tested, the same is conducted in this analysis. The main reason for testing these two λ is their significant dissimilarity in almost all aspects of performance. In this way, significant differences can be presented for comparison between extreme operating conditions. The two λ tested are λ = 2 and λ = 4. For each simulation, the moment coefficient of one blade is recorded and the final rotation is presented in Figure 6.3. It can be seen that the upwind performance at λ = 4 is considerably better than at λ = 2 with more than double the maximum T_b predicted at T_b =

0.98N·m. The stalling is also very much delayed in the higher λ while a ripple of the T_b curve is present in the lower λ indicating the shedding of vortices. Much of the blade torque is negative at λ = 2 while the opposite is observed at λ = 4. The predominantly negative torque at λ = 2 explains the negative CP at this λ. Point 1 in the T_b curve of λ = 4 is at θ = 82.5°, the maximum value of T_b for the rotation. At this azimuth in the first quadrant of rotation, the lift is close to maximum at C_l = 0.92, almost double that of the CFD–derived static stall lift of $C_{l,ss}$ = 0.59 at angle of attack α_{ss} = 11° (Figure 6.4). The increased lift is due to the dynamic stall effect as the blade moves in a pitching–type motion relative to the flow. Drag at this point is also higher at C_d = 0.11, almost double that of the static stall drag of $C_{d,ss}$ = 0.06 (Figure 6.5). These observations are typical of dynamic stall phenomenon [31] and are expected even at this λ since the computed α at point 1 is higher than α_{ss} at 13.5° (Figure 6.6). The effects of dynamic stall are more evident at λ = 2 where the maximum lift before stall exceeds that of λ = 4. Even after stall, lift is still increasing as vortices are shed from the blade up until α reaches maximum at 30° with C_l topping at 1.5. Despite the high lift, T_b is negative because of the overpowering effect of drag which has reached an upwind maximum of C_d = 0.97. Even at high values of α, the drag is still more aligned to the tangential direction than the lift, inducing drag dominated performance.

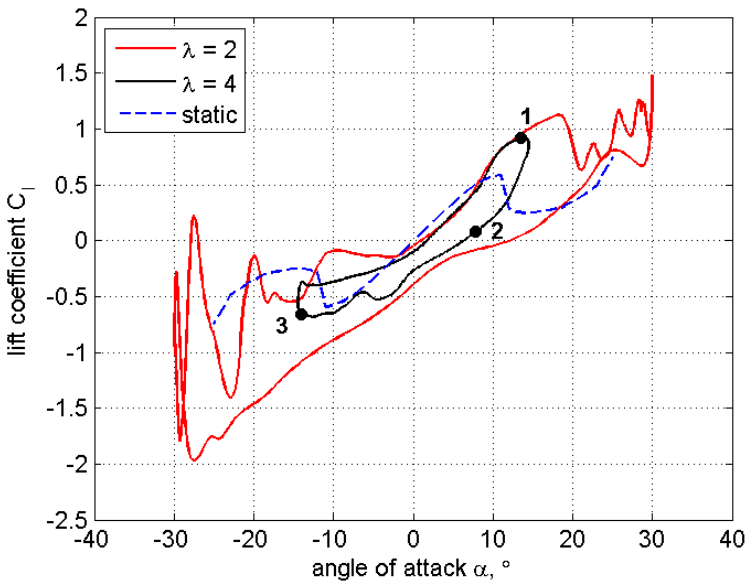

Figure 6.4. Lift coefficient plot of two λ cases at U_∞ = 7m/s.

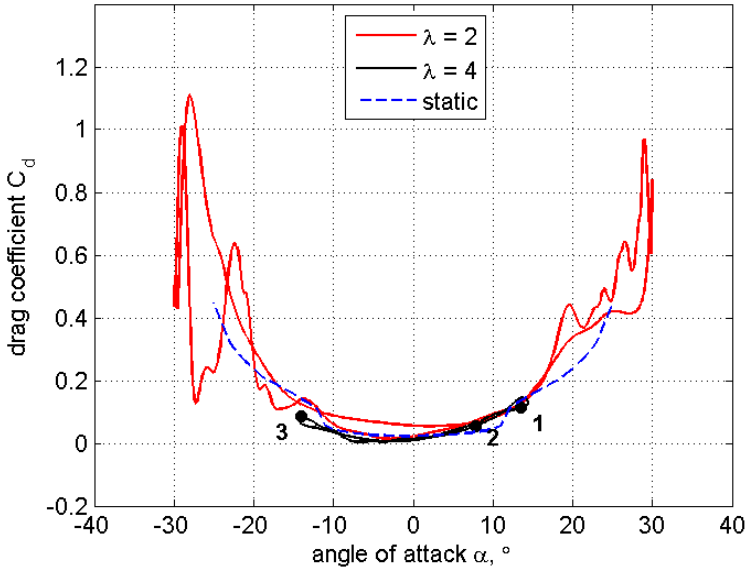

Figure 6.5. Drag coefficient plot of two λ cases at U_∞ = 7m/s.

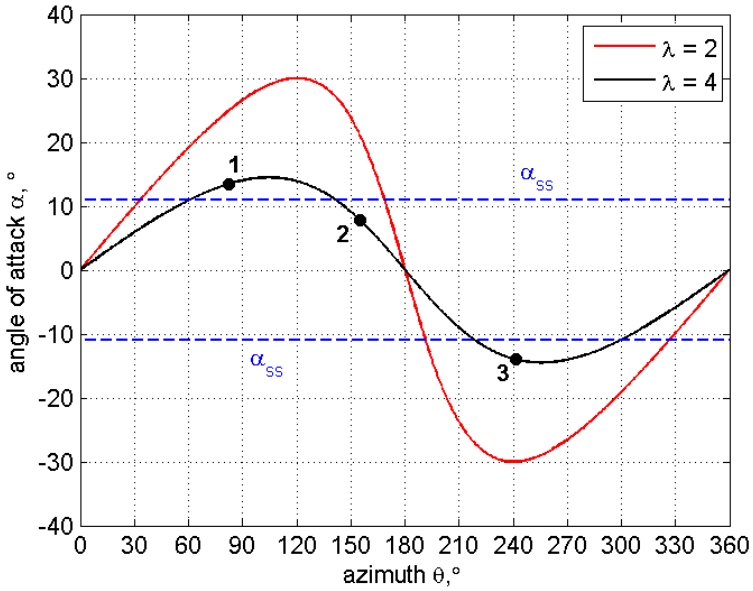

Figure 6.6. Variation in α of two λ cases at U_∞ = 7m/s, α_{ss} is the static stall α.

After point 1, T_b rapidly drops and reaches the negative region as the blade sees stalled flow. The lowest point of the T_b curve in the second quadrant is at θ = 155° (point 2). The α at this point is 7.8° and while this is not particularly low with static C_l around 0.5, lift on the blade has dramatically dropped to C_l = 0.08 with the drag halved at C_d = 0.06. The relatively high drag and an almost negligible lift is the main reason why the T_b at this point is negative at –0.16N·m. Just after the third quadrant at θ = 241.5°, maximum T_b = 0.28N·m is attained in the downwind at point 3 just before the blade interacts with the wake of the centre post. Although

the α at this point is 14° which should bring the blade into dynamic stall, lift is much lower than the upwind maximum at C_l = 0.66 while drag is also lower at C_d = 0.09. This is not surprising since there is velocity induction in the upwind due to power extraction subsequently lowering the available energy content in the flow.

6.2.2 Flow Visualisations

A better appreciation of the variation in lift and drag can be attained through the inspection of the flow visualisations as the blade goes around the rotation. Although there are three blades present in the rotor, the symmetry of the rotor allows for a set of images for one blade going around one full rotation to be sufficient in giving a complete picture of the problem. Corresponding torque values plotted in polar coordinates compliment the visualisations to make a concise summary of the performance. This diagram style is adapted for both test cases of λ.

Flowfield at λ = 2

The variation of blade torque T_b through one full rotation is plotted in Figure 6.7 alongside flow visualisations. Large regions of negative torque are visible and huge fluctuations in magnitude agree closely with azimuth positions showing deep stall and vortex shedding. Most of the positive torque in the upwind is produced between θ = 30° and θ = 60° while negative values are seen all the way until mid rotation. This poor performance is a consequence of the very steep α that the blade sees inducing the persistent large scale vortex shedding seen. In the downwind, a similar picture is observed with blade scale vortices being shed after θ = 210° until past θ = 300°. Delayed reattachment occurs at θ = 330°, despite the expected low α at this point in the rotation further lowering the performance.

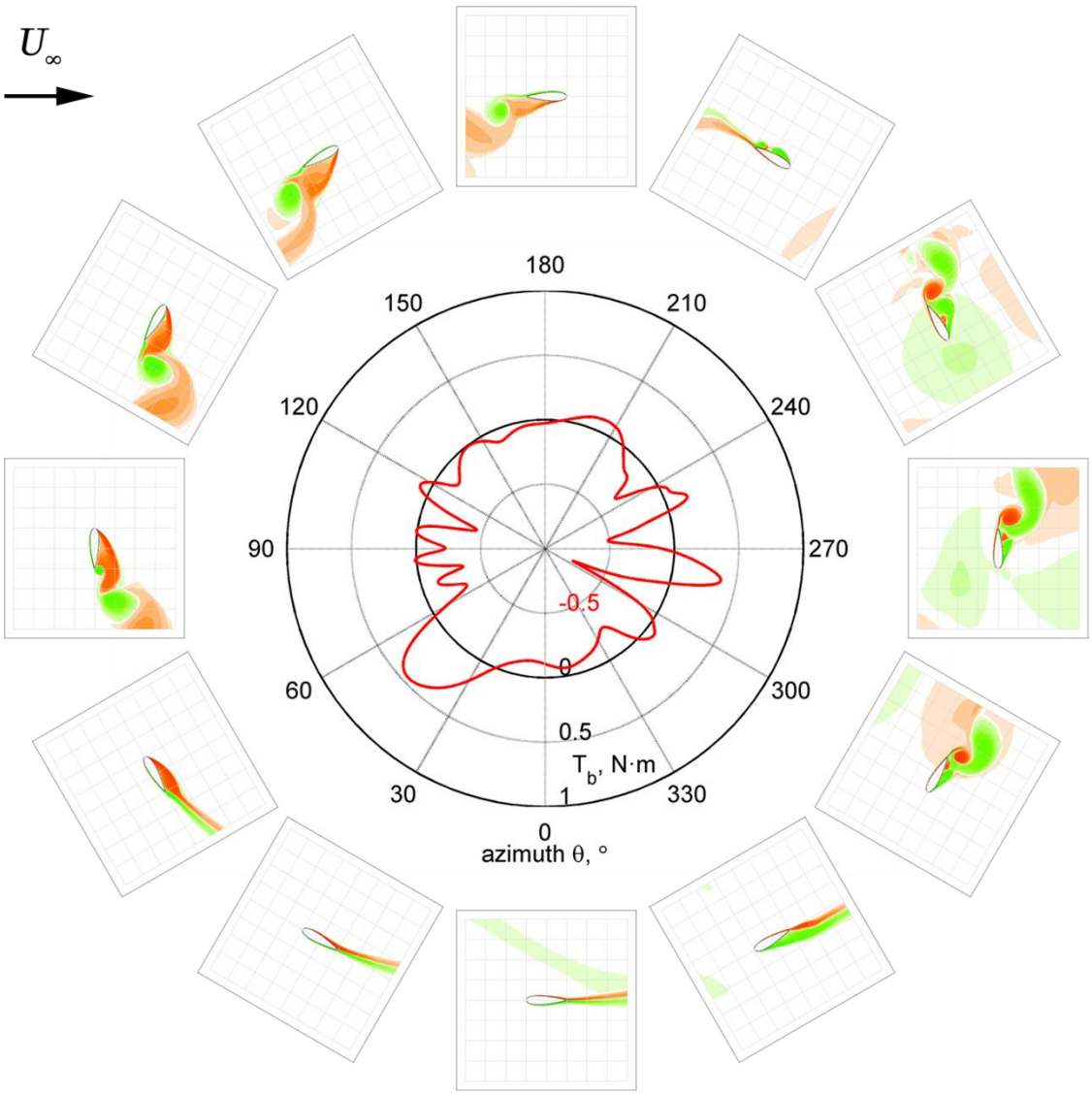

Figure 6.7. Plot showing blade torque and flow field variation with azimuth for steady wind case U_∞ = 7m/s at λ = 2.

Flowfield at λ = 4

In Figure 6.8, the variation of blade torque T_b through one rotation is plotted alongside flow visualisations. Clearly T_b is largely positive throughout, with notably high values from around θ = 60° up to just before θ = 120°. Blade stall within this azimuth range is relatively shallow and only becomes significant after θ = 120° where negative torque is generated until the end of the upwind at θ = 180°. The high values of T_b in the upwind are due to the unperturbed wind and α near

static stall that the blade sees. The generation of high torque in the upwind that reduces the downwind flow velocity results in a flat positive T_b generated from θ = 210° to θ = 300° with a prominent drop at θ = 270° due to the shaft wake.

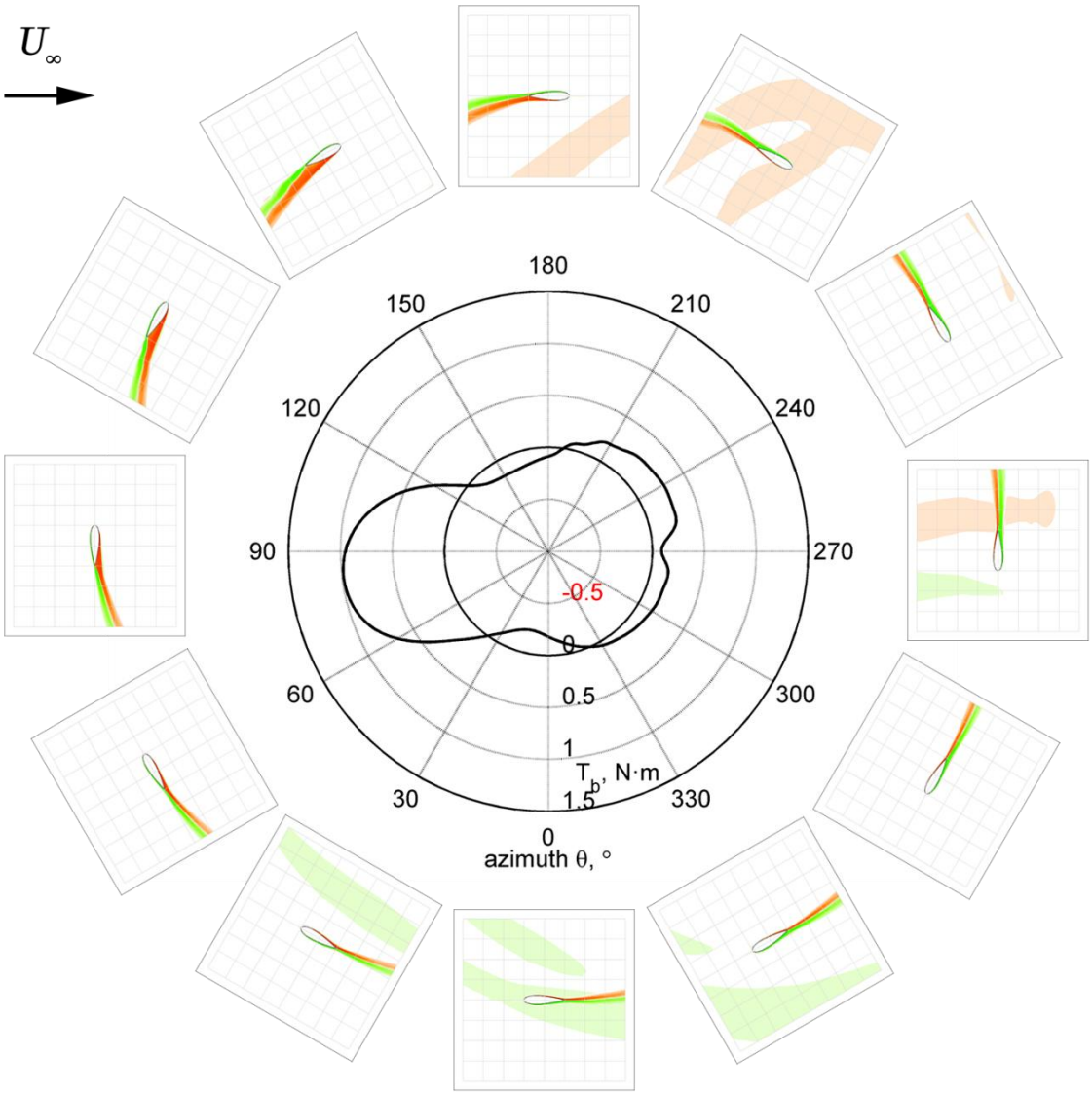

Figure 6.8. Plot showing blade torque and flow field variation with azimuth for steady wind case U_∞ = 7m/s at λ = 4.

6.2.3 Comparison to Literature

Only a handful of published works present a comparison of VAWT performance under different λ conditions. Of this short list, not all show both

force data and flow visualisations. Some of the early attempts to describe VAWT performance over different λ conditions have either force data or flow visualisations. Discussed in the following are studies that detail both the force and flow aspects of the problem.

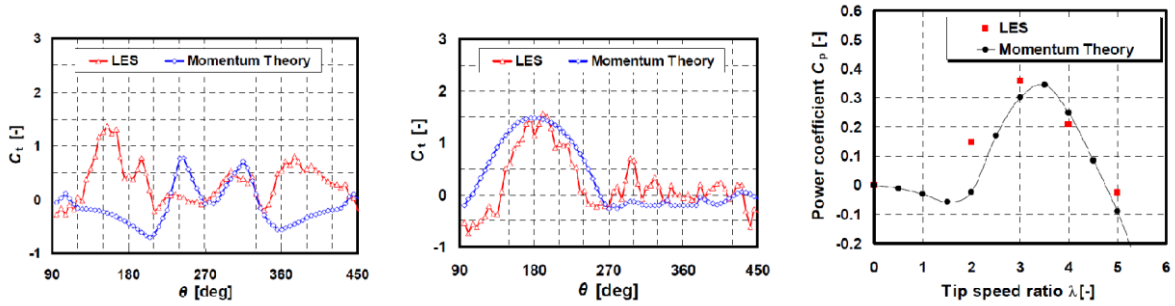

a. b. c.

Figure 6.9. Iida et al [32] study using LES and momentum theory: a) λ = 2, b) λ = 4, c) CP.

In 2007, Iida et al [32] presented results of LES simulations on a three–bladed Darrieus VAWT and showed that there was small divergence of flow and dynamic stall effects on a high λ case, whereas large influence was observed at low λ. Maximum tangential force coefficients were comparable between two extreme λ but the slightly more prolonged high values of torque in the high λ case increased the overall CP from about 0.15 to just above 0.2 (Figure 6.9). There was no mention of the scale of the VAWT tested but their momentum theory study shows a negative band of CP in the low λ range and the maximum CP between 0.3 and 0.4, which imply that their VAWT is of comparable scale to the one tested in this body of work. Variations in C_t between blades were seen in the LES results despite the steady wind conditions and symmetric rotor geometry. The random nature of turbulence, as better captured in LES, is the likely cause of the observed difference. The similarity of the Iida et al work to the present study is only seen on the values of λ being compared. Major differences are observed notably on the predicted CP at λ = 2, the position of the CP at λ = 4 relative to λ^*, and the λ^* itself. Of the flow field images presented by Iida et al, vorticity contours for one rotor position at various λ are presented. No detailed azimuth snapshots were shown and analysed.

Amet et al [44] carried out 2D numerical work in 2009 on a VAWT that Laneville and Vittecoq [45] experimentally tested back in 1986. Detailed analysis of the blade forces was reported for a high solidity 2–bladed VAWT of similar scale and Reynolds number conditions to the present study. Extreme cases of λ were considered: $\lambda = 2$ and $\lambda = 7$. It can be seen in Figure 6.10 that the maximum C_l generated by a blade at $\lambda = 2$ occurs in the upwind and is more than three times the maximum C_l generated at $\lambda = 7$. A crossover of the experimental lift curve is seen in the downwind for the low λ case that indicates increased lift despite the blades seeing decreasing α. This however is not captured by the numerical model. On the contrary, the Amet model shows lower lift values as α decreases from $\alpha = -30°$ down to $\alpha = -10°$. Maximum C_l in the downwind for the high λ case is about nine times smaller than the upwind maximum. In terms of the general shape of the lift curves, the present study is similar to Amet et al. The variation and proportion of the force coefficients between the two extreme λ are alike. Amet et al also show multiple flow field visualisations of streamlines and vorticity at azimuth positions covering an entire rotation. However, only the low λ is inspected where more interesting flow features are visible like deep stall and vortex shedding.

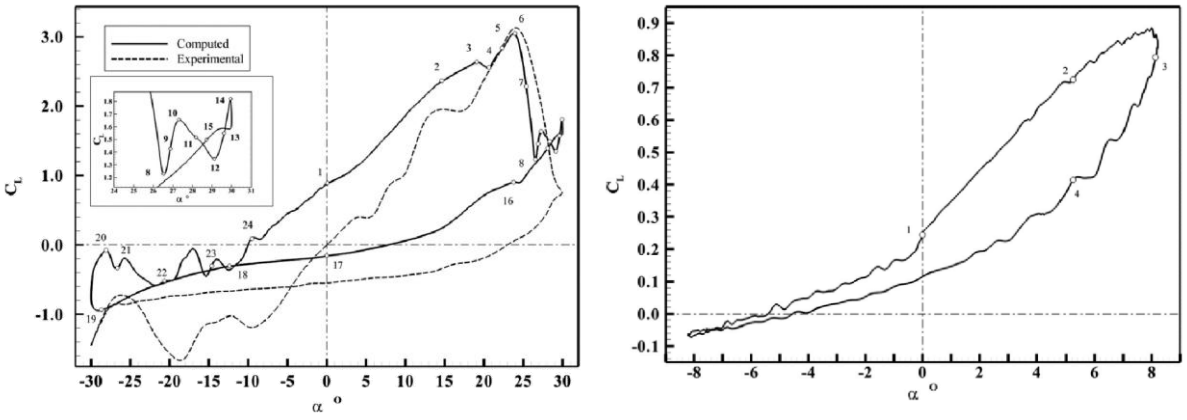

a. b.

Figure 6.10. Amet et al [44] URANS study showing large difference in C_l between two extreme λ cases: a) $\lambda = 2$, b) $\lambda = 7$.

In 2011, Raciti Castelli et al [7] proposed their CFD model as a performance prediction tool for the Darrieus VAWT. The analysis of VAWT performance is

carried out using corrected α derived from an averaging process of the locally measured α over one rotation instead of geometric α and the presentation of rotor loading in polar coordinates to match the actual azimuth position of the blades. A wide range of λ cases was analysed including points at the extremes of the CP curve. Two of these extreme cases are shown in Figure 6.11. The position of 0° azimuth is in the north while the free stream wind is coming from the west. The VAWT used in their study is a three–bladed rotor that has a solidity of 0.5 and a NACA0021 blade profile. An inspection of the C_t variation for both the low and high λ cases reveals a striking similarity to the results of the present study. Peak torque is attained at later azimuths with higher λ due to delayed stalling and lower perceived α. Maximum corrected α at λ = 1.44 is about 45° while it is roughly 20° at λ = 2.33. Peak C_t at λ = 1.44 is approximately 0.21 while peak C_t at λ = 2.33 is about 0.25. Peak C_t does not correspond to maximum α in both λ cases but occur at earlier azimuth positions. This agrees with the results of the present study. Although the analysis of blade forces is very thorough, there is a lack of visualisation that link the rotor performance to flow characteristics like flow separation and reattachment.

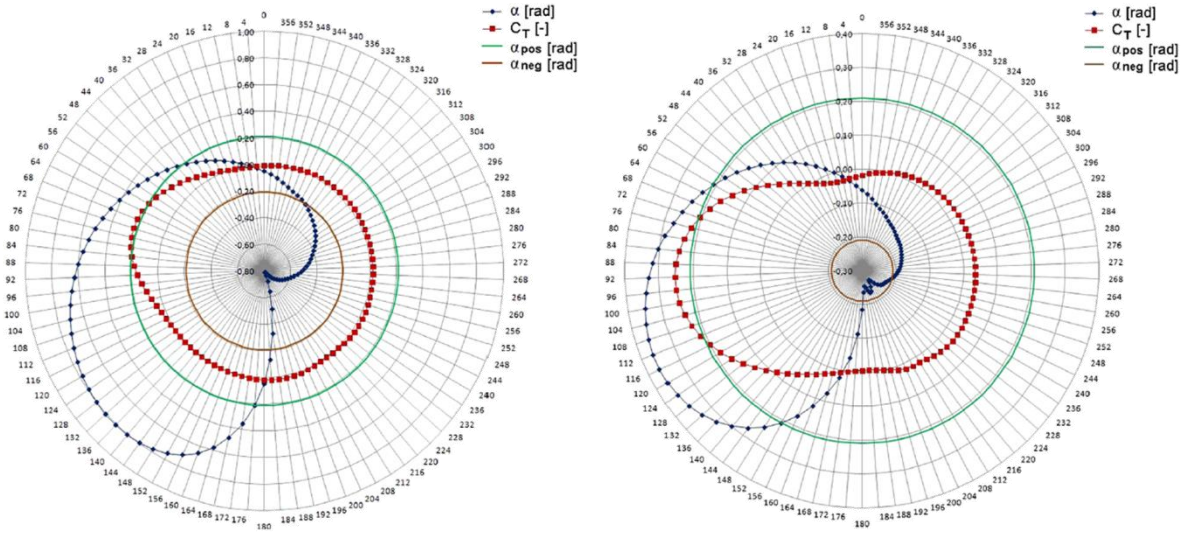

a. b.

Figure 6.11. Raciti Castelli et al [7] study using corrected α: a) λ = 1.44, b) λ = 2.33.

6.3 Unsteady Wind Performance

Numerical modelling of the unsteady wind inflow through the tunnel was carried out by specifying the velocity inlet magnitude as a time–dependent variable and running the simulation for approximately 1.5 wind cycles. This is necessary so as to attain not just periodic convergence in the simulations, but also to generate a contiguous set of converged data that covers the entire cycle of the wind fluctuation. It has been determined by the Author that in order to match the experimental wind cycle with a fluctuation frequency of 0.5Hz, the simulations had to be run for 40 full rotations of the VAWT. For each run, a total of about 5,400 processor hours was required to complete 40 rotations in the University of Sheffield's Intel–based Linux cluster using 16 cores of Intel Xeon X5650 2.66GHz processors.

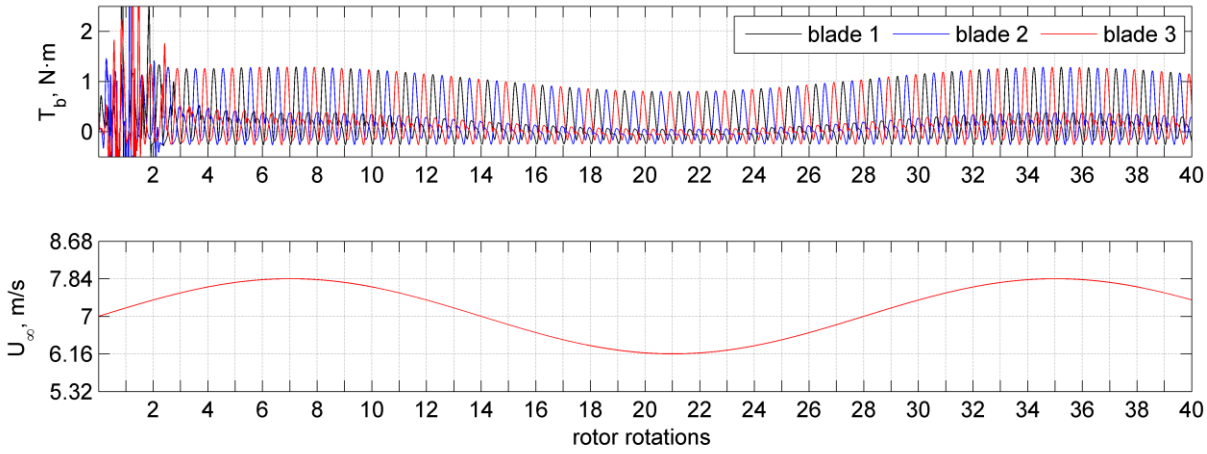

Figure 6.12. Plot of unsteady T_b and U_∞ over 40 VAWT rotations.

The numerical model used in the unsteady wind simulations is the optimised model developed for the steady wind case. Apart from the varying velocity inlet boundary condition, the only other difference of the unsteady wind model is the force monitor, where not only one blade is monitored but all three. A plot of T_b for all three blades is presented in Figure 6.12 alongside the fluctuating free stream. The unconverged T_b is clearly shown in the first three rotations. Full convergence per time step was achieved after 6 rotations when residuals of all conserved

variables fell below 1×10^{-6}. For the case shown where the VAWT rotational speed is ω = 88rad/s, one wind cycle is about 28 VAWT cycles.

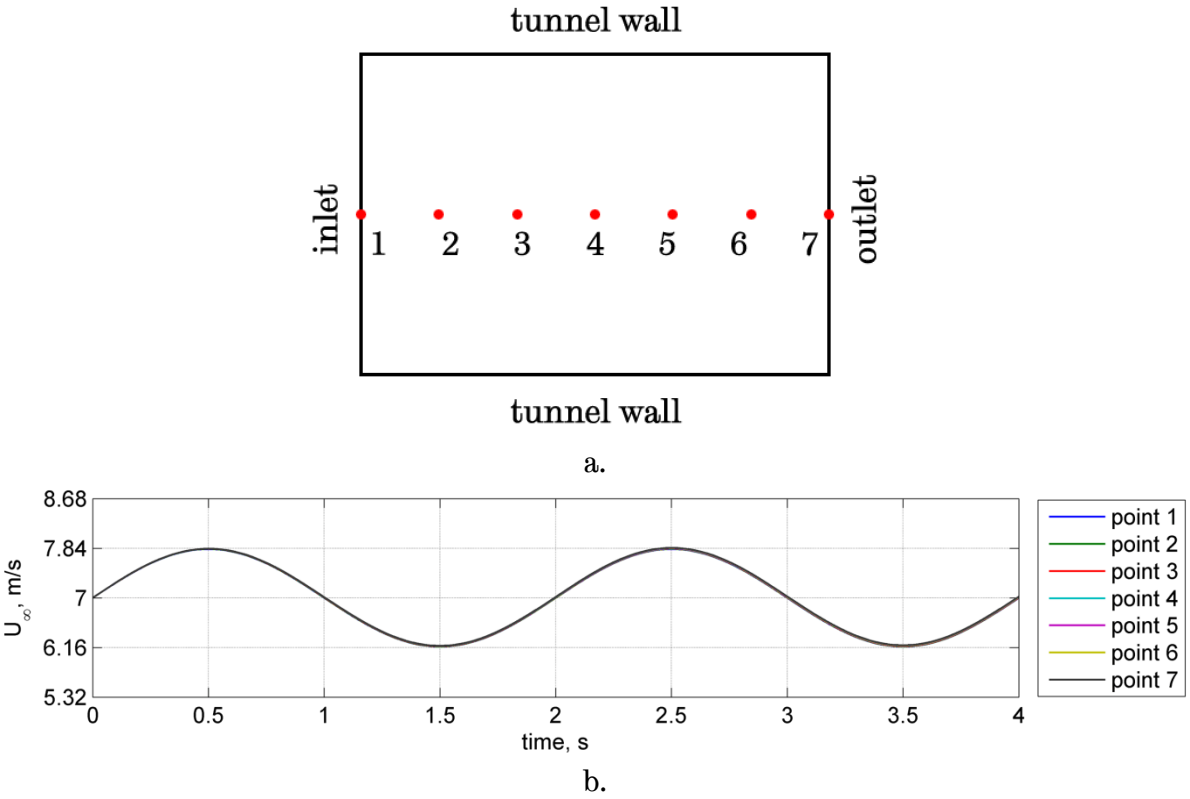

Figure 6.13. Study of U_∞ variation in an empty tunnel domain with fluctuating inlet condition: a) position of monitor points along tunnel length, b) results of simulation showing velocities fluctuating in sync along the domain length.

One major assumption in the computation of unsteady CP is the free stream velocity in the wind power term. Since the inlet velocity is the specified parameter in all simulations, one may assume that there is a delay in the fluctuating wind that the VAWT sees as a consequence of its position downstream. However, the model is constrained within the wind tunnel and conditions are well within the limits of incompressible flow regime. Additionally, an incompressible solver is used for all runs. As such, a change in the inlet velocity results in the entire domain changing in flow velocity. A test was conducted to verify this assumption by running a simulation with an empty wind tunnel domain under fluctuating velocity inlet condition. Seven monitor points were placed between the two wall boundaries along the length of the domain.

Results confirm that velocities downwind are in sync with the fluctuating inlet velocity and are shown in Figure 6.13.

6.3.1 Reference Case

A reference case is selected to act as the baseline model to which parametric variations are compared. The mean wind speed is U_{mean} = 7m/s with a fluctuating amplitude of U_{amp} = ±12% (±0.84m/s) and fluctuation frequency of f_c = 0.5Hz. The rotor angular speed is a constant ω = 88rad/s (840rpm) resulting in a mean tip speed ratio of λ_{mean} = 4.4. When inspected against the steady CP curve, this condition is just before peak performance at λ^* = 4.5. Although this λ_{mean} is greater than the highest experimental λ_{mean} of 4.1 (see Sec. 5.3.1), its position in the steady CP curve matches closely to the low λ_{mean} case of the experiments that was just below peak performance.

A total of 28 rotor rotations completes one wind cycle. As shown in Figure 6.14, the λ changes with the fluctuating U_∞. Increasing U_∞ causes the λ to fall owing to their inverse relationship and a constant ω. Maximum U_∞ is 7.84m/s and occurs at the end of the 7th rotation with λ dropping to its minimum of 3.93. The maximum α of each blade per rotation can be seen to increase with the increasing U_∞ reaching a peak value of α = 14.74° between the 6th and 8th rotation depending on the blade considered. Following the maximum U_∞ is the gradual drop of U_∞ back to the mean wind speed. It continues to fall until it reaches the minimum value of U_∞ = 6.16m/s at the end of the 21st rotation. At this U_∞, the λ rises to its maximum value at 5.0. Within this part of the wind cycle, the maximum α per rotation falls to 11.55° between the 20th and 22nd rotation depending on the blade in question. The subsequent increase of U_∞ back to the mean value causes the λ to drop in magnitude and the peak α per rotation to increase.

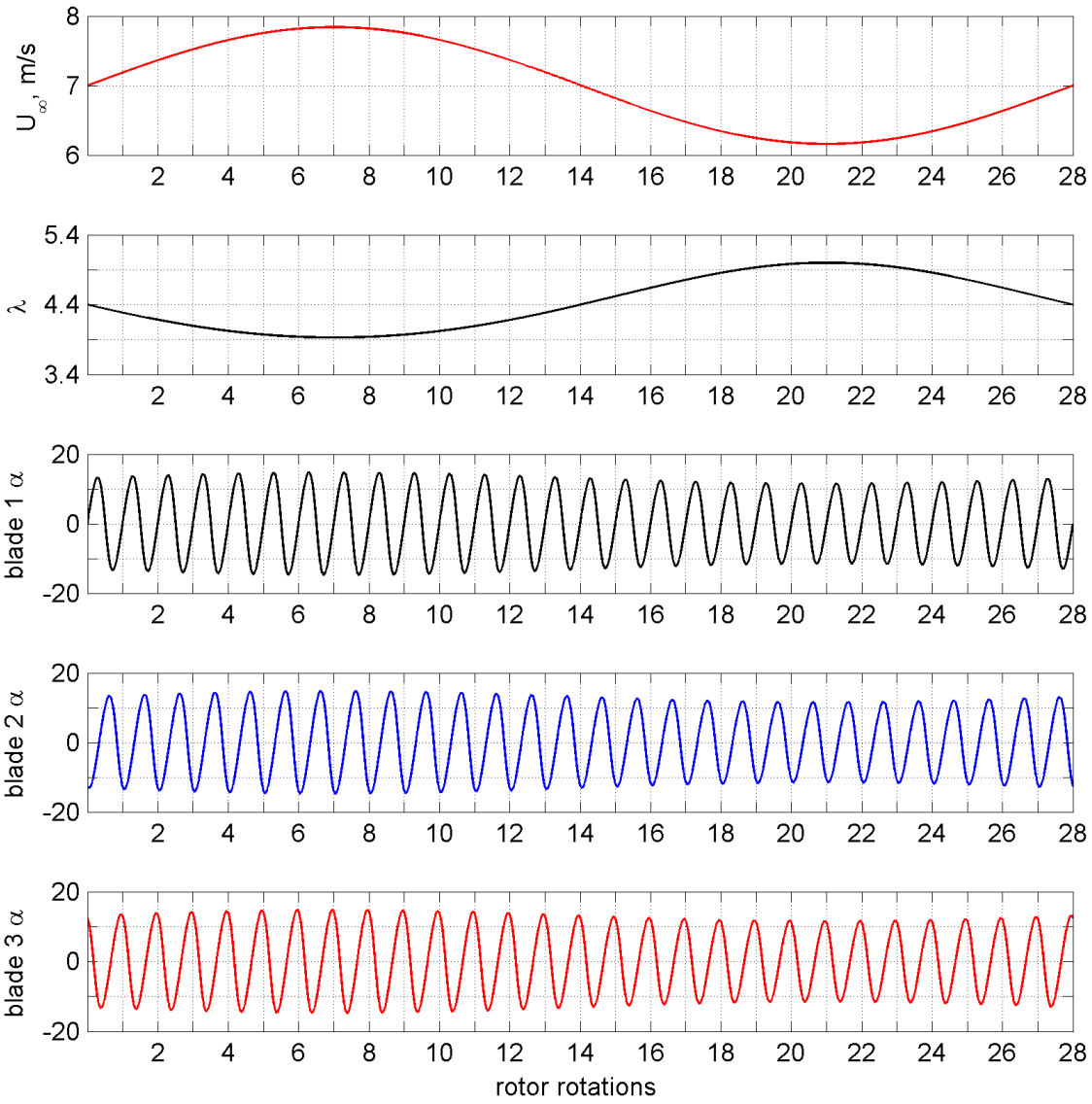

Figure 6.14. Variation of U_∞, λ, and α for the reference case.

The peak T_b of each rotor cycle increases together with increasing U_∞, all three blades showing similar trends and each with maximum T_b value of roughly 1.28N·m generated within the 8th rotation (Figure 6.15). The maximum combined blade torque T_B is 1.59N·m, also within the 8th rotation. In the second half of the wind cycle, the peak T_b of each rotor cycle drops to 0.79N·m within the 22nd rotation for each of the three blades while the lowest peak T_B registers at 0.76N·m within the same rotor cycle. It is observed that T_B is mostly positive, which suggests positive overall performance. Also, the huge fluctuations in the T_B with characteristic frequency equal to three times the rotor frequency would result in huge fluctuations in the rotor power P_B. The variation of P_B is shown in Figure

6.16 together with the fluctuating wind power P_w. As expected, the peaks of P_B follow the wind variation much like the T_B does. Maximum P_B is 140Watts generated as P_w maximizes at the end of the 7th rotation, with magnitude of 207W. Also presented are the unsteady CP and quasi–steady CP using moving average smoothing. Smoothing the unsteady CP provides a useful comparative plot to the experimental data presented in the Chapter 5, where the unsteadiness of the experimental CP over one rotor cycle is not captured. In addition, this is shown to be consistent with the cycle averaged method of computing for the rotor CP in steady wind conditions, that filters out the fluctuating nature of the blade torque to give a single value prediction of VAWT performance.

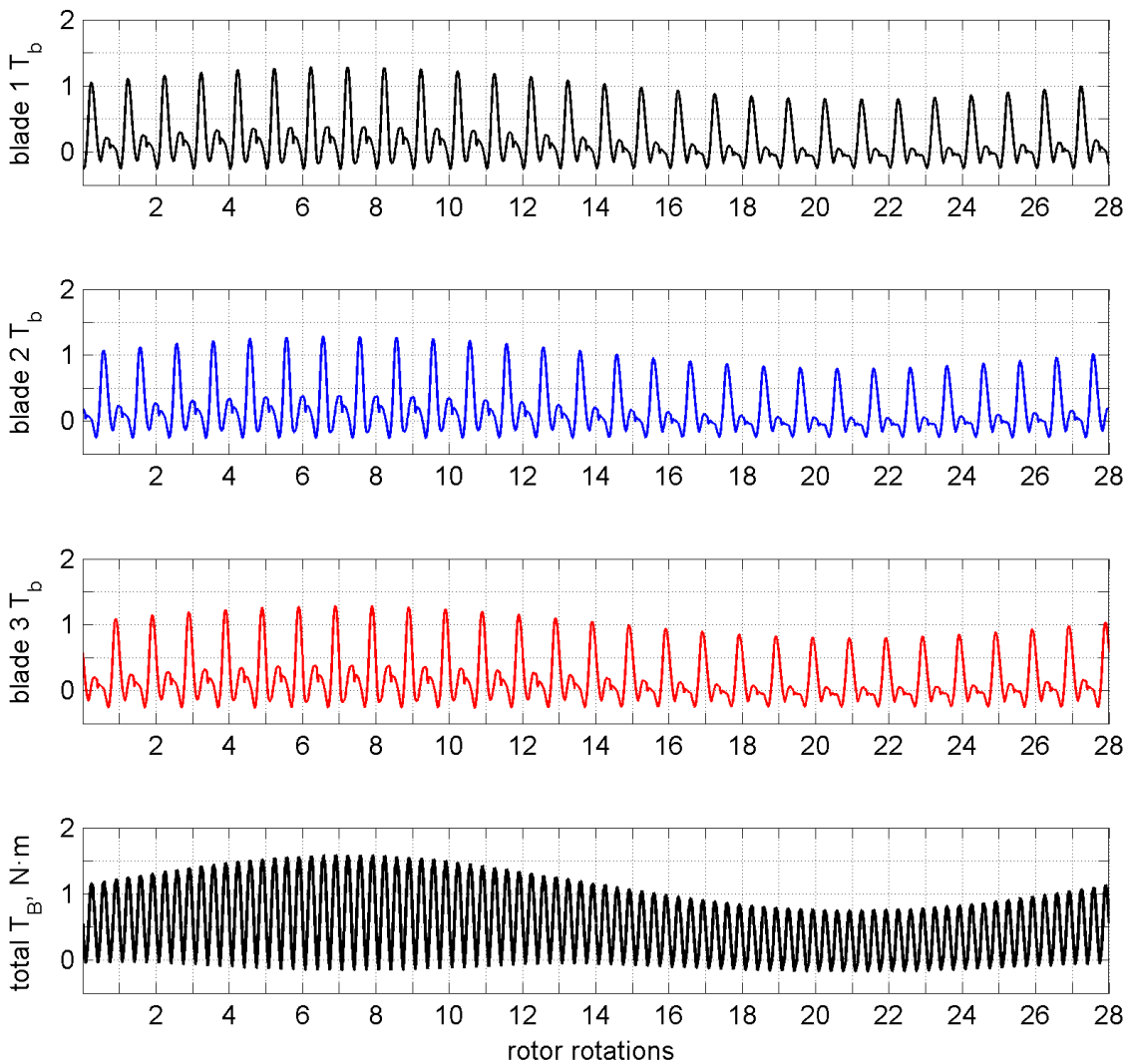

Figure 6.15. Variation of T_b and T_B for the reference case.

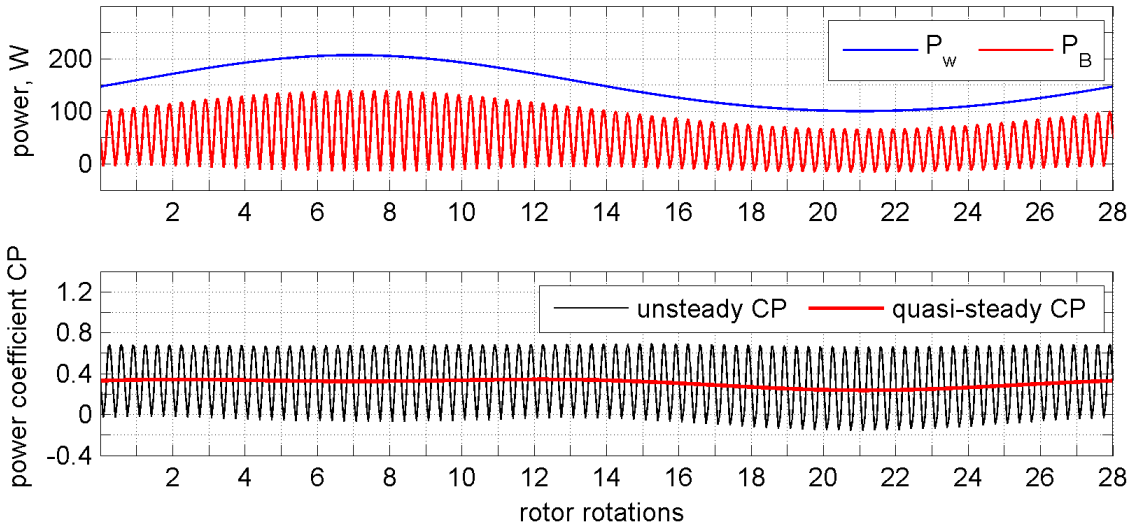

Figure 6.16. Variation of power and CP through one wind cycle.

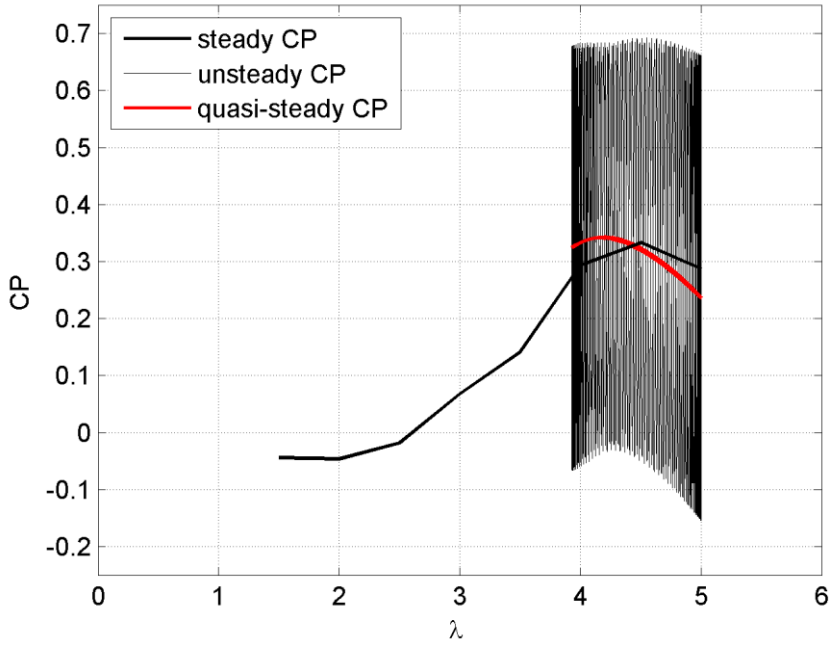

Figure 6.17. Performance of the VAWT in 12% fluctuating free stream.

In Figure 6.17, the plots of the unsteady CP and quasi–steady CP versus λ are shown relative to the steady wind performance at 7m/s. The fluctuations in the unsteady CP over the band of operating λ show a massively varying VAWT performance that greatly exceeds the limits of the steady wind CP. The maximum CP is recorded at 0.69 and occurs just after the 15th rotation (λ = 4.55). The minimum CP is seen to take place after the 21st rotation with a value of –0.15 (λ =

5). The wind cycle–averaged CP is computed to be 0.33 (λ_{mean} = 4.4) and is equal to the maximum steady wind CP of 0.33 at λ = 4.5. It is clear from the figure that the quasi–steady CP crosses the steady CP curve in a similar manner as presented in the experimental results in Sec. 5.3. Increasing wind speeds cause the CP to deviate from the steady CP curve and rise to higher levels as the λ falls to lower values. On the other hand, decreasing wind speeds cause the CP to drop below the steady CP curve as the λ rises. This behaviour is consistent to the Reynolds dependent nature of the quasi–steady CP discussed in Sec. 5.3. There is no discernible hysteresis in the quasi–steady CP curve.

Scheurich and Brown [60] observed similar results in the unsteady CP from their vortex transport model. At a low frequency of wind fluctuation f_c = 0.1Hz, a 5kW scale VAWT with a radius of R = 2m takes 14 full rotations to complete one wind cycle. The unsteady CP varies greatly in magnitude even for fluctuations in wind speed of only 10%. As shown in Figure 6.18a, the unsteady CP fluctuates within the limits of the steady wind CP variations. They theorize that the VAWT with swept blades essentially traces the steady CP performance curve when subjected to unsteady wind with low f_c's. A similar conclusion is derived by McIntosh et al [63] in their free vortex model. They do not present a highly fluctuating unsteady CP but a quasi–steady CP based on an assumption that the VAWT CP is a function solely of λ evaluated at the centre of the rotor. This assumption requires steady CP curves of different wind speeds as the basis for the lookup of unsteady wind CP thereby eliminating the aerodynamic fluctuations as seen by the blades. Their results show that at low f_c = 0.05Hz, the quasi–steady CP traces the steady CP curve at λ higher than λ^* (Figure 6.18). It can be deduced from the results of both studies that a fluctuating free stream is not detrimental to the VAWT performance. There is a chance of increased performance as predicted by McIntosh in conditions near peak steady CP while Scheurich asserts a VAWT unsteady CP can be traced using steady CP curves.

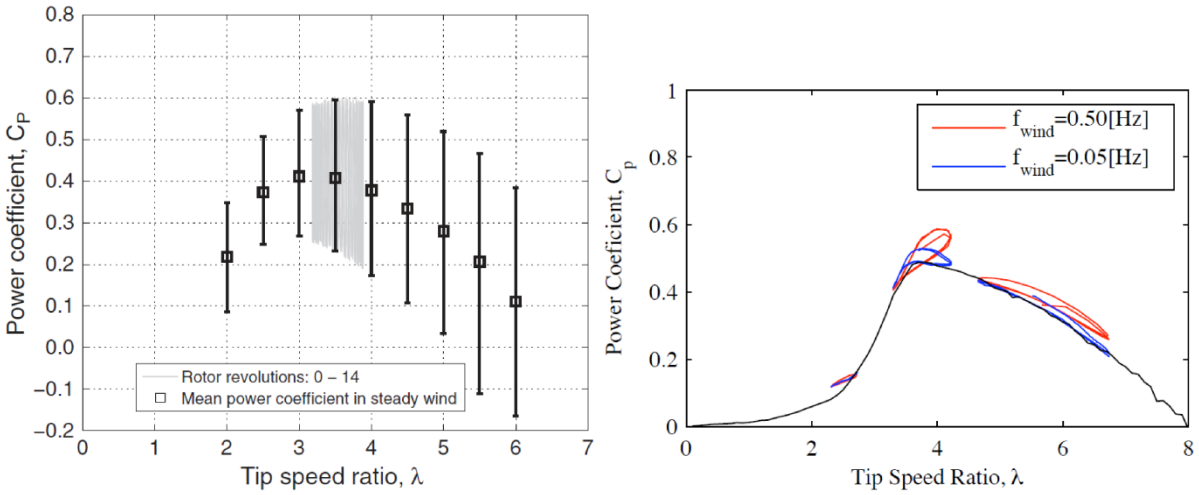

a. b.

Figure 6.18. Unsteady wind results of two numerical studies: a) Scheurich and Brown [60], b) McIntosh et al [63].

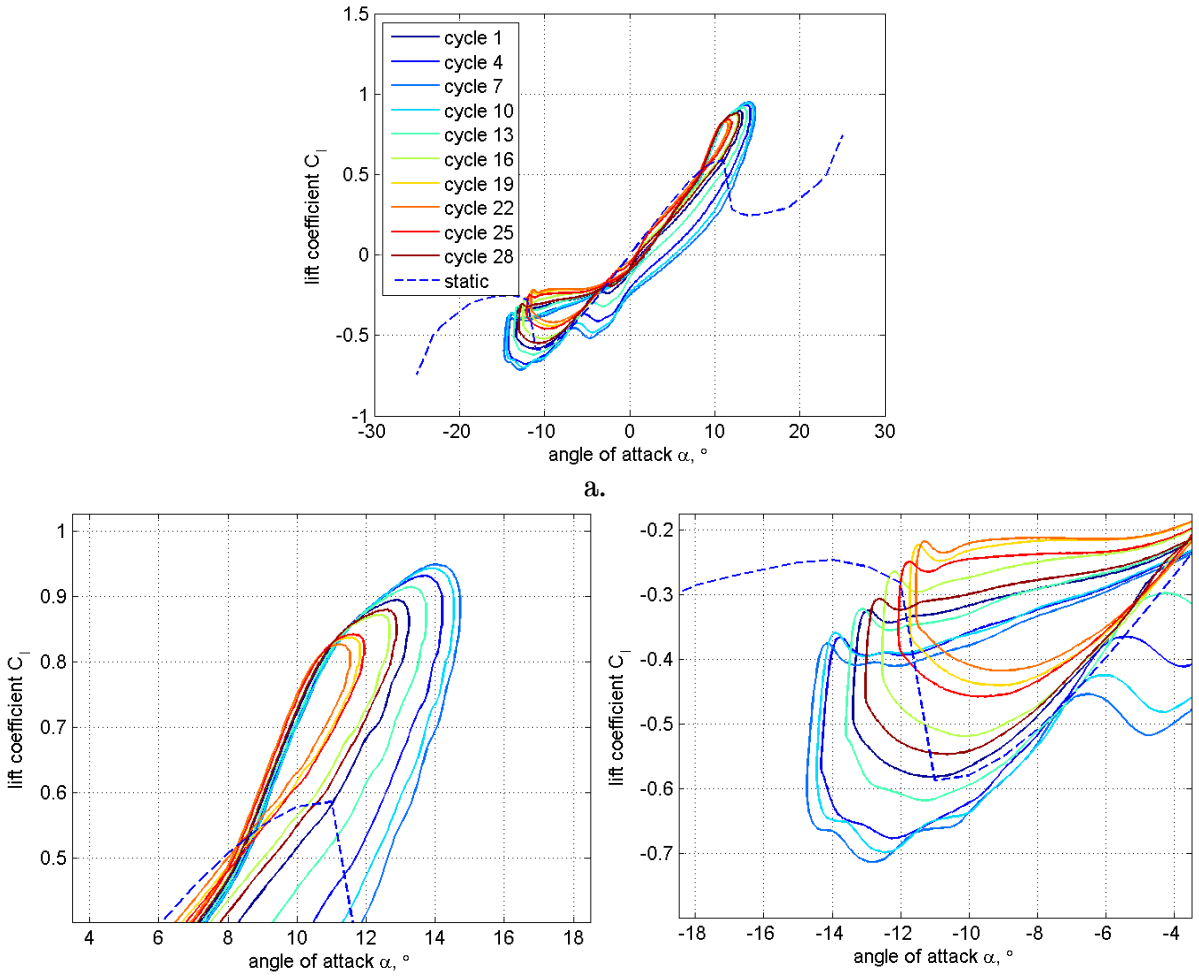

a.

b. c.

Figure 6.19. Lift coefficient plot for the reference case: a) full plot of cycles, b) zoom view of upwind loops, c) zoom view of downwind loops.

The lift coefficient loops for selected cycles are shown in Figure 6.19. It is evident that all cycles exceed the static stall lift in the upwind (Figure 6.19b) with maximum C_l = 0.94 generated during the 7th rotor cycle. At this point in the wind cycle, the wind speed is nearing its maximum value. Lowest peak of C_l loop is seen at the 22nd rotor cycle when the wind speed is close to its minimum. Downwind performance is not so similar. Maximum C_l of 0.71 is still generated in the 7th rotor cycle (Figure 6.19c). However, all rotor cycles within the second half of the wind cycle (cycles 15th to 28th) see their C_l not exceed the static stall lift.

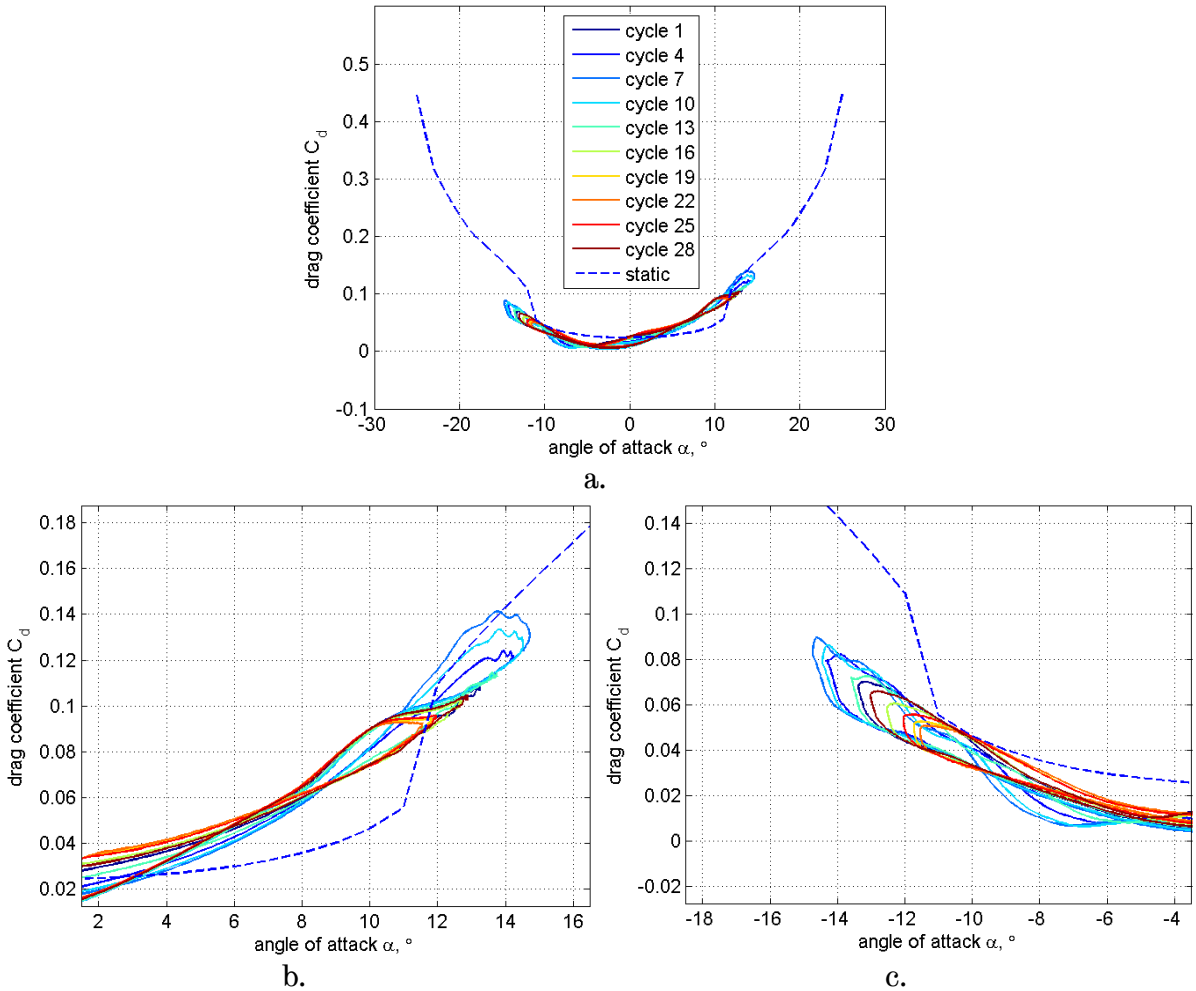

Figure 6.20. Drag coefficient plot for the reference case: a) full plot of cycles, b) zoom view of upwind loops, c) zoom view of downwind loops.

The drag coefficient loops for selected cycles are shown in Figure 6.20. It can be seen that all cycles exceed the static stall drag in the upwind (Figure 6.20b) with maximum C_d = 0.14 generated during the 7th rotor cycle. The trends of the C_d loops seem to follow the C_d line of the stalled condition for static aerofoil indicating that not only increases in lift are observed, but also in drag. Downwind drag does not follow the same trend. Maximum C_d of 0.09 is still generated in the 7th rotor cycle (Figure 6.20c). However, all rotor cycles have their C_d loops follow the C_d line of the un–stalled condition for a static aerofoil.

Although maximum C_l is at the 7th cycle, this is counteracted by the C_d, which is also at its maximum. Hence, the quasi–steady CP is not at its peak when U_∞ is at the highest value. In fact, maximum quasi–steady CP is seen to occur at the 3rd and 12th cycles, when maximum C_d is 15% lower than the 7th cycle maximum of 0.14 while maximum C_l is only 2% lower than the 7th cycle maximum of 0.94.

Flowfield visualisations of the reference case are shown in Figure 6.21. Only selected cycles and azimuth positions are shown for brevity, since a complete set of visualisations for an entire wind cycle will compose of 3,024 images from three blades that see completely different free stream conditions at a conservative 36 azimuth positions per rotor cycle. The first half of the wind cycle has been selected since most of the interesting flow features occur at λ lower than λ_{mean}, whereas higher λ would only show mostly attached flow with light or no separation at all. Presented are visualisations using vorticity at azimuth positions with the deepest stall for each blade in the upwind region of the rotor cycle shown.

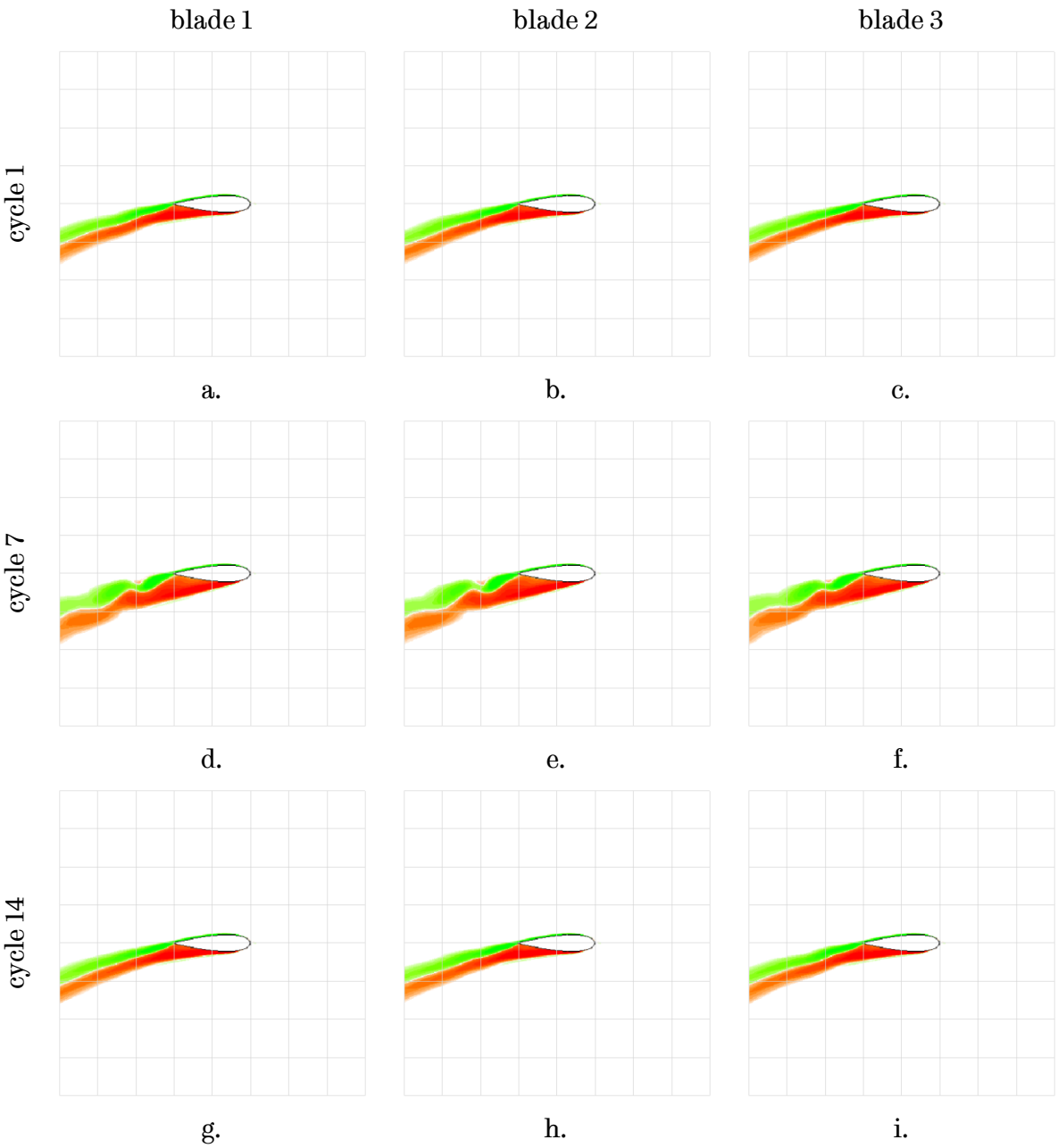

Figure 6.21. Flow visualisations of vorticity from selected rotor cycles in the first half of the wind cycle of the reference case: a to c – θ = 130°; d to f – θ = 140°; g to i – θ = 130°.

It is clear that as the wind speed increases, the stall on blade 1 becomes deeper and occurs at a later azimuth (Figure 6.21a & d) due to decreasing λ. Also, the separation point moves from mid–chord to the leading edge. As the wind speed falls back to U_{mean}, λ increases, the depth of stall reduces, deepest stall occurs at an earlier azimuth, and the separation point moves back to mid–chord position (Figure 6.21d & g). A similar observation is seen for blades 2 (Figure 6.21b, e & h) and 3 (Figure 6.21c, f & i). One thing to point out is there is no visible difference

between the three blades at the same θ. The reason behind this is the low frequency of the wind speed cycle compared to the rotor cycle causing a quasi–steady condition relative to the VAWT. As blades pass a specific θ within one rotation, the free stream wind speeds between blades differ by only 0.04m/s. Furthermore, the stalling mechanism at cycle 14, where the wind speed has dropped back to U_{mean} is very similar to the stalling in cycle 1. For the full +12% change in the wind speed, the azimuth of the deepest stall in the upwind region changes by only 10° from 130° in cycle 1 to 140° in cycle 7 and goes back again to 130° in cycle 14.

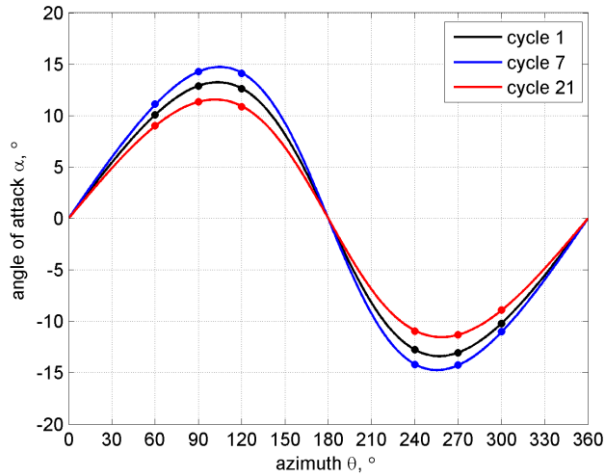

Figure 6.22. Variation of angle of attack for the three chosen rotor cycles.

A second set of rotor cycles has been chosen to illustrate the effects of extreme conditions within the wind cycle that a blade is subjected to and the resulting blade forces generated under such conditions. The variation of α for the three cycles, namely 1, 7, and 21, is shown in Figure 6.22 for reference. In this section of the analysis, attention is directed to only one blade, due to the quasi–steady condition previously seen between the three blades within one rotor cycle.

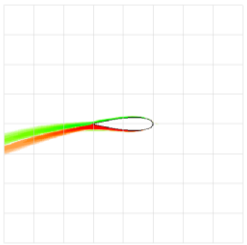

a. $\theta = 60°$

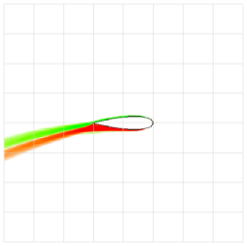

b. $\theta = 90°$

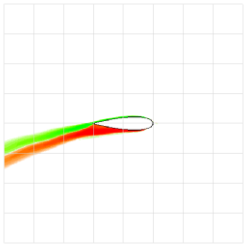

c. $\theta = 120°$

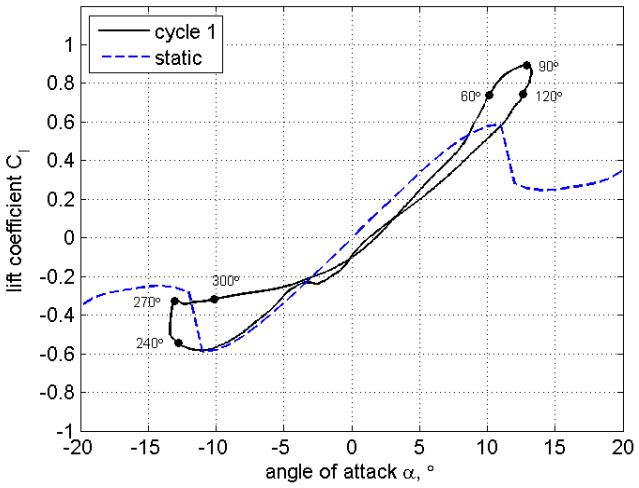

d. C_l vs. α

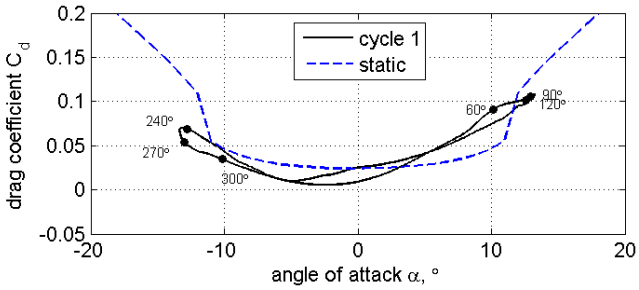

e. C_d vs. α

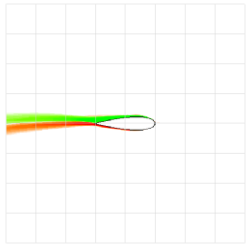

f. $\theta = 240°$

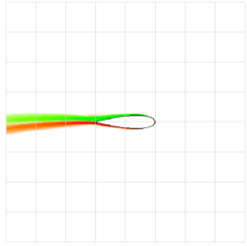

g. $\theta = 270°$

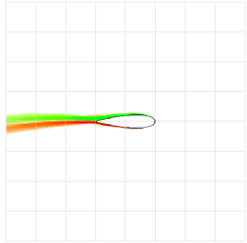

h. $\theta = 300°$

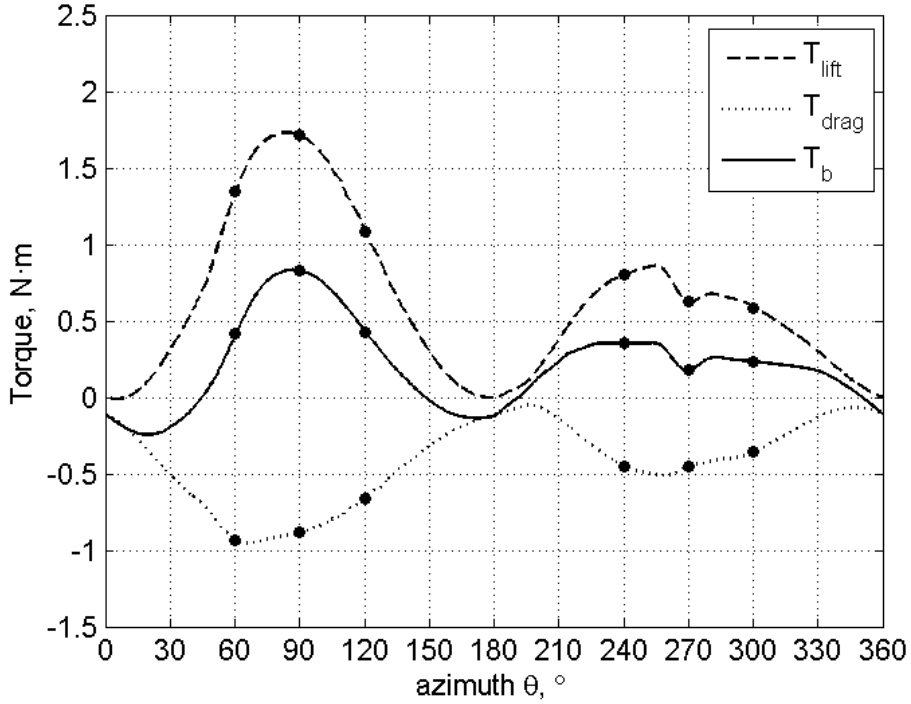

i. T_b vs. θ

Figure 6.23. Visualisations and blade forces generated within cycle 1 of the reference case.

The first condition analysed is cycle 1, where the conditions are close to the mean wind speed of U_{mean} = 7m/s. At this condition, the blade does not experience deep stall and no large vortices are shed at any point in the cycle. Partial separation is observed in the upwind region (Figure 6.23a–c) with the deepest stall occurring at θ = 130° (not shown). At θ = 0° corresponding to α = 0°, the computed C_l is negative at –0.1 (Figure 6.23d). At this azimuth, the blade velocity vector is parallel to the free stream wind vector hence α = 0°. However, the local streamlines within the blade vicinity are actually diverted due to the impedance of the VAWT, causing streamtube expansion and resulting in a local effective α that is negative. From θ = 0° up to θ = 60°, C_l (Figure 6.23d) is seen to steadily rise along with the increase in C_d (Figure 6.23e). C_l at θ = 60° is already greater than the static stall lift indicating dynamic stall has been initiated.

As shown in Figure 6.23a, there is no visible flow separation on the blade. With further rotation of the blade to θ = 90° C_l reaches maximum at 0.89 with the traling edge region starting to show separation creeping towards mid–chord (Figure 6.23b). The C_d slightly rises from 0.09 at θ = 60° to C_d = 0.11 at θ = 90° but its tangential component T_{drag} is lower (Figure 6.23i), because of a higher perceived α from 10.1° at θ = 60° to 12.9° at θ = 90°. As the blade passes θ = 120°, C_l has dropped to 0.75, while C_d is still high at 0.10. At this point in the rotation, the blade already shows mid–chord to trailing edge separation, which is the primary cause of the high drag. The low lift, the high drag and a slightly lower α of 12.6° versus the θ = 90° position (Figure 6.22) means that T_b at θ = 120° is predicted to be significantly lower at 0.43N·m, 48% lower than the T_b at θ = 90° which is calculated to be 0.83N·m. T_b crosses the zero line into the negative region at θ = 147°. A hysteresis loop is seen in the C_l due to the more rapid 'pitch down' motion of the blade in the second quadrant.

The entire downwind region showed attached flow, with C_l values below static stall prediction. Although the computed α at θ = 240° is –12.8°, the T_b is seen to be 0.36N·m. This is lower than the predicted T_b at θ = 120° mainly because the flow

velocity has already dropped in the upwind region resulting in a higher relative flow velocity, a likely lower effective α than the geometric –12.8°, the drag being more aligned to the tangential direction than lift, and hence lower T_b. C_l reduces from 0.54 at θ = 240° to 0.33 at θ = 270° clearly due to the centre shaft wake that reduces the flow velocity in this portion of the blade path. A more pronounced hysteresis loop of the C_l is observed in the downwind most likely due to combined effects of the skewed sinusoid variation of α and the reduced, assymmetric flow velocity. C_l at θ = 300° is 0.32, C_d is 0.03, while T_b is 0.23N·m and gradually get smaller until it drops to the negative region as the blade passes θ = 350°.

The second condition analysed is the first extreme condition that the VAWT sees at the 7th rotor cycle where U_∞ approaches its maximum value of 7.84m/s. At this point in the wind cycle, the λ is pushed from 4.4 down to 3.93. With the reduction in λ come increased α (maximum value at 14.73° versus 13.24° for cycle 1, Figure 6.22) and subsequently higher C_l and C_d. From a value of 0.89 in cycle 1, C_l rises to 0.95 at the same azimuth position of θ = 90° (Figure 6.24d). A significant drop in C_l to 0.71 is observed at θ = 120° creating a much larger hysteresis in the C_l loop. In fact, C_l forms a hysteresis loop throughout the entire cycle. Much higher perceived α means a steeper and faster 'pitch down' motion in the second quadrant inducing stalled flow that is worse than what is seen in cycle 1. Stall is developed on the blade surface as shown in Figure 6.24c that is much deeper when compared to the same azimuth in cycle 1 (Figure 6.23c). Deepest stall is at a later azimuth of θ = 140° (not shown) accompanied by a rippled and much thicker wake. Maximum torque due to lift (T_{lift}) in the upwind jumps to 2.07N·m for cycle 7 from 1.73N·m for cycle 1. However, the drag contribution to torque (T_{drag}) barely changes from a maximum of –0.95N·m for cycle 1 to –1.04N·m for cycle 7. This explains the difference in maximum T_b in the upwind between the two cycles where T_b = 0.83N·m for cycle 1 and T_b = 1.04N·m for cycle 7.

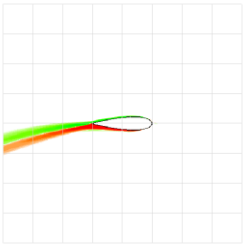

a. $\theta = 60°$

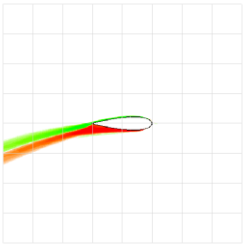

b. $\theta = 90°$

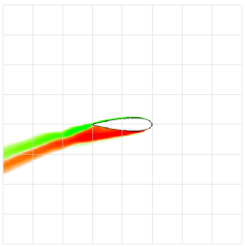

c. $\theta = 120°$

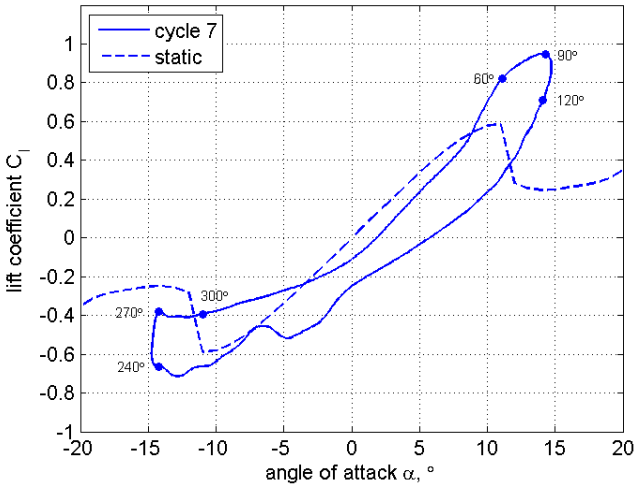

d. C_l vs. α

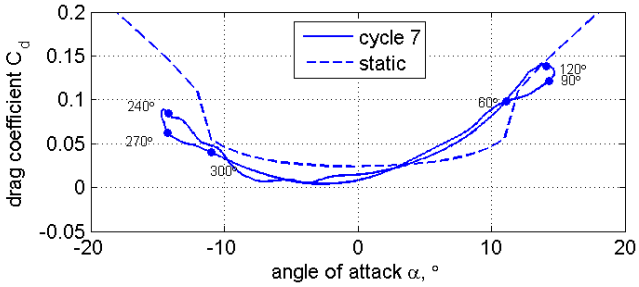

e. C_d vs. α

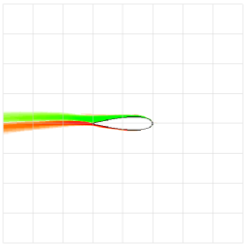

f. $\theta = 240°$

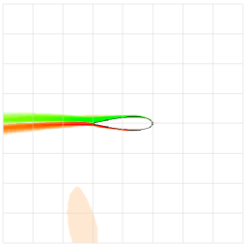

g. $\theta = 270°$

h. $\theta = 300°$

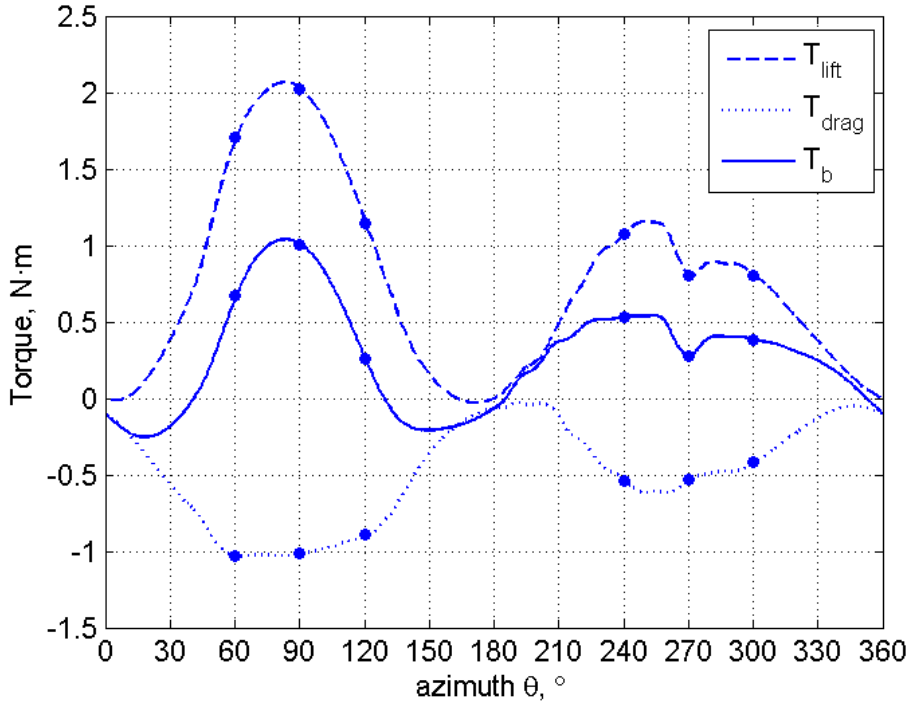

i. T_b vs. θ

Figure 6.24. Visualisations and blade forces generated within cycle 7 of the reference case.

Downwind performance follows the same trend with higher T_b observed in cycle 7 dictated mostly by the higher C_l and comparable C_d generated by the blade. C_l at θ = 240° rises from 0.54 in cycle 1 to 0.66 in cycle 7, while C_d barely changes from 0.07 in cycle 1 to 0.08 in cycle 7 resulting in higher T_b for cycle 7. No visible flow separation is seen except for θ = 200° (not shown) when the blade interacts with a high vorticity wake of a previous blade pass inducing a mid–chord to trailing edge partial stall.

The third condition analysed is the other extreme condition that the VAWT is subjected to within the wind cycle. At the 21st rotor cycle, U_∞ has dropped to its minimum value of 6.16m/s, thereby increasing the λ to its highest value of 5. As a result, the α as seen by the blades reduces with a maximum value just slightly exceeding static stall angle at 11.56° (Figure 6.22). Maximum C_l recorded still exceeds static stall value of 0.83 at θ = 90° (Figure 6.25d) but is 7% lower than the maximum C_l of cycle 1 and 13% lower than the maximum at cycle 7. This is expected because limiting the α perceived by the blades also limits the maximum lift that the blades generate. A milder 'pitch down' motion minimises the hysteresis of the C_l loop and suppresses the enlargement of trailing edge separation in the upwind (Figure 6.25a–c), essentially throughout the entire rotor cycle. A mild separation of flow is observed from θ = 120° to θ = 140° (not shown) with the separation point only a quarter chord from the trailing edge at worst.

Downwind C_l values do not reach static stall lift with the maximum value only at 0.42 (Figure 6.25d), 22% reduction in the maximum downwind C_l of cycle 1. T_{lift} at θ = 240° is 0.49N·m while T_{drag} is –0.34N·m resulting in a low T_b of 0.15N·m, less than half of the T_b in cycle 1 at the same azimuth and less than a third that of cycle 7 at the same azimuth. The fourth quadrant performance is very poor with maximum T_b registering at only 0.08N·m.

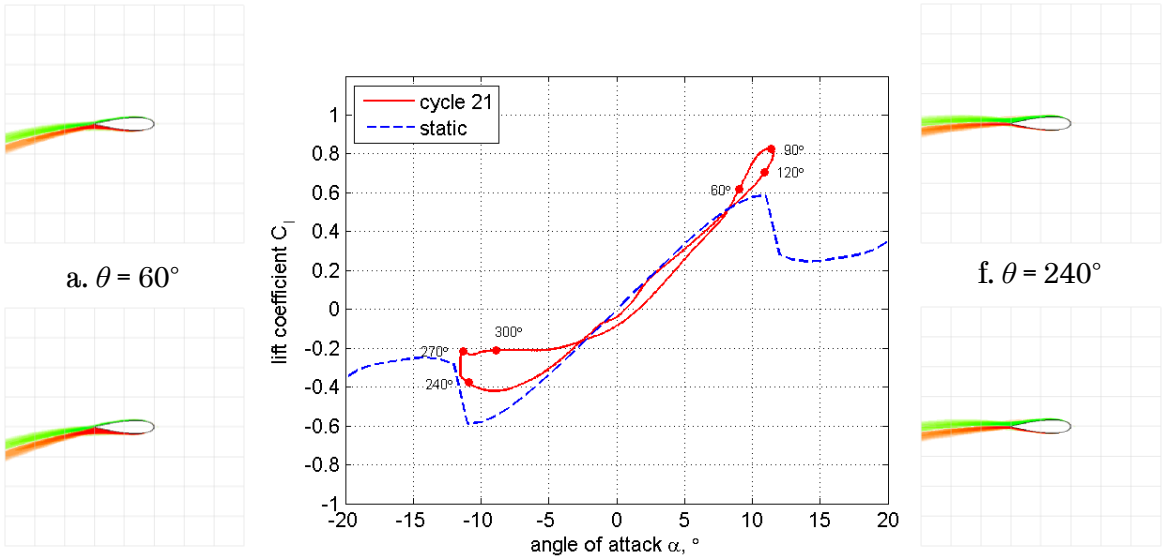

a. $\theta = 60°$

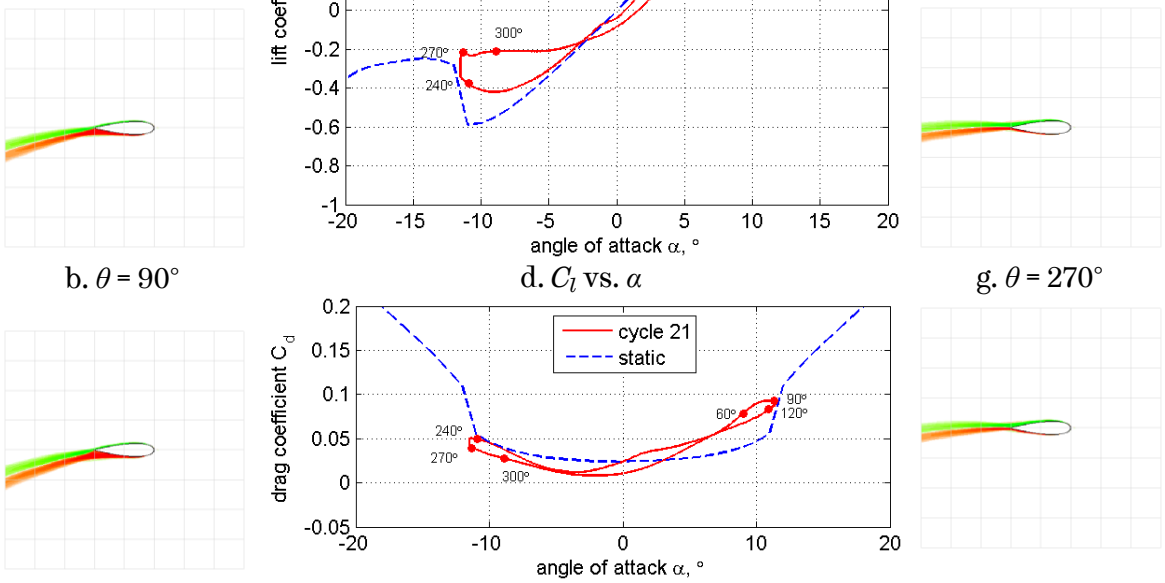

b. $\theta = 90°$

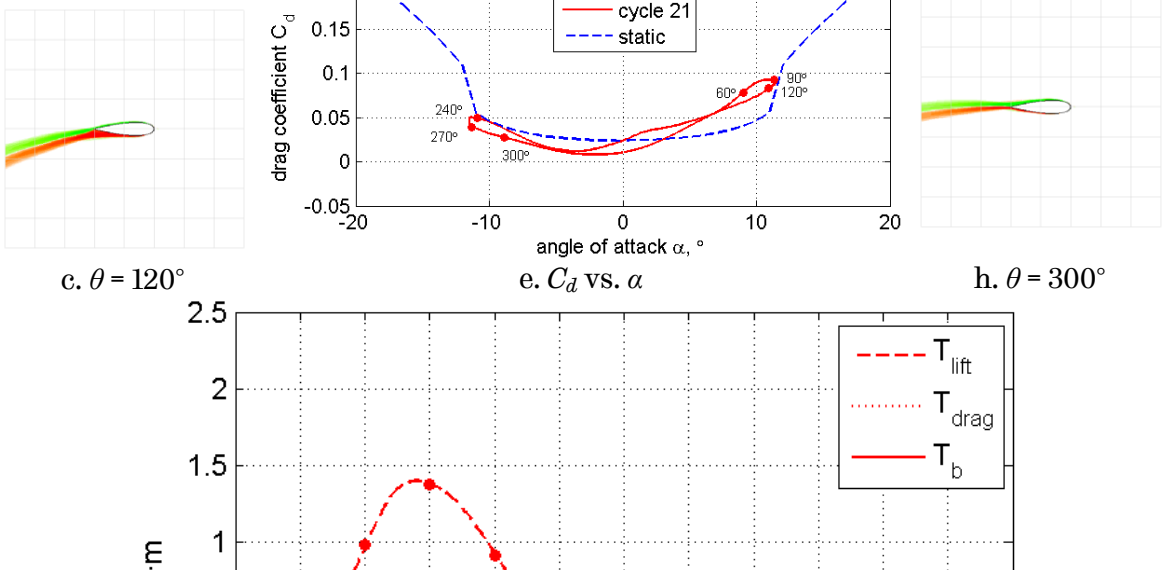

c. $\theta = 120°$

d. C_l vs. α

e. C_d vs. α

f. $\theta = 240°$

g. $\theta = 270°$

h. $\theta = 300°$

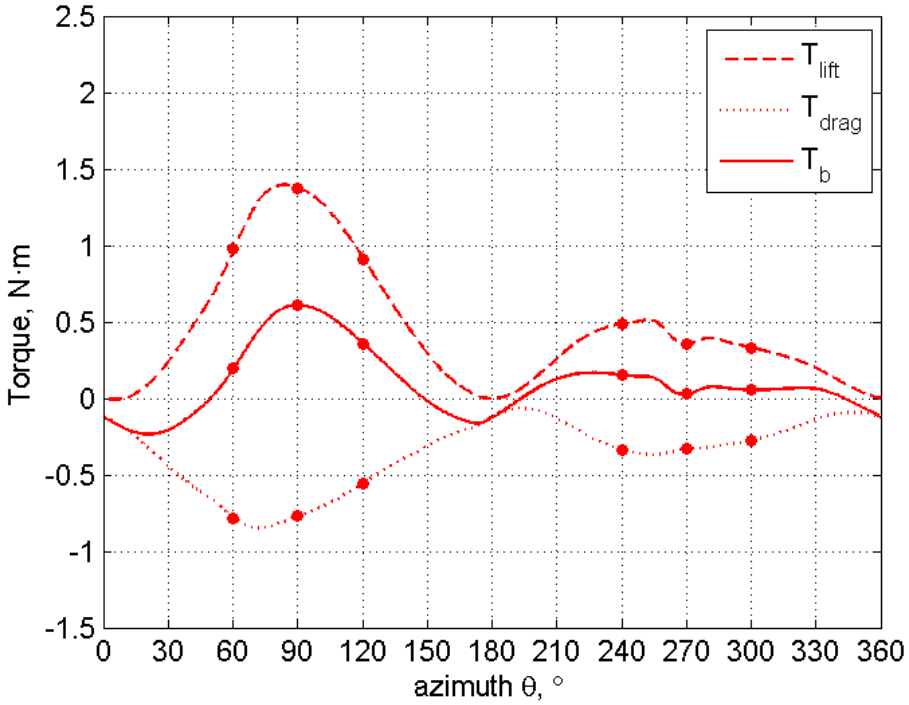

i. T_b vs. θ

Figure 6.25. Visualisations and blade forces generated within cycle 21 of the reference case.

6.3.2 Effect of Varying the Mean λ

The reference case ω was a constant 840rpm giving a λ_{mean} = 4.4. To investigate the effects of different λ_{mean}, two simulations were run at ω = 78rad/s (745rpm) and ω = 95rad/s (907rpm) resulting in λ_{mean} = 3.9 and λ_{mean} = 4.75, respectively. The variation of λ in time for the three λ_{mean} cases is shown in Figure 6.26a. Looking at the reference case of λ_{mean} = 4.4, the maximum λ is recorded at 5.0, while the minimum is at 3.93. The peak–to–peak value is for this case is 1.07. The case with the highest λ_{mean} at 4.75 shows the maximum λ has moved up to 5.4, while the minimum is now at 4.24 resulting in a peak–to–peak value of 1.16. The opposite behaviour is observed when λ_{mean} is lower at 3.9. The maximum λ is seen to be 4.43 while the minimum is 3.48, giving a peak–to–peak value of 0.95. With the same fluctuation amplitude of U_{amp} = ±12%, the peak–to–peak value increases as the λ_{mean} increases; an expected consequence of the direct relationship of ω and λ. The trends of the CP curves do not follow the simple and straightforward trend of λ. It can be seen in Figure 6.26b that the behaviour of CP as U fluctuates depends on the λ at the start of the cycle. The reference case, which starts at λ = 4.4, is closest to the steady CP maximum λ^* of 4.5. As a result, the starting CP = 0.33 is highest of the three cases. The λ_{mean} = 4.75 case comes next with a starting CP of 0.31 and the λ_{mean} = 3.9 case is last with a starting CP of 0.27. Both λ_{mean} = 4.4 and 4.75 cases see their CP rise as the wind speed increases while the λ_{mean} = 3.9 case CP falls with increasing wind speed. The position of the starting λ of the λ_{mean} = 3.9 case is way lower than λ^* and is within the drop–off part of the steady CP curve. Low λ's mean higher α and greater occurrence of stalled flow that lead to poorer performance. Maximum CP for the λ_{mean} = 4.75 case is 0.37 and coincides with the point of maximum wind speed and minimum λ. The other two cases do not have their maximum CP at the extreme values of U_∞ but rather between the U_{mean} and a U_∞ extremum. Minimum CP for the λ_{mean} = 3.9 case is 0.2 and occurs at the point of maximum wind speed and minimum λ while the other two cases have their minimum CP at the point of minimum wind speed and maximum λ.

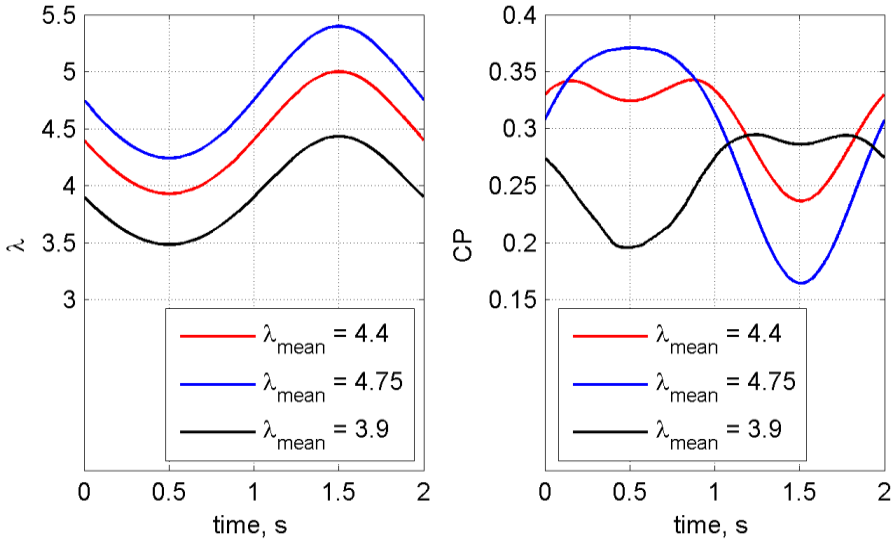

a. b.

Figure 6.26. Quasi–steady performance of the VAWT for the different λ_{mean} cases: a) λ vs. time, b) CP vs. time.

λ_{mean}	3.9	4.4	4.75
cycle–averaged CP	0.24	0.33	0.35

Table 6.1. Wind cycle–averaged CP at different λ_{mean}.

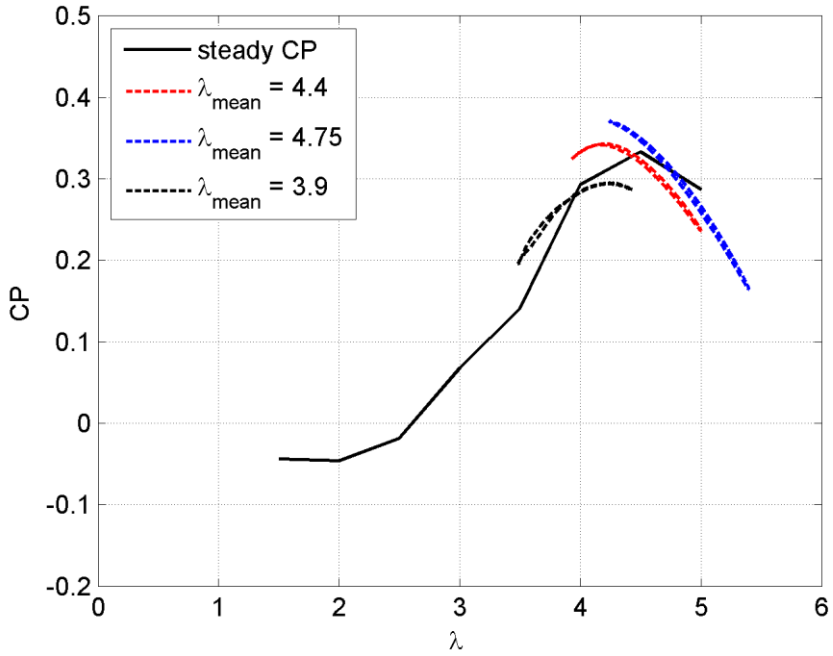

Figure 6.27. Study on the effect of varying λ_{mean}.

As can be seen from Figure 6.27, all quasi–steady CP curves cross the steady CP curve as the wind fluctuates. For the λ_{mean} = 4.75 case, maximum CP is 0.37 at λ = 4.24 while minimum CP is 0.16 at λ = 5.4. These two points are essentially the points of maximum and minimum wind speeds in the wind cycle. At this λ_{mean}, an increase in wind speed induces an improvement in the performance of the VAWT while falling wind speeds cause the VAWT performance to drop. The cycle–averaged CP, defined as the ratio of the mean blade power P_B to the mean wind power P_w over one wind cycle, is 0.35 which is higher than the maximum steady wind CP of 0.33 at λ = 4.5 and also higher than the cycle–averaged CP of the reference case equal to 0.33. The case when λ_{mean} = 3.9 shows a contrasting behaviour. As the wind speed increases, the quasi–steady CP falls together with the decreasing λ. At the minimum λ = 3.48, the CP is at its lowest with a value of 0.2. Maximum CP is attained in the second half of the wind cycle with a value of 0.29 at λ = 4.24. At maximum λ = 4.43 when the wind speed is at its lowest, the computed CP is 0.28. The cycle–averaged CP for this case is 0.24. An interesting result of all three cases is the λ^* of maximum CP. All cases have their maximum CP close to λ^* = 4.2.

Figure 6.28 shows the stalling of one blade at different rotor cycles within the first quarter of the wind cycle as U_∞ rises from 7m/s to 7.84m/s. All images shown are for one azimuth position, θ = 130°. A most obvious observation of the images is the very deep stall on the blade for the λ_{mean} = 3.9 case (Figure 6.28a, d & g). There are also large vortex structures shed from the blade leaving a very thick trailing wake. T_b values at this θ are negative and lower than –0.2N·m (Figure 6.29a). The reference case of λ_{mean} = 4.4 shows significantly shallower stall than the λ_{mean} = 3.9 case, with no shed vortices, stall induced by trailing edge separation and a much thinner wake (Figure 6.28b, e & h). All T_b values are positive, though the T_b for cycle 7 is very low at 0.05N·m (Figure 6.29b). The third case, where λ_{mean} = 4.75 shows the shallowest stall of the three with all cycles experiencing trailing edge separation extending only up to the mid chord (Figure 6.28c, f & i). The wake produced is also thin, with negligible ripple in the tail. All T_b values are positive

and greater than 0.4N·m (Figure 6.29c). Negative T_b generated by the blades is not due to deep stall inducing high drag, but rather the limited α that the blades see affecting the lift generated.

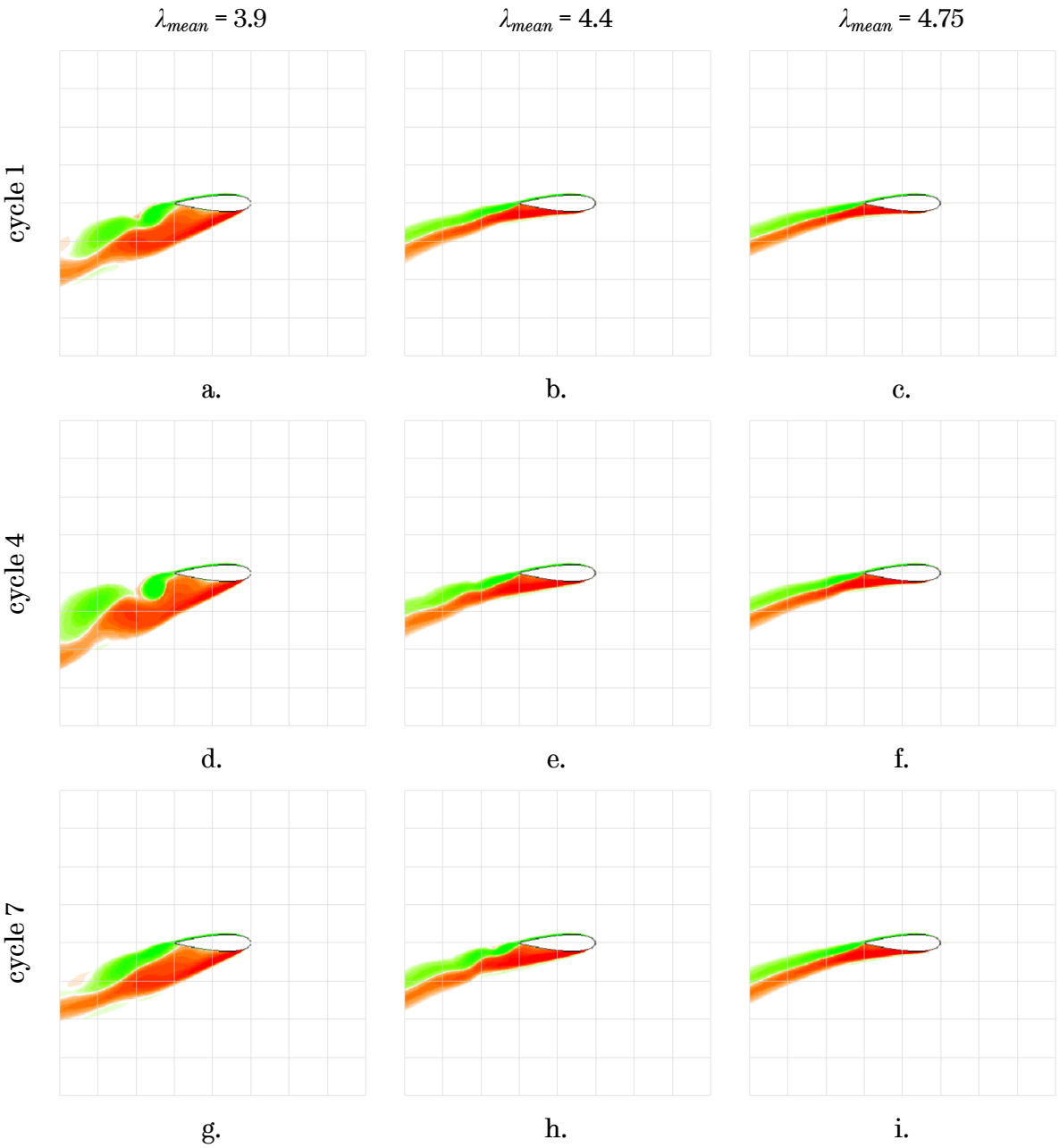

Figure 6.28. Flow visualisations of vorticity from selected rotor cycles in the first quarter of the wind cycle showing effects of varying λ_{mean} at θ = 130°.

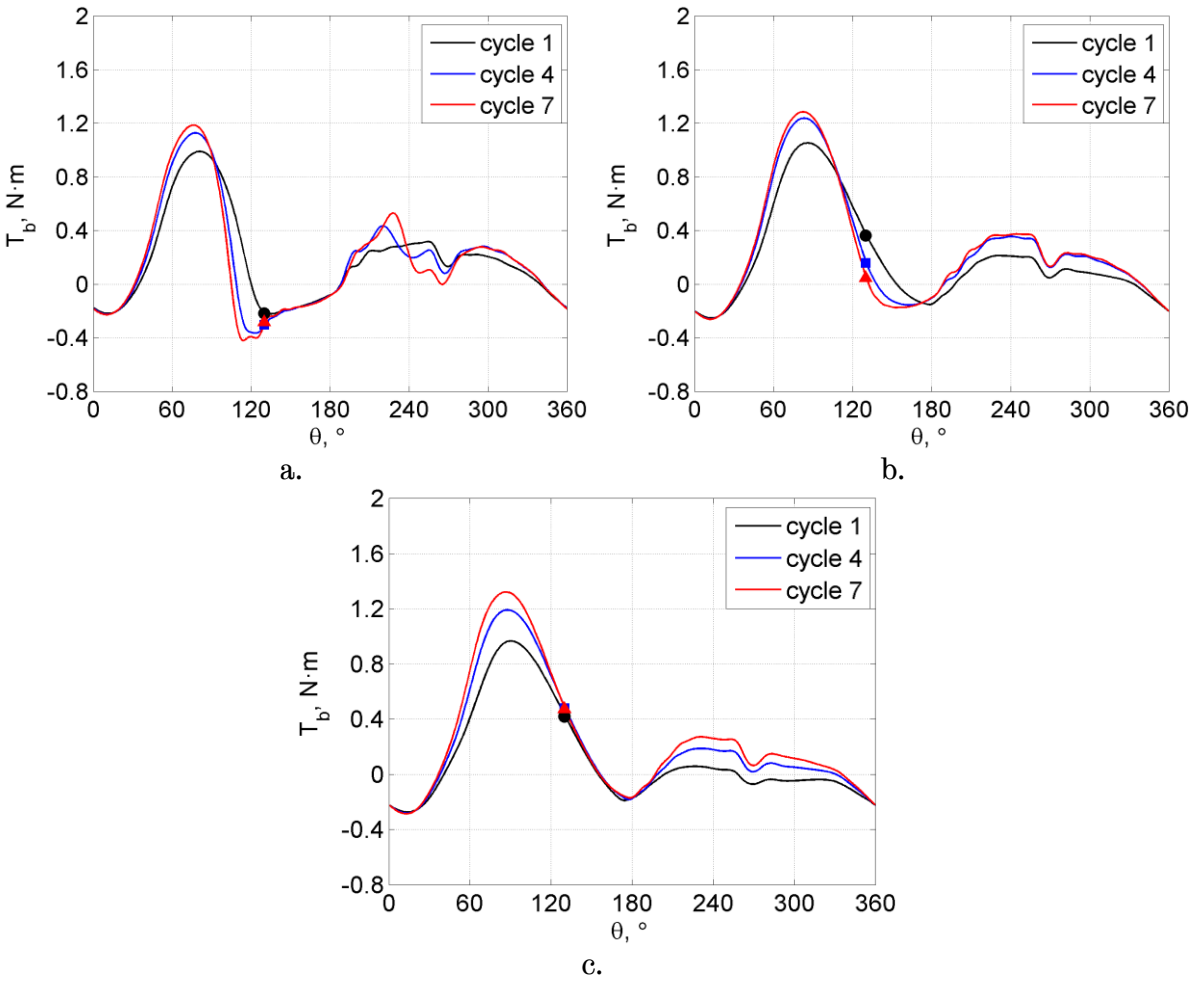

Figure 6.29. Blade torque T_b plots from three rotor cycles of the different λ_{mean} cases (markers are T_b at θ = 130°): a) λ_{mean} = 3.9, b) λ_{mean} = 4.4, c) λ_{mean} = 4.75.

6.3.3 Effect of Varying the Fluctuation Amplitude

The effects of the amplitude of fluctuation U_{amp} was investigated by running two simulations at U_{amp} = ±7% (±0.49m/s) and U_{amp} = ±30% (±2.1m/s) and compared to the reference case of U_{amp} = ±12% (±0.84m/s). The variation of λ in time for the three λ_{mean} cases is shown in Figure 6.30a. From Sec. 6.3.2, the maximum λ of the reference case at U_{amp} = ±12% is recorded at 5.0 while the minimum is at 3.93. The peak–to–peak value is for this case is 1.07. The case with the highest U_{amp} = ±30% shows the maximum λ has jumped to 6.28 while the minimum is now at 3.38 resulting in a peak–to–peak value of 2.9. A not so extreme behaviour is observed when U_{amp} = ±7%. The maximum λ is seen to be 4.73 while the minimum is 4.11 giving a peak–to–peak value of 0.62. With a common ω = 88rad/s (840rpm), the

peak–to–peak value increases as the U_{amp} increases due to the expanding limits of U_∞. The trend of the CP curves is simple and straightforward. Each half of the wind cycle shows a trough in the CP curve at the point of an extreme value of U_∞ specifically at the quarter cycle (t = 0.5s) and three quarter cycle (t = 1.5s). From Figure 6.30b, the CP at quarter cycle falls from 0.34 to 0.32 then to 0.23 with increasing U_{amp} from 7% to 12% then to 30%. A more severe drop in CP is seen at the three quarters cycle where the increasingly negative U_{amp} from –7% to –12% then to –30% cause the CP to plummet from 0.29 to 0.24 down to –0.19. The CP at the start, middle and end of the wind cycle is common for all U_{amp} cases.

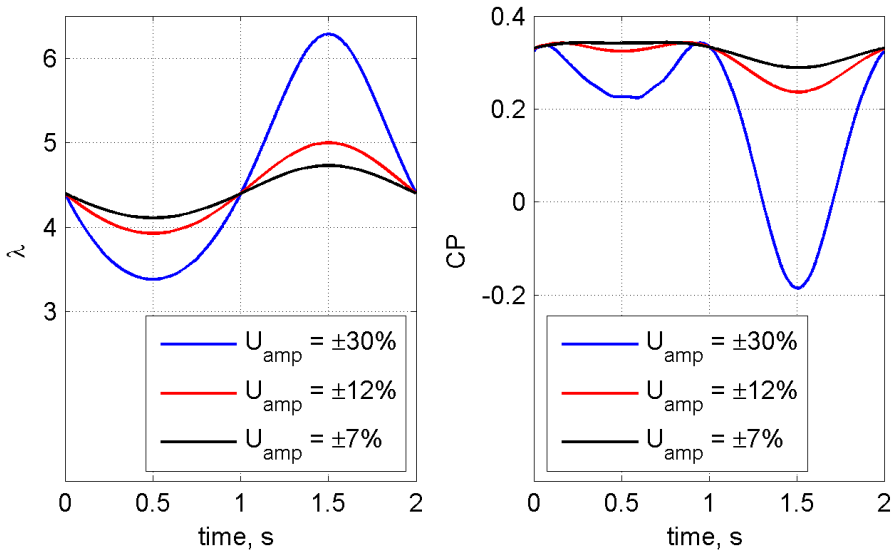

a. b.

Figure 6.30. Quasi–steady performance of the VAWT for the different U_{amp} cases: a) λ vs. time, b) CP vs. time.

U_{amp}	±7%	±12%	±30%
cycle–averaged CP	0.35	0.33	0.25

Table 6.2. Wind cycle–averaged CP at different U_{amp}.

The quasi–steady CP curves of all three cases are shown in Figure 6.31. It can be seen from the figure that the curves are overlapping and essentially coincident, over their ranges of λ. Both the U_{amp} = ±7% and U_{amp} = ±12% cases trace the quasi–steady CP curve of the U_{amp} = ±30% case. Maximum instantaneous CP is 0.34 for all three cases close to λ = 4.2. The cycle–averaged CP for U_{amp} = ±7% is 0.35 while

that of U_{amp} = ±30% is 0.25. When compared to the reference case cycle–averaged CP of 0.33, a significant drop (24% reduction) in performance is observed for the largest fluctuation amplitude of U_{amp} = ±30% while a marginal improvement (6% increase) is seen for the smallest fluctuation amplitude at U_{amp} = ±7%. At the highest instantaneous λ, the CP registers at –0.19 (λ = 6.29) for the U_{amp} = ±30% case, while it is 0.29 (λ = 4.73) for the U_{amp} = ±7% case. The extent of the quasi–steady CP curve is longer relative to the λ_{mean} point as the wind cycle goes through the second half causing the λ to rise to much higher values versus the first half. The non–linear inverse relationship of U_∞ to λ is the primary factor behind the asymmetric behaviour of the quasi–steady CP.

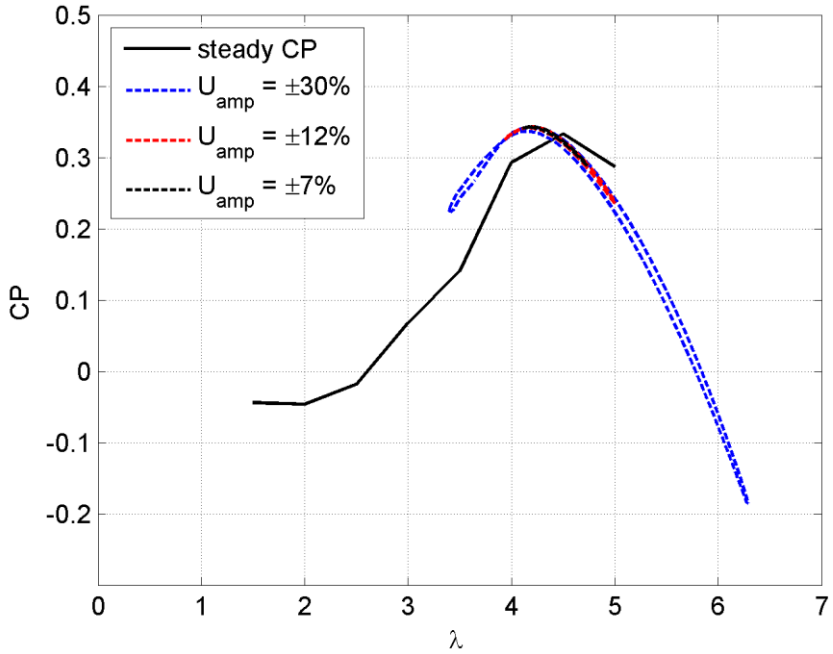

Figure 6.31. Study on the effect of varying U_{amp}.

The stalling of one blade at different rotor cycles within the first quarter of the wind cycle is shown in Figure 6.32. Again, all images shown are for the azimuth position θ = 130°. Starting with the smallest fluctuation amplitude of U_{amp} = ±7%, the deepest stall that the blades see is only partial stall from the trailing edge to mid–chord of the blade (Figure 6.32a, d & g). The wake is thin and there are no visible structures shed from the blade, as well as pronounced wiggling of the wake tail, likely due to the stagnation point staying near or at the trailing edge. The T_b

for the three cycles at θ = 130° do not differ very much, as shown in Figure 6.33a where it is 0.36N·m for cycle 1, 0.30N·m for cycle 4, and 0.27N·m for cycle 7. The reference case of U_{amp} = ±12% shows a progressively deepening stall but with no shed vortices and slight wiggling of the trailing edge wake (Figure 6.32b, e & h). The T_b values at θ = 130° range from a high 0.36N·m at cycle 1 to a low of 0.05N·m at cycle 7 (Figure 6.33b).

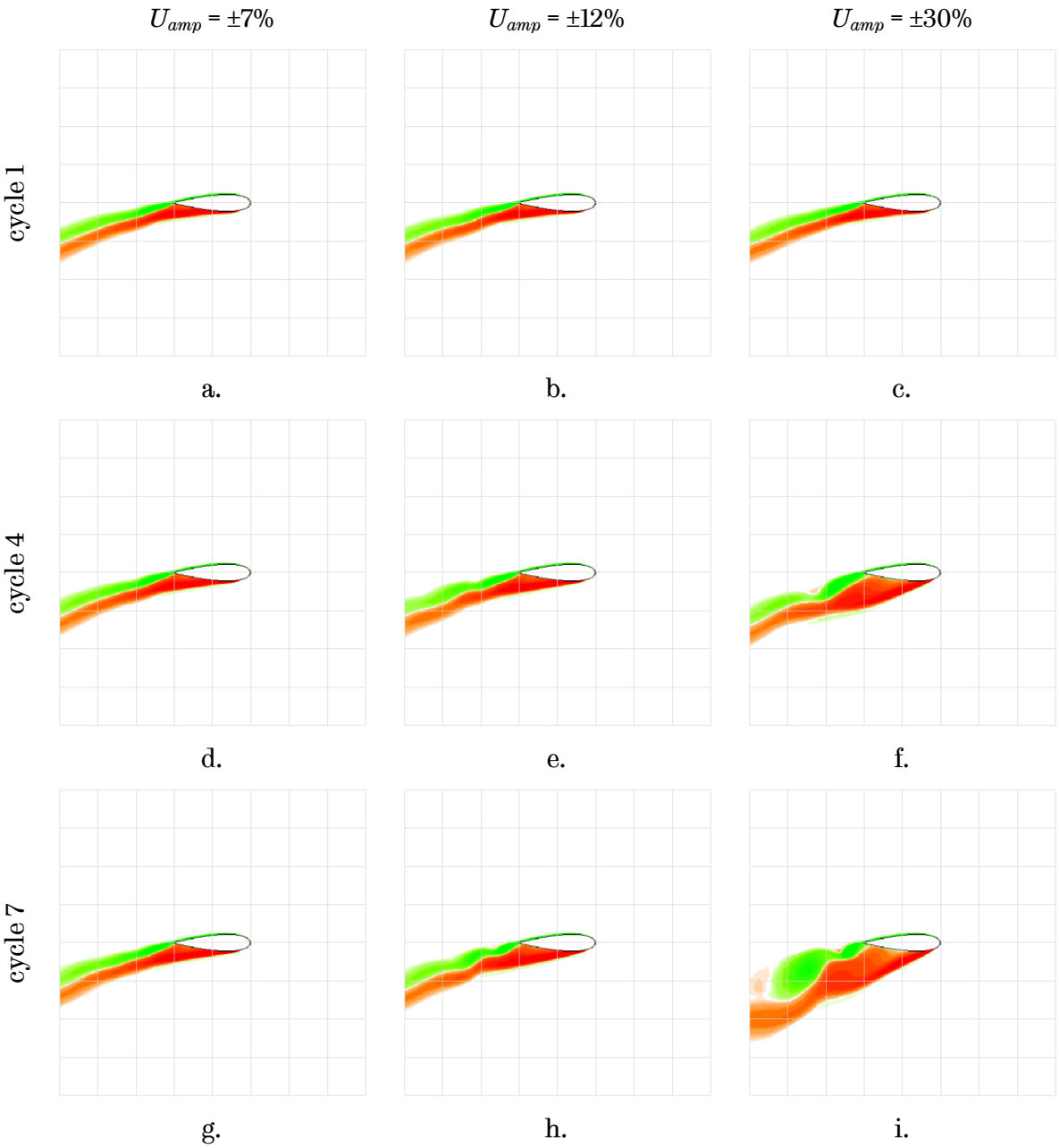

Figure 6.32. Flow visualisations of vorticity from selected rotor cycles in the first quarter of the wind cycle showing effects of varying U_{amp} at θ = 130°.

The last case with the largest fluctuation amplitude at U_{amp} = ±30% shows a drastic change in stalling behaviour from shallow stalling at cycle 1 to very deep stalling at cycle 4 and cycle 7 (Figure 6.32c, f & i). The wake of the blade changes from a thin strip at cycle 1 to a thick and complex wake at cycle 7 that involves alternating pairs of almost chord–sized shed vortices. These huge differences in stalling affect the T_b generated by the blades as Figure 6.33c shows. Cycle 1 T_b is positive 0.36N·m while cycle 4 and cycle 7 T_b are –0.38N·m and –0.39N·m, respectively.

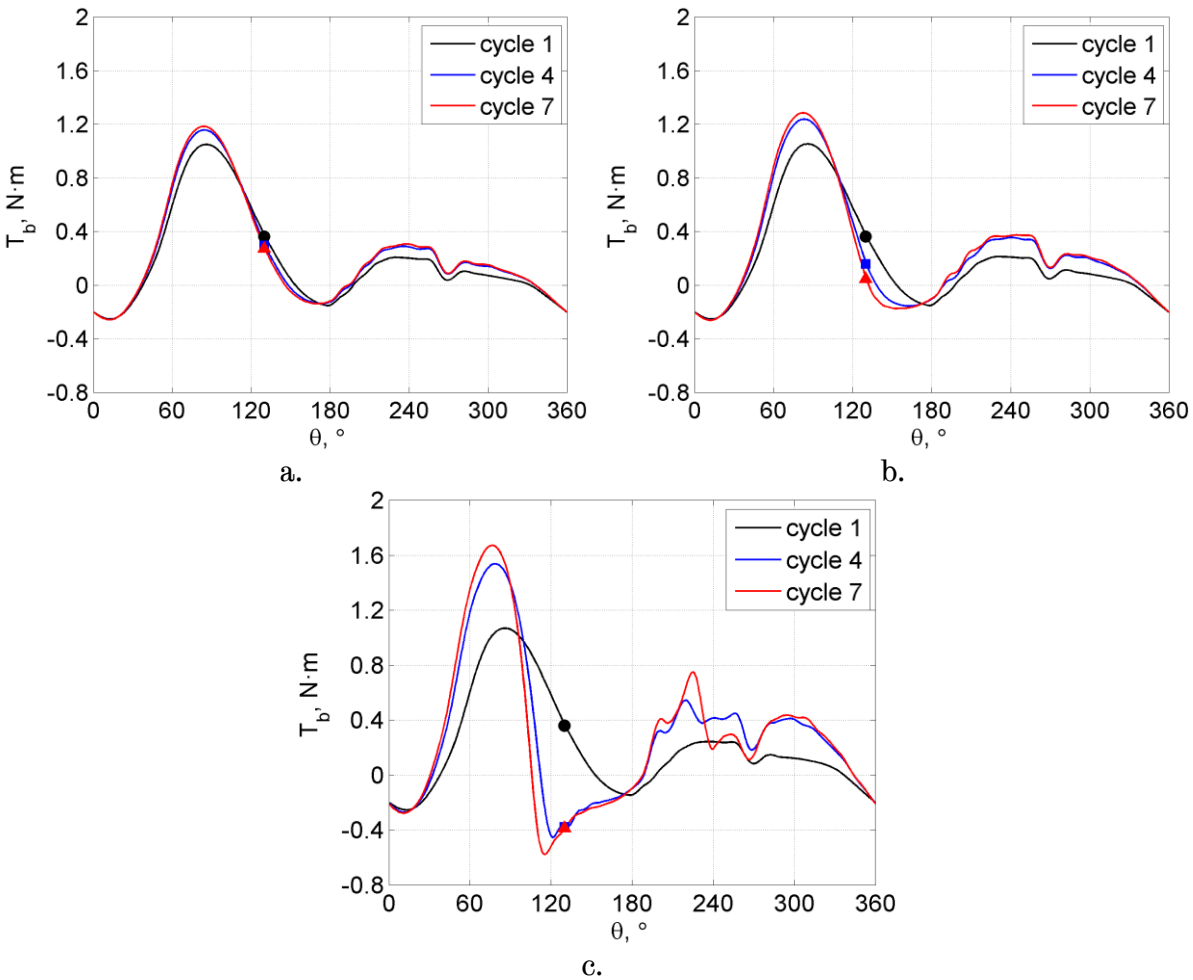

Figure 6.33. Blade torque T_b plots from three rotor cycles of the different U_{amp} cases (markers are T_b at θ = 130°): a) U_{amp} = ±7%, b) U_{amp} = ±12%, c) U_{amp} = ±30%.

Scheurich and Brown [60] conducted a study to investigate the influence of fluctuation amplitude on the overall performance of a 5kW VAWT. Results are presented in Figure 6.34 and it is apparent in the figures that the behaviour of the

unsteady CP almost follows the steady profile as a result of the low reduced gust frequency of k_g = 0.08, which requires 14 rotor cycles to complete one wind cycle. The width of the λ range is wider for the U_{amp} = ±30% case than the U_{amp} = ±10% case. What they have found was that the cycle–averaged CP of the straight–bladed VAWT was greatly affected by the magnitude of the U_{amp} and when compared to an 'ideal' case VAWT in steady wind, the cycle–averaged CP dropped to 92% of the ideal CP when U_{amp} = ±30% while the cycle–averaged CP slightly fell to 99% of the ideal CP when U_{amp} = ±10%. Kooiman and Tullis [66] determined in their field tests that fluctuation amplitude has a linear effect on the performance of the VAWT and that a ±15% fluctuation only reduced performance by 3.6% from ideal wind conditions.

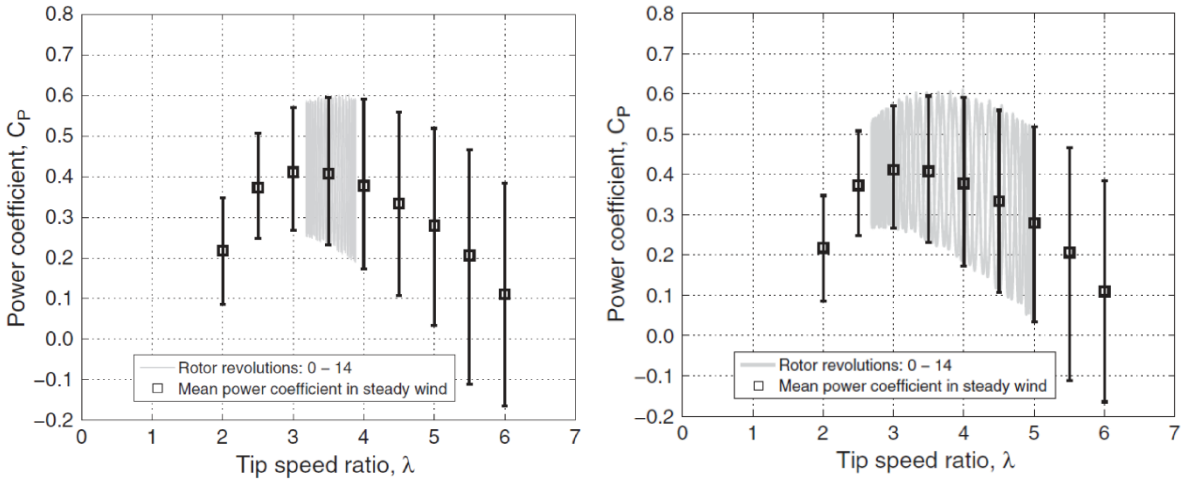

Figure 6.34. Fluctuation amplitude study by Scheurich and Brown [60]: a) U_{amp} = ±10%, b) U_{amp} = ±30%.

6.3.4 Effect of Varying the Fluctuation Frequency

The effects of the varying fluctuation frequencies f_c was investigated by running two simulations at f_c = 1Hz and f_c = 2Hz and compared to the reference case of f_c = 0.5Hz. The variation of λ in time for the three f_c cases is shown in Figure 6.35a. It is evident that the λ variations of the two higher f_c cases have the same maximum of 5 and minimum of 3.93 as the reference case. The λ plots are

seen to be compressed laterally as f_c increases resulting in shorter periods (t_c = 1s for f_c = 1Hz, t_c = 0.5s for f_c = 2Hz).

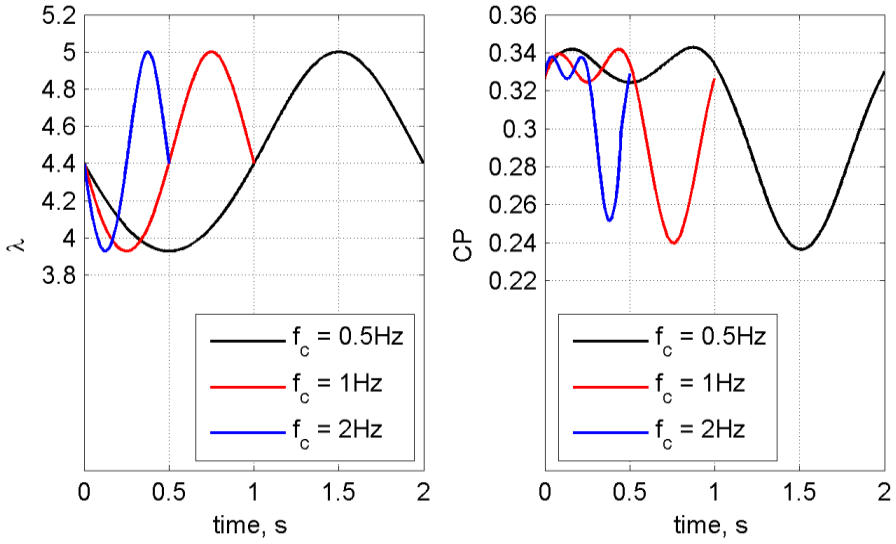

a. b.

Figure 6.35. Quasi–steady performance of the VAWT for the different f_c cases: a) λ vs. time, b) CP vs. time.

f_c	0.5Hz	1Hz	2Hz
cycle–averaged CP	0.33	0.33	0.34

Table 6.3. Wind cycle–averaged CP at different f_c.

The CP variations between f_c cases show some slight contraction in the peaks and troughs as f_c increases. From Figure 6.35b, the minimum CP of the reference case is 0.236 while the case with f_c = 1Hz shows a small rise of the minimum to 0.24 and with f_c = 2Hz to 0.25. The maximum CP also changes in decreasing values of 0.343, 0.342, and 0.338 for f_c = 0.5Hz, 1Hz, and 2Hz, respectively. At points within the wind cycle where U_∞ = 7m/s (start, midway, and end), the predicted CP for all f_c cases are within the 0.32 – 0.33 range. These changes are considered to be negligible as the cycle–averaged CP marginally changes from 0.33 for the reference case and the f_c = 1Hz case to 0.34 for the f_c = 2Hz case. This is shown more clearly in the CP–λ plot in Figure 6.36. The CP curves of the three f_c cases are essentially on top of each other with very little deviation of the highest f_c case in the high λ region. As far as this study is concerned, these differences are

insignificant and can be considered negligible within the test parameters that have been investigated.

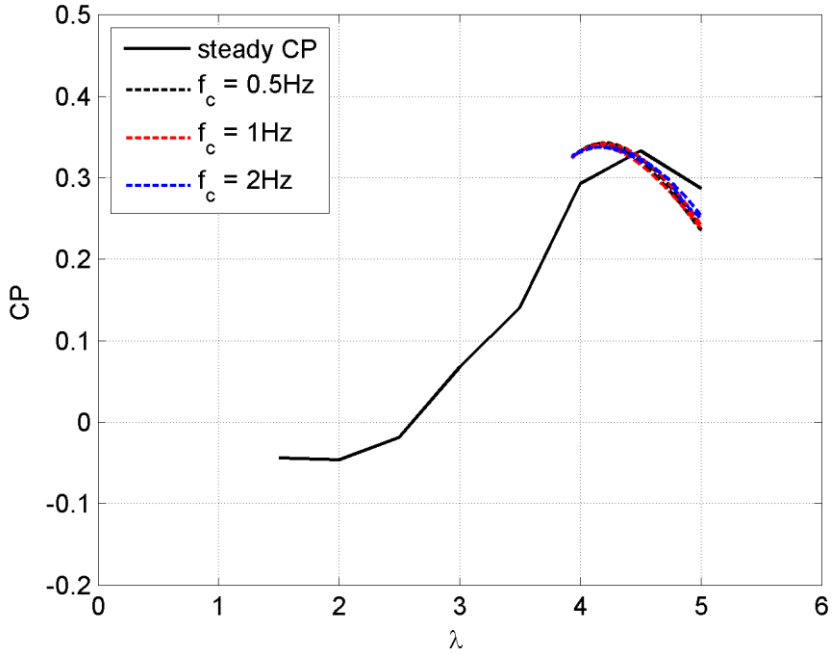

Figure 6.36. Study on the effect of varying f_c.

A study on the effects of fluctuation frequency was conducted by Scheurich and Brown [60] for fluctuation amplitudes of ±10% and ±30%. For each fluctuation amplitude, two f_c's were tested, a low f_c of 0.1Hz and a high f_c of 1Hz. The results for the U_{amp} = ±30% are shown in Figure 6.37a–b. The most apparent observation is that the unsteady CP of both f_c cases generally fall within the limits of the steady CP performance band. As the higher f_c entails fewer rotor cycles per wind cycle, the resulting plot is less condensed with sparsely crisscrossing unsteady CP lines. Cycle–averaged CP increases by less than 2% when f_c changes from 0.1Hz to 1Hz. At a lower U_{amp} of ±10%, the cycle–averaged CP change is even smaller at less than 1% for the same f_c change from 0.1Hz to 1Hz. In contrast, McIntosh et al [63] present increased performance as f_c rises from 0.05Hz to 0.5Hz, especially at operating conditions near peak performance. Danao and Howell [51] studied the effects of different fluctuating frequencies on a VAWT subjected to unsteady wind with U_{mean} = 6.64m/s, U_{amp} = ±50% and λ_{mean} = 4. All of the cases predict performance degradation under any fluctuation frequency. While the present work shows a 25% drop in cycle–averaged CP for conditions of f_c = 0.5Hz and U_{amp}

= ±30%, their data show a 75% drop in cycle–averaged CP when conditions are f_c = 1.16Hz and U_{amp} = ±50%. An even higher and unrealistic f_c = 2.91Hz shows the cycle–averaged CP to be very close to the slower case, thus agreeing to the results of the present work. The case with the highest f_c at 11.6Hz is equal to the rotational frequency of the VAWT and is likely not observable in actual conditions, but results still show a drop in performance by about 50%.

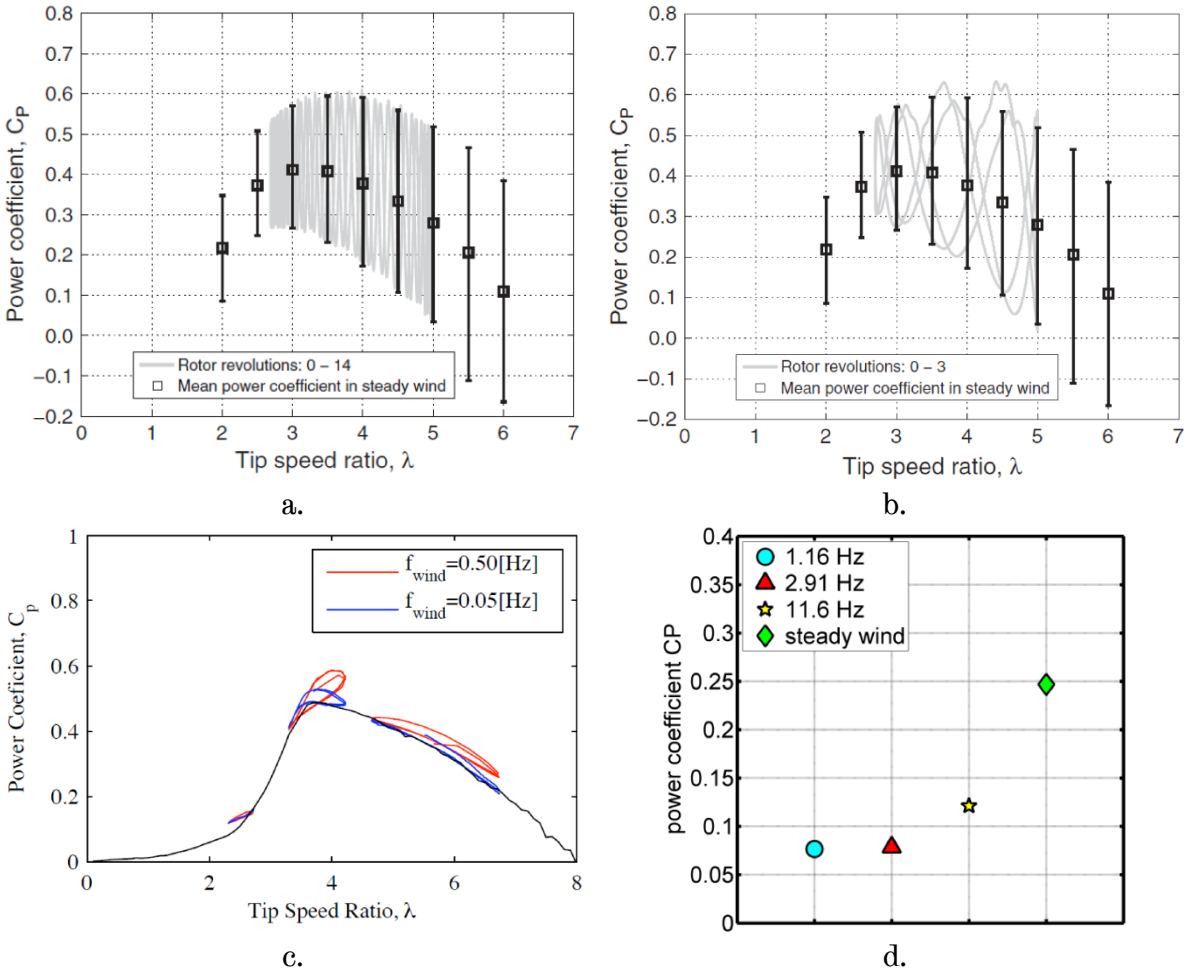

Figure 6.37. Fluctuation frequency study: a) Scheurich and Brown [60], f_c = 0.1Hz, b) Scheurich and Brown [60], f_c = 1Hz; c) McIntosh et al [63], d) Danao and Howell [51].

6.4 Summary

Numerical simulations using RANS–based CFD have been utilised to carry out investigations on the effects of steady and unsteady wind in the performance of a wind tunnel VAWT. Using a validated CFD model, steady wind simulations at U_∞ = 7m/s were conducted and results have shown a typical performance curve prediction for this particular VAWT scale. Within the low λ range, there is a distinct negative trough, with drag–dominated performance consistent to experimental results. Minimum CP is computed to be –0.04 at λ = 2 and positive CP is predicted to be attained at λ's higher than 2.5. Maximum CP is 0.33 at λ^* = 4.5 and a shift in the CFD–predicted CP curve to higher λ's is observed relative to the experimental CP profile. A closer inspection of two λ's reveals the fundamental aerodynamics driving the performance of the VAWT. At λ = 2, the blades experience stalled flow initially from a separation bubble forming at θ = 60° with subsequent shedding of vortices alternately cast from the blade surface until reattachment occurs very much delayed beyond halfway of the rotation. The same delayed reattachment is observed as the blade completes the rotation with partial stall still visible at θ = 330°. At λ = 4, blade stall is only observed in the second quadrant of rotation with the deepest stall seen at θ = 130°. High values of positive blade torque T_b reaching 1N·m are predicted in the upwind while most of the downwind region from θ = 190° to θ = 340° also produce positive performance that contribute to the overall positive CP of just below 0.3.

Unsteady wind simulations revealed a fundamental relationship between instantaneous VAWT CP and Reynolds number. Following the dependency of CP to Reynolds number from experimental data, CFD data shows a CP variation in unsteady wind that cuts across the steady CP curve as wind speed fluctuates. A reference case with U_{mean} = 7m/s, U_{amp} = ±12%, f_c = 0.5Hz and λ_{mean} = 4.4 has shown a wind cycle mean CP of 0.33 that equals the maximum steady wind CP at λ = 4.5. Lift coefficient loops uncover performance characteristics of a blade at different points in the wind cycle that depict the presence of dynamic stall as lift values

consistently exceed static stall lift in the upwind region. Increasing wind speed causes the instantaneous λ to fall which leads to higher effective α and deeper stalling on the blades. Stalled flow and rapid 'pitch down' motion of the blade induce hysteresis loops in both lift and drag. However, CP–λ loops do not show any hysteresis due to the quasi–steady effect of the very slow fluctuating wind relative to VAWT ω. Increasing wind speeds have more effect on the tangential component of lift than on drag, which helps improve the performance of the VAWT. Decreasing wind speeds limit the perceived α seen by the blades to near static stall thus reducing the positive effect of dynamic stall on lift generation.

Three cases of different λ_{mean} were run to study the effects of varying conditions of VAWT operation on the overall CP. The case with the highest λ_{mean} = 4.75 predict a cycle–averaged CP = 0.35 that is marginally higher than the peak steady wind CP of 0.33. In both the reference case with λ_{mean} = 4.4 and the higher λ_{mean} case, the quasi–steady CP is seen to increase as the wind speed rises. On the other hand, the case with λ_{mean} = 3.9 behaves differently with falling quasi–steady CP as the wind speed increases. All three cases predict cycle–averaged CPs that are close to steady wind performance at λ's corresponding to the λ_{mean} of each case. Maximum quasi–steady CP is observed to occur near λ = 4.2 for all cases.

The effects of varying amplitudes of fluctuation were studied by conducting unsteady wind simulations at U_{amp} of ±7%, ±12% and ±30%. As the magnitude of U_{amp} is increased, a biased detrimental effect is seen in the quasi–steady CP due to the non–linear inverse relationship between U_∞ and λ. Within the second half of the wind cycle where the U_∞ falls below the mean wind speed, the case with U_{amp} = ±30% shows the quasi–steady CP drop to –0.19 as λ shoots to above 6. The U_{amp} = ±30% case is the worst performing with a cycle–averaged CP of 0.25 while the U_{amp} = ±7% case sees an improvement in cycle–averaged CP at 0.35.

Different fluctuation frequencies were also tested and compared to the reference case of f_c = 0.5Hz. Results show performance invariance with respect to fluctuation frequency with cycle–averaged CP changes not exceeding 0.01. The case with the highest f_c of 2Hz has a quasi–steady CP curve that almost traces the CP curve of the reference case, despite it being 4 times faster. Cycle–averaged CP predictions are near the steady wind CP maximum of 0.33.

The following conclusions can be derived from the results. When a VAWT operates in periodically fluctuating wind conditions, overall performance slightly improves if the following are satisfied: the mean tip speed ratio is just above the λ of the steady CP maximum, the amplitude of fluctuation is small (< 10%), and the frequency of fluctuation is high (> 1Hz). Operation in λ_{mean} that is lower than λ^* causes the VAWT to run in the λ band with deep stall and vortex shedding, to the detriment of the VAWT CP. Large fluctuations in wind speed causes the VAWT to run in λ conditions that are drag dominated, thus reducing the positive performance of the wind turbine. Within realistic conditions, higher frequencies of fluctuation marginally improve the performance of the VAWT.

Chapter 7
Conclusions and Recommendations

7.1 Conclusions

An investigation into the effects of unsteady wind inflow on the aerodynamics and performance of a Vertical Axis Wind Turbine (VAWT) was conducted. The motivation of this research was the lack of substantive work regarding VAWT performance in unsteady wind that is conclusive and rigorous. The approach of the very challenging work carried out for this dissertation was to develop and conduct experiments in a wind tunnel environment to establish a reference data set of both steady wind and unsteady wind conditions. To further understanding, a RANS–based Computational Fluid Dynamics model validated against the experimental data was utilised to provide additional insight into VAWT behaviour, where experimental measurement was deemed impractical.

A new method of generating unsteady flow in a wind tunnel has been presented. The consistency and reliability of the results prove that with simple mechanisms, it is possible to conduct unsteady wind experiments for performance testing of VAWTs and similar machines with ease and with minimal alterations to the wind tunnel. It has also been shown that the spin down method previously used in steady wind performance testing can be utilised for unsteady wind performance measurements with modifications.

A CFD model of the wind tunnel scale VAWT has been developed and validated. The excellent agreement of the numerical results versus the experimental data permits the extraction and use of blade force data from the numerical model, an endeavour that is not practical in VAWT experiments, particularly at the scales involved in this investigation. The rigorous verification and validation of the CFD model has shown that with the right experimental data, numerical modelling can be a useful tool in VAWT aerodynamics and performance research. The coupling of experiments and numerical models provide an invaluable set of tools to VAWT research and further the current understanding of VAWT performance and the aerodynamics driving it under any wind condition.

The findings of this study are split into four sections: steady wind performance in experiments, unsteady wind performance in experiments, steady wind performance in CFD, and unsteady wind performance in CFD.

7.1.1 Steady Wind Performance in Experiments

The spin down technique and PIV visualisations have revealed the fundamental aerodynamics and performance of VAWTs in steady wind conditions characterised by large variations in angle of attack resulting in blade stall and vortex shedding, especially at low tip speed ratios (λ). The performance of the VAWT over a wide range of λ revealed a negative performance from $\lambda \approx 1$ up to $\lambda \approx 3$, suggesting an inability to self–start, a property characteristic of a rotor

with low solidity and small scale. The negative trough is observed to reduce in depth as wind speeds, and so Reynolds numbers, increase. PIV visualisations at low λ have shown the azimuth positions of stalled flow corresponding to poor performance of the VAWT. At low λ, the blade stalled around $\theta \approx 60°$, with the development of a leading edge separation bubble, eventually forming into a dynamic stall vortex. This vortex grows in size before it is eventually shed and a trailing edge vortex rolls up and is cast off from the blade surface. A series of vortex pairs is shed until reattachment past $\theta = 180°$. Higher λ caused the stalling of the blade in the upwind taking place at a much later azimuth of $\theta \approx 130°$ and reattachment of flow occurring as the blade passes the $\theta = 180°$ position. Stalling and reattachment are observed to be very much delayed when compared to static aerofoil data, which shows the importance of correct and accurate techniques when VAWT modelling is carried out.

7.1.2 Unsteady Wind Performance in Experiments

Unsteady wind experiments show VAWT performance that does not trace steady CP curves. The instantaneous unsteady CP rose above the steady CP curve of the starting wind speed U_∞ and approached the steady CP profile of a higher U_∞. The maximum unsteady CP is greater than the steady CP maximum of U_{mean}. The fall of U_∞ from the mean to its lowest value caused the CP to fall and move towards the steady CP profile of a lower U_∞. The cycle–averaged CP of the VAWT is lower compared to the steady CP value at the corresponding λ_{mean}.

Variations in test conditions have revealed interesting CP behaviour:

- Lowering the λ_{mean} shows the unsteady CP also cutting across steady CP curves. However, a large hysteresis in the CP profile is produced that drastically affects the overall performance of the VAWT, despite a smaller range of CP fluctuation. This hysteresis is a result of deep stall and much delayed reattachment that normally happens at λ below peak performance point λ^*.

- A change in amplitude of wind fluctuation reveals a similar decrease in performance, with the range of the unsteady CP much smaller than the reference case. No visible hysteresis in the CP curve is seen and the deterioration in cycle–averaged CP is much less. Overall, unsteady wind causes a drop in performance of the laboratory scale VAWT tested.

7.1.3 Steady Wind Performance in CFD

Numerical modelling using RANS–based CFD has been carried out to conduct investigations on the effects of steady and unsteady wind in the performance of a wind tunnel VAWT. A validated CFD model reveals a typical steady wind performance curve for this particular VAWT scale. Within the low λ range, there is a distinct negative trough with drag–dominated performance consistent to experimental results. A shift in the CFD–predicted CP curve to higher λ's is observed relative to the experimental CP profile explained by finite blade span effects. A closer inspection of two extreme λ's revealed the fundamental aerodynamics driving the performance of the VAWT. At low λ, the blades experience stalled flow initially from a separation bubble forming at $\theta \approx 60^{\circ}$ followed by the shedding of vortices from the blade surface until reattachment past halfway of the rotation. The same delayed reattachment is observed as the blade completes the rotation with partial stall still visible at $\theta \approx 330^{\circ}$. At high λ, blade stall is only seen in the second quadrant of rotation. High values of positive blade torque T_b are predicted in the upwind, while most of the downwind region produced lower, but positive performance.

7.1.4 Unsteady Wind Performance in CFD

Unsteady wind simulations have shown a fundamental relationship between VAWT CP and Reynolds number. CFD data show a CP variation in unsteady wind that cuts across steady CP curves. A reference case with relatively small wind fluctuations operating near peak steady wind performance has shown a wind

cycle mean CP that equals the maximum steady wind CP. Lift coefficient loops show the presence of dynamic stall phenomenon as lift values consistently exceed static stall lift in increasing wind speed and cause the instantaneous λ to fall causing higher effective α and deeper stalling on the blades. Stalled flow and rapid 'pitch down' motion of the blade are seen as the key reasons of hysteresis loops in both lift and drag. CP–λ loops however do not show similar hysteresis due to the quasi–steady effect of the very slow fluctuating wind in a fast rotating VAWT. Decreasing wind speeds limit the perceived α seen by the blades to near static stall, thus reducing the positive effect of dynamic stall on lift generation.

Studies on the effects of different test conditions show that numerical results mostly agree to experimental data:

- The effects of varying λ_{mean} conditions of VAWT operation on the cycle–averaged CP were explored and compared to the reference case. The case with the highest λ_{mean} predicted a marginally higher cycle–averaged CP than the reference case and the steady wind maximum. When λ_{mean} is higher than λ^*, the quasi–steady CP is seen to increase with the wind speed. On the other hand, when λ_{mean} is lower than λ^*, the quasi–steady CP falls as the wind speed rises. This result is not consistent with observations in the experiments when λ_{mean} was lower from the reference case. All tested cases predict peak quasi–steady CPs occurring near λ = 4.2, lower than the steady wind λ^* = 4.5.

- The effects of varying amplitudes of fluctuation were also studied. Increasing U_{amp} induced a biased negative effect in the quasi–steady CP due to the non–linear inverse relationship between U_∞ and λ. Worst performance is observed within the second half of the wind cycle, where the U_∞ falls below the mean wind speed. In general, increasing U_{amp} brings about a decrease in cycle–averaged CP. A marginal increase in cycle–averaged CP is observed at the lowest U_{amp} with a prediction greater than both the reference case and the steady wind maximum. Experimental results have a slightly conflicting trend

with the cycle–averaged CP of the lowest U_{amp} being higher than the reference case, but not exceeding the steady wind maximum.

- Variation in fluctuation frequencies were also tested and compared to the reference case. Results show that within the frequencies tested, there is no discernible effect of frequency change to the VAWT cycle–averaged CP. Cycle–averaged CP predictions are also seen to be near the steady wind CP maximum.

Periodically fluctuating wind conditions affect the overall performance of the VAWT with slight improvement observed when certain conditions are satisfied: the mean tip speed ratio is just above the λ of the steady CP maximum, the amplitude of fluctuation is small, and the frequency of fluctuation is high. Operation outside these defined conditions may cause the VAWT to run in λ bands with deep stall and vortex shedding or λ conditions that are drag dominated, to the detriment of the VAWT cycle–averaged CP. Within realistic fluctuation frequencies, faster fluctuations marginally improve the performance of the VAWT.

7.1.5 Implications for turbine design

The results presented in this body of work have important implications to the design of VAWTs. The selection of the blade profile is critical to the aerodynamics since it dictates the point and time of stall. The operating Reynolds numbers of the wind tunnel VAWT used in this thesis is between 40,000 and 80,000. Although not presented in this thesis, the Author discussed in a published journal article [50] the effects of various blade profiles on the aerodynamics of a commercial–sized VAWT (Re = 200,000 – 400,000). It was shown that from an aerodynamic point of view, thinner blades are preferred in large scale VAWTs due to increased torque generation as a result of higher pressure gradients. The azimuth position of blade stall was observed to be similar between different blade profiles indicating that at these high Reynolds numbers, performance is

influenced more by pressure forces than by stall. A VAWT with thinner blades is better able to handle the velocity fluctuations in unsteady wind than a thicker blade, given that the mean operating λ is higher than λ^*, because a decrease in wind velocity would result in increased λ and higher drag for thicker blades while an increase in wind velocity would result in lower λ and higher lift for thinner blades. From the results presented here, one can conclude that large scale VAWTs will perform better in unsteady wind conditions when blade profiles used promote greater torque generation from increased lift and reduced drag.

7.2 Recommendations

The work presented in this dissertation is an important step towards a fuller understanding of VAWT performance in unsteady wind conditions. Experiments and numerical investigations described herein address some of the burning questions, but unfortunately are not completely transferable to practical applications, due to the inherent differences between wind tunnel VAWTs and commercial scale VAWTs. Reynolds numbers seen by VAWTs in the field are many times greater than wind tunnel machines. In addition, the simplification of the unsteady wind into a periodic fluctuation does not model the actual conditions in the urban environment. The following suggestions are presented for consideration by future research efforts:

- Although the methods presented in this thesis are translatable to larger scale VAWTs, results remain to be seen and may or may not confirm the relevant flow physics discovered in this study. Larger wind tunnels will permit the testing of VAWT scales that are closer to actual installations. Although more expensive, bigger wind tunnels will allow the testing of some rotors that are sold in the market so that manufacturer's data could be independently verified and tested. Furthermore, more data could be provided beyond that where manufacturers usually stop, i.e. unsteady wind performance. Larger test sections will also allow testing of rotors for blockage effects without being

influenced by Reynolds number issues. This will facilitate the transfer of wind tunnel performance data to open field predictions. Lastly, field tests of full–sized VAWT will provide invaluable data to numerical models such as CFD which will most definitely increase the validity of such numerical predictions.

- One of the disadvantages of the work conducted in this thesis is the inability of the setup to control the behaviour of the rotor. The presence of a control system in the experimental setup will aid in the testing of a larger range of unsteady wind conditions. Control of the rotor speed is essential in testing different λ_{mean}'s, most especially in the region of low λ where the absence of an input drive means the inevitable stopping of VAWT rotation due to negative performance. Additionally, a control and a variable ratio speed reducer in the drive of the shutter mechanism will permit better manipulation of the unsteady wind characteristics, such as larger U_{amp} and faster f_c. A control system that manages all individual modules of the experiment setup will also allow the conduct of PIV visualisations in unsteady wind experiments since fewer variations in rotor rpm will be seen and matching of conditions within the wind cycle will be 'easier' for triggering image acquisition.

- Full three dimensional CFD models will eliminate the effects of infinite blade span in the 2D simulations of this study. A more definite conclusion can be made regarding the accuracy of the turbulence model used as a one–to–one comparison of performance and aerodynamics can be carried out against experimental data. Despite the numerical cost of these models, the amount of information that can be derived from them will dramatically increase the understanding of VAWT behaviour. No deduction will be necessary when predicting actual VAWT performance. Finite blade span effects, such as stall suppression due to end effects and tip–vortex wake entrainment can be scrutinised for improved understanding of performance degradation. Optimised mesh settings and minimal test conditions will make full 3D investigations feasible as computing power increases and more advanced CFD codes are developed.

- The idealised assumptions used in the unsteady wind study can be extended to actual wind fluctuations. The installation of an actual VAWT and a weather station in the built environment for research purposes will be most beneficial as this will supply realistic performance data that will complement the data from controlled wind tunnel conditions. This will reduce the reliance of research endeavours on the limited, if not completely absent, manufacturer field testing data which is of high importance to unsteady wind performance studies. For best results, all efforts should be made to mount the turbine as high as possible to mitigate the severe effects of high roughness terrain.

References

[1] "Climate Change 2007: The Physical Science Basis," Technical Report No. AR4, Intergovernmental Panel on Climate Change, Cambridge, United Kingdom and New York, NY, USA.

[2] Department of Energy Change and Climate. Renewable Energy in 2011, June 2012, Accessed online 31 August 2012, http://www.decc.gov.uk.

[3] Department of Energy Change and Climate. UK Energy in Brief 2012, July 2012, Accessed online 31 August 2012, http://www.decc.gov.uk.

[4] Iida, A., Mizuno, A., and Fukudome, K., 2004, "Numerical Simulation of Aerodynamic Noise Radiated Form Vertical Axis Wind Turbines," The 18th International Congress on Acoustics, Kyoto, Japan.

[5] Mertens, S., Van Kuik, G., and Van Bussel, G., 2003, "Performance of an H-Darrieus in the Skewed Flow on a Roof," Journal of Solar Energy Engineering, 125(4), pp. 433-440.

[6] Edwards, J. M., Danao, L. A., and Howell, R. J., 2012, "Novel Experimental Power Curve Determination and Computational Methods for the Performance Analysis of Vertical Axis Wind Turbines," Journal of Solar Energy Engineering, 134(3), pp. 11.

[7] Raciti Castelli, M., Englaro, A., and Benini, E., 2011, "The Darrieus Wind Turbine: Proposal for a New Performance Prediction Model Based on Cfd," Energy, 36(8), pp. 4919-4934.

[8] Templin, R. J., 1974, "Aerodynamic Performance Theory for the Nrc Vertical-Axis Wind Turbine," Technical Report No. LTR-LA-160, National Research Council of Canada, Ottawa, ON, Canada.

[9] Glauert, H., 1948, *The Elements of Aerofoil and Airscrew Theory, 2nd Ed.*, Cambridge Universtiy Press., Cambridge, UK.

[10] Mcintosh, S. C., 2009, "Wind Energy for the Built Environment," Ph.D. thesis, Cambridge University, Cambridge.

[11] Strickland, J. H., 1975, "The Darrieus Turbine: A Performance Prediction Model Using Multiple Streamtubes," Technical Report No. SAND75-0431, Sandia National Laboratories, Albuquerque, New Mexico.

[12] Wilson, R. E., and Lissaman, P., 1974, "Applied Aerodynamics of Wind Power Machines," Technical Report No. Oregon State University, Corvallis, OR, USA.

[13] Paraschivoiu, I., 1981, "Double-Multiple Streamtube Model for Darrieus Wind Turbines," Second DOE/NASA wind turbines dynamics workshop NASA CP-2186, Cleveland, Ohio, USA.

[14] Larsen, H. C., 1975, "Summary of a Vortex Theory for the Cyclogiro.," Proceedings of the 2nd US National Conferences on Wind Engineering Research, Colorado State University, Colorado, USA.

[15] Fanucci, J., and Walters, R., 1976, "Innovative Wind Machines: The Theoretical Performance of a Vertical-Axis Wind Turbine," In: Proceedings of the vertical-axis wind turbine technology workshop, L. Wetherholt, eds. Albuquerque, NM, USA, pp. 61-93.

[16] Holme, O., 1977, "A Contribution to the Aerodynamic Theory of the Vertical-Axis Wind Turbine," In: Proceedings of the International Symposium on Wind Energy Systems, H. S. Stephens, et al., eds. Cambridge, England, pp. C4 55-72.

[17] Wilson, R. E., 1980, "Wind-Turbine Aerodynamics," Journal of Wind Engineering and Industrial Aerodynamics, 5(3–4), pp. 357-372.

[18] Strickland, J. H., Webster, B. T., and Nguyen, T., 1979, "A Vortex Model of the Darrieus Turbine: An Analytical and Experimental Study," Journal of Fluids Engineering, 101(4), pp. 500-505.

[19] Cardona, J. L., 1984, "Flow Curvature and Dynamic Stall Simulated with an Aerodynamic Free-Vortex Model for Vawt," Wind Engineering, 18(3), pp. 135-143.

[20] Migliore, P., Wolfe, W., and Fanucci, J., 1980, "Flow Curvature Effects on Darrieus Turbine Blade Aerodynamics," Journal of Energy, 4(2), pp. 49-55.

[21] Mcintosh, S. C., and Babinsky, H., 2009, "Aerodynamic Modeling of Swept Bladed Vertical Axis Wind Turbines," 47th AIAA Aerospace Sciences Meeting, Orlando, Florida, USA.

[22] Dixon, K., Simao Ferreira, C. J., Hofemann, C., Van Brussel, G. J. W., and Van Kuik, G., 2008, "A 3d Unsteady Panel Method for Vertical Axis Wind Turbines," European Wind Energy Conference & Exhibition (EWEC) 2008, eds. Brussels, pp. 1-10.

[23] Scheurich, F., Fletcher, T. M., and Brown, R. E., 2011, "Simulating the Aerodynamic Performance and Wake Dynamics of a Vertical-Axis Wind Turbine," Wind Energy, 14(2), pp. 159-177.

[24] Brown, R. E., 2000, *Rotor Wake Modeling for Flight Dynamic Simulation of Helicopters*, American Institute of Aeronautics and Astronautics, Reston, VA, USA.

[25] Simão Ferreira, C. J., Van Brussel, G. J. W., and Van Kuik, G., 2007, "2d Cfd Simulation of Dynamic Stall on a Vertical Axis Wind Turbine: Verification and Validation with Piv Measurements," *45th AIAA Aerospace Sciences Meeting and Exhibit*, Reno, Nevada.

[26] Hamada, K., Smith, T. C., Durrani, N., Qin, N., and Howell, R., 2008, "Unsteady Flow Simulation and Dynamic Stall around Vertical Axis Wind Turbine Blades," 46th AIAA Aerospaces Sciences Meeting and Exhibit, Reno, Nevada, USA

[27] Howell, R., Qin, N., Edwards, J., and Durrani, N., February 2010, "Wind Tunnel and Numerical Study of a Small Vertical Axis Wind Turbine," Renewable Energy, 35(2), pp. 412-422.

[28] Edwards, J., Durrani, N., Howell, R., and Qin, N., 2007, "Wind Tunnel and Numerical Study of a Small Vertical Axis Wind Turbine," 45th AIAA Aerospace Sciences Meeting and Exhibit, Reno, Nevada, USA

[29] Mclaren, K., Tullis, S., and Ziada, S., 2011, "Computational Fluid Dynamics Simulation of the Aerodynamics of a High Solidity, Small-Scale Vertical Axis Wind Turbine," Wind Energy, 15(3), pp. 349-361.

[30] Shedahl, R. E., and Klimas, P. C., 1981, "Aerodynamic Characteristics of Seven Symmetrical Airfoil Sections through 180-Degree Angle of Attack for Use in Aerodynamic Analysis of Vertical Axis Wind Turbines.," Technical Report No. SAND80-2114, Sandia National Laboratories, Albuquerque, New Mexico.

[31] Lee, T., and Gerontakos, P., 2004, "Investigation of Flow over an Oscillating Airfoil," Journal of Fluid Mechanics, 512(pp. 313-341.

[32] Iida, A., Mizuno, A., and Fukudome, K., 2007, "Numerical Simulation of Unsteady Flow and Aerodynamic Performance of Vertical Axis Wind Turbines with Les," 16th Australasian Fluid Mechanics Conference, P. Jacobs, et al., eds. Gold Coast, Australia, pp. 1295-1298.

[33] Simão Ferreira, C. J., Bijl, H., Van Bussel, G., and Van Kuik, G., 2007, "Simulating Dynamic Stall in a 2d Vawt: Modeling Strategy, Verification and Validation with Particle Image Velocimetry Data," Journal of Physics: Conference Series, 75(1), pp. 012023.

[34] Wilcox, D. C., 1994, *Turbulence Modeling for Cfd*, Griffin Printing, Glendale.

[35] Mccroskey, W. J., 1981, "The Phenomenon of Dynamic Stall," Technical Report No. NASA TM-81264, Ames Research Center, Moffett Field, California.

[36] Martinat, G., Braza, M., Hoarau, Y., and Harran, G., 2008, "Turbulence Modelling of the Flow Past a Pitching Naca0012 Airfoil at 10^5 and 10^6 Reynolds Numbers," Journal of Fluids and Structures, 24(2008), pp. 1294-1303.

[37] Wang, S., Ingham, D. B., Ma, L., Pourkashanian, M., and Tao, Z., 2010, "Numerical Investigations on Dynamic Stall of Low Reynolds Number Flow around Oscillating Airfoils," Computers and Fluids, 39(9), pp. 1529-1541.

[38] Wang, S., Ma, L., Ingham, D. B., Pourkashanian, M., and Tao, Z., 2010, "Turbulence Modelling of Deep Dynamic Stall at Low Reynolds Number," World Congress on Engineering 2010, London, UK.

[39] Wernert, P., Geissler, W., Raffel, M., and Kompenhans, J., 1996, "Experimental and Numerical Investigations of Dynamic Stall on a Pitching Airfoil," AIAA Journal, 34(5), pp. 982-989.

[40] Beri, H., and Yao, Y., 2011, "Effect of Camber Airfoil on Self Starting of Vertical Axis Wind Turbine," Journal of Environmental Science and Technology, 4(pp. 302-312.

[41] Untaroiu, A., Wood, H. G., Allaire, P. E., and Ribando, R. J., 2011, "Investigation of Self-Starting Capability of Vertical Axis Wind Turbines Using a Computational Fluid Dynamics Approach," Journal of Solar Energy Engineering, 133(4), pp. 041010-8.

[42] Raciti Castelli, M., Ardizzon, G., Battisti, L., Benini, E., and Pavesi, G., 2010, "Modeling Strategy and Numerical Validation for a Darrieus Vertical Axis Micro-Wind Turbine," ASME Conference Proceedings, 2010(44441), pp. 409-418.

[43] Menter, F. R., Kuntz, M., and Langtry, R., 2003, "Ten Years of Industrial Experience with the Sst Turbulence Model," Turbulence, Heat and Mass Transfer IV, K. Hanjalic, et al., eds. Antalya, Turkey, pp. 625–632.

[44] Amet, E., Maitre, T., Pellone, C., and Achard, J. L., 2009, "2d Numerical Simulations of Blade-Vortex Interaction in a Darrieus Turbine," Journal of Fluids Engineering, 131(11), pp. 111103-15.

[45] Laneville, A., and Vittecoq, P., 1986, "Dynamic Stall: The Case of the Vertical Axis Wind Turbine," Journal of Solar Energy Engineering, 108(2), pp. 140-145.

[46] Nobile, R., Vahdati, M., Barlow, J., and Mewburn-Crook, A., 2011, "Dynamic Stall for a Vertical Axis Wind Turbine in a Two-Dimensional Study," World Renewable Energy Congress - Sweden, Linköping, Sweden.

[47] Simão Ferreira, C. J., Van Zuijlen, A., Bijl, H., Van Bussel, G., and Van Kuik, G., 2010, "Simulating Dynamic Stall in a Two-Dimensional Vertical-Axis Wind Turbine: Verification and Validation with Particle Image Velocimetry Data," Wind Energy, 13(1), pp. 1-17.

[48] Dai , Y. M., and Lam, W., 2009, "Numerical Study of Straight-Bladed Darrieus-Type Tidal Turbine," Proceedings of the Institution of Civil Engineers - Energy, 162(2), pp. 67 -76.

[49] Consul, C. A., Willden, R. H. J., Ferrer, E., and Mcculloch, M. D., 2009, "Influence of Solidity on the Performance of a Cross-Flow Turbine " Proceedings of the 8th European Wave and Tidal Energy Conference., Uppsala, Sweden.

[50] Danao, L. A., Qin, N., and Howell, R., 2012, "A Numerical Study of Blade Thickness and Camber Effects on Vertical Axis Wind Turbines," Proceedings of the Institution of Mechanical Engineers, Part A: Journal of Power and Energy, pp. 15.

[51] Danao, L. A., and Howell, R., 2012, "Effects on the Performance of Vertical Axis Wind Turbines with Unsteady Wind Inflow: A Numerical Study," 50th AIAA Aerospace Sciences Meeting including the New Horizons Forum and Aerospace Exposition, Nashville, Tennessee.

[52] Jacobs, E., and Sherman, A., 1937, "Airfoil Section Characteristics as Affected by Variations of the Reynolds Number," Technical Report No. 586, National Advisory Committee for Aeronautics, Washington, D.C.

[53] Healy, J. V., 1978, "The Influence of Blade Thickness on the Output of Vertical Axis Wind Turbines," Wind Engineering, 2(1), pp. 1-9.

[54] Healy, J. V., 1978, "The Influence of Blade Camber on the Output of Vertical-Axis Wind Turbines," Wind Engineering, 2(3), pp. 146-155.

[55] Danao, L. A., Qin, N., and Howell, R., (accepted for publication 2012), "A Numerical Study of Blade Thickness and Camber Effects on Vertical Axis Wind Turbines," Proceedings of the Institution of Mechanical Engineers, Part A: Journal of Power and Energy, pp.

[56] Baker, J. R., 1983, "Features to Aid or Enable Self Starting of Fixed Pitch Low Solidity Vertical Axis Wind Turbines," Journal of Wind Engineering and Industrial Aerodynamics, 15(1–3), pp. 369-380.

[57] Kirke, B. K., 1998, "Evaluation of Self-Starting Vertical Axis Wind Turbines for Stand-Alone Applications," Ph.D. thesis, Griffith University, Gold Coast, Australia.

[58] Bertenyi, T., Wickins, C., and Mcintosh, S. C., 2010, "Enhanced Energy Capture through Gust-Tracking in the Urban Wind Environment," 48th AIAA Aerospace Sciences Meeting Including the New Horizons Forum and Aerospace Exposition, Orlando, Florida.

[59] Scheurich, F., Fletcher, T. M., and Brown, R. E., 2010, "The Influence of Blade Curvature and Helical Blade Twist on the Performance of a Vertical-Axis Wind Turbine," 48th AIAA Aerospace Sciences Meeting Including the New Horizons Forum and Aerospace Exposition, Orlando, Florida.

[60] Scheurich, F., and Brown, R. E., 2012, "Modelling the Aerodynamics of Vertical-Axis Wind Turbines in Unsteady Wind Conditions," Wind Energy, pp. 17.

[61] Armstrong, S., Fiedler, A., and Tullis, S., 2012, "Flow Separation on a High Reynolds Number, High Solidity Vertical Axis Wind Turbine with Straight and Canted Blades and Canted Blades with Fences," Renewable Energy, 41(2012), pp. 13-22.

[62] Armstrong, S., and Tullis, S., 2011, "Power Performance of Canted Blades for a Vertical Axis Wind Turbine," Journal of Renewable and Sustainable Energy, 3(1), pp. 013106-11.

[63] Mcintosh, S. C., Babinsky, H., and Bertenyi, T., 2008, "Unsteady Power Output of Vertical Axis Wind Turbines Operating within a Fluctuating Free-Stream," 46th AIAA Aerospace Sciences Meeting and Exhibit, Reno, Nevada.

[64] Mcintosh, S. C., Babinsky, H., and Bertenyi, T., 2007, "Optimizing the Energy Output of Vertical Axis Wind Turbines for Fluctuating Wind Conditions," 45th AIAA Aerospace Sciences Meeting and Exhibit, Reno, Nevada.

[65] Hayashi, T., Hara, Y., Azui, T., and Kang, I.-S., 2009, "Transient Response of a Vertical Axis Wind Turbine to Abrupt Change of Wind Speed," Proceedings of the European Wind Energy Conference and Exhibition, Marseille, France.

[66] Kooiman, S. J., and Tullis, S. W., 2010, "Response of a Vertical Axis Wind Turbine to Time Varying Wind Conditions Found within the Urban Environment," Wind Engineering, 34(4), pp. 389-401.

[67] Hara, Y., Hara, K., and Hayashi, T., 2012, "Moment of Inertia Dependence of Vertical Axis Wind Turbines in Pulsating Winds," International Journal of Rotating Machinery, 2012(2012), pp. 12.

[68] Edwards, J., 2012, "The Influence of Aerodynamic Stall on the Performance of Vawt Blades," Ph.D. thesis, University of Sheffield, Sheffield.

[69] Fujisawa, N., and Takeuchi, M., 1999, "Flow Visualization and Piv Measurement of Flow Field around a Darrieus Rotor in Dynamic Stall," Journal of Visualization, 1(4), pp. 379-386.

[70] Fujisawa, N., and Shibuya, S., 2000, "Observations of Dynamic Stall on Darrieus Wind Turbine Blades," Journal of Wind Engineering and Industrial Aerodynamics, 89(2001)(pp. 201-214.

[71] Simão Ferreira, C. J., Dixon, K., Hofemann, C., Van Kuik, G., and Van Brussel, G. J. W., 2009, "The Vawt in Skew: Stereo-Piv and Vortex Modeling," AIAA 2009-1219, 47th AIAA Aerospace Sciences Meeting, Orlando, Florida, USA.

[72] Simão Ferreira, C. J., Van Brussel, G. J. W., Scarano, F., and Van Kuik, G., 2008, "Piv Visualization of Dynamic Stall Vawt and Blade Load Determination," 46th AIAA Aerospace Sciences Meeting and Exhibit, Reno, Nevada, USA.

[73] Simão Ferreira, C. J., Van Kuik, G., Van Brussel, G. J. W., and Scarano, F., 2009, "Visualization by Piv of Dynamic Stall on a Vertical Axis Wind Turbine," Experiments in Fluids, 46(1), pp. 97-108.

[74] Raffel, M., Willert, C. E., Wereley, S. T., and Kompenhans, J., 2007, *Particle Image Velocimetry: A Practical Guide*, Springer Berlin Heidelberg,

[75] Ansys Inc. Fluent 13.0 Documentation, 2010.

[76] Tullis, S., Fiedler, A., Mclaren, K., and Ziada, S., 2008, "Medium-Solidity Vertical Axis Wind Turbines for Use in Urban Environments," 7th World Wind Energy Conference, St. Lawrence College, Kingston, Ontario.